NORTHWESTERN UNIVERSITY

Atomic-scale Interfacial Studies of Supported Catalysts Using Synchrotron X-rays

A DISSERTATION

SUBMITTED TO THE GRADUATE SCHOOL
IN PARTIAL FULFILLMENT OF THE REQUIREMENTS

for the degree

DOCTOR OF PHILOSOPHY

Field of Materials Science and Engineering

By

Anusheela Das

EVANSTON, ILLINOIS

March 2022

Abstract

Atomic-scale interfacial studies of supported catalysts using synchrotron X-rays

Anusheela Das

Interfacial science brings together diverse areas of interest such as electronic materials, quantum materials, bio-membranes and catalysts. In-situ X-ray characterization techniques can be used to understand the assembly of atoms, molecules and supported nanoparticles at interfaces in complex environments. This thesis work focuses on the use of various X-ray characterization techniques to study redox-induced changes at catalyst-support interface. During redox reactions catalytic systems undergo complex atomic-scale changes. Improving subsequent catalytic properties requires an understanding of these structural and chemical state changes. Vanadium and molybdenum oxides, which represent commercially important materials, form a fascinating class of compounds concerning their crystal structure as well as their electronic properties. The rich and diverse chemistry of these oxides results from the fact that the metal ions can adopt different formal oxidation states in the oxides, ranging from +2 to +5 in the case of vanadium and from +4 to +6 in the case of molybdenum. The versatility of the properties of both oxides leads to their use as active and selective catalysts in many reactions belonging to redox or acid-base processes.

The primary focus of this thesis is on the use of X-ray standing wave excited X-ray photoelectron spectroscopy to follow atomic positional and chemical state changes of vanadium oxide and molybdenum oxide thin film catalyst supported on rutile TiO_2 (110). This gives us 3D composite atomic maps that include the bulk substrate atoms, and surface V or Mo atoms as well as surface O atoms. These results have shown good agreement with density functional theory predictions. The thesis work also extends to X-ray absorption spectroscopy studies of powder molybdenum oxide catalysts which investigates the local coordination and bond lengths around the scattering Mo atom. All the X-ray measurements were made at the two different synchrotron sources: the Advanced Photon Source (APS) in USA and the Diamond Light Source (DLS) in UK.

The XSW-XPS studies were carried out with VO_x and MoO_x thin films grown by atomic layer deposition on α-TiO_2 (110) single crystals. The in-situ X-ray studies were also supported by ex-situ atomic force microscopy and low-energy electron diffraction. Thus, the goal of this thesis work is to explore novel X-ray characterization techniques to study various catalytic systems and get a detailed understanding of the dynamic changes in the atomic scale structures of the catalyst/support interface.

Acknowledgements

I would like to thank my advisor, Prof. Michael Bedzyk, for his tremendous support and guidance throughout my PhD at Northwestern. He is a pioneer in the field of X-ray physics, and it has been an honor to be a part of his group. He has been an excellent teacher and has guided me through my experiments at Northwestern University, the Advanced Photon Source (APS) and the Diamond Light Source (DLS). He has always been available to clear any doubts or discuss various concepts and it has been a privilege to be able to get his mentorship for my PhD. He has been extremely patient and flexible throughout my PhD duration and a constant source of motivation which has enabled me to carry out this thesis work. This has in turn motivated me to continue pursuing a future career in academia.

I am extremely grateful to each of my committee members. I would like to thank Dr. Denis Keane who has been a constant support for all my experiments at APS. His help and guidance during the week-long beamtimes, even at 4 AM, have been instrumental, without which a vast majority of this thesis work wouldn't even be possible. He has always helped in overcoming the obstacles that we faced for our experiments and has been a great guide and teacher.

I am very fortunate to have gotten the opportunity of collaborating with the group of Prof. Tobin Marks for three very interesting projects. This helped me in learning a lot of new concepts and techniques and it has broadened the scope of my research. Prof. Marks has been extremely supportive and have greatly helped and motivated me during my PhD work.

I am very thankful for the guidance of Prof. Justin Notestein. As the director of the Center for Catalysis and Surface Science at Northwestern, he has always been actively involved and extremely helpful in the progress of the research of each student. His valuable advice during and beyond ICEP meetings has helped me in answering some very important research questions and his guidance has propelled me towards successfully completing my PhD thesis work.

I am extremely grateful to all my collaborators without whose contributions this thesis work wouldn't have been possible. I would like to thank Dr. Devika Choudhury, Dr. Haesun Park, Dr. Qing Ma, Dr. Leighton Jones, Dr. Jiaqi Li, Dr. Yosi Kratish, Yiqi Liu, Dr. Jeff Elam, Dr. Peter Zapol, Prof. George Schatz, Dr. Tien-Lin Lee, Dr. Anil Mane. I am also thankful to Jim Rix and Dr. Mike Guise at who have gone out of their way to help with my experiments at sector 5. At DLS, I am thankful for the help of Dr. Pradeep Thakur, Dave McCue and Dr. David Duncan who helped with our experiments in any possible way. At Northwestern, I am thankful for the help of Jerry Carsello from the J.B. Cohen X-ray Diffraction facility and Dr. D. Bruce Buchholz from the Pulsed Laser Deposition facility. Their expertise have helped in the success of this thesis work.

My colleagues in the Bedzyk group have supported me throughout my time here at Northwestern. Firstly, I would like to thank Dr. Yanna Chen, who has not only been a collaborator in my research but has been an excellent partner in the beamtimes. I am very grateful to her for the long discussions about my work which helped tremendously and for being a guide through experiences beyond work, like our camping trips and train ride across USA. I am also thankful to Dr. Achari and Dr. Bo-Hong Liu who have been mentors and partners in beamtimes and whose expertise have helped me learn a lot during my time as a PhD student. I am grateful for the valuable interactions with Dr. Sumit Kewalramani, Dr. Guennadi Evmenenko, Elise Goldfine, Carlos

Torres, Roger Reinertsen, Joseph McCourt, David Garcia, Amol Agarwal and Daniel Duplessis. I also want to thank some of the alumni of the Bedzyk group who has been great mentors: Dr. Li Zeng, Dr. Liane Moreau, Dr. Stephanie Moffitt, Dr. Bor-Rong Chen, Dr. Katherine Harmon, Dr. Kurinji Krishnamoorthy, Dr. Gavin Campbell and Dr. Boris Harutyunyan.

I am extremely grateful to my aunt who has been a great motivation for me. She overcame all obstacles and pursued her PhD in Astrophysics at the age of fifty. She showed me that anything is possible if you want it enough. I am also thankful to my undergraduate advisor Prof. Jayanta Das who played a massive role in sparking my enthusiasm in pursuing a PhD.

I am very thankful to my friend Tathagata Srimani who has been a constant support at each step and has been a key source of motivation. I am also extremely fortunate to have made great friends at Northwestern. Utthara Rameshbabu, who has been a member of my cohort and my roommate, has given me the essence of a home away from home. Surabhi Madhvapathy has been another great friend and a support. Lastly, I would like to thank two of my school friends who have stuck by me for the past 20 years, Oindrila and Anurupa, who have always been ready to talk to discuss any topic in the world anytime.

Finally, I would like to thank parents. I am grateful to them beyond words for their support in my life and for providing an enriching environment where it has been possible to pursue my passion without any barriers. Without them nothing would have been possible and there is no end to how much I am grateful for everything that they have done for me.

The research in this thesis was supported by the U.S. Department of Energy, Office of Science, Office of Basic Energy Sciences, ICEP program, under Award DE-FG02-03ER15457. This work made use of the Keck-II facility and SPID facility of Northwestern University's NUANCE Center, which has received support from the SHyNE Resource (NSF ECCS-2025633), IIN, and Northwestern's MRSEC program (NSF DMR-1720139). This work also used the J. B. Cohen X-ray diffraction facility at Northwestern University supported by the MRSEC program of the National Science Foundation (DMR-1720139). The BRXSW-XPS work used Diamond Light Source (DLS) beamline I09 (DLS proposal number SI15748). The XSW-XPS, XRF and XAS work used DND-CAT at the Advanced Photon Source (APS) at Argonne National Lab funded by DOE (DE-AC02-06CH11357). The ALD work by Dr. Devika Choudhry and Dr. Jeff Elam was done at ANL funded by DOE (DE-AC02-06CH11357). DFT work of Dr. Haesun Park and Dr. Peter Zapol is supported by Laboratory Directed Research and Development (LDRD) funding from Argonne National Laboratory, provided by the Director, Office of Science, of the U.S. Department of Energy under Contract No. DE-AC02-06CH11357. DFT work of Dr. Leighton Jones and Prof. George Schatz is supported by U.S. Department of Energy, Office of Science, Office of Basic Energy Sciences, ICEP program, under Award DE-FG02-03ER15457.

to

The Guru

Table of Contents

List of Abbreviations

BRXSW	Back-reflection X-ray standing wave	**GO**	Graphene oxide
ALD	Atomic Layer Deposition	**rGO**	Reduced graphene oxide
XSW	X-ray standing wave	**DI**	De-ionized
XPS	X-ray photoelectron spectroscopy	**NDC**	Non-dipolar correction
XAS	X-ray absorption spectroscopy	**UHV**	Ultra-high vacuum
EXAFS	Extended X-ray absorption fine structure	**IMFP**	Inelastic mean free path
XANES	X-ray absorption near edge structure	**EAL**	Effective attenuation length
XRF	X-ray fluorescence	**ID**	Information depth
AFM	Atomic force microscopy	**Ox**	Oxidized
LEED	Low energy electron diffraction	**Re**	Reduced
DFT	Density functional theory	**VA**	Vacuum annealed
FWHM	Full width at half maxima	**SO**	Surface oxygen
APS	Advanced Photon Source	**BO**	Bulk oxygen
DLS	Diamond Light Source	**AT**	Atop
ANL	Argonne National Laboratory	**BR**	Bridging
STM	Scanning tunneling microscopy	**NP**	Nanoparticle
DND-CAT	Dupont-Northwestern-Dow Collaborative Access Team	**ML**	Monolayer

List of Figures

List of Tables

Chapter 1

Introduction

1.1 Motivation

Today, the global chemical industry depends critically on catalysts. Nearly every chemical and chemical-derived product, from polymers to pharmaceuticals to fertilizers, requires a catalyst at some point in its production. The multi-billion-dollar catalysis industry is extremely competitive, as new catalysts can drastically reduce the operating costs and feedstock requirements for largescale chemical reactions. A catalyst increases the rate of a chemical reaction by providing a chemical pathway with a low activation energy barrier. It modifies the reaction pathway to reduce the rate-limiting step.

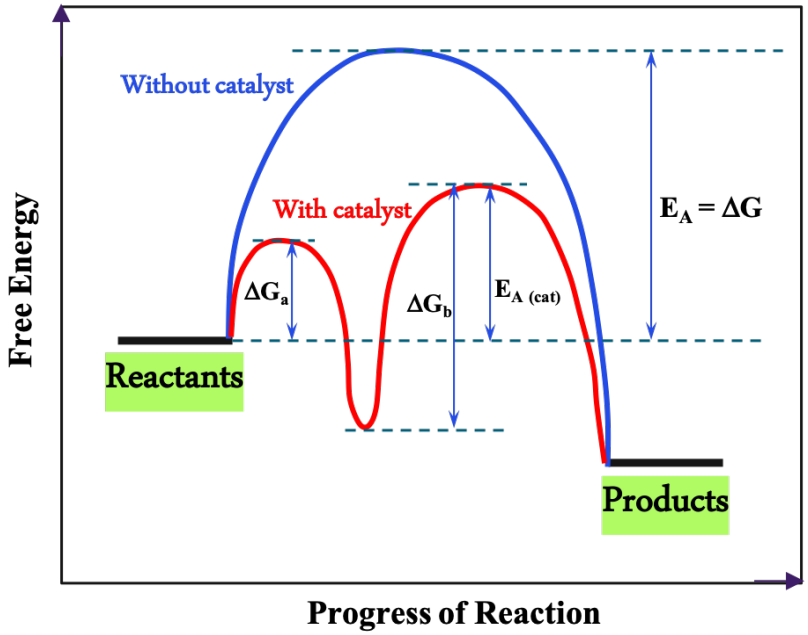

Figure 1.1 *Two pathways for an exothermic reaction with and without the use of a catalyst*

Fig. 1.1 shows two possible pathways for a hypothetical exothermic reaction, with the reaction coordinate proceeding from reactants (on the left) to products (on the right). Although the difference in free energies ΔG between the reactants and products is negative, some activation energy barrier E_A prevents the reaction from occurring spontaneously. The blue line shows the pathway for the reaction without the presence of a catalyst which has a large activation energy barrier. The red line shows the effect of a catalyst on this barrier. The highest energy barrier $E_{A\,(cat)}$ is much lower than E_A, and therefore the rate-limiting step will proceed much faster over the catalyst. The catalyst provides anchoring sites for atoms, molecules, and transition states and can also donate or accept electrons, destabilizing bonds or activating otherwise stable molecules. This improved reactivity at the interface is heterogeneous catalysis[1]. The objective of using a catalyst is to get high conversion of reactants, i.e. high activity and high selectivity to a desired product. High selectivity helps in preventing several purification processes which would otherwise lead to economic and environmental issues. Catalysts are crucial in the energy sector for cracking larger molecules from crude oil into smaller ones for use as fuels, and so advances in catalysis can help us make the most efficient use of non-renewable fuels. Hence, it is very important to study the fundamental behavior of catalysts at the atomic scale in order to understand the structure and function of catalytically active species.

Metal oxides are of immense importance in heterogeneous catalysis. Solid catalysts are structurally very complex. These materials typically consist of metal or metal oxide nanoparticles supported on oxide substrates such as porous silica, zeolites or metal oxides. Metal oxide monolayers or clusters anchored to an oxide support are important catalysts for several industrial catalytic processes such as o-xylene oxidation to phthalic anhydride reaction, pollution abatement of nitrous oxides with NH_3, oxidative dehydrogenation of propane, dehydrogenation of alkanes and selective

oxidation of alcohols/alkanes with only a few byproducts. They also find catalytic application for gas sensors, humidity sensors, Li-ion batteries and fuel cells[2]. There has been extensive research on these catalytic materials to define their molecular-scale structure, however there is very little experimental information on the atomic positions of the metal cations on the support. In addition, theoretical calculations have not been performed for a surface structure that is found experimentally since it is extremely complicated and instead it is based on a simplified or model structure. Therefore, it is necessary to better understand the atomic-scale electronic and geometric structure of these catalysts. Individually, the catalyst and support particles span a range of shapes and sizes, and they feature a variety of surface defects and a great deal of crystallographic inhomogeneity. Interfacial effects between the catalyst and support must also be considered. The catalyst surface may support a variety of physisorbed and chemisorbed species on various surface sites. Catalysis research focuses on defining and understanding the sites on the catalyst surface that are most responsible for their useful behavior. The performance of metal-oxide catalysts depends on their nature, size, shape, and, surface area, and their relationship is a critical factor in determining catalytic activity and selectivity.

This dissertation focuses on the use of various advanced X-ray techniques, combined with other surface characterization methods, to study redox induced atomic-scale structural changes in metal oxide catalysts (VO_X, MoO_X) supported on high surface area substrates (α-TiO_2 (110), carbon). The main focus is on X-ray standing waves (XSW) which interrogates the formation of new surface structures that may or may not be correlated with the underlying single crystal support lattice. Combining XSW with X-ray photoelectron spectroscopy (XPS) can define relationships between the atomic-scale structure and chemical behavior of the catalytically active cations. This enables us to replace chemically intuitive models of oxide-supported catalysts with X-ray standing

wave measured 3D atomic density maps with chemical state sensitivity. Fig. 1.2(a) shows the simple intuitive model of vanadium oxide catalyst supported on α-TiO_2 single crystal with a one monolayer (ML) VO_2 rutile on TiO_2 rutile epitaxial structure, whereas Fig. 1.2(b) gives the composite 3D atomic density map showing surface V and O obtained from the in-situ XSW-XPS experiments. Density functional theory (DFT) will be used to fill in the undetected H atoms in the surface hydroxyl groups.

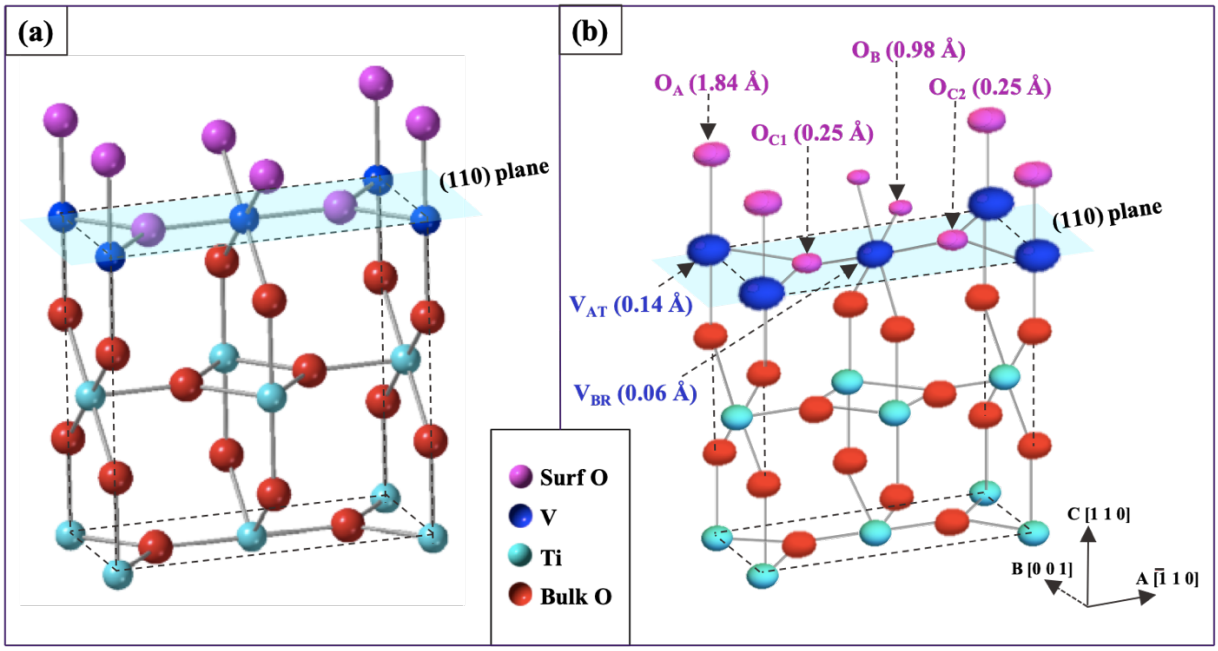

Figure 1.2 (a) *A ball and stick model for the rutile VO_2 on rutile TiO_2 (110) structure* ***(b)*** *XSW measured 3D V and O composite atomic density map for ALD grown 0.5 ML VO_x/α-TiO_2 (110).*[3]

The other focus is on X-ray absorption spectroscopy (XAS) which includes X-ray absorption near edge structure (XANES) and extended X-ray absorption fine structure (EXAFS). This is used to study the coordination environment and bond structure of supported powder catalysts.

A better understanding of these types of catalytic materials could make a broad impact, leading to new opportunities in the development of more advanced heterogeneous catalysts.

1.2 Outline

This dissertation is organized into 9 chapters. **Chapter 2** serves as a background review of the catalytic systems studied. It describes the two catalyst supports studied and also gives a brief background of the two main heterogeneous catalysts that are the focus of this dissertation. **Chapter 3** introduces the film growth and characterization techniques employed in this dissertation. It gives detailed description of each method and instrumentation used for these experiments. **Chapter 4** presents vanadium oxide supported on rutile TiO_2(110) catalytic system. This includes synthesis and characterization, data analysis and results based on X-ray standing wave excited photoelectron spectroscopy. **Chapter 5** talks in detail about 3D atomic density mapping of surface oxygens on this VO_x / α-TiO_2 (110) system using the XSW-XPS method. This is followed by **Chapter 6** which moves onto another important catalytic system: MoO_x / α-TiO_2 (110). This chapter presents X-ray standing wave results for molybdenum oxide monolayer film with details about film growth, characterization, data analysis and results. As chapter 6 focused on molybdenum oxide catalyst supported on single crystal substrate, the next two chapters shift focus to powder supports. **Chapter 7** presents X-ray absorption spectroscopy results for molybdenum oxide grown on various carbon supports. Chapters 4 to 7 also includes theoretical DFT calculations from our collaborators that support the experimental results. Finally, **Chapter 8** summarizes the main findings in this dissertation as well as some future directions.

Chapter 2

Background

Metals and their oxides are heavily used as catalysts for refining of petroleum, conversion of automobile exhaust, hydrogenation of carbon monoxide, hydrogenation of fats, and many other processes.

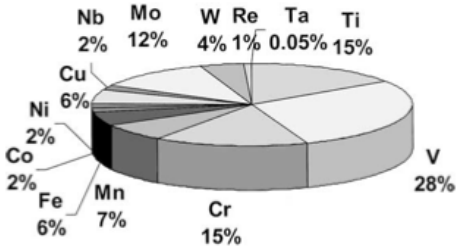

Figure 2.1. *A summary of the usage of several transition metals in the field of metal oxide catalysis.*[4]

Two systems, which receive the most attention in recent studies, are vanadium and molybdenum oxides. These catalytic materials deposited on a high surface area support (e.g., Al_2O_3, SiO_2, TiO_2, C, etc.) improve their catalytic properties. The high surface area stabilizes the main catalyst dispersed on the support and leads to optimal performance. It is more convenient to recycle which leads to a high turnover rate. Most catalyst supports have pores that allow reactants and product to be into and out of the interior volume, which provide high-area internal platforms for the catalysts and help reactions. In heterogeneous catalysis, the interface between supported catalysts and the substrates is speculated to be the site of catalytic activity and not the 3D islands[5-6]. Catalytic activity is a surface phenomenon and is governed by the structure of substrate, catalyst and their correlation. The focus of this chapter would be on the discussion of the various catalysts and the supports that have been studied in this work.

2.1 Supports for Heterogeneous Catalysts

2.1.1 Rutile α−TiO_2

Rutile (α−TiO_2) is a popular substrate material in surface science. Titanium dioxide has a wide range of applications in products such as paints and coatings, plastics, foods, pharmaceuticals and cosmetics. Its UV light resistance property helps prevent the discoloration of plastics in sunlight. Sunscreens also use TiO_2 as a blocker because of its high refractive index and the ability to protect the skin from UV light. Titanium dioxide is seeing growing demand as photocatalysts due to its oxidative and hydrolysis properties[7]. As a photocatalyst, it can improve the efficiency of electrolytic splitting of water into hydrogen and oxygen, and it can produce electricity in nanoparticle form[8]. Some of the applications include light-emitting diodes, liquid crystal displays (LCDs) and electrodes for plasma displays. Under exposure to UV light, it becomes increasingly hydrophilic and can be used for anti-fogging coatings and self-cleaning windows[9]. In mildly reducing atmospheres, TiO_2 tends to lose oxygen and becomes a semiconductor. The electrical resistivity of the material can be correlated to the oxygen content of the atmosphere and hence it can be used as an oxygen sensor[10]. TiO_2 can be prepared simply by sputtering and annealing, and thus various companies and vendors provide polished crystals with a high surface quality.

For our research, α−TiO_2(110) single crystals were purchased from MTI Corporation, USA. The substrates with dimensions of 10mm x 10mm x 1mm and $<0.1^0$ miscut were prepared by floating zone crystal growth method that grows single crystals with 99.99% purity. The samples were single-side epi-polished. The substrates were sonicated in acetone and then methanol for 5 min each and finally rinsed in ultrapure (18 MΩ cm) DI water before drying under a compressed air

jet. Substrates were then annealed in flowing oxygen in a quartz tube furnace for 30 min at 400°C followed by for 1 hr at 900°C to produce clean atomically flat steps.

TiO_2 is found in three different crystallographic structures: rutile (tetragonal a=b=4.584 Å, c=2.953 Å, space group: $P4_2/mnm$,), anatase (tetragonal a=b=3.784 Å, c=9.515 Å, space group: $I4_1/amd$) and brookite (orthorhombic a=9.184 Å, b=5.447 Å, c=5.145 Å, space group: Pbca) (Fig. 2.2). Rutile is thermodynamically the most stable phase and the (110) plane of rutile has the lowest surface energy and hence is the best supporting surface for catalysts.

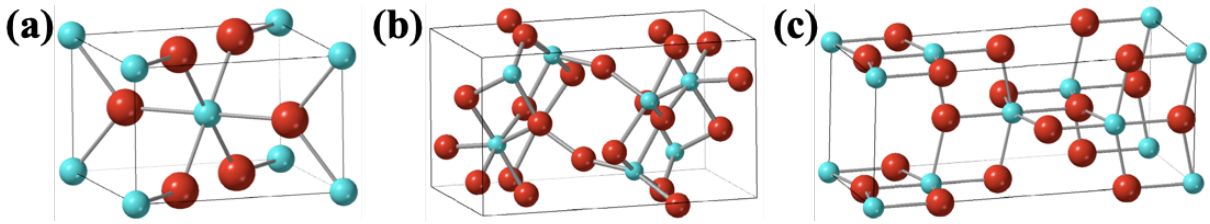

Figure 2.2. *Ball-and-stick models of the primitive unit cells of (a) Rutile (b) Anatase (c) Brookite.*

Fig. 2.3 (a) shows the bulk-terminated (1×1) surface of rutile TiO_2. Along the [001] direction, rows of six-fold-coordinated Ti atoms (as in the bulk) alternate with five-fold-coordinated Ti atoms with one 'dangling bond' perpendicular to the surface. Two kinds of oxygen atoms are present: oxygens within the main surface plane are three-fold-coordinated as in the bulk and bridging oxygen atoms which are two-fold coordinated. Because of their coordinative under-saturation these bridging oxygens can be removed relatively easily by thermal annealing. Fig. 2.3 (b) shows an STM image of the resulting point defects. The protruding bridging oxygen atoms are imaged black and the rows of fivefold-coordinated Ti atoms are imaged bright. If the surface oxygen atoms of the TiO_2 (110) surface are replaced by hydroxyl groups, it generates multiple different adsorption sites for catalysts. Fig. 2.4 shows two such adsorption sites, atop (AT) and bridging (BR) site.

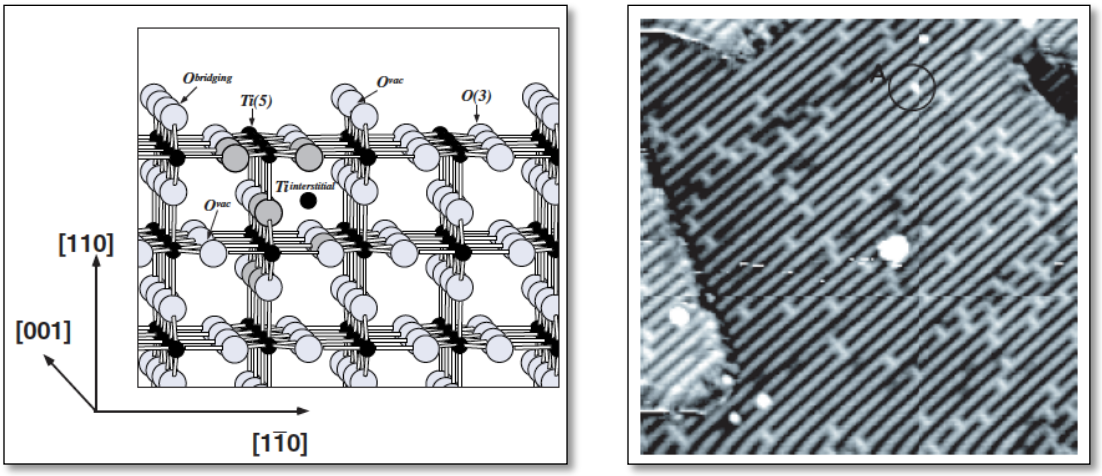

Figure 2.3 (a) *Ball-and-stick model of the rutile TiO_2(110)-(1×1) surface* ***(b)*** *STM image (200 Å×200 Å) of a TiO_2(110) (1×1) surface with point defects ('A').*[11]

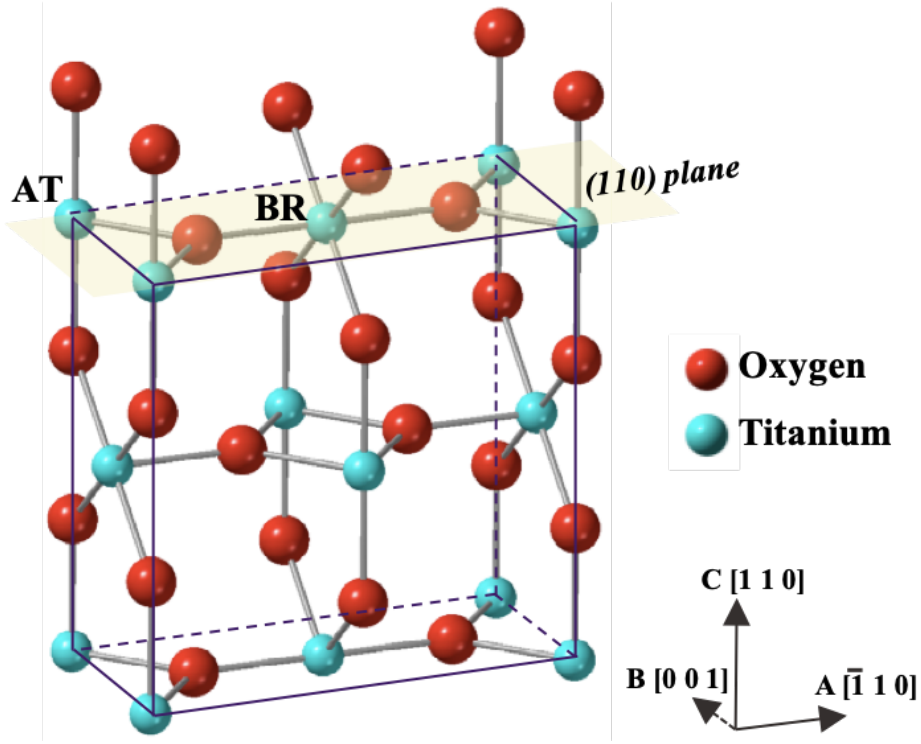

Figure 2.4. *Ball-and-stick model of α-TiO_2 showing a non-primitive unit cell where the c axis is perpendicular to the (110) surface. Also the (110) surface shows the symmetry inequivalent atop (AT) and bridging (BR) sites.*

2.1.2 Carbon

Carbon is a leading material for chemical and enzymatic biomass transformation reactions due to its high porosity, excellent electron conductivity, large surface area and chemical inertness. Carbon materials can be easily prepared from residual biomass and can be chemically functionalized with metallic nanoparticles (NPs) to improve its catalytic activity. Porous carbon materials are promising supports for heterogeneous catalysis as compared to conventional oxide supports due to high surface area, low cost, good thermal stability, tunable surface functionality, and varying degrees of structural regularity. Fig. 2.5 shows the various allotropes of carbon and their respective hybridization. In this dissertation, the focus is on two types of carbon supports for heterogenous catalysis: activated carbon and reduced graphene oxide.

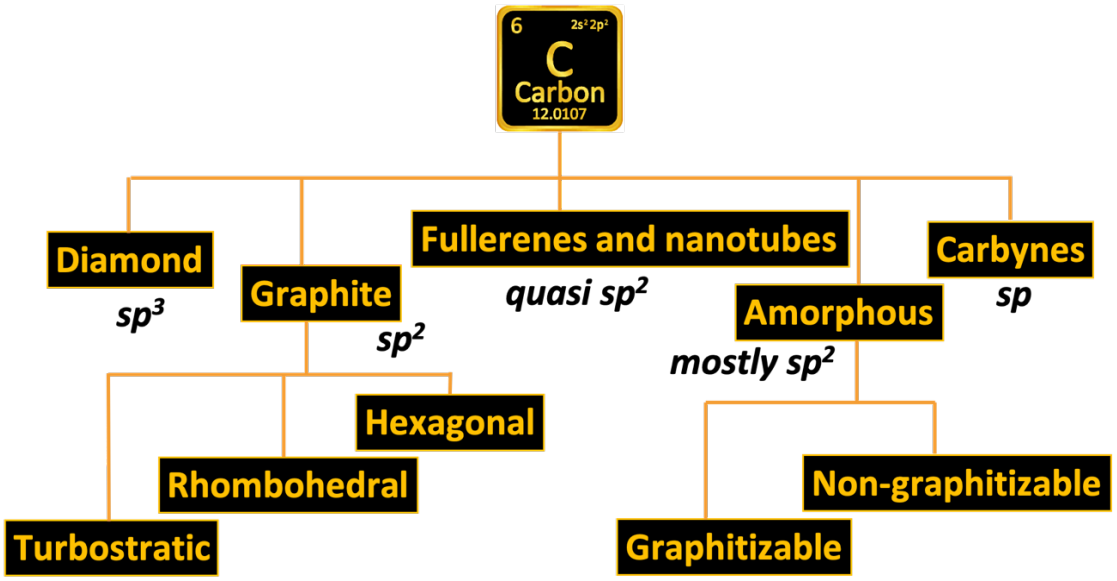

Figure 2.5. *Allotropes of elemental carbon. Adapted from Ref.* [12].

Activated Carbon

Activated carbon is a high surface-area and porous adsorptive material with an amorphous structure. It is composed primarily of aromatic configurations of carbon atoms joined by random

cross-linkages. Activated carbon has groups of atoms that are stacked unevenly in a disorganized manner. The degree of order varies based on the starting raw material and thermal history[12]. Depending on the source material, the process of producing activated carbon can be carried out using either physical activation or chemical activation[13-15]. Physical activation goes through two main processes: carbonization and activation. During carbonization, the raw material is thermally decomposed in an inert environment at temperatures 600-800°C and through gasification, elements such as O, H, N, S are removed from the source material. The carbonized material is then activated to fully develop the pore structure necessary for a good catalyst support. This is done by oxidizing it at temperatures between 800-1200°C in the presence of oxygen or steam. For chemical activation, the source material is impregnated with certain chemicals which are typically either an acid, a strong base or a salt. The carbon is then subjected to higher temperatures (300-600°C) which activates the carbon by forcing the material to open up and have more microscopic pores[16]. Chemical activation requires lower temperatures and has better quality consistency than physical activation. In this dissertation, the activated carbon that has been used as a support for the catalyst is in the form of powder activated carbon. Fig. 2.6 shows a scanning electron micrograph of activated carbon from wood and mineral. As can be clearly seen, the structure is highly porous and has high surface area and hence is ideal as a catalyst support[17].

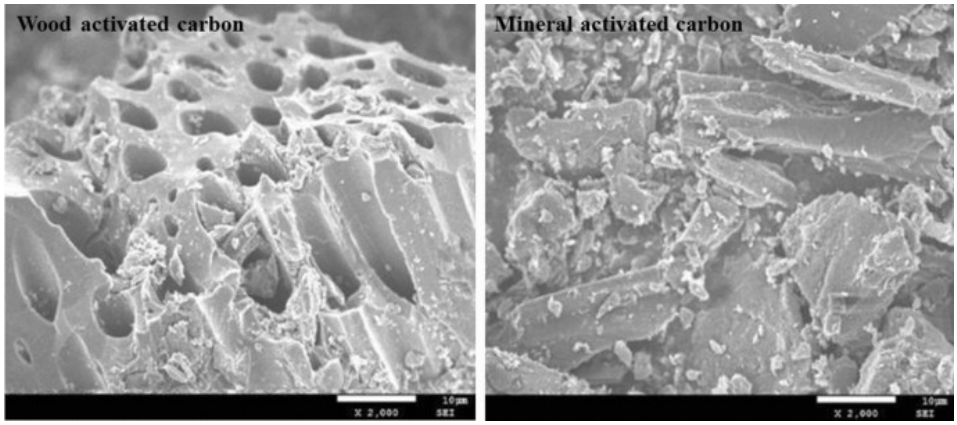

Figure 2.6. *Scanning electron micrograph of activated carbon from (a) wood (b) mineral.*[17]

Graphene oxide

Graphene oxide (GO) is a single monomolecular layer of graphite with various oxygen-containing functionalities such as epoxide, carbonyl, carboxyl, and hydroxyl groups[18]. As a functionalized single atomic layer of carbon, the thickness of GO is approximately 1 nm however, the lateral length of GO sheets can span up to μms. Thus, GO stretches across two abruptly different length scales. Reduced graphene oxide (rGO) has a high specific surface area, which is highly desirable in a catalyst support, and acts as a two-dimensional support for metallic nanoparticles with high dispersion. In addition, it also has a high adsorption capacity, and structural defects that can generate new surface functionalities and increase the interactions with the metal nanoparticles. The mechanical properties of rGO allow high stability and durability thus increasing the lifetime of the catalyst[19-21].

This section describes the synthesis process of GO and rGO for the purpose of this dissertation. This was synthesized by Yiqi Liu from the the Northwestern University Chemistry group of Prof. Tobin Marks. Graphene oxide (GO) was synthesized from graphite following a modified Hummers method with a pre-oxidative treatment[19-23]. In a round-bottom flask with a stir bar, concentrated H_2SO_4 (100 mL) was heated to 80°C. $K_2S_2O_8$ (20 g) and P_2O_5 (20 g) were then added and stirred until fully dissolved. Graphite powder (25 g) was next added to the solution and the mixture was kept at 80°C for 4.5 h. The mixture was then cooled in an ice-bath, carefully diluted with deionized (DI) water, collected by filtration on filter paper, and further washed with additional DI water (5 L). After drying in air overnight, 9 g of the pre-treated graphite powder was transferred to an Erlenmeyer flask and concentrated H_2SO_4 (345 mL) was added. After the mixture was chilled to 0°C in an ice bath, $KMnO_4$ (45 g) was slowly added. The flask was then moved to a 35 °C water bath and stirred for 2 h. Next, the flask was transferred back into the ice bath and cooled DI water (750 mL) was carefully added in portions while stirring. Then, 30% H_2O_2 solution (35 mL) was

slowly added. After the color of the mixture turned brown, it was removed from the ice bath, sonicated, and then centrifuged at 3000 rpm. The collected solid was rinsed with 3.4% HCl solution (2 L), followed by acetone (2 L). The GO obtained was then dried in air. XPS analysis showed that the GO is composed of 61.0 at% C and 37.6 at% O, as well as minor S impurities. Thermal reduction was used to remove redundant GO oxygen-containing functional groups to afford reduced graphene oxide (rGO) with good stability. In a round-bottom-flask with stir bar, GO was heated with stirring under air at 110°C for 1 h, and then at 150 °C for 1 h to obtain rGO. XPS analysis showed that the rGO had lower O content with a significantly higher percentage of aromatic C=C groups than GO. The rGO is composed of 85.1 at% C and 14.9 at% O. Fig. 2.7 shows the C 1s XPS spectra of the synthesized GO and rGO[24].

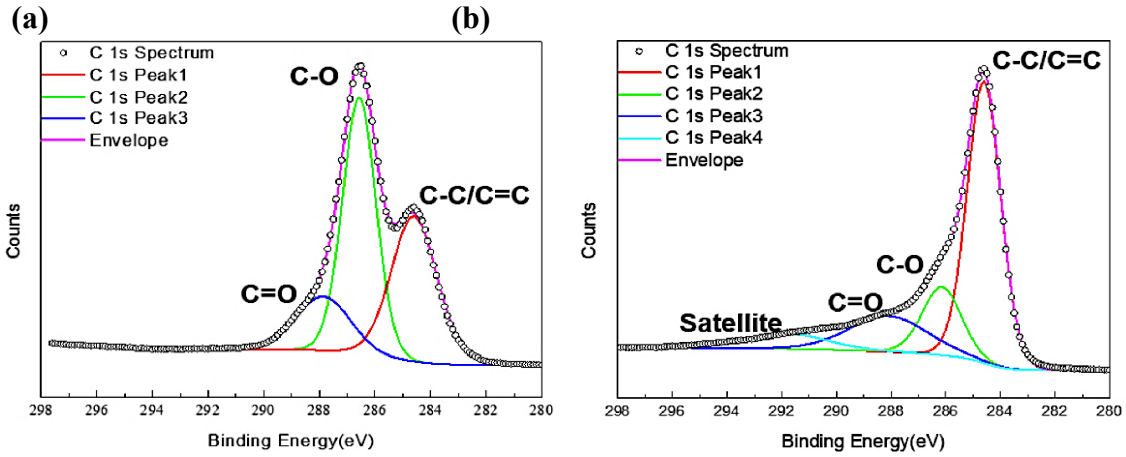

Figure 2.7. *C 1s XP spectra of (a) graphene oxide (b) reduced graphene oxide.*[25]

2.2 Supported Catalysts

Transition metal oxides have a large variety of physical and chemical properties and several of these materials undergo phase transitions with unique structural, electronic and magnetic behavior[4, 26-27]. Some exhibit superconductivity and exciting optical properties whereas some have great catalytic activity. Among these, vanadium and molybdenum oxides represent an important class of materials because of their large variety of crystal structures and chemical properties and hence having very high catalytic activity.

2.2.1 Vanadium oxide (VO_x)

Vanadium oxide monolayers (ML) or clusters deposited on oxide surfaces are widely used in various chemical reactions such as in gas sensors, electrochemical and optical switching devices, reversible cathode materials for Li batteries. As a catalyst, some of its most common reactions are o-xylene oxidation to phthalic anhydride reaction[28], pollution abatement of nitrous oxides with NH_3, oxidative dehydrogenation of propane, dehydrogenation of alkanes and selective oxidation of alcohols/alkanes[29-30]. Supported vanadium oxide is active as compared to the bulk material and TiO_2 is one of the most studied oxide supports for vanadium catalysts. Traditionally, TiO_2 is mainly used in selective oxidation reactions on mixed vanadia/titania catalysts. The strong metal support interaction is partly due to encapsulation of the metal particles by a reduced TiO_x overlayer. Deposition of vanadium in an oxygen ambient results in vanadium oxide that interacts weakly with the support. When vanadium is deposited in a molecular oxygen environment (1×10^{-7} Torr) on stoichiometric TiO_2 (110), disordered vanadium oxide is formed. Sambi et al[31] proposed that the adsorbed V atoms occupy a well-defined atomic site that corresponded to a Ti bulk-like substitutional site within the first surface layer. There was no diffraction evidence of diffusion of

the vanadium before the initial surface layer and it was suggested that the mild annealing provided the necessary energy for bulk oxygen to diffuse to the TiO_2 surface and fully oxidize the surface Ti and V atoms. Sambi et al also reported the growth of several monolayers of epitaxial VO_2 on the TiO_2 (110) surface. The VO_2 oxide layer was prepared with successive depositions of vanadium. After each deposition step, the TiO_2 surface was annealed in an oxygen environment. This growth process was described as 'deposition under thermodynamic control', in which the post-deposition annealing process was intended to enhance the order and oxidation of the surface. It was determined that the resulting vanadium oxide layer was well-ordered and pseudomorphic to the TiO_2 (110) substrate. The above studies provide clues about how to prepare vanadium oxides for heterogeneous catalysis. In supported vanadia catalysts, a phenomenon known as monolayer catalysis has been reported[32-33]. Here a sub-ML metal-oxide film supported by an appropriate oxide displays greater catalytic activity when compared to the thicker multilayer film. This would indicate that the supporting oxide plays a significant role in ML catalysis and is crucial for catalytic reactions. Of those chemical reactions, oxidization-reduction (redox) is a common yet very important reaction for supported vanadia catalysts. We will be looking at redox-induced transformations for catalysts on oxides surfaces, for example vanadium species on the TiO_2 surface. During redox reactions, the fundamental basis for the catalytic performances of supported vanadia lies in the variability in geometric and electronic structure of surface vanadium oxides. If the surface structure of vanadia could be predicted, this would have an enormous impact upon our understanding of numerous chemical processes.

Supported vanadium oxides show different chemical and electronic properties from those of unsupported vanadium oxide, both in aqueous media and in the solid state. The principal vanadium oxides are V_2O_5, VO_2, V_2O_3 and VO, in which the formal oxidation state of vanadium changes from +5 to +2. Other rarer VO_x compounds are mixed valence oxides and can be expressed as

V_nO_{2n-1}. Generally, there are three different bonds present in VO_x. Fig. 2.8 shows the possible molecular configurations for supported vanadium oxides. In the catalytic process, the reduction of supported vanadium oxide catalysts at high temperature in the presence of, e.g. CO and H_2 may lead to the formation of a variety of oxidation states (i.e. V^{5+}, V^{4+} and V^{3+}) and coordination environments (i.e. VO_4, VO_5 and VO_6). However, there is still much to learn about the quantitative distribution of the different vanadium oxide oxidation states (%V^{5+}, %V^{4+} and %V^{3+}) and their exact coordination environment at the catalyst surface after reduction and the parameters influencing the reduction degree of supported vanadium oxides.

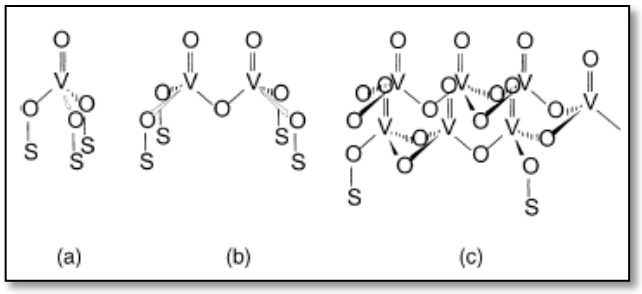

Figure 2.8. *Possible molecular configurations for supported vanadium oxides (with S the support cation): (a) isolated vanadium oxide species (b) dimeric vanadium oxide species (c) two-dimensional vanadium oxide chains.*[4]

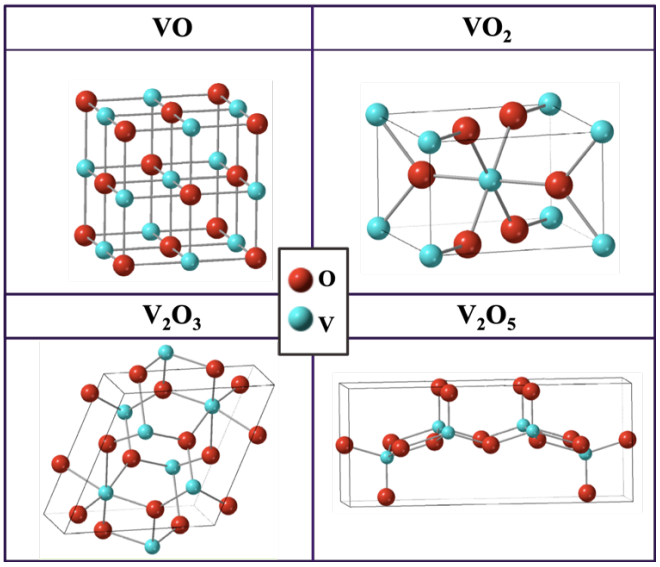

Figure 2.9. *Ball and stick model of vanadium (V^{2+}, V^{3+}, V^{4+}, V^{5+}) oxide crystal structures (created using CrystalMaker)*[34-35]

2.2.2 Molybdenum oxide (MoO_x)

Molybdenum plays important roles in mediating numerous catalytic transformations, ranging from elaborate metalloenzyme systems to large-scale industrial processes, and high-valent oxo-molybdenum complexes serve as excellent catalysts in numerous laboratory-scale oxidation and reduction reactions[36-42]. Molybdenum oxide is widely used as an oxidation catalyst for acid-mediated catalytic reactions. Photocatalytic conversion of cyclohexane to benzene by oxygen gas at very low temperature is assisted by TiO_2-supported molybdenum oxide catalyst.

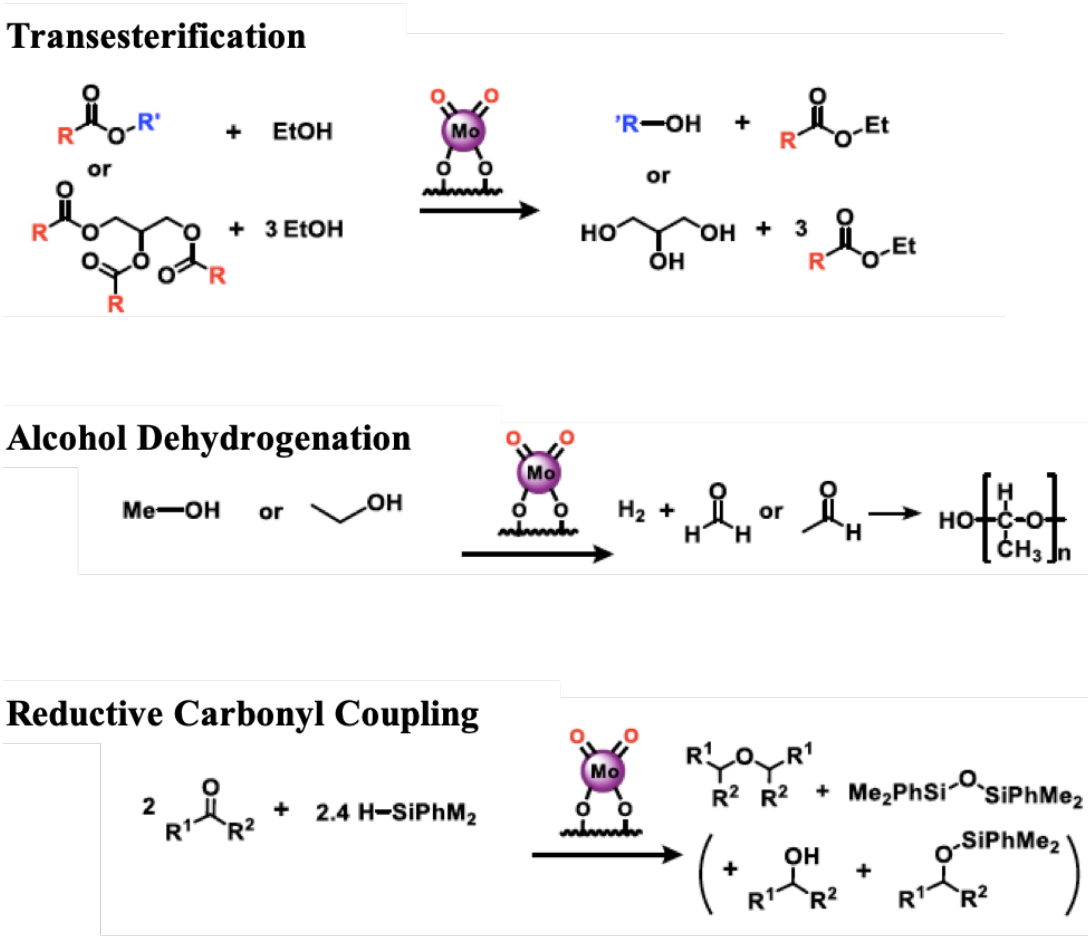

Figure 2.10. *Several reactions that use Molybdenum oxide as the catalyst*[43-45]

Molybdenum oxides form a large group of materials resulting from the ability of molybdenum to possess different formal oxidation states as well as different local coordination. Molybdenum has two single valency oxides, MoO_3 (Mo^{6+}) and MoO_2 (Mo^{4+}). Single crystals of these two single valency molybdenum oxides can be characterized both by arrangements of distorted MoO_6 octahedra. The corresponding crystal lattices differ by the connectivity of these octahedra and by their Mo-O distances as well as O-Mo-O angles.

The trioxide MoO_3 forms an orthorhombic crystal lattice where the elementary cell contains four chemical MoO_3 units shown in Fig. 2.11 (a). It has a layered structure with weakly binding bilayers parallel to the (010) crystal plane. Each bilayer consists of two planes of comer-linked distorted MoO_6 octahedra where octahedra from adjacent planes share edges. The MoO_3 unit cell is orthorhombic-P and has lattice parameters of a = 3.76 Å, b = 3.97 Å, c = 14.43 Å, $\alpha = 90^o$, $\beta = 90^o$, $\gamma = 90^o$. Bulk MoO_3 contains three symmetry inequivalent oxygen sites, i) terminal oxygen coordinated to only one Mo center, ii) bridging oxygen doubly and iii) triply coordinated to molybdenum centers.

The dioxide MoO_2, crystallizes in a monoclinic lattice that deviates only slightly from the tetragonal rutile structure and is very similar to the structure of VO_2. The monoclinic unit cell contains four MoO_2 units. Fig. 2.11 (b) shows the MoO_2 unit cell where the monoclinic axes are marked as $\mathbf{a_M}$, $\mathbf{b_M}$ and $\mathbf{c_M}$ and the rutile unit cell axes are marked as $\mathbf{a_R}$, $\mathbf{b_R}$ and $\mathbf{c_R}$. The lattice parameters for the monoclinic cell are $a_M = 4.86$ Å, $b_M = c_M = 5.63$ Å, $\alpha = 90^o$, $\beta = 121^o$, $\gamma = 90^o$. The lattice parameters for the rutile cell are $a_R = b_R = 4.86$ Å, $c_R = 2.82$ Å, $\alpha = 90^o$, $\beta = 90^o$, $\gamma \sim 90^o$.

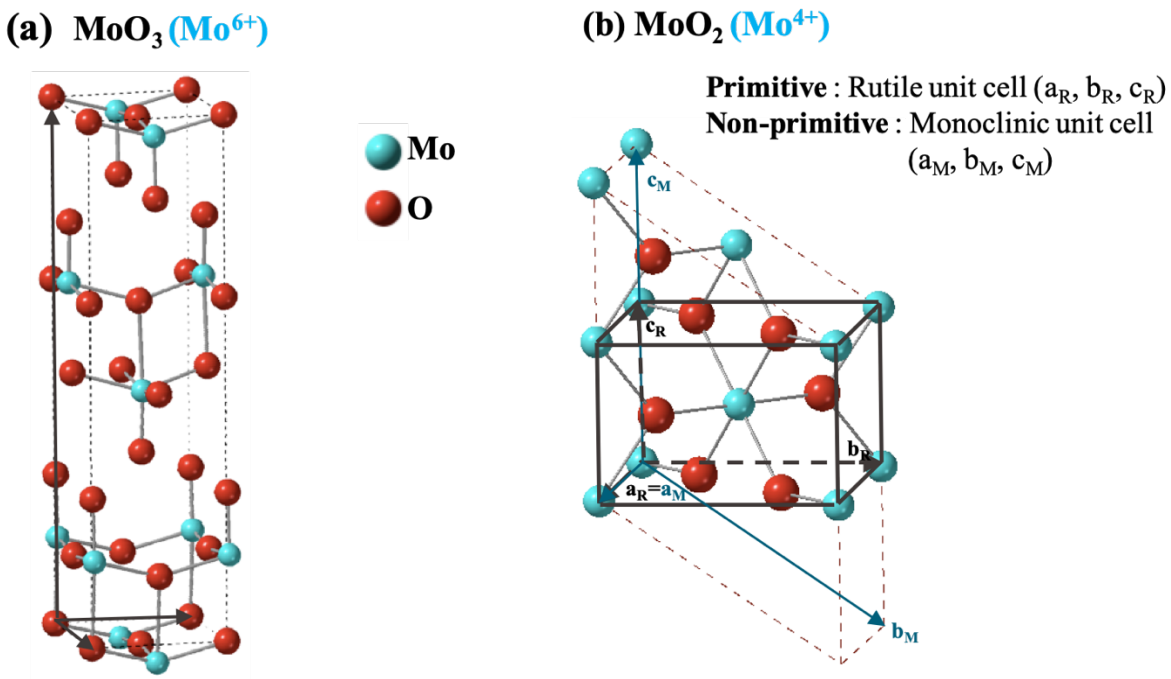

Figure 2.11. Ball and stick model of (a) MoO_3 and (b) MoO_2 unit cells (created using CrystalMaker)[46]

The orthorhombic phase of MoO_3 has a highly anisotropic layered structure as illustrated in Fig. 2 .11 (a) and because of this weak bonding between the sheets of corner and edge-sharing MoO_6 octahedra perpendicular to [010], the crystals are micaceous. The Mo atoms on the (010) surface have their full complement of six oxygen nearest neighbors. However, termination of the bulk structure in other directions leaves the surface Mo atoms on lateral facets with fewer than six neighboring O. The hypothesis is that, this difference in coordination number of Mo will lead to differences in the catalytic properties of the different facets. However, it is difficult to demonstrate that experimentally. Using XSW-XPS it is possible to observe redox induced changes to each surface Mo atomic site and hence it would be possible to conclude which is the more catalytically active site.

Chapter 3

Experimental Methods

3.1 Film growth technique

Thin film deposition techniques can range from liquid phase growth to gaseous phase growth. In this thesis work, the focus is on a gas phase thin film growth technique[47]. Gas phase growth can be categorized into chemical deposition and physical deposition techniques. In physical techniques, a solid material is converted to vapor through heating (evaporation) or energetic ion bombardment. The material in form of vapor finally condenses on the substrate surface as a thin film. In the chemical deposition techniques, the growth occurs directly from gases which react and give place to a new product that condenses as a thin film on the substrate.

***Table. 3.1**. Overview of common thin film deposition techniques*

GAS PHASE		LIQUID PHASE
Chemical deposition techniques	**Physical vapor depositions**	• Chemical solution deposition • Electroless deposition • Electroplating (ECD) • Spin coating • Dip coating • Liquid-phase epitaxy
• Chemical vapor deposition (CVD) • Vapor-phase epitaxy (VPE) • Atomic layer deposition (ALD) • Atomic layer epitaxy (ALE)	• E-beam evaporation • Sputter deposition • Pulsed laser deposition (PLD) • Molecular beam epitaxy (MBE)	

3.1.1 Atomic Layer Deposition

In this thesis work, atomic layer deposition (ALD) is the main technique that has been used to grow oxide thin films on single crystal substrates. ALD is a thin film deposition technique that uses gaseous precursors in a sequence of self-limiting chemical surface reactions at a controlled temperature[48-52]. It uses cycles of saturating reactions between gaseous precursor molecules and a substrate to deposit films in a layer-by-layer fashion as illustrated in Fig. 3.1. By repeating the binary reaction sequence in an ABAB fashion, and using current viscous flow reactor designs, monolayer-by-monolayer growth rates as high as 1 micron/hour are possible. This alternating reaction mechanism eliminates the drawbacks of constant exposure and line-of-sight requirements that make it impossible for other vapor deposition techniques to coat porous, high-surface-area catalyst supports. Since the deposit is conformal to the support at the atomic scale, the surface area is largely preserved.

The technique was first patented in the year 1974[53-54], however it has gained great interest in the recent years because of an expansion in the possibility of growing a large number of thin films ranging from semiconductors to metals to their oxides. ALD is of particular significance in the semiconductor industry as they require highly uniform and controlled thickness thin films, for example growing hafnium oxide as a gate material.

Precursors typically constitute an organometallic compound and an oxidizing or reducing agent such as oxygen, hydrogen, H_2O_2 or steam. The first precursor (the organometallic) dose would saturate the reactive sites on the surface through chemisorption and the second precursor (oxidizing or reducing agent) reacts with the adsorbed species from the first dose. The second precursor removes the excess organic ligands from the surface and makes the surface reactive to the next dose of the organometallic compound for the next ALD cycle.

The formation of a thin film does not start immediately after the first ALD cycle as it depends on the efficiency of precursor adsorption. The efficiency of ALD is related to the precursor pressure, flow rate, dosing time, temperature and surface functionalization. These factors are optimized to obtain a growth recipe where the film nucleates and eventually combines leading to the steady state growth regime as the number of cycles increase.

For our work, our collaborators in the Elam lab at ANL employed ALD to deposit uniform monolayers and of vanadium oxide and molybdenum oxide on the surface of α-TiO_2 (110) single crystals.

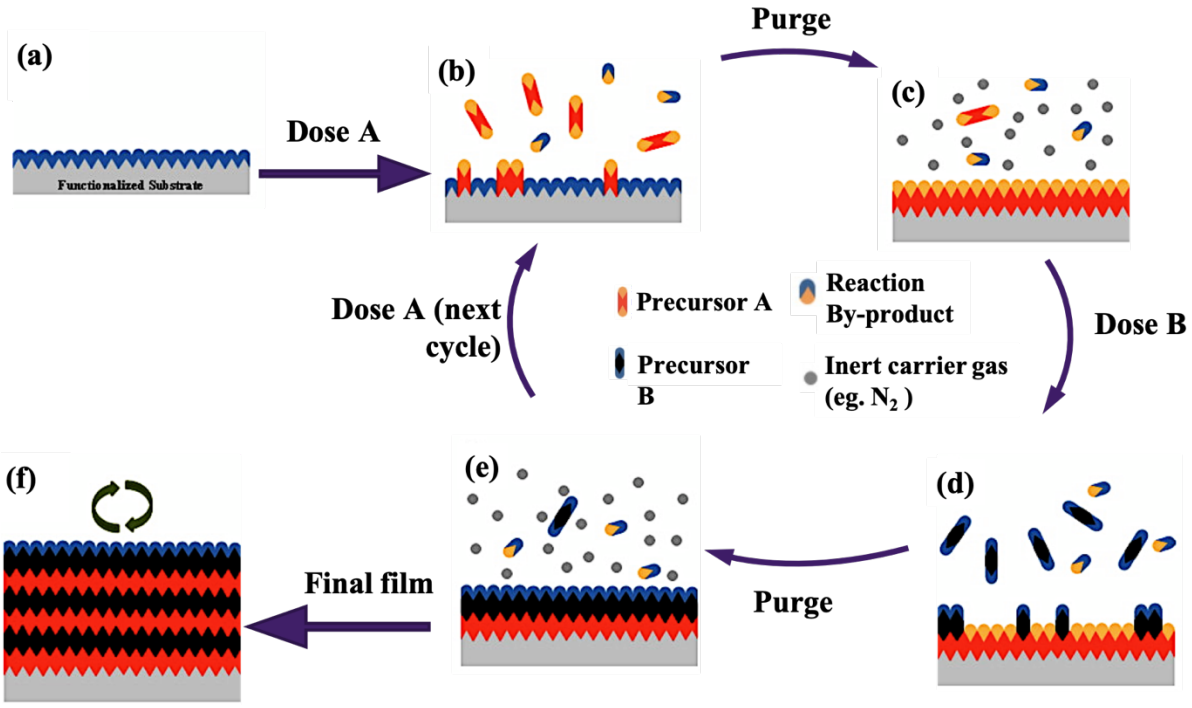

Figure 3.1. *Schematic representation of ALD using a binary (AB) precursor system. This shows (a) substrate with reactive sites, (b) dosing of the first precursor and formation of active sites and reaction byproducts, (c) purging of byproducts and unreacted precursor, (d) dosing of the second precursor, (e) purging of byproducts and second precursor that is unreacted, and (f) film resulting from several ALD cycles.*[55]

3.2 Characterization techniques

The primary methods of surface and interface studies are mostly of two types: local probe methods and surface averaging methods. Local probe methods include techniques such as scanning tunneling microscopy (STM), atomic force microscopy (AFM), Kelvin probe force microscopy (KPFM) and electron microscopy. These methods yield images of the surface structure from nanometer to sub-Å length scales. While they can provide local atomic-scale insight, they only provide views of small areas on the surface, and the resolution of atomic positions in the surface normal direction is limited. Surface averaging methods, such as X-ray and electron scattering, provide results averaged over a larger (μm-mm-scale) portion of the surface. The combined signal from the various ensembles of atoms provide sensitivity to structural details that is not achievable at smaller scales. Surface stoichiometry and chemical states can be determined by X-ray and electron spectroscopies, while X-ray scattering from surfaces can provide measurements of atomic position with sub-Å resolution. These two families of characterization tools are complementary, and together they can provide a view of the entire surface at several length scales, especially when paired with first-principles theoretical calculations. Details of the characterization techniques and instrumentation used are provided in subsequent sections of this chapter.

3.2.1 Introduction to X-ray characterization

Since Röntgen's discovery of X-rays in 1895, we have used this radiation for probing matter that is invisible to us. In materials science, we use the ability of X-rays to probe length scales well beyond the visible. Our work mostly focuses on X-ray scattering and spectroscopy to study phenomena at the scale of atoms. Electromagnetic radiation with wavelengths of 0.1 – 100 Å makes up the X-ray spectrum, with wavelengths of 0.1 – 3 Å defined as "hard" X-rays and 3 – 100

Å called “soft” X-rays. Because their wavelength is on the order of the spacing between atoms and molecules in solids and liquids, we can use the scattering of X-rays to learn about the structure of condensed matter. Additionally, these wavelengths correspond to the characteristic energies that bind core-shell electrons to their atoms. The absorption of X-rays at characteristic energies (and the corresponding emission of X-rays or electrons) enables X-ray spectroscopies that probe the chemistry of materials. X-rays, like any electromagnetic radiation, can be described as an oscillating electric field **E** propagating along the wavevector **k** with an amplitude E_0 pointing in the polarization direction $\hat{\boldsymbol{\varepsilon}}$

$$\mathbf{E}(\mathbf{r}, t) = \hat{\boldsymbol{\varepsilon}} E_0 e^{i(\mathbf{k}\cdot\mathbf{r} - \omega t)} \qquad (3.1)$$

where **r** is the position vector, ω is the frequency of the radiation, and t is the time. Wavevector **k** is related to the wavelength λ of the radiation by $\mathbf{k} = (2\pi/\lambda)\,\hat{\mathbf{u}}$, where $\hat{\mathbf{u}}$ is the unit vector of propagation of the X-ray. X-ray scattering from an atom will not be isotropic, but rather will depend on the angle between the incident beam and the point of measurement of the scattered beam. We therefore discuss scattering in terms of the scattering vector (or momentum transfer vector) $\mathbf{Q} = \mathbf{k}' - \mathbf{k}$, where **k** and **k′** represent the incident and scattered X-ray wavevectors, which are separated by a scattering angle 2θ. Since $\mathbf{k} = (2\pi/\lambda)\,\hat{\mathbf{u}}$, the magnitudes are $|\mathbf{k}| = 2\pi/\lambda$ and $|\mathbf{Q}| = 4\pi\sin\theta/\lambda$. The atomic form factor $f^0(\mathbf{Q})$ takes into account the intra-atomic interference effect in X-rays scattering from the electrons in an atom:

$$f^0(\mathbf{Q}) = \int \rho(\mathbf{r})\, e^{i\mathbf{Q}\cdot\mathbf{r}}\, d\mathbf{r} \qquad (3.2)$$

where $\rho(\mathbf{r})$ is the electron density of the atom at a point **r**. The value of the form factor is the atomic number *Z* of the atom at $\mathbf{Q} = 0$ but decreases monotonically at higher **Q**. The absorption of X-rays by the atom, including resonant effects near absorption edges, are accounted for in the

complete atomic scattering factor $f(\mathbf{Q}, \mathrm{E}) = f^0(\mathbf{Q}) + f'(\mathrm{E}) + if''(\mathrm{E})$, where $f'(\mathrm{E})$ and $f''(\mathrm{E})$ account for photon energy-dependent anomalous scattering near absorption edges and absorption effects, respectively.

3.2.2 X-ray standing wave

Kinematical X-ray scattering

In an ensemble of atoms, such as a crystal, scattered X-rays will interfere with each other. Since a crystal is composed of planes of atoms, coherent addition of X-rays resulting in intense reflection from the crystal will only occur at particular geometries. Here, we assume that X-rays are not undergoing multiple scattering within the crystal. The scattering of E-field plane wave by a crystal unit cell is described by the structure factor F ($\mathbf{Q}$, E), which builds on the atomic scattering factor by accounting for the positions $\boldsymbol{r_j}$ of multiple atoms in the unit cell.

$$F(\boldsymbol{Q}, E) = \sum_j f_j(\boldsymbol{Q}, E) e^{i\boldsymbol{Q}\cdot\boldsymbol{r_j}} \tag{3.3}$$

The intensity of scattered X-rays is proportional to the square of the modulus of the structure factor. If we consider a 3-dimensional crystal of finite dimensions N_1, N_2, N_3, where N_i is the number of unit cells in a particular direction, and $\mathbf{R}_n = n_1\mathbf{a} + n_2\mathbf{b} + n_3\mathbf{c}$, where n are integers and $\mathbf{a}$, $\mathbf{b}$, and $\mathbf{c}$ are the crystallographic basis vectors, for large values of N_1, N_2 and N_3, the intensity will approach zero except when the Laue conditions are satisfied.

$$\mathbf{Q}\cdot\mathbf{a} = 2\pi h,\ \mathbf{Q}\cdot\mathbf{b} = 2\pi k,\ \mathbf{Q}\cdot\mathbf{c} = 2\pi l \tag{3.4}$$

hkl are the Miller indices of a set of diffraction planes. This is an important principal of X-ray crystallography, since diffracting planes of crystals will result in intense reflections only at particular values of **Q**. Namely, when

$\boldsymbol{Q} = 2\pi \boldsymbol{H} = 2\pi (h\boldsymbol{a^*} + k\boldsymbol{b^*} + l\boldsymbol{c^*})$.

Here, $\boldsymbol{H}$ is the reciprocal lattice vector for the *hkl* planes and $\boldsymbol{a^*}$, $\boldsymbol{b^*}$ and $\boldsymbol{c^*}$ are the basis vectors for the reciprocal lattice. At the Laue condition the structure factor becomes

$$F_H = \sum_{j=1}^{N} f_j \, e^{2\pi i(hx_j + ky_j + lz_j)} \ ,$$

where x_j, y_j, z_j are the fractional unit cell positions of the j^{th} atom.

Since the intensity of the reflection will be in part proportional to the square of the unit cell structure factor amplitude, $(I_H \sim |F_H|^2)$ the pattern of diffracted intensities from a crystal can be used to help solve its structure[56]. Of course, there is no simple conversion of diffracted intensities to structure because of the well-known phase problem in diffraction physics (i.e., the structure factor phase is lost when measuring diffracted intensities).

Dynamical Bragg diffraction

The above discussion of kinematical scattering theory assumes that X-rays only scatter once in the crystal. However, in the case of large highly perfect single crystals, multiple scattering must be included to correctly describe the forward and diffracted E-fields. This phenomenon is rigorously accounted for by solving Maxwell's equations for electromagnetic waves in a 3-dimensional periodic dielectric medium[57-58]. In the case of diffraction from a crystal in which the polarization vectors of the incident and diffracted E-fields are perpendicular to the scattering plane (σ-polarization), the behavior in the region of X-ray reflectivity near a Laue condition is described in terms of the complex normalized angular coordinate

$$\eta = \frac{b\,\Delta\theta\,\sin(2\theta_B) + \frac{1}{2}\Gamma\,F_0(1-b)}{\Gamma\sqrt{|b|}\sqrt{F_{\mathbf{H}}F_{\bar{\mathbf{H}}}}} \tag{3.5}$$

where $\Delta\theta = \theta - \theta_в$ is the angle displacement from the geometrical Bragg angle $\theta_в$, constant $\Gamma = r_e\lambda^2/\pi V_C$, V_C is the crystal unit cell volume, the classical electron radius $r_e = 2.818 \times 10^{-5}$ Å, and $b = \hat{k}_0 \bullet \hat{n} \,/\, \hat{k}_H \bullet \hat{n}$ is the crystal surface asymmetry factor. $\hat{n}$ is the inward pointing surface normal unit vector. $\hat{k}_0$ *and* $\hat{k}_H$ are unit vectors in the $\mathbf{k_0}$ and $\mathbf{k_H}$ directions. b <0 for Bragg reflection geometry and b = -1 for Bragg symmetric reflection geometry. $F_{\mathbf{H}}$ and $F_{\bar{H}}$ are the unit cell structure factors at the Laue conditions **H** = hkl and $\bar{\mathbf{H}} = -\mathbf{H} = \overline{hkl}$, and F_0 is the structure factor at hkl = 0, 0, 0 (the forward scattering condition). The structure factor may be broken down into real and imaginary components: $F_{\mathbf{H}} = F_{\mathbf{H}}' + iF_{\mathbf{H}}''$

The region in which the real component of the complex angular coordinate $\eta' < -1$ is called the β branch of the dispersion surface, and the region $\eta' > +1$ is the α branch. As the crystal is rotated from $\eta = +1$ to $\eta = -1$ (corresponding to an increase in θ), the crystal passes through the Bragg bandgap between the two branches in which total external reflection occurs. The electric field amplitude ratio between the diffracted (E_H) and incident (E_0) electromagnetic waves through this transition is

$$\frac{E_{\boldsymbol{H}}}{E_0} = -\sqrt{|b|}\sqrt{\left(\frac{F_{\boldsymbol{H}}}{F_{\bar{\boldsymbol{H}}}}\right)}\left(\eta \pm \sqrt{\eta^2 - 1}\right) \tag{3.6}$$

In the β branch, the right-most side of the equation is $(\eta + (\eta^2 - 1)^{1/2})$, whereas it is $(\eta - (\eta^2 - 1)^{1/2})$ elsewhere. There is a significant imaginary component to $E_{\mathbf{H}}/E_0$ when $|\eta| < 1$, corresponding to the Bragg bandgap which connects the α branch and β branch. This solution satisfies the boundary

condition imposed by conservation of energy; otherwise, the energy exiting the crystal in the diffracted wave would be larger than that transferred into the crystal by the incident wave. The reflectivity R, which is the square of the electric field amplitude ratio: $R = I_{\mathbf{H}}/I_0 = |\, E_{\mathbf{H}}/E_0 \,|^2$, approaches unity in the Bragg band gap for a symmetric reflection geometry, where b = -1. This condition of total reflection occurs over a very narrow angular width, referred to as the Darwin width of:

$$\omega \;=\; \Delta\theta_{\eta=-1} - \Delta\theta_{\eta=+1} \;= \frac{2\Gamma\sqrt{F_{\boldsymbol{H}}{}'F_{\overline{\boldsymbol{H}}}{}' + F_0{}''^{\,2} - F_{\boldsymbol{H}}{}''F_{\overline{\boldsymbol{H}}}{}''}}{\sqrt{|b|}\,\sin(2\theta_B)} \tag{3.7}$$

In the hard X-ray regime, Darwin widths are typically on the order of 0.0001° – 0.001° (2 – 20 μrad) which is a departure from kinematical theory, which predicts an infinitesimally narrow rocking curve for an semi-infinite perfect crystal. Additionally, due to refraction of X-rays at the crystal surface, the center of the rocking curve is offset from the nominal Bragg angle by

$$\Delta\theta_{\eta=0} = \frac{\Gamma\, F_0'\,(1+|b|)}{2\,|b|\sin(2\theta_B)} \tag{3.8}$$

While the amplitude of E_H is relatively large and constant in traversing from the α branch to the β branch, there is also a shift in the phase of E_H by $-\pi$. On the low-angle side of the rocking curve, E_H and E_0 are out of phase with each other on the diffraction planes, whereas they are in phase on the high-angle side. The position of the H=hkl diffraction planes for this purpose are defined by the maximum in the Real part of the Hth Fourier component of the effective electron density.[59] This phase shift occurs through the Bragg bandgap, and it is the foundation of the X-ray standing wave (XSW) technique[60-62].

X-ray Standing Wave

The X-ray standing wave (XSW) field can be produced by the superposition of two coherently coupled X-ray beams, as shown in Fig. 3.2. The XSW period D is given by $D = \lambda / 2\sin\theta = 2\pi / Q$ where λ is the X-ray wavelength. The XSW period will change when the angle θ changes. If the two interfering plane-waves are produced by Bragg diffraction as pictured in Fig. 3.2, then the XSW period $D = d_{hkl}$, the diffraction plane spacing. If the relative phase between the two waves, ν, changes, the XSW field will shift in space. As shown in figure 3.3(a) and (b), upon shifting one wave with respect to another by $\lambda/2$, i.e., the relative phase between them changes from $\nu = 0$ to $\nu = \pi$, while keeping the XSW period the same, the XSW anti-node positions (marked with solid line) moves by half the d-spacing, i.e., the XSW field shifts by D/2. These features of the XSW field can be taken advantage of as an atomic scale probe by monitoring the photoelectric effect, such as photoelectron emission, X-ray fluorescence, and/or Auger electron emission[59, 61, 63-66].

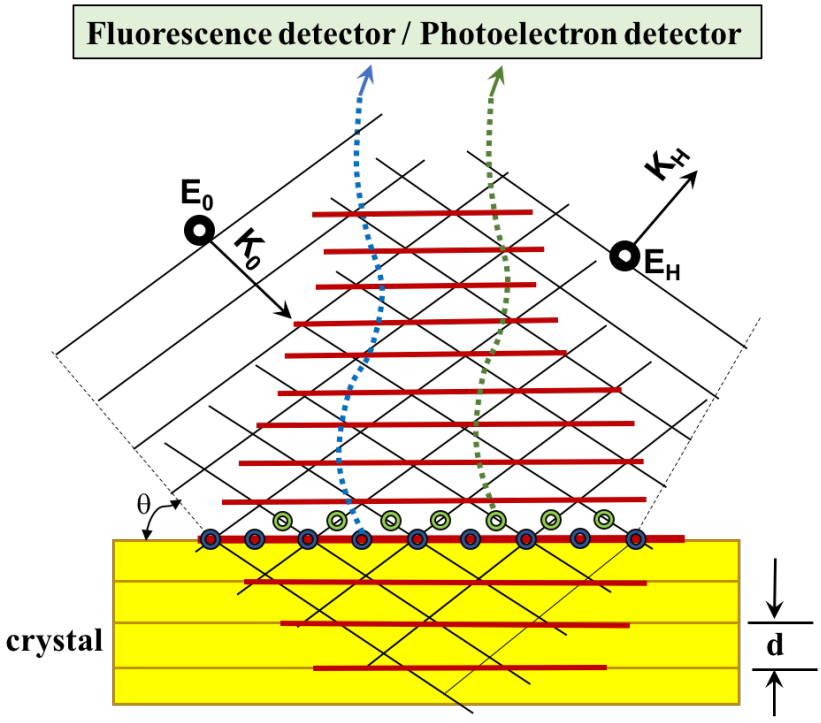

Figure 3.2. *Superposition of 2 plane waves generates XSW. Standing wave vector* $\boldsymbol{Q = K_H - K_0}$

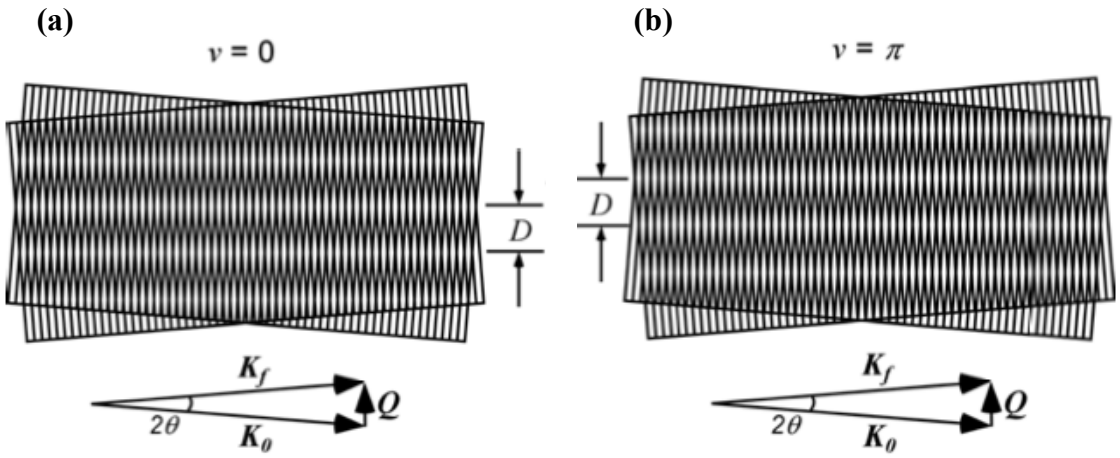

Figure 3.3. *The XSW period is D, the wavelength is λ and two beams traveling with angle 2θ. The phases between the two plane waves, v, are (a) 0 and (b) π, respectively.*

There are several ways to generate XSW fields, such as the strong Bragg reflection from a single crystal,[67] total external reflection (TER) from a mirror surface,[68] the strong Bragg reflection of a periodic layered synthetic microstructure,[69] etc. This thesis work used single crystal Bragg diffraction to generate the XSW. At the Bragg condition, as shown in Fig. 3.2, the diffracted X-rays interfere coherently with incoming X-rays to form a standing wave field in and above the surface of the single crystal. The normalized XSW intensity for the σ-polarized case is described as

$$I_{XSW} = 1 + R + 2\sqrt{R}\cos(v - 2\pi \mathbf{H}\bullet\mathbf{r}).$$

The XSW period matches the period of the diffraction planes. When the incident angle is scanned from the low-angle side to the high-angle side of this arc-second wide **H** (= hkl) Bragg condition, the relative phase (v) of XSW field decreases by π radians. This causes the XSW anti-nodal planes to move by one-half of a d spacing ($d_{\mathbf{H}}$) in the –**H** direction. On the low-angle side (α-branch) the XSW nodes are aligned with the diffraction planes and on the high-angle side (β-branch) the

antinodes are aligned with the diffraction planes. The position of the diffraction planes is directly linked to the phase of the structure factor.[59] When scanning across the rocking curve, the shift of the XSW can induce a modulation in the X-ray fluorescence (XRF) and X-ray photoelectron emission. X-ray photoemission or fluorescence of near-surface atoms can therefore be used as a near-field "phase detector" of the XSW phase shift. In the dipole approximation the photoelectric effect cross section is proportional to the E-field intensity at the center of the atom. Thus, for the σ-polarized case, the XPS or XRF yield Y_H of a particular atomic surface species with distribution $\rho(\boldsymbol{r})$ near a reflection condition **H** and normalized to the "off-Bragg" yield, is

$$Y_{\mathbf{H}} = \int \rho(\boldsymbol{r}) I_{XSW} d\boldsymbol{r} = 1 + \mathrm{R}_{\boldsymbol{H}} + 2\sqrt{\mathrm{R}_{\boldsymbol{H}}}\, f_{\mathbf{H}} \cos(v - 2\pi P_{\mathbf{H}}) \tag{3.10}$$

Where $R_H = |E_H / E_0|^2$, ν is the phase between the reflected and the incident plane waves, $f_{\mathbf{H}}$ is the amplitude and P_H is the phase of the $\boldsymbol{H}^{th}$ Fourier component of the distribution of the selected atomic species. f_H and P_H are also known as coherent fraction and coherent position. By measuring the fluorescence yield or the photoelectron yield and reflectivity and fitting for f_H and P_H, XSW can be used to identify the position of surface or near-surface atoms with sub-Å precision, so long as they are well-ordered along the $\boldsymbol{H}$ direction. By measuring $f_{\mathbf{H}}$ and $P_{\mathbf{H}}$ at several different hkl reflections, an accurate density distribution can be resolved by the Fourier summation

$$\rho(\boldsymbol{r}) = 1 + 2 \sum_{\substack{H \neq -H \\ H \neq 0}} f_H \cos[2\pi(P_H - \boldsymbol{H} \bullet \boldsymbol{r})] \tag{3.11}$$

Atomic density maps derived this way can be used to pinpoint particular high-symmetry occupation sites for surface species or bulk impurities. They can also be used to inform models for fitting multiple occupation sites, since two symmetry-inequivalent sites may be impossible to resolve at particular **H** conditions[70-71].

Back-reflection X-ray standing wave (BRXSW)

In the majority of the XSW experiments the rocking curve width from Eq. 3.7, i.e., the width of the Darwin reflectivity curve, is very narrow, often only a few arc seconds. This places some key requirements on the XSW experiment, namely that the incident radiation must be highly collimated and the crystalline sample should be highly perfect, with a mosaicity smaller than this rocking curve width. To avoid this another commonly used method is back-reflection XSW (BRXSW) which uses a near-normal incidence to the diffraction planes to set up the standing wave field. Using 2θ=180° geometry minimizes the gradient of Braggs law $d\lambda/d\theta$ and produces rocking curves with Darwin widths on the order of milliradians. This expanded Darwin width allows elemental metals and other more imperfect single-crystals to be used to generate standing waves. In the BRXSW method,{Woodruff, 2005 #100} the incident X-ray energy, E_γ, is scanned across the eV-wide Bragg condition causing a modulation in both the amplitude $\sqrt{R_H}$ and phase v of the reflected plane wave, which causes modulations in the measurable reflectivity R_H and photoelectron yield Y_H. As the standing wave shifts inward from being out-of-phase to being in-phase with the diffraction planes, the resulting XPS yield modulation can be analyzed to obtain the $\Delta d/d$ positions of each atomic chemical state with respect to the substrate *hkl* diffraction planes. In this thesis work, BRXSW has been used for studying VO_x and conventional XSW has been used to study MoO_x. The XSW experiments have been performed at Sector 5ID-C at DND-CAT, Advanced Photon Source, USA, whereas the BRXSW experiments were performed at beamline I09 at the Diamond Light Source, UK.

Non-dipolar corrections (NDC)

For XSW excited XPS, non-dipolar terms in the photoelectric effect cross section can play a significant role. In which case the normalized yield of Eq. 3.10 is modified to become:

$$Y_H = 1 + S_R R_H + 2\sqrt{R_H}\, f_H\, |S_I| \cos[\upsilon - 2\pi P_H + \psi] \qquad (3.12)$$

S_R, S_I and ψ are parameters corresponding to small non-dipolar corrections (NDCs) to the 2-beam photoelectric-effect cross section[72]. In the most general sense, f_H and P_H are the amplitude and phase of the H = hkl Fourier component of the spectroscopically selected atomic distribution. For the simple case of a distribution with a single atomic position relative to the hkl planes, P_H is the outward $\Delta d/d$ displacement of this position relative to the unit cell origin. (This origin was chosen when formulating the hkl substrate structure factor.) If the distribution of selected atoms about this single position is a delta-function, then $f_H = 1$. If the time-averaged displacements of the selected atoms about this single position form a Gaussian distribution, a Debye-Waller-like analysis gives $f_H = D_H = \mathrm{Exp}[-2(\pi\sigma/d_H)^2]$.[63] For the case of N equally occupied identical Gaussians centered at positions r_n, f_H and P_H are the amplitude and phase of the unitary geometric sublattice structure factor adjusted by the Debye-Waller factor.

$$\mathcal{F}_H = f_H e^{2\pi i P_H} = \frac{D_H}{N}\sum_{n=1}^{N} e^{2\pi i\, H.r_n} \qquad (3.13)$$

The non-dipolar correction parameters[72] for an initial s-state in Eq. 3.12 in the back-reflection geometry are defined as:

$$S_R = \frac{1+Q'}{1-Q'}\,,\ \tan\psi = \frac{S_R-1}{S_R+1}tan\Delta\,,\ |S_I| = \frac{1}{2}(S_R+1)\sqrt{1+tan^2\psi}$$

$\Delta = \delta_d - \delta_p$, where δ_p and δ_d are the scattered phase shifts of the s → p and s → d transitions obtained from Ref.[73].

$$Q' = \frac{(\delta + \gamma \cos^2\theta_p)\sin\theta_p \cos\phi_p}{1+\beta P_2(\cos\theta_p)} \quad ,$$

where β is the dipole asymmetry parameter. γ and δ account for non-dipolar effects. P_2 is the 2nd order Legendre polynomial ($P_2(x) = ½ (3x^2-1)$). Angles θ_p and ϕ_p are the spherical coordinates for the direction of the emitted photoelectron, where the z-axis is the polarization direction of the incident X-ray.

For our experimental geometry the central axis of the acceptance cone for the photoelectron detector is aligned with the polarization direction (z-axis). If the full cone is collected (as is the case for the off-specular reflections) the integration of Q' over the full 2π radians in ϕ_p leads to Q' = 0 and thus $S_R = |S_I| = 1$ and $\psi = 0$. Details of NDC calculations for our sample is described in subsequent chapters.

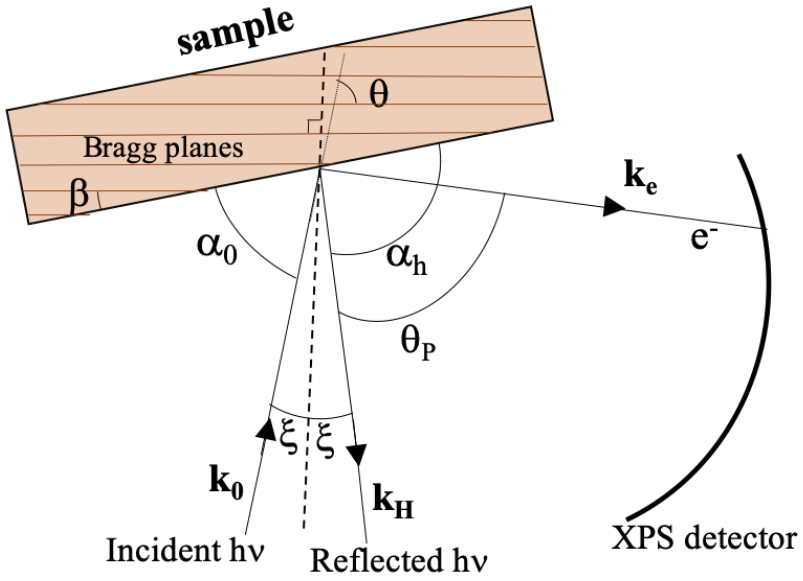

Figure 3.4. *Schematic overhead view of the experimental geometry for π-polarized X-ray diffraction.* $\mathbf{k_0}$ *and* $\mathbf{k_h}$ *are the incident and diffracted X-ray wave vectors, respectively. The angle* $2\xi = 180 - 2\theta$ *is the deviation from back-reflection* ($\theta = \pi/2$) *geometry.* θ *is the angle between the incident beam and the lattice planes (Bragg angle).* α_0 *is the angle between the incident beam and sample surface and* α_h *is the angle between the diffracted beam and sample surface.* β *is the angle between the surface and the lattice planes. The photoelectrons are detected in the direction* $\mathbf{k_e}$*. The angle* θ_p *is the angle between the emitted photoelectron and the diffracted X-ray beam* $\mathbf{k_H}$*.*

3.2.3 X-ray photoelectron spectroscopy

For a free atom, core electrons occupy orbitals with discrete binding energies. Upon excitation by photonic radiation at or above a particular binding energy, there is a probability for the electron to be ejected from the atom into the vacuum. This photoelectric effect is key to X-ray spectroscopy, as by probing the energy of these orbitals or observing the effect of photoemission in a material, we can learn the chemical identity, chemical state, and coordination environment of its atoms. The core electrons in an atom of an element such as a transition metal are shown schematically in Fig. 3.5(a). These energy levels correspond to electron binding energies that are specific to each element. In Fig. 3.5(b), an incident photon causes an excitation in an atom resulting in the ejection of an electron from the 1*s* orbital (*K* shell). The removal of a core-shell electron leaves an unstable core hole, and an electron from a higher shell moves into this hole (Fig. 3.5(c)). The energy gained in this process can be transferred to a fluorescent photon (as shown) or an Auger electron. The probability of an excitation event causing fluorescence or an Auger event depends on the atomic number *Z*; the probability of fluorescence increases with increasing *Z*. These three types of ejected particles – a photoelectron, a fluorescent photon, or an Auger electron – can all be detected and their energies measured, and from this information the composition or chemical details of their parent atom can be obtained.

X-ray photoelectron spectroscopy (XPS) is a powerful technique for non-destructive compositional and chemical analysis of surfaces. Samples are exposed to an X-ray beam (typically from an Al, Mg, or synchrotron source), which excites core-shell photoelectrons. These are collected by an energy-dispersive spectrometer, such as a hemispherical analyzer or a cylindrical mirror analyzer. Because of the short mean-free path length of photoelectrons in matter, XPS is typically performed in an ultra-high vacuum (UHV) chamber at pressures below 10^{-7} mbar;

however, ambient pressure XPS is becoming widely accessible for *in situ* studies at pressures up to 1 mbar. A review for XPS is given in Ref [74].

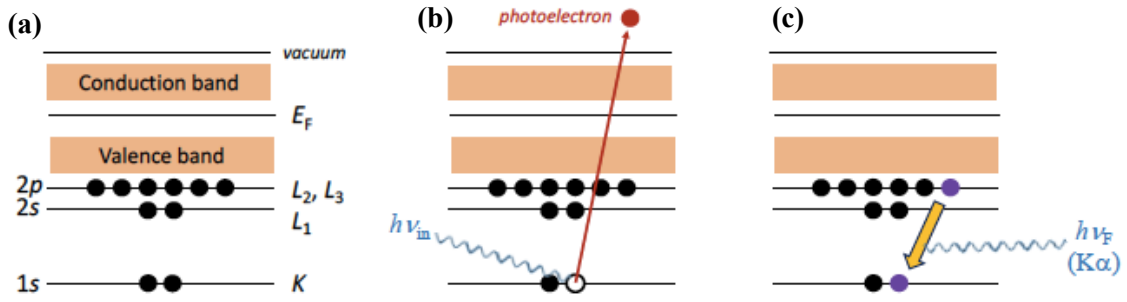

Figure 3.5 *Schematic of (a) the electron levels of an atom, with the core electrons shown as black dots occupying the levels; (b) a photoemission event caused by an incident X-ray with energy* $h\nu_{in}$*, wherein a photoelectron is ejected and a 1s core hole is created; and (c) a 2p – 1s relaxation event leading to the emission of a* $K\alpha$ *fluorescent photon.*

The kinetic energy E_k of a photoelectron excited by X-rays depends on the binding energy of the electron E_b and the X-ray energy hν. By conservation of energy, E_b is calculated as: $E_b = h\nu - E_k - \phi$. The work function ϕ accounts for kinetic energy lost in the electron analyzer. Every orbital of every atom has a particular binding energy that can be used to "fingerprint" the presence of an atomic species. The photoelectron signal of a species in a material surface is broadened due to the core-hole lifetime, final state effects, sample charging, phonon structure, and instrumental resolution. All orbitals beyond the *s* orbital may demonstrate spin-orbit splitting into doublets. The chemical state of the species can also shift the binding energy by several eV from the electron binding energy in a neutral atom. A core electron in a positively charged metal cation will experience less charge screening by other electrons than it would in a neutral atom, resulting in a higher binding energy. Thus, specific binding energy shifts indicate differences in charge state.

While XPS has good chemical sensitivity, it can only detect photoelectrons emitted from the top few nanometers of material due to the short mean-free path length of photoelectrons[75].

XPS data fitting

For fitting the XPS data, CasaXPS software was used[76]. For background subtraction Shirley algorithm has been used. This is an iterative determination of a background using the areas A1 and A2 to compute the background intensity S(E) at energy E,

$$S(E) = I_2 + \kappa\, A2(E) / (A1(E) + A2(E)) \quad \text{where } \kappa \text{ is } I_1 - I_2 \qquad (3.13)$$

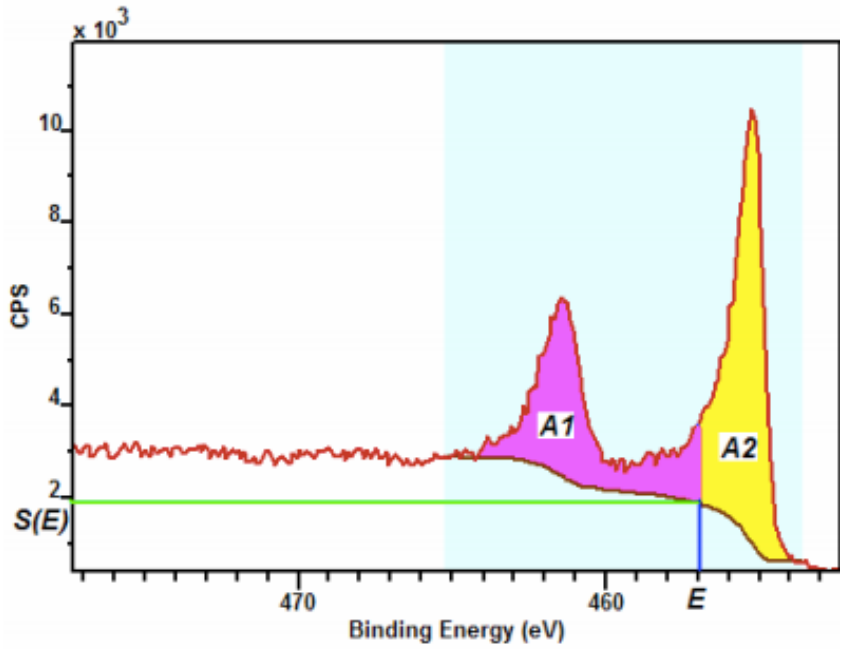

Figure 3.6. *Example of XPS curve fitting using CasaXPS.*

Initially the integrated areas A1(E) and A2(E) for each point on the background E is computed using an approximation to S(E). This is then refined using the background computed from the first approximation as input to improve the values computed for A1(E) and A2(E). To fit the

components the line shape used [LF (α,β,w, m)] is Lorentzian Asymmetric which is generated by convolution of a Lorentzian with a Gaussian

$$LF(\alpha,\beta) = [L(y)]^{\alpha} \quad y <= E$$

$$[L(y)]^{\beta} \quad y > E \qquad (3.14)$$

where L(y) = 1/(1+4((y-E)/F)^2)

The parameter m defines the width of the Gaussian and specified values of α and β are forced to increase to a constant value via a smooth function determined by the width parameter w.

Inelastic mean free path calculations

Since the x-ray absorption length is typically much longer than the photoelectron inelastic mean free path (IMFP), the information depth (ID) is restricted solely by the IMFP. Above a certain low energy threshold, as hν increases, so does the IMFP and hence ID.

$$IMFP = (0.73 + 0.0095\, E_k^{0.872})/Z^{0.3} \qquad (3.15)$$

where Z = atomic number and E_k is the kinetic energy of the outgoing photoelectron. While the IMFP provides a first-order estimate of the depth sensitivity realized by XPS, elastic scattering also plays a significant role. The effective attenuation length (EAL) takes elastic scattering into account. It is modeled as a linear relationship with the IMFP and the single-scattering albedo, ω.

$$EAL = IMFP\,(1 - 0.738\omega)\sin\theta \qquad (3.16)$$

where $\omega = e^{(\sum_{i=1}^{4} B_i (\ln E_k)^i}$ and θ is the electron-emission angle.

The ID in an XPS measurement is defined as the depth normal to the surface from which useful information can be obtained. It is specified as the percent of detected signal, P, from within that depth.

$$ID = IMFP\,(-1 + 0.787\omega)\sin\theta \ln\left[1 - \left(\frac{P}{100}\right)\right] \qquad (3.17)$$

A review discussing the IMFP, EAL and ID is given in Ref [77].

3.2.4 X-ray fluorescence

When an X-ray of sufficient energy excites a core-shell electron into vacuum level, the ion relaxes by filling the core-hole with an outer electron accompanied by the ejection of a photon (fluorescence) or another electron (Auger). Measured photons emitted is the basis of X-ray fluorescence (XRF), which provides quantitative information about the elemental composition and coverage of material. The emitted X-ray fluorescence (XRF) energy is the difference in energy between the inner shell containing the core hole and the outer shell from which an electron moves into it. Both electron shells involved in this transition are affected similarly by changes in charge screening due to different valence states, so the energy of the emitted fluorescent photon does not change substantially with a change in the atomic charge unless the outer shell is near the Fermi level. As the energy resolution of most energy-dispersive X-ray detectors is on the order of 100 eV or more, they are insensitive to shifts of a few eV. However, as X-rays interact very weakly with matter, XRF can be used to detect the composition of surfaces and interfaces in gaseous, liquid, or other *in situ* environments of interest. XRF can also be used to accurately quantify the composition of a surface by comparison with a calibrated standard sample. Analyzing the characteristic energies at which XRF photons are emitted gives the atomic composition of a sample at sub-monolayer concentrations. Measuring relative XRF photon intensities allows one to extract the effective coverage of the atomic species, provided geometry, XRF emission efficiency, and absorption effects are properly accounted for[78].

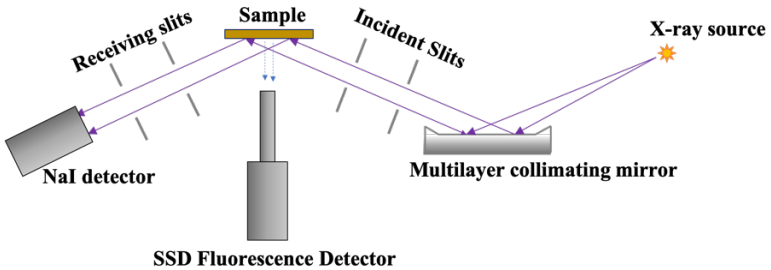

Figure 3.7. *Schematic showing X-ray fluorescence measurement set-up at J.B. Cohen X-ray Facility at Northwestern University*

3.2.5 X-ray absorption spectroscopy

X-ray absorption spectroscopy (XAS) is a unique tool for studying, at the atomic and molecular scale, the local structure around selected elements that are contained within a material. XAS can be applied not only to crystals, but also to materials that possess little or no long-range translational order: amorphous systems, glasses, quasicrystals, disordered films, membranes, solutions, liquids, metalloproteins and molecular gases. The physical quantity that is measured in XAS is the X-ray absorption coefficient μ(E), which describes how strongly X-rays are absorbed as a function of X-ray energy E. Generally, μ(E) smoothly decreases as the energy increases (approximately as $1/E^3$), i.e. the X-rays become more penetrating. However, at specific energies that are characteristic of the atoms in the material, there are sudden increases called X-ray absorption edges. These occur when the X-ray photon has sufficient energy to liberate electrons from the low-energy bound states in the atoms. XAS consists of two main techniques which has been used in this thesis work: extended X-ray absorption fine structure (EXAFS) and X-ray absorption near edge structure (XANES). XAS is intrinsically a quantum mechanical phenomenon that is based on the X-ray photoelectric effect in which an X-ray photon incident on an atom of the sample is absorbed and liberates an electron from an inner atomic orbital. The photoelectron wave scatters from the atoms around the X-ray absorbing atom, creating interferences between the outgoing and scattered parts of the photoelectron wavefunction. These quantum interference effects cause an energy-dependent variation in the X-ray absorption probability, which is proportional to the X-ray absorption coefficient. These modulations provide information about the structure, atomic number, structural disorder, and thermal motions of neighboring atoms. The probability that x-rays will be absorbed is given according to the Beer's Law: $I_T = I_0 e^{-\mu t}$, where I_0 is the x-ray intensity incident on a sample, t is the sample thickness, and I_T is the intensity transmitted through the sample.

At most x-ray energies, the absorption coefficient μ is a smooth function of energy. However, when the incident x-ray has an energy equal to that of the binding energy of a core-level electron, there is a sharp rise in absorption. This is called an absorption edge corresponding to the promotion of this core level to the continuum. An XAS measurement is a measure of the energy dependence of μ at and above the binding energy of a known core level of an atomic species. Since every atom has core-level electrons with well-defined binding energies, we can select the element to probe by tuning the x-ray energy to an appropriate absorption edge. Following an absorption event, the atom moves into an excited state, with one of the core electron levels empty (called a core hole), and a photo-electron. The excited state will then decay. During this decay process, a higher energy electron fills this core hole thus ejecting x-ray fluorescence of well-defined energy. The fluorescence emitted is characteristic of the atom and hence can be used to identify the atoms in a system and to quantify their concentrations.

XAS can be measured either in transmission mode (Fig. 3.8) or in fluorescence mode (Fig. 3.9). In transmission mode the absorption coefficient $\mu(E) \propto$-log (I_T / I_0) and in x-ray fluorescence $\mu(E) \propto (I_F / I_0)$. In both cases, the incident X-ray passes through an ion chamber (marked in yellow) and then hits the sample. In the transmission geometry, the transmitted X-ray passes through a second ion chamber (marked in brown). In the fluorescence geometry, the fluorescence signal for the element of interest is collected using an XRF detector (marked in purple).

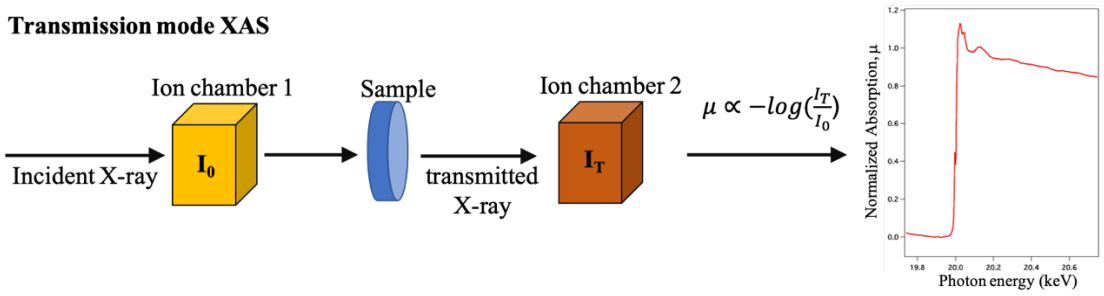

Figure 3.8. *Schematic showing XAS experimental setup in transmission mode.*

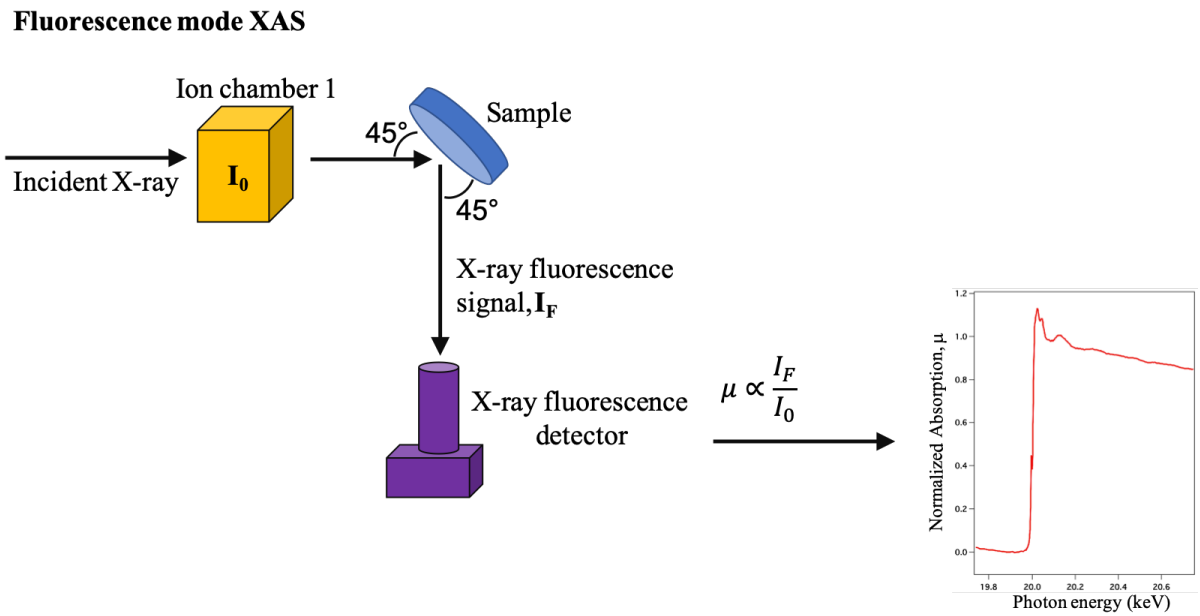

Figure 3.9. *Schematic top-view showing XAS experimental setup in fluorescence mode*

XAS consists of two distinct portions: the near-edge spectra (XANES) which is typically within 30 eV of the absorption edge and the extended fine-structure (EXAFS) which is the portion after the XANES region. Fig. 3.10 shows an example of an X-ray absorption spectra.

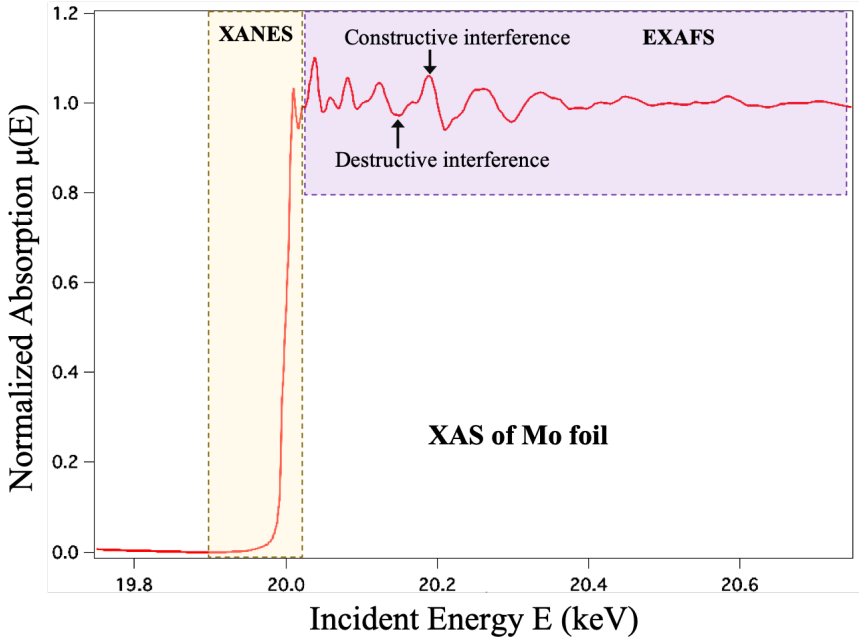

Figure 3.10. *XAS spectrum of a Mo foil at the Mo K-edge (20 keV). The XANES and EXAFS regions are marked in the figure.*

The XANES region contains the information about the occupation of the energy states, which is related to the oxidation state of the absorbing element. The EXAFS region provides the local atomic structure, such as the coordination number and bond length to the surrounding atoms. The absorption coefficient depends strongly on the interaction between the photoelectron and the neighboring atoms near the absorbing atom (referred to as the "shell"). The outgoing electron wave from the absorbing atom can be backscattered by its neighboring atoms. The interference between the outgoing and the backscattered wave functions can either be constructive or destructive, depending on the distances and the electron wavelength. The interference results in oscillations above the absorption edge. Moreover, the configuration of the shells also modulates μ(E). By analyzing the oscillations of μ(E), the local coordination structure can be obtained.

The XAS experiments were carried out at the Advanced Photon Source DND-CAT Beamline 5-BM-D. This is a bending magnet beamline which contains dedicated EXAFS setup. Fig. 3.11 shows a photo of the experimental set-up in the beamline. The beamline has a Linux running custom control system for motors.

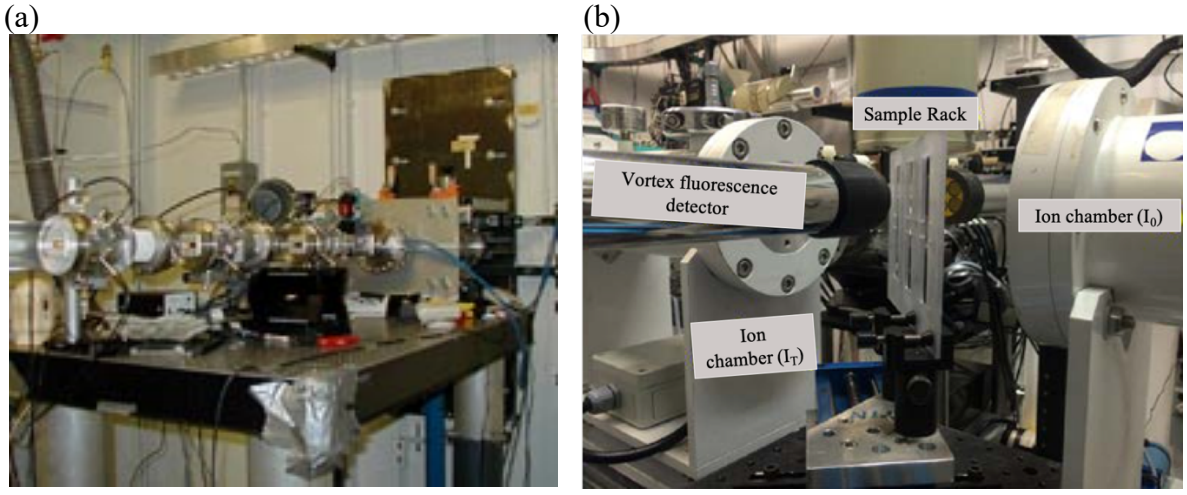

Figure 3.11. *(a) XAS set-up at the 5-BM-D beamline at the Advanced Photon Source (b) side-view of the setup for fluorescence mode XAS measurements at 5BM-D.*

XAS data reduction and modelling

This section describes the process of X-ray absorption spectrum data reduction[79-80]. At first the measured intensity is converted to μ(E) after correcting systematic measurement errors such as self-absorption effects and detector dead-time. Then a smooth pre-edge function is subtracted from μ(E) to get rid of any instrumental background and absorption from other edges. Next, the threshold energy E_0 is identified, typically as the energy of the maximum derivative of μ(E). Then μ(E) is normalized to go from 0 to 1, so that it represents the absorption of one x-ray. The next step is to remove a smooth post-edge background function to approximate $\mu_0(E)$. Then the EXAFS, χ(k), is isolated where $k = (2m(E - E_0)/\hbar^2)^{1/2}$. When plotting $\chi(k)$, the $\chi(k)$ is usually multiplied by k, k^2 or k^3. This is called k-weighting, which helps emphasize the features of $\chi(k)$ in the higher k region in order to obtain an even oscillation throughout the k-region of interest. The k-weighted $\chi(k)$ diagram is the superposition of several sinusoidal waves, usually with a dominating wave and several smaller waves. These sinusoidal waves correspond to the scattering between the electron from absorbing atom and its neighbors located at different bond distances (R_j). The final step is to apply Fourier transform, by which the sinusoidal waves in $\chi(k)$ can be deconvoluted and represented as multiple peaks in real space, R-space. The $\chi(k)$ is a combination of different near-neighbor coordination shells, which is a sum over the j^{th} coordination shells:

$$\chi(k) = -\sum_j \frac{N_j}{kR_j^{\,2}} \left|f_j(k)\right| e^{-\frac{2R_j}{\lambda_e(k)}} e^{-2k^2\sigma_j^2} \sin[2kR_j + \delta_j(k) + arg(f_j(k)] \tag{3.18}$$

where $k = (2m(E - E_0)/\hbar^2)^{1/2}$, E_0 is the absorption edge energy, N_j is the coordination number, σ_j^2 is the Debye-Waller factor that accounts for the structural and thermal disorder, Rj is the

average distance to the neighboring atom, $f_j(k)$ is a factor related to the probability of the photoelectron scattering from the j^{th} neighboring atom, δ_j is the phase shift resulting from the scattering process. Through EXAFS modeling and fitting procedure, important local structural parameters, such as E_0, N_j, R_j, and σ_j can be determined. Note that $\chi(R)$ is not a radial distribution function. Due to the "phase shift" term, $sin[2kRj+\delta j(k)+\arg(f_j(k)]$, in eq. (3.18), the position of the Fourier transformed peaks are not the real distances of the atomic shell and should be determined by EXAFS modeling. Because a range of incident X-ray energies is needed to create XAS spectra and a broad energy range is required to study a variety of elements, a synchrotron radiation X-ray source have to be used for measurements. A review of XAS is given in Refs. [79-80].

3.2.6 Low-energy electron diffraction (LEED)

The low-energy electron diffraction (LEED) technique can be used to sense the 2D crystal structure of a surface by the diffraction of a collimated beam of electrons (20-200 eV) with wavelength λ[Å] = 12.3/ √V[eV]. The low electron energy makes LEED sensitive to the top 5-10 Å of a surface, owing to a large interaction cross section ~1 $Å^2$, over 106 times greater than X-rays with matter. The downside of the strong interaction between electrons and matter is that the kinematic approximation does not hold for LEED, so any analysis based on LEED spot intensities requires the implementation of dynamical diffraction theory. In this thesis work, LEED is used as a qualitative in-situ monitor to observe the evolution and reconstruction of the surface structures, whereas X-ray and other surface science techniques are used for structure determination. See Ref. [81] for a review of LEED.

3.2.7 Atomic Force Microscopy (AFM)

Statistically averaging methods are complemented by local probe measurements, which give real-space images of nanoscale phenomena. Scanning probe microscopy (SPM) is particularly well-suited to surface studies as it involves an interaction of a narrow tip with the surface, yielding spatially-resolved information about the surface. The SPM family includes atomic force microscopy (AFM), scanning tunneling microscopy (STM), Kelvin probe force microscopy (KPFM), magnetic force microscopy (MFM), and a variety of other methods which provide topographic, electronic, thermal, magnetic, mechanical, and chemical information at the nanometer or atomic scale. AFM is one of the most robust and widely-used SPM methods. It involves a direct physical interaction between the surface and a hard, extremely sharp tip (with curvature on the order of nanometers) at the end of a cantilever. The movement of the tip in the surface-normal direction causes deflections in the cantilever, which are measured using a laser reflected from the cantilever into a split photodiode detector. In contact-mode AFM, the tip is rastered across the surface and is deflected by surface features. Because the tip "drags" along the surface, this type of measurement is potentially locally destructive. Tapping-mode AFM addresses this issue by oscillating the cantilever near some resonance frequency and measuring the modulation of the oscillation amplitude as the tip is rastered across the surface. This results in a much softer interaction of the tip with the surface, preserving surface features and retaining the integrity of the tip. In non-contact (NC) AFM, the tip is kept further from the sample surface, and the interaction between the tip and surface is measured as a modulation in the frequency of cantilever oscillation. See Ref. [82] for a review of AFM.

Chapter 4

VO_x / α-TiO_2 (110) Interface

4.1 Introduction

Global environmental pollution has reached a worrisome level where it has been causing adverse health effects at all stages of life. A clean environment has become a necessity in this high energy consuming economy with the chemical industries contributing to high levels of atmospheric emission. Release of NO_x from burning coal, oil, gas especially in power plants is a major source of toxic and carcinogenic pollutants. TiO_2 supported vanadium oxide is the most widely used catalytic system for selective catalytic reduction of NO_x with NH_3 resulting in non-toxic end products. In heterogeneous catalysis, activity and selectivity of a catalytic system are strongly linked to the structure of the catalyst (VO_x) and the support (α-TiO_2). The support structure provides a base for arrangement of the catalytic species to achieve highest possible activity and selectivity. The interface between the support and the catalyst (V-O-S bonds) plays a major role in controlling the structure and in turn the activity of the catalyst. During a redox reaction, these catalytic systems undergo structural and chemical changes as they become active participants in the overall catalytic process. Hence, it is very important to understand the atomic-scale structures with chemical state specificity of catalysts under reaction conditions which will help tune the growth parameters to obtain improved catalytic properties. Since sub-monolayer vanadia is significantly more catalytically active than V_2O_5 nanoparticles or multilayer films, in this work we studied 0.5 ML vanadia film. In this work we devised a novel model-independent 3D atomic

mapping technique with atomic-scale chemical state specificity using in-situ X-ray standing-wave (XSW) excited X-ray photoelectron spectroscopy (XPS). Previous XSW-XRF studies of oxide-supported monolayer catalysts were not able to distinguish the various chemical states of the catalyst which is very important for understanding the structural changes during a redox process[83-94]. This method also allows us to map the surface hydroxylated oxygen atoms which have not been possible in previous works which used X-ray fluorescence rather than X-ray photoelectrons and will be discussed in chapter 5 of this thesis. We use this novel method to study 0.5 ML of VO_x grown on α-TiO_2 rutile (110) surface and directly observe *in situ* redox-induced atomic-scale structural and chemical state modification of the catalyst. These observations of structural transformations and coherence of supported catalyst accompanying changes of the oxidation state V^{5+} to V^{4+} under redox cycling provides information on the structure of active sites and helps in understanding complex catalytic reactions. In addition, we use density functional theory (DFT) calculations to further improve our understanding of this complex catalytic system[95-97].

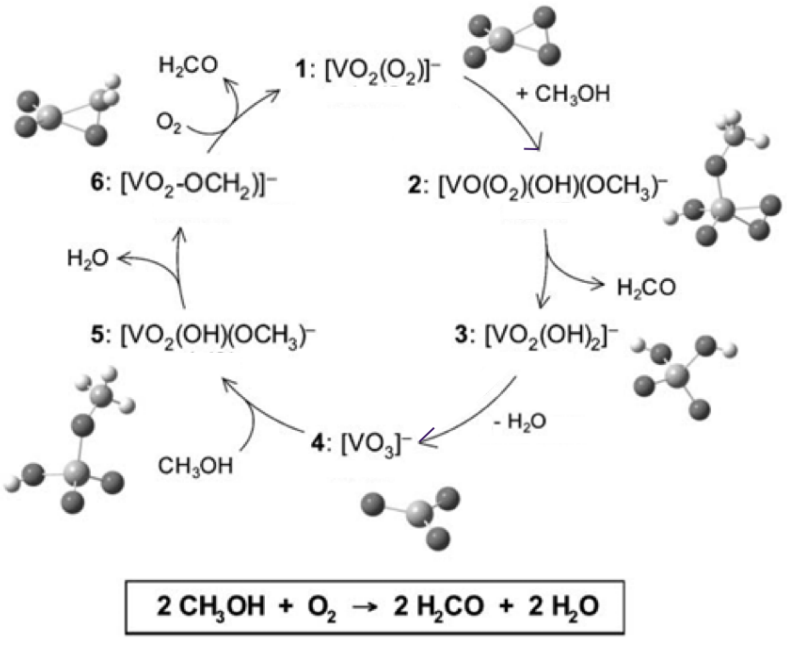

Figure 4.1. *Schematic showing gas phase cycle for the oxidation of methanol to formaldehyde using vanadium oxide catalyst*[98]

4.2 Experimental Methods

Surface preparation

Sample growth

Rutile α-TiO_2 (110) single crystals, float zone grown by MTI Corp., were used as substrates. The single crystals were 10 x 10 x 1 mm^3 with one-side polished and with a surface miscut < 0.1°. α-TiO_2 is tetragonal with space group $P4_2/mnm$ and with room-temperature (RT) lattice constants a = b = 4.594 Å and c = 2.959 Å. α-TiO_2 substrates were annealed in a tube furnace with flowing O_2 (~500 sccm) at 400°C for 0.5 h, followed by 900 °C for 1 h. Atomic force microscopy (AFM) showed the formation of flat atomically clean step-separated terraces, 0.1 to 0.5 μm in width.

Prior to atomic-layer deposition (ALD), the substrates were first immersed in DI water (resistivity > 10^7 Ω cm) for 1 h at 90°C to hydroxylate the surface. This was followed by a dip in a 10% HCl solution, a thorough DI water rinse, and then drying under ultra-high pure nitrogen (99.999%). The treated substrates were then loaded into a custom built cross-flow ALD reactor, heated to 300°C and maintained under ultra-high-purity nitrogen flow of 360 sccm at a pressure of 1 Torr for 1 h. Surface cleaning of the substrates was then carried out in-situ by flowing 400 sccm of ozone over the surface. A vanadia (VO_x) layer was deposited on the treated α-TiO_2 (110) substrates by sequential exposure of $1x10^5$ L of vanadyl oxytriisopropoxide (VOTP) and 4 x 10^5 L of hydrogen peroxide (H_2O_2) separated by a nitrogen purge for 5 s. These four steps of dose-purge-dose-purge, which constitute a single ALD cycle, were repeated 4 times. The film was grown by Dr. Devika Choudhury from the group of Dr. Jeff Elam at Argonne National Laboratory.

Redox treatment

The sample was annealed inside the Diamond Light Source I09 UHV preparation chamber at 350°C for 1 hr. An Oxford Applied Research TC50 thermal gas cracker cell temporally installed on this chamber was used for oxidation and reduction of the surface. Molecular oxygen was slowly leaked through the fine bore inert cracker tubes, into the preparation chamber until the chamber pressure stabilized at 7.5 x 10^{-7} Torr. The cracker cell power was set to 60 W, which gave a 50% cracking efficiency indicating that 50% of the molecular O_2 was converted to atomic oxygen. The cracker cell was directed almost perpendicular to the sample surface and was at a distance of 15 cm from the surface. The sample was heated to 220°C and the cracker cell was directed towards the sample for 0.5 h which oxidized the 0.5 ML vanadia film. The reduced surface was produced in a similar manner by using molecular H_2 at a pressure of 7.5 x 10^{-7} Torr. The cracker cell power was set to 60 W which converted 50% of the molecular H_2 to atomic hydrogen. For reduction the sample was heated to 400 °C and the cracker cell was directed towards the sample for 0.5 h which reduced the 0.5 ML vanadia film.

Coverage measurement

To find the coverage of the vanadium oxide film we used X-ray fluorescence measurements. In this TiO_2 supported VO_x sample, V Kα and Ti Kβ fluorescence peaks overlap. As a result, the V Kβ peak has to be considered, but it is a very low intensity peak. Hence the coverage measurement was performed at Sector 5BM-C beamline at the Advanced Photon Source which gave a significant V Kβ signal as seen in Fig. 4.2 (a). The standard sample used to calibrate the fluorescence yield was Ba implanted on Si(111) whose coverage was measured using RBS as 8.6 atoms/nm^2. Ba Lα fluorescence line is close to V Kβ line in energy and hence was chosen as the standard (Fig. 4.2(b)).

After normalizing the yields of V Kβ and Ba Lα for (i) incident counts (ii) input count rate: output count rate (iii) acquisition time (iv) fluorescence cross-section (v) vortex detector sensitivity (vi) attenuation due to air, we get a ratio of 0.6 : 1 for V : Ba atoms. Knowing the standard sample coverage gives us a vanadium coverage of 5.2 atoms/nm^2. Since 1 ML corresponds to 10.4 atoms/nm^2, the coverage of VO_x on α-TiO_2(110) comes out to be 0.5 ML.

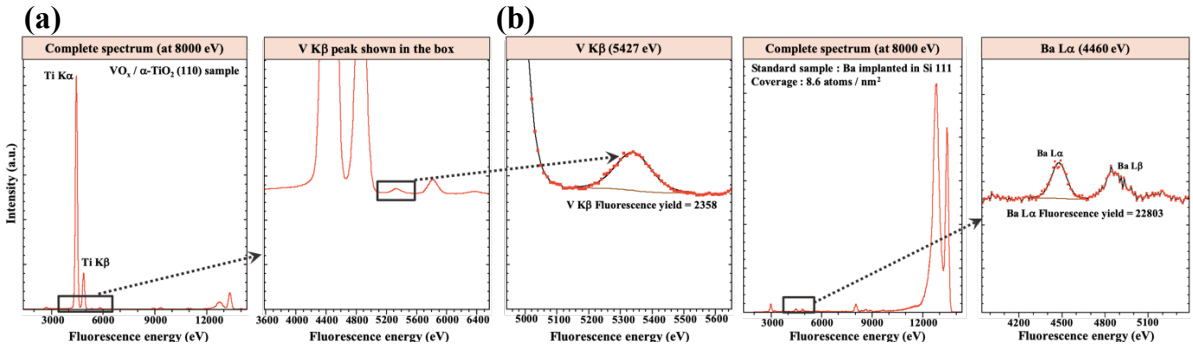

Figure 4.2. (a) *Fluorescence spectrum of VO_x/α-TiO_2(110) sample showing the Ti and V peaks* ***(b)*** *Fluorescence spectrum of Ba implanted on Si(111) sample showing the Ba peaks.*

Surface Characterization

A Bruker Dimension FastScan AFM was used for *ex situ* examination of the surface morphology before and after the VOx growth and after the redox reactions. An OCI-MCP low-energy electron diffraction (LEED) system was used to study the room temperature 2D crystal structure of the rutile TiO_2 (110) surface before and after growth of the vanadia sub-monolayer. Back-reflection XSW excited XPS measurements were carried out at the I09 beamline at Diamond Light Source in Didcot, UK.

Diamond Light Source I09 beamline

The I09 beamline is split into three branches. Branch I delivers hard X-rays, and branches J and K deliver soft X-rays. I and J merge in Experimental Hutch 2 (EH2), allowing dual hard and soft X-

ray experiments. The energy of the hard X-rays is selected by an in-house-developed Si(111) double-crystal monochromator (DCM) designed to work between 2.1 and 20 keV. The design of the soft X-ray branches is based on a plane grating monochromator (PGM) using a collimated light. The soft X-ray branch goes from 100 eV to 2.1 keV. The experimental station in EH2 consists of an analysis chamber and two sample preparation chambers. The analysis chamber is equipped with a Scienta EW4000 high-voltage electron analyzer and a low-energy electron diffraction (LEED) optic. The preparation chambers, each fitted with a standard LEED optic, allow ion sputtering, sample heating (up to 1500°C), gas dosing, and physical vapor deposition for in-situ surface preparation. A large manipulator that positions the sample and provides polar and azimuth rotations is used for X-ray measurements at temperatures between 60 and 900 K. I09 provides a wide range of X-ray characterization techniques among which we used BRXSW excited XPS characterization[99].

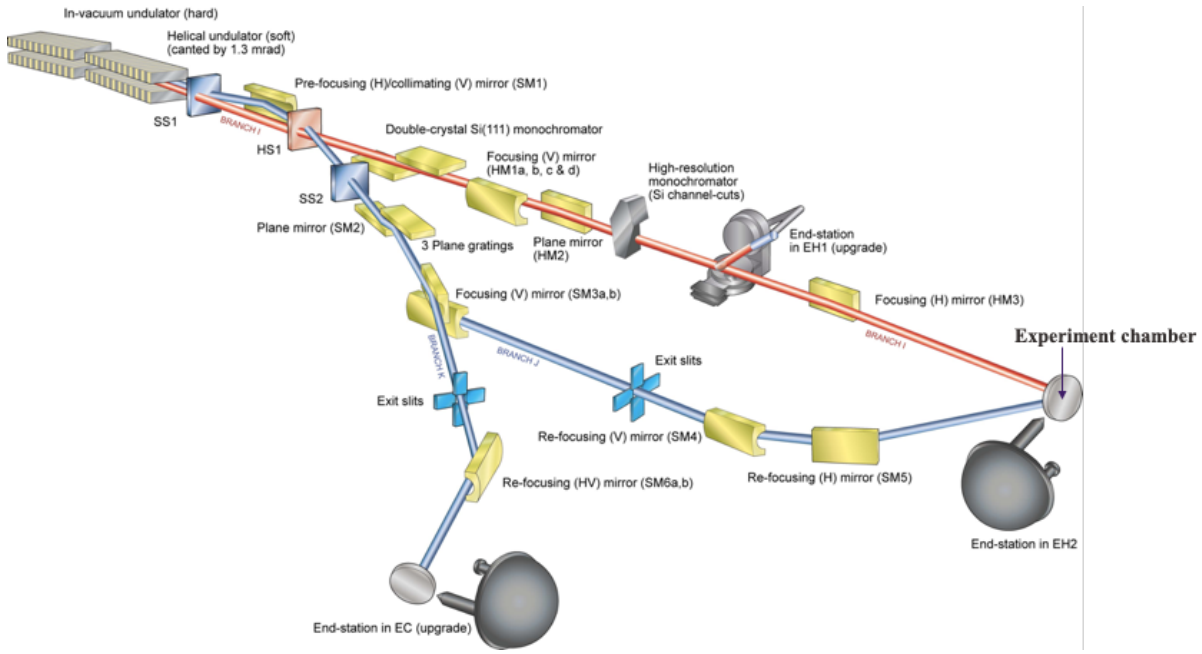

Figure 4.3. *Schematic of Diamond Light Source I09 beamline showing how the soft (blue) or hard (red) undulator x-ray beams were directed to be incident on the sample inside the UHV chamber used for this experiment. The hard X-rays (1900 – 2900 eV) were used for the XSW excited XPS measurements. The soft X-rays (900 eV) were used for higher-resolution XPS.*

4.3 Results and discussion

AFM and LEED

The AFM image shows a rough surface for the as-received TiO_2 (110) surface (Fig. 4.4 (a)). After O_2 annealing (Fig. 4.4(b)) the surface atoms rearrange to form atomically- clean flat ~250 nm wide terraces separated by 0.3 nm steps with an rms surface roughness of 0.1 nm. After 0.5 ML VO_x growth and after redox reactions, steps are still seen, indicating a uniform VO_x growth (Fig. 4.4(c)) and no clustering as a result of the redox reactions (Fig. 4.4(d)). A (1x1) low-energy electron diffraction (LEED) pattern was observed both before and after 0.5 ML VO_x growth and after the redox reaction (Figs. 4.4(e-g)).

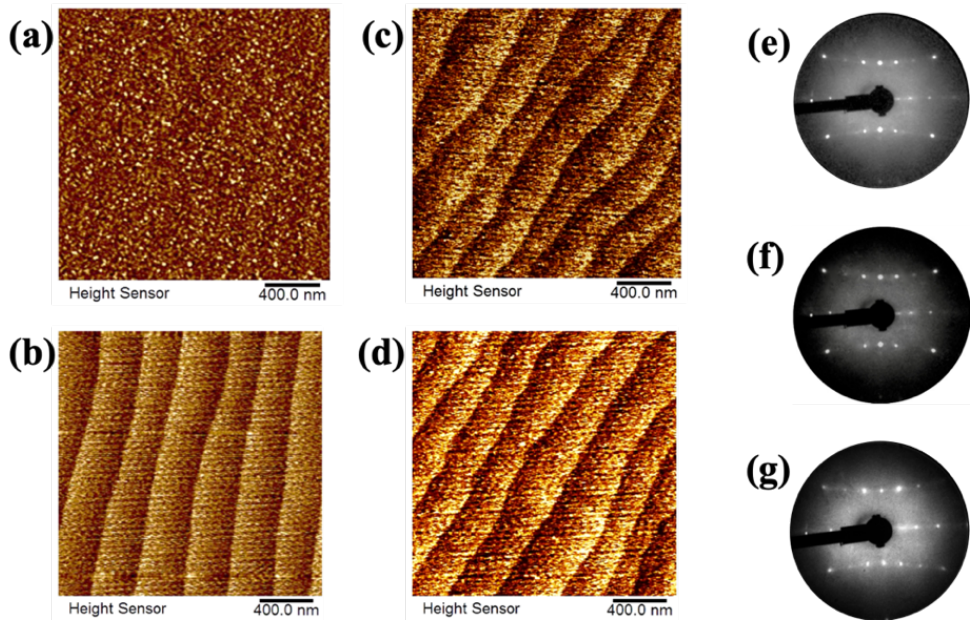

Figure 4.4. *AFM images of α-TiO_2 (110) surface:* ***(a)*** *As-received;* ***(b)*** *After annealing in O_2;* ***(c)*** *After 0.5 ML VO_x growth;* ***(d)*** *After redox reactions. LEED patterns of α-TiO_2 (110) surface:* ***(e)*** *after O_2 annealing; (f) after 0.5 ML VO_x growth; (g) after the redox reactions. The LEED was collected at 79 V.*

Soft and Hard X-ray Photoelectron Spectroscopy

Soft X-ray (Eγ = 900 eV) beam at I09 was used for obtaining high-resolution XPS survey spectra. Soft X-ray measurements were performed at an incident angle of 30° to maximize the collected photoelectron emission from the sample. The area of the XPS detector was divided into 14 angular slices over the usable angular acceptance range of 56°. Vacuum annealing, oxidation and reduction removed adventitious C including C from the residual ligands from the VOTP ALD precursor. Thus, the survey scan (Fig. 4.5) shows an insignificant C contamination of 0.02 ML. The C 1s peak was used as a reference to calibrate the BE scale for the O and V XPS peaks. After each in situ treatment (VA, Ox and Re), the sample was UHV transferred from the I09 preparation chamber to the analysis chamber for soft X-ray survey scans followed by XSW-XPS measurements.

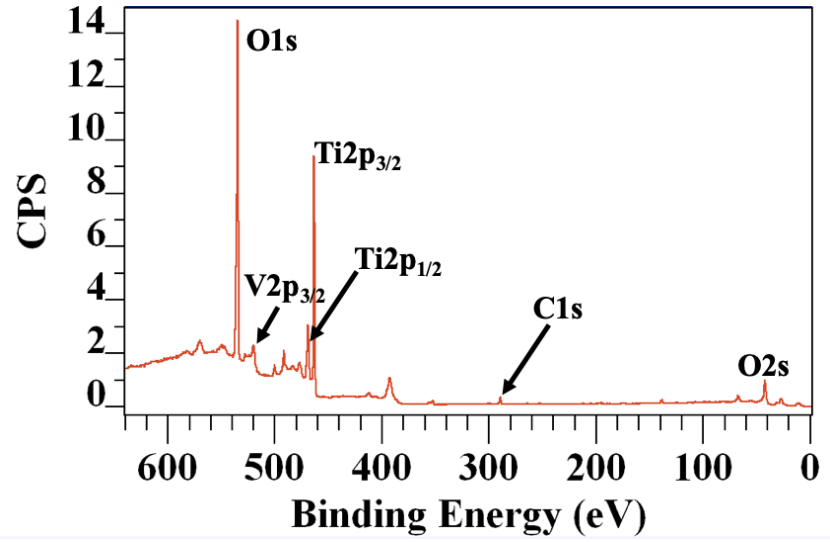

Figure 4.5. *Soft X-ray survey scan at incident energy = 900 eV showing the important XPS peaks.*

Each V $2p_{3/2}$ peak can be deconvoluted into two different oxidation states of vanadium. Based on the binding energy difference (BED) between the O 1s and V $2p_{3/2}$, these peaks can be identified as V^{4+} (BED = 14.6 eV) and V^{5+} (BED = 13.1 eV). Comparing the area of these two peaks gives

us an estimate of the amount of V in each chemical state. After vacuum annealing, 30% (0.15 ML) of vanadium is V^{5+} and the remaining 70% (0.35 ML) is V^{4+}. Upon oxidation, 64% of the V (0.32 ML) becomes V^{5+} and the remainder 36% (0.18 ML) is V^{4+}. Reduction reverses the reaction causing two-thirds of the V^{5+} species to gain electrons and convert back to V^{4+}; resulting in 23% (0.11 ML) V^{5+} and 76% (0.39 ML) V^{4+} .

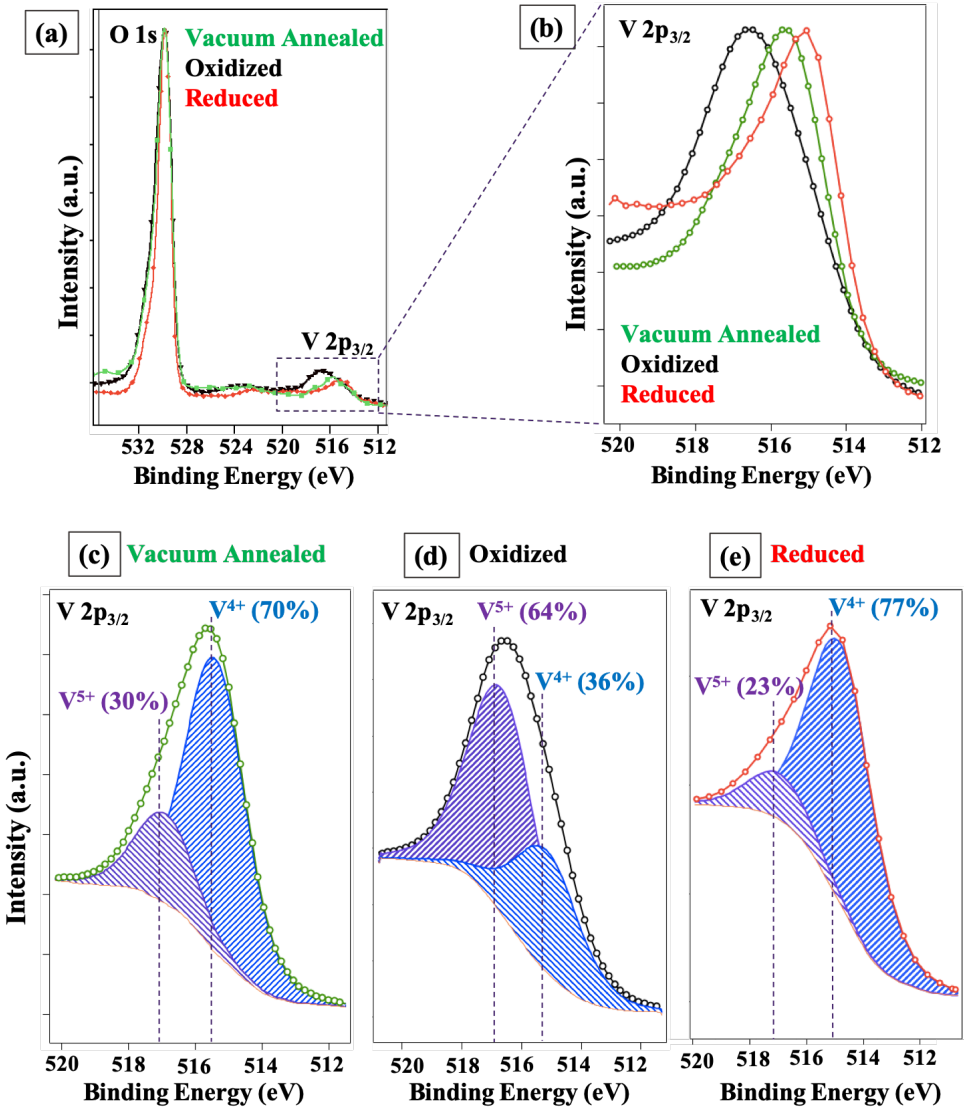

Figure 4.6. ***(a)*** *O 1s and V 2p XP spectra at 1.9 keV.* ***(b)*** *V $2p_{3/2}$ spectra of VA, Ox and Re surfaces showing chemical shifts wrt O 1s peak. V $2p_{3/2}$ XP spectra at 1.9 keV incident energy for the* ***(c)*** *vacuum annealed surface* ***(d)*** *oxidized surface and* ***(e)*** *reduced surface.*

α-TiO_2 (110) unit cell transformation

Since the vanadium oxide film was grown on the (110) surface of the TiO_2 single crystal, hence, for convenience in generating and displaying the XSW 3D atomic maps, we defined a non-primitive tetragonal unit cell (Fig. 4.7) with a C-axis normal to the (110) surface of the primitive unit cell. The transformation from the primitive tetragonal unit cell to the non-primitive tetragonal unit cell is $\begin{pmatrix} A \\ B \\ C \end{pmatrix} = \begin{pmatrix} -1 & 1 & 0 \\ 0 & 0 & 1 \\ 1 & 1 & 0 \end{pmatrix} \begin{pmatrix} a \\ b \\ c \end{pmatrix}$.

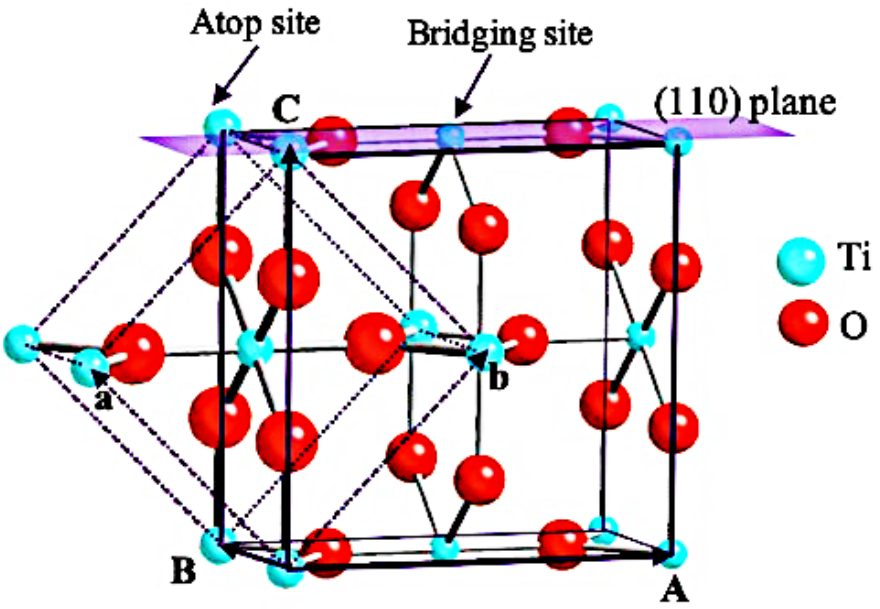

Figure 4.7. *α-TiO_2 tetragonal primitive unit cell (a, b, c) and non-primitive tetragonal unit cell (A, B, C). a=b=4.594 Å, c=2.958 Å and A=C=6.496 Å, B=2.958 Å. The fractional primitive unit cell coordinates x y z for Ti are 0 0 0 and ½ ½ ½ and for O are ε ε 0 , –ε –ε 0 , ζ –ζ ½ and -ζ ζ ½ where ε = 0.3053 and ζ= 0.1947.*

X-ray standing wave results

To generate 3D atomic density maps, XSW-XPS modulations from multiple sets of hkl reflections need to be measured so that eq. 3.11 can be used for the Fourier summation with the f_H and P_H values obtained from each reflection according to eq. 3.12. By using the symmetry of the single crystal substrate and its surface, we obtain a larger set of f_H and P_H values than measured. For example, in XSW measurements of α-TiO_2 (110), measured f_H and P_H values of (200) reflection will be the same as (020). When picking symmetry equivalent hkl's for a surface adatom distribution, we must preserve the fact that the symmetry is broken in the vertical direction. Fig. 4.8 shows the five symmetry-inequivalent hkl reflections that we chose for this experiment as it is important to select a complete set within a limited range of reciprocal space. Fig. 4.9 shows the reciprocal space with the symmetry equivalent reflections marked.

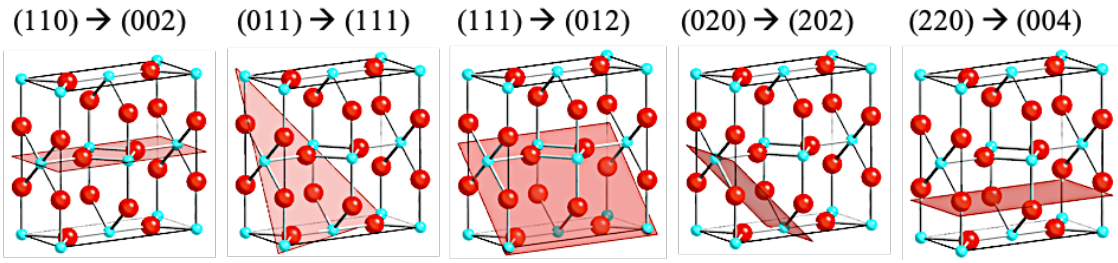

Figure 4.8. *Non-primitive rutile TiO_2 unit cells showing the 5 hkl planes that were studied and the respective primitive hkl → non-primitive HKL indices.*

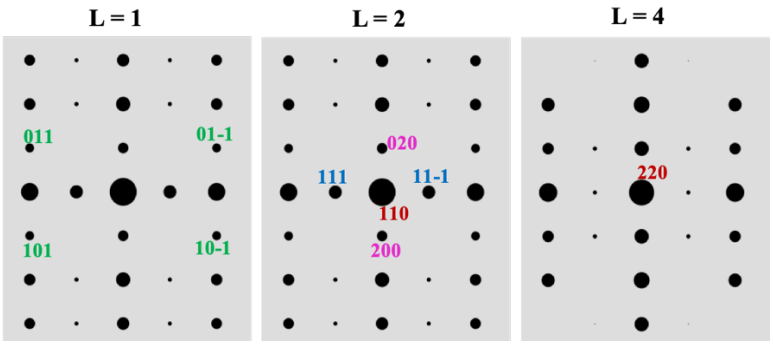

Figure 4.9. *The location of hkl Bragg reflections in the L = 1, L=2 and L=4 reciprocal space plane. Symmetry equivalent reflections are given the same color.*

XSW-XPS measurements used a Scienta EW4000 hemispherical XPS analyzer with its lens axis aligned horizontally along the polarization direction of the incident X-ray beam. Fig. 3.4 shows a top view schematic of our experimental setup. An upstream position sensitive detector indicating the position of the incident and back-reflected X-ray beams determined that the Bragg condition was set for a Bragg angle of 88° in the π-polarization geometry with the diffracted beam deflected in the horizontal plane toward the XPS lens. In our experimental setup $\xi = 2°$. The asymmetry parameter $b = -\sin \alpha_0 / \sin \alpha_h$. b had up to 5% effect on coherent fraction. The polarization factor $|P| = |\cos 2\theta| = 0.998$ had no significant effect on our coherent fraction and position and was approximated at P = 1. Table 4.1 gives the values of b for each reflection.

Table 4.1. *Tabulated values for the incident energy used to achieve the BRXSW condition for each hkl reflection used from the α-TiO_2 (110) single crystal. Also listed are the Fig. 3.4 β angles between the hkl planes and (110) surface plane; along with the asymmetry parameter b for all 5 reflections*

Reflection	**Bragg energy (eV)**	**Angle wrt (110) β**	**Asymmetry parameter, b**
1 1 0	1911	0°	-1.00
1 0 1	2499	67.5°	-0.85
1 1 1	2842	47.7°	-0.92
2 0 0	2707	45°	-0.93
2 2 0	3308	0°	-1.00

Table 4.2. *Some parameters related to each hkl reflection that was studied.*

Reflections	**d-spacing (Å)**	**Energy E_γ (keV) (for θ_B=90º)**	**K.E. (keV) of V $2p_{3/2}$ at E = E_γ**	**Photoelectric C.S. (kb)**	**Inelastic mean free path (IMFP) (Å)**	**Take-off angle (χ)**	**Information depth for 70% of signal (From Eq. 3.16) (Å)**
(110)	3.248	1.908	1.392	18.03	24.13	18.0º	9.4
(101)	2.488	2.492	1.982	9.99	31.86	67.5º	38.6
(200)	2.297	2.700	2.188	8.02	34.47	45.0º	32.2
(111)	2.187	2.835	2.324	6.95	36.17	47.7º	35.5
(220)	1.624	3.820	3.308	2.89	48.13	18.0º	20.2

X-ray standing wave results: Bulk Titanium

As a system check, XSW-XPS analysis is used on the bulk Ti 2p signal to show that the Ti atoms show up at bulk like positions. The Ti was in 4+ state as expected for TiO_2 crystal. The XPS peak did not shift upon oxidation and reduction which showed that the substrate crystal was stable under redox conditions. This was true even for the very surface sensitive grazing emission geometry of the (110) XSW measurement. f_{meas} and P_{meas} are the values obtained from experiment and f_{calc} and P_{calc} are values calculated considering ideal Ti positions. As we can see from Table 4.3, the values match very well indicating the validity of our measurements and analysis. After oxidation and reduction the f and P values remained unchanged further proving the stability of the support substrate TiO_2.

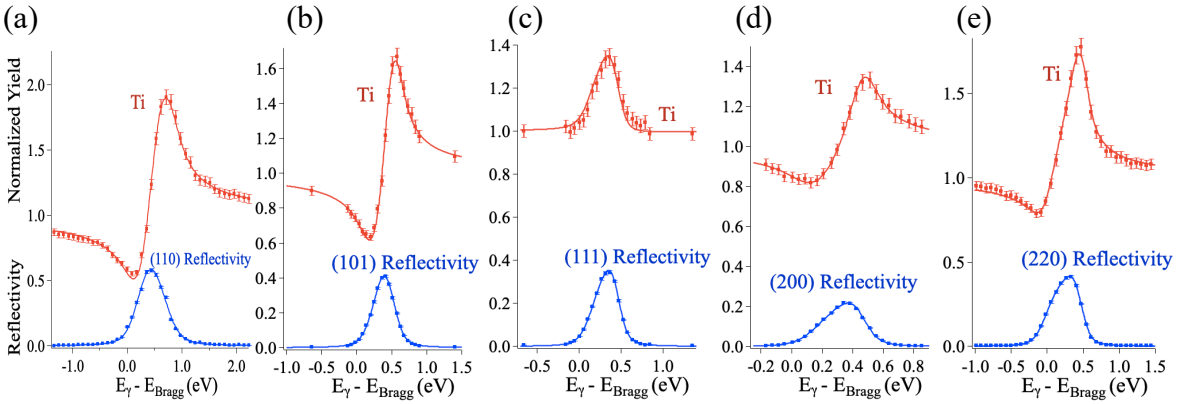

Figure 4.10. (a-e) *Measured data and theory fits for the reflectivity and Ti $2p_{3/2}$ XPS yields for the energy scans through the five reflections (110), (101), (111), (200), (220).*

Table 4.3. *f_H and P_H as measured from XSW-XPS and calculated for bulk Ti atoms.*

	Titanium			
h k l	**f_{meas}**	**f_{calc}**	**P_{meas}**	**P_{calc}**
1 1 0	0.99 (1)	0.98	-0.01 (1)	0
1 0 1	1.00 (1)	0.97	-0.03 (2)	0
1 1 1	0.03 (1)	0	---	--
2 0 0	0.92 (2)	0.96	-0.02 (1)	0

X-ray standing wave results: Vanadium

This section shows the results for XSW induced modulation in V $2p_{3/2}$ XPS signal as the sample was scanned across 5 symmetry inequivalent *hkl* reflections. This gave us 5 sets of f_H and P_H for each oxidation state of vanadium, V^{4+} and V^{5+}. These values are shown in Tables 4.4 – 4.6 as f_{meas} and P_{meas} for each oxidation state of Vanadium.

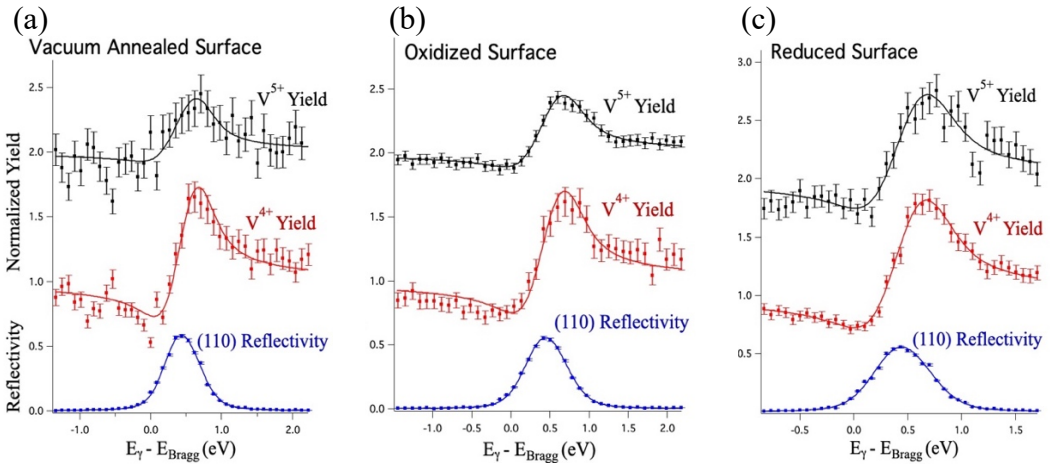

Figure 4.11. (a-c) *Modulations in V^{4+} and V^{5+} XPS normalized yields through the (110) reflection energy scan of the VA, Ox, Re surfaces, respectively. The V^{5+} normalized yield is offset by +1.*

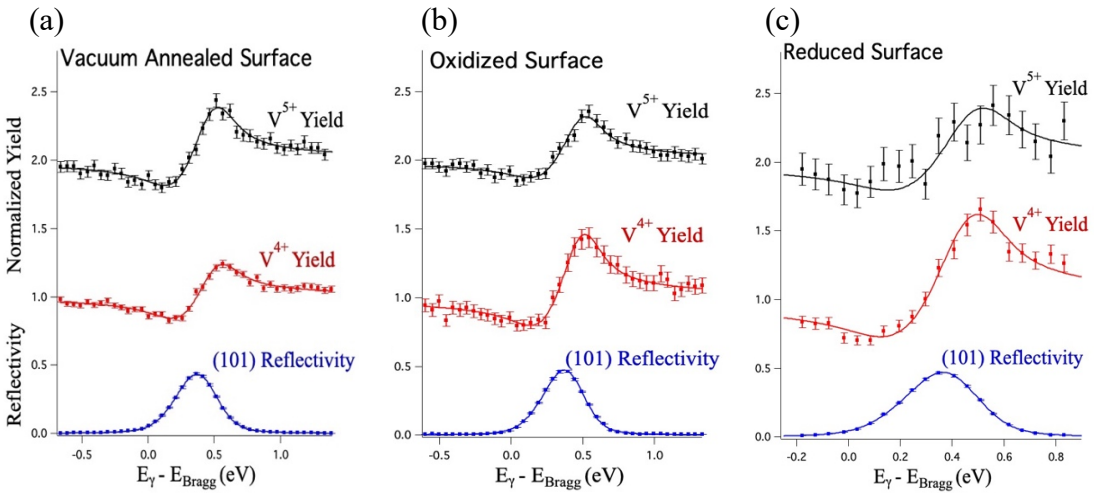

Figure 4.12. (a-c) *Modulations in V^{4+} and V^{5+} XPS yields through the (101) reflection energy scan of the VA, Ox, Re surfaces, respectively. The V^{5+} normalized yield is offset by +1.*

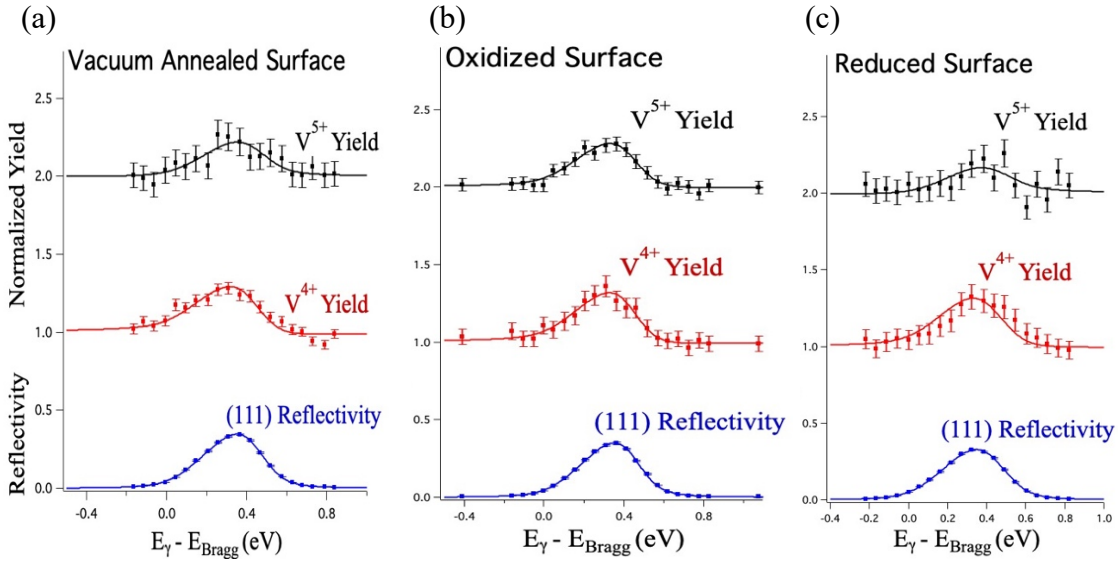

Figure 4.13. (a-c) *Modulations in V^{4+} and V^{5+} XPS yields through the (111) reflection energy scan of the VA, Ox, Re surfaces, respectively. The V^{5+} normalized yield is offset by +1.*

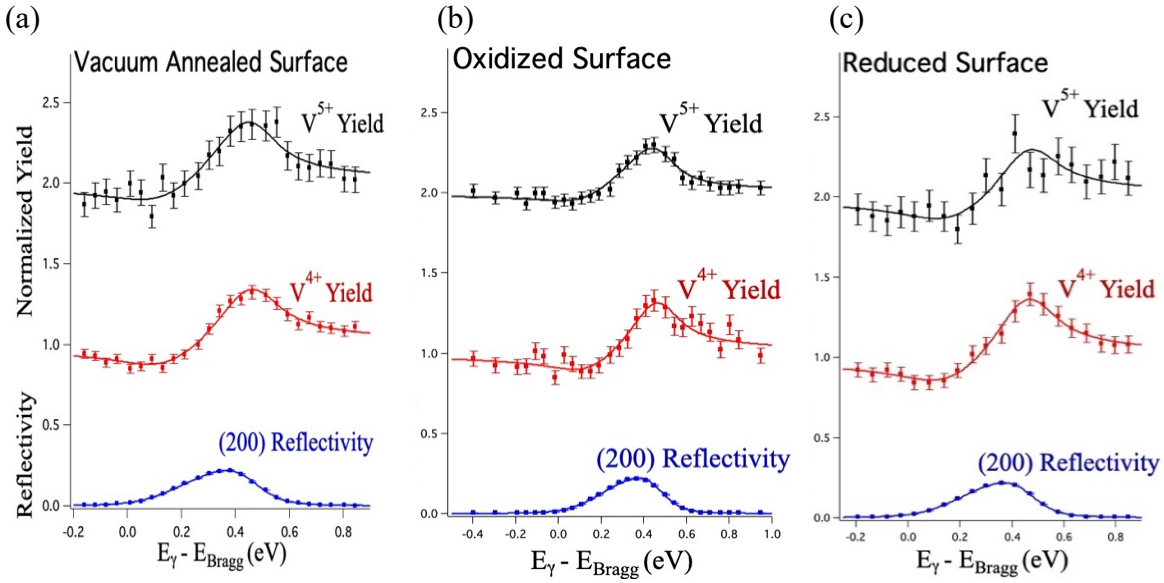

Figure 4.14. (a-c) *Modulations in V^{4+} and V^{5+} XPS yields through the (200) reflection energy scan of the VA, Ox, Re surfaces, respectively. The V^{5+} normalized yield is offset by +1.*

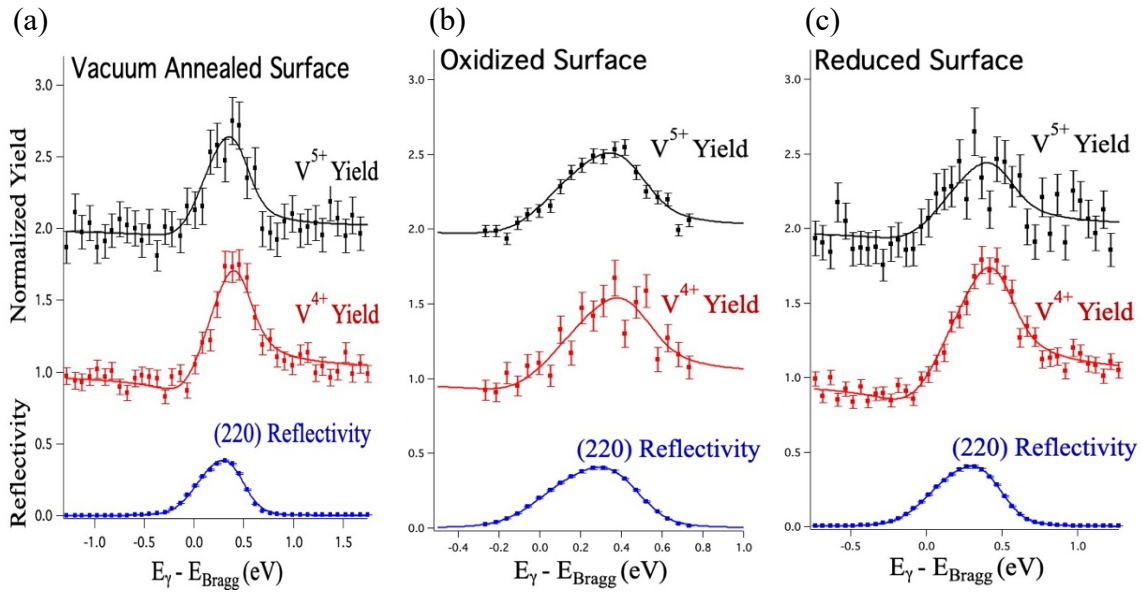

Figure 4.15. (a-c) *Modulations in V^{4+} and V^{5+} XPS yields through the (220) reflection energy scan of the VA, Ox, Re surfaces, respectively. The V^{5+} normalized yield is offset by +1.*

3D atomic density mapping of surface vanadium

The in situ XSW measurements induced distinctive modulations for each oxidation state of Vanadium from scans across five reflections. A Fourier summation of the five sets of Fourier components, listed in tables 4.4 - 4.6 as f_{meas} and P_{meas}, and their symmetry equivalents is then used to generate model-independent 3D atomic density $\rho(\mathbf{r})$ maps (eq. 3.11).

After vacuum annealing, 30% (0.15 ML) of vanadium is V^{5+} and the remaining 70% (0.35 ML) is V^{4+}. Upon oxidation, 64% of the V (0.32 ML) becomes V^{5+} and the remainder 36% (0.18 ML) is V^{4+}. Reduction reverses the reaction causing two-thirds of the V^{5+} species to gain electrons and convert back to V^{4+}; resulting in 23% (0.11 ML) V^{5+} and 76% (0.39 ML) V^{4+} .

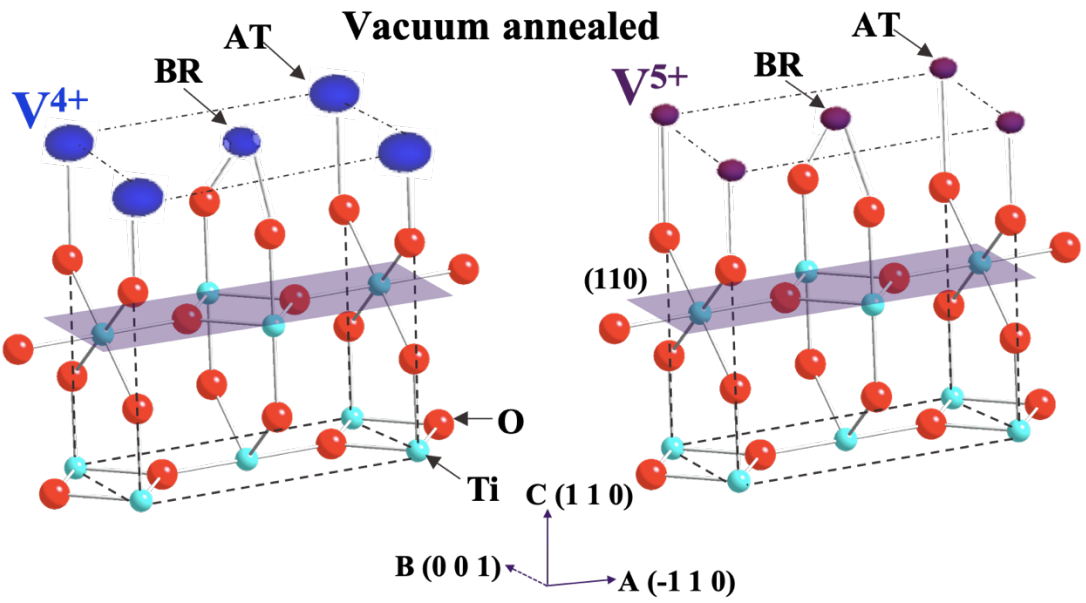

Figure 4.16. *XSW-XPS for the vacuum annealed surface: Atomic density map of V^{4+} and V^{5+}. Oval sizes represent the relative occupation of each chemical state of V on each surface site.*

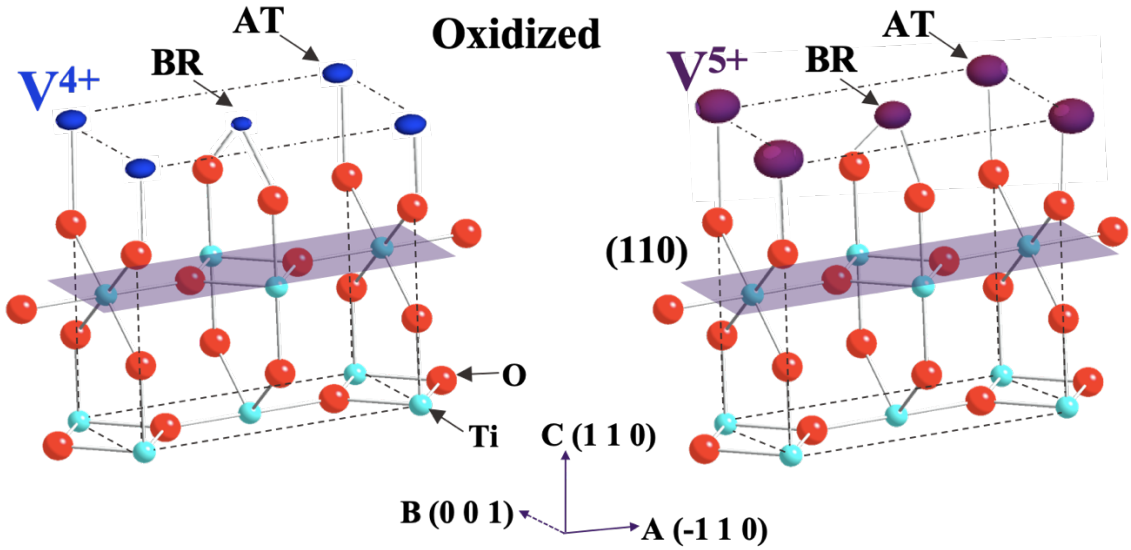

Figure 4.17. *XSW-XPS for oxidized surface: Atomic density map of V^{4+} and V^{5+}. Oval sizes represent the relative occupation of each chemical state of V on each surface site.*

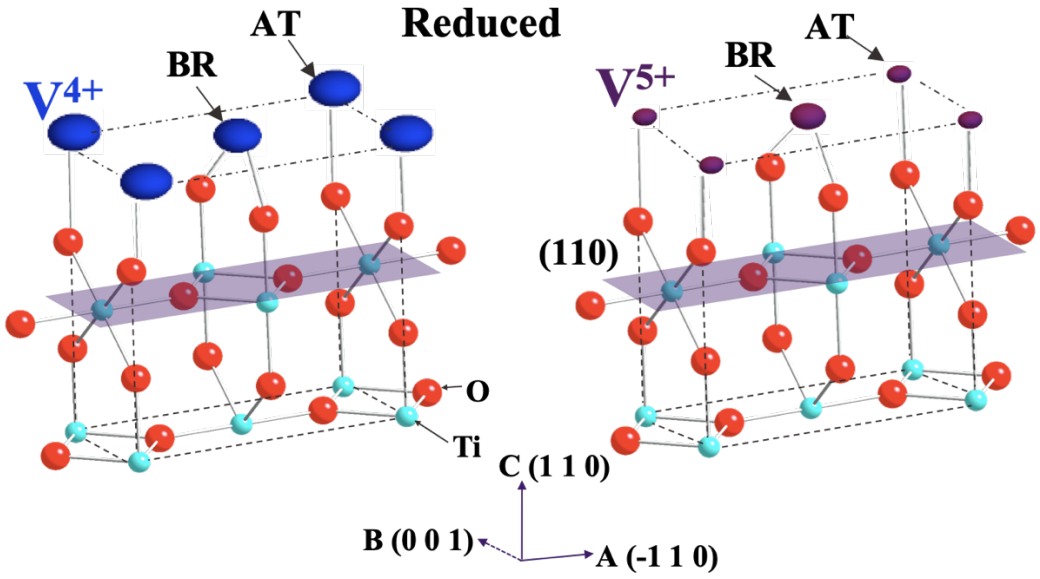

Figure 4.18. *XSW-XPS for the reduced surface: Atomic density map of V^{4+} and V^{5+}. Oval sizes represent the relative occupation of each chemical state of V on each surface site.*

Model-dependent analysis

The direct-space imaging is model-independent and can provide useful information, however, the resolution in a given direction is equivalent to one-half of the smallest d-spacing measured in that direction[60]. Therefore, the subsequent step of model-dependent analysis is necessary for better understanding. To further improve our understanding of this complex catalytic system, based on the model independent results, we created a 2-site model to quantitatively analyze the experimental data. Then a global fitting procedure helped refine the parameters to get information such as the ordered fraction of adsorbed atoms at certain sites and heights of those atoms. The model partitions the V to sit at either atop (AT) or bridging (BR) sites or to be random. To quantify the structural parameters associated with these two adsorption sites, we performed a least-squares global fit of

each condition to the experimentally measured f_H and P_H values. Here, the H^{th} Fourier component for the V atomic distribution is defined as

$$\mathrm{F_H} = f_{\mathbf{H}}\, e^{i2\pi \mathrm{P_H}} = \alpha_{AT}\, e^{i2\pi \mathbf{H}.\mathbf{r_{AT}}} + \alpha_{BR}\, e^{i2\pi \mathbf{H}.\mathbf{r_{BR}}} \quad (4.1)$$

where α_X denotes the fraction of V occupying site X = AT or BR with positions $\mathbf{r}_{AT} = (0\ ,\ 0\ ,\ \mathbf{z}_{AT})$ and $\mathbf{r}_{BR} = (\frac{1}{2}\ ,\ \frac{1}{2}\ ,\ \mathbf{z}_{BR})$. z_x is the height of V at site X = AT or BR above the TiO (110) bulk-like plane. The global fits of Eq. 4.1 to the sets of measured f_H and P_H values in Tables 4.4 - 4.6, give the occupation fractions of V^{4+} and V^{5+} at AT and BR sites for the vacuum annealed, oxidized and reduced surfaces along with the z heights of each site for each species. Table 4.7- 4.9 lists the amount (in ML) that each chemical state of V occupies at the AT and BR sites for the VA, Ox and Re surfaces respectively. Table 4.10 - 4.11 lists the heights of V^{4+} and V^{5+} above the (110) plane of TiO_2 at the AT and BR sites for the VA, Ox and Re surfaces respectively.

Density functional theory (DFT)

In addition, we have used DFT calculations to further improve and extend our understanding of this complex catalytic system. DFT calculations were carried out by Dr. Haesun Park from the group of Dr. Peter Zapol at Argonne National Laboratory. Density functional theory calculations were performed as implemented in Vienna Ab initio Simulation Package (VASP). The interactions between core and valence electrons are treated by the projector-augmented wave (PAW) potentials and the plane-wave cutoff energy of 520 eV was used. The atom positions are fully relaxed to the atomic force tolerance of 0.03 eV/Å using conjugated gradient method. The unit cell geometry was fully relaxed for bulk TiO_2 and in-plane cell parameters were kept at bulk values in surface calculations using periodic slab of 11 TiO_2 tri-layers and adsorbed vanadia. The Bader charge analysis was used to evaluate the charge state of V ions at the surface[100-101].

Coherent fractions and positions

The following tables list and are used to show consistency between XSW model-independent (meas), XSW model-dependent (calc) and density functional theory (DFT) determined values for coherent fractions (f) and positions (P).

Table 4.4. *XSW-XPS results of V^{4+} and V^{5+} for the Vacuum Annealed surface of the ½ ML VO_x / α-TiO_2 (110)*

	V^{4+}						V^{5+}					
hkl	f_{meas}	f_{calc}	f_{DFT}	P_{meas}	P_{calc}	P_{DFT}	f_{meas}	f_{calc}	f_{DFT}	P_{meas}	P_{calc}	P_{DFT}
110	0.66(3)	0.71	0.69	-0.03(1)	0.02	0.01	0.41(5)	0.50	--	-0.11(1)	0.00	--
101	0.65(2)	0.69	0.69	-0.13(2)	0.01	0.00	0.66(7)	0.52	--	-0.07(2)	0.00	--
111	0.15(1)	0.15	0.21	0.11(2)	0.09	-0.12	0.20(1)	0.19	--	0.28(1)	0.28	--
200	0.71(2)	0.69	0.69	0.00(1)	0.02	0.01	0.58(5)	0.50	--	0.04(2)	0.02	--
220	0.63(1)	0.62	0.56	0.04(1)	0.04	0.02	0.35(1)	0.35	--	0.08(3)	0.04	--

Table 4.5. *XSW-XPS results of V^{4+} and V^{5+} for the Oxidized surface of the ½ ML VO_x / α-TiO_2 (110)*

	V^{4+}						V^{5+}					
hkl	f_{meas}	f_{calc}	f_{DFT}	P_{meas}	P_{calc}	P_{DFT}	f_{meas}	f_{calc}	f_{DFT}	P_{meas}	P_{calc}	P_{DFT}
110	0.65(3)	0.61	0.61	-0.02(1)	-0.01	-0.05	0.45(2)	0.43	0.46	-0.08(1)	0.00	-0.05
101	0.67(4)	0.60	0.60	-0.06(2)	-0.01	-0.03	0.45(1)	0.45	0.45	-0.13(2)	0.01	-0.03
111	0.11(4)	0.16	0.14	0.08(3)	0.13	-0.18	0.13(4)	0.18	0.10	0.17(2)	0.21	-0.22
200	0.61(3)	0.58	0.59	0.00(1)	-0.01	-0.05	0.38(3)	0.41	0.44	0.02(2)	0.00	-0.05
220	0.38(4)	0.48	0.51	0.04(3)	-0.02	-0.11	0.22(5)	0.28	0.38	-0.06(1)	0.01	-0.1

Table 4.6. *XSW-XPS results of V^{4+} and V^{5+} for the Reduced surface of the ½ ML VO_x / α-TiO_2 (110)*

	V^{4+}						V^{5+}					
hkl	f_{meas}	f_{calc}	f_{DFT}	P_{meas}	P_{calc}	P_{DFT}	f_{meas}	f_{calc}	f_{DFT}	P_{meas}	P_{calc}	P_{DFT}
110	0.71(3)	0.81	0.78	0.00(1)	0.00	0.01	0.66(2)	0.68	--	-0.02(1)	0.02	--
101	0.81(1)	0.80	0.78	-0.02(2)	0.00	0.03	0.68(3)	0.71	--	-0.08(3)	0.01	--
111	0.05(1)	0.05	0.19	0.05(1)	0.05	-0.19	0.28(2)	0.31	--	0.29(2)	0.31	--
200	0.79(1)	0.78	0.76	0.00(1)	0.00	0.01	0.67(2)	0.65	--	-0.01(1)	0.02	--
220	0.69(2)	0.71	0.63	0.02(2)	0.00	0.03	0.41(1)	0.42	--	-0.01(3)	0.04	--

Occupation fractions

Table 4.7. *XSW determined fraction (in ML) of V^{4+} and V^{5+} occupying each surface site of the vacuum annealed surface. The table also list the fraction of uncorrelated V.*

Sites	Occupational Fraction [ML]		
	V^{4+}	V^{5+}	Total
AT	0.16(2)	0.04(1)	0.20(2)
BR	0.10(1)	0.05(2)	0.15(2)
Uncorrelated	0.09(2)	0.06(1)	0.15(2)
Total	0.35(3)	0.15(3)	0.50

Table 4.8. *XSW determined fraction (in ML) of V^{4+} and V^{5+} occupying each surface site of the oxidized surface. The table also list the fraction of uncorrelated V.*

Sites	Occupational Fraction [ML]		
	V^{4+}	V^{5+}	Total
AT	0.07(2)	0.09(1)	0.16(2)
BR	0.05(2)	0.07(1)	0.12(2)
Uncorrelated	0.06(2)	0.16(1)	0.22(2)
Total	0.18(3)	0.32(2)	0.50

Table 4.9. *XSW determined fraction (in ML) of V^{4+} and V^{5+} occupying each surface site of the reduced surface. The table also list the fraction of uncorrelated V.*

Sites	Occupational Fraction [ML]		
	V^{4+}	V^{5+}	Total
AT	0.18(1)	0.04(2)	0.22(2)
BR	0.16(1)	0.05(2)	0.21(2)
Uncorrelated	0.05(1)	0.02(2)	0.07(2)
Total	0.39(2)	0.11(3)	0.50

Vertical Heights above the TiO (110) plane

The next three tables list the XSW determined best fit vertical heights of V^{4+} and V^{5+} above the bulk TiO (110) plane and heights obtained from DFT. This Z(Å) heights above the (110) plane of TiO_2 is obtained in Å using $Z = z\,C$, where $C = 2d_{110} = 6.496\ Å$.

Table 4.10. *XSW determined heights of V^{4+} and V^{5+} above the bulk TiO (110) plane and heights obtained from DFT for the vacuum annealed surface.*

Sites	Z(Å)			
	V^{4+}		V^{5+}	
	Exp	DFT	Exp	DFT
AT	0.06(4)	-0.01	0.26(3)	--
BR	0.00(3)	0.04	-0.13(3)	--

Table 4.11. *XSW determined heights of V^{4+} and V^{5+} above the bulk TiO (110) plane and heights obtained from DFT for the oxidized surface.*

Sites	Z(Å)			
	V^{4+}		V^{5+}	
	Exp	DFT	Exp	DFT
AT	-0.06(5)	0.06	0.18(4)	0.06
BR	0.13(3)	0.05	0.06(3)	0.05

Table 4.12. *XSW determined heights of V^{4+} and V^{5+} above the bulk TiO (110) plane and heights obtained from DFT for the reduced surface.*

Sites	Z(Å)			
	V^{4+}		V^{5+}	
	Exp	DFT	Exp	DFT
AT	0.01(3)	-0.01	0.33(5)	--
BR	-0.01(4)	0.04	-0.13(4)	--

Discussion

In our group, previous XSW-XRF experiments were carried out for ¾ ML ALD-grown VO_X catalyst on α-TiO_2(110) support[88]. That study demonstrated the atomic-scale analysis for the redox-driven cation dynamics under ambient flowing H_2 and O_2 gas conditions. In these previous studies, *ex-situ* XPS showed that O_2 oxidized all V to the 5+ state and that H_2 reduced part of the V^{5+} cations. In-situ XSW analysis of the oxidized (Ox) surface showed that 0.36 ML of the vanadium atoms occupied bridge (BR) or atop (AT) sites on rutile (110) surface and the remaining V ions were uncorrelated to the substrate lattice. XSW also showed that reduction caused 0.16 ML of the correlated V structure to become uncorrelated, and this process was reversible. The limitations of using XSW-XRF were discussed before. This current study used XSW-XPS instead of XRF, which allowed us to not only generate chemical-state sensitive 3D maps of the V but also map the surface oxygens distinct from the bulk oxygens which was not accessible while using X-ray fluorescence.

To compare our current XSW-XPS studies with the previous XSW-XRF results, we should note some key differences in the sample treatment. In this study we looked at a lower coverage of VO_x : ½ ML. Also, we used atomic O and H from a cracker cell for the *in situ* redox reactions instead of using ambient pressure O_2 and H_2. In our results the oxidized surface had 64% V^{5+} instead of 100% and upon reduction it converted to 77% V^{4+} and 23% V^{5+}. This process was reversible

similar to the previous studies. The oxidized surface for the ½ ML film had 44% uncorrelated V which is similar to the previous ¾ ML sample which had 50% uncorrelated V. Upon reduction the ½ ML sample has only 14% uncorrelated V which is again close to the previous ¾ ML results which had 20% uncorrelated V in the reduced surface. Thus, we see that the results for the two different coverages of VO_x/α-TiO_2 (110) are comparable and hence proves that sub-monolayer vanadium coherency is consistent. These findings will help us understand redox-induced structural and chemical changes in supported sub-ML catalysts and be useful for improving catalytic activity. In the present case of ½ ML VO_x/α-TiO_2 (110), model-independent 3D atomic density maps showed the vertical heights and correlation of each oxidation state of vanadium on the surface and how this changed as the surface was oxidized and reduced. Several different reduced surface models were evaluated using DFT calculations to get as close as possible to the experimental results.

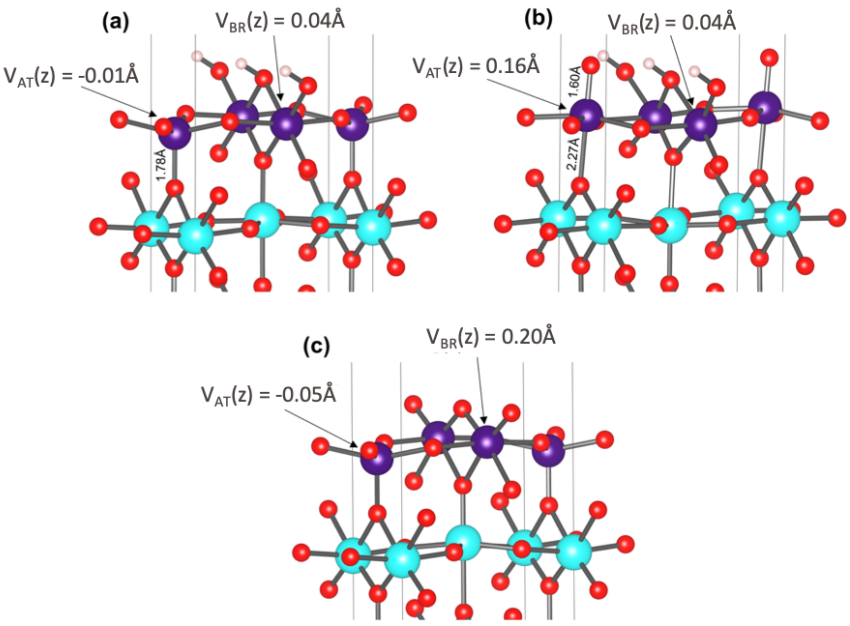

Figure 4.19. (a) *Ball-stick model of DFT-optimized structure of reduced surface along with positions of surface V atoms. The structures with* ***(b)*** *additional O on top of the atom-V (V_{AT}) and* ***(c)*** *without H atom are also described. The purple, blue, and red spheres represent V, Ti, and O atoms, respectively.*

The best agreement with the vertical positions and the formal charge states of V atoms is obtained for the structure shown in Fig. 4.19 (a), where V ions are in isomorphic positions with rutile substrate and surface oxygens in VO layer are partially hydrogenated. The calculated Bader charges of V (V_{AT}: 2.058, V_{BR}: 2.01) indicate the reduced states of V as compared to V in VO_2 (Bader charge of V: 2.17) in agreement with the XPS measurements where V^{4+} dominates the surface. The vertical positions of V^{4+} atoms on the AT- and BR-sites deviates from the ideal bulk-like Ti sites only by -0.01Å and 0.04Å, respectively in agreement with XSW-XPS results. In the model shown in Figure 4.19(a), only the BR-site V is bonded to the OH group, while the AT-site V has no terminal O atom. The presence of terminal O atom determines the vertical height of V on BR-site. The strong bond with the O atom shifts the V^{4+} atom upward from the bulk-like Ti position as shown, however, the absence of such terminal O atom keeps the vertical position of BR-site V^{4+} unchanged as is also seen from the XSW-XPS experiments. The height of the BR-site V is affected by the presence of hydroxylated O atom. The hydration of the terminal O atom elongates the bonding to V atom on BR-site, resulting in a small displacement of BR-site V atom as compared to the surface with no hydrogenation where the V atom is highly displaced upward relative to bulk-like position (Figure 4.19 (c)). When we compare with the experimental results, we see a small displacement this proving that the DFT model shown in Fig. 4.19 (a) has the best agreement with experiment. On the basis of these results, a possible interpretation of the reduced surface structure is consistent with formation of 2D islands of hydrogenated VO_2 coherent with TiO_2.

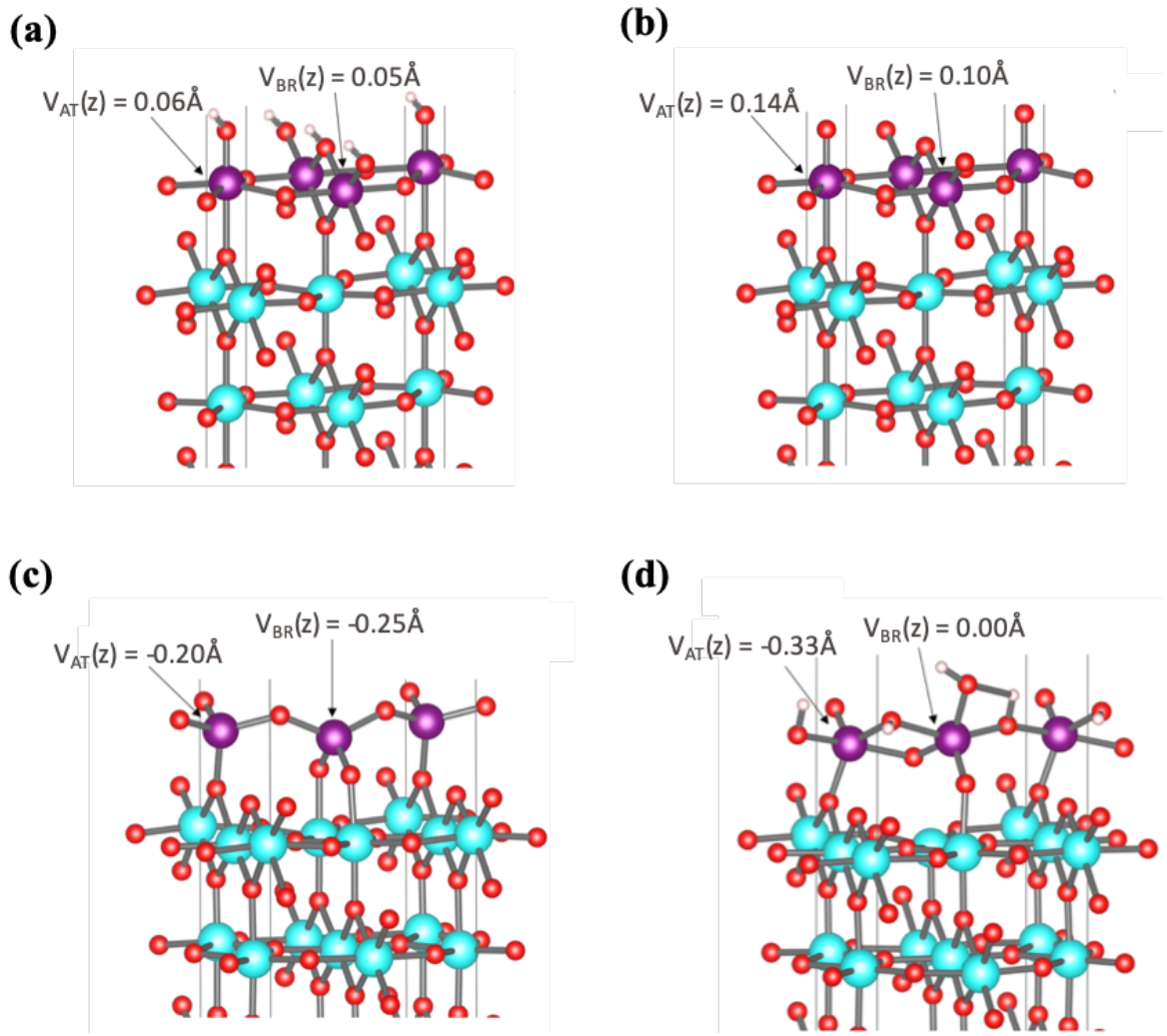

Figure 4.20. *Ball-stick models for the hypothetical structures of oxidized VO_x/TiO_2 surfaces obtained from DFT calculations. The purple, blue, and red spheres represent V, Ti, and O atoms, respectively.*

Upon oxidation, the islands hydroxylate and results in considerable incoherent fraction and possible chain formation with more difficult interpretation. Several different DFT models were examined as shown in Fig. 4.20. Among these, the model shown in Fig. 4.20 (a) shows the best agreement with the experimentally determined heights and coverage of Vanadium and oxygen on the surfaces.

4.4 Conclusion

This chapter presents our studies of 0.5 ML ALD-grown VO_x catalyst on α-TiO_2 (110) support demonstrating chemical-state specific atomic-scale analysis for the redox-driven cation dynamics under oxidation and reduction processes. XSW-XPS analysis allowed us to generate distinct 3D atomic density maps of individual chemical states of V. These observations of structural transformations and changes in coherence of the supported catalyst accompanying changes of the oxidation state V^{5+} to V^{4+} under redox cycling provides information on the structure of active sites and helps in understanding complex catalytic reactions. By comparing V coherent fractions and coherent positions obtained from experiment to those calculated from structures optimized using DFT, we found that reduced VO_2 forms partially hydrogenated structure isomorphic with TiO_2, while oxidized VO_2 has much smaller fraction of coherent structure. These findings helped in understanding the redox-induced atomic-scale structural changes with chemical state specificity which in turn will help tune the growth parameters to obtain more active and selective catalysts.

Chapter 5

3D mapping of surface oxygens

5.1 Introduction

Oxide-supported catalysts are very commonly used in the chemical industry and in pollution abatement. Several reactions such as hydrogenation, transesterification and dehydrogenation have increased efficiency with supported metal-oxide catalysts than with bulk catalysts. The use of a supported catalyst reduces the amount needed and increases the active surface area, thus decreasing cost and increasing efficiency. In Chapter 4 we talked about the chemical state sensitive 3D mapping of Vanadium in one such system, TiO_2 supported vanadium oxide, which is widely used for selective catalytic reduction of NOx and catalytic oxidation of organic compounds resulting in non-toxic end products[88, 90, 102].

In this chapter, we will discuss how this novel model-independent 3D atomic mapping technique follows the change in surface site locations of chemically distinct surface atoms during a redox reaction. This method, using X-ray standing-wave (XSW) excited X-ray photoelectron spectroscopy (XPS)[103-104], is uniquely suited for locating surface oxygen atoms, which are distinguished from oxygens in the supporting oxide substrate, by a chemical shift to their binding energy. For the presented case of ½ monolayer (ML) vanadium on α-TiO_2(110), the interface between the support and the catalyst plays a major role in controlling the structure and in turn the

activity of the catalyst. The surface oxygen atoms take part in the catalytic reaction and hence their positions are modified during the process. Herein, we use the XSW-XPS method to directly observe in-situ reversible redox-induced atomic-scale structural and chemical state modifications of the VO_x/α-$TiO_2(110)$ interface. This is combined with density functional theory (DFT) calculations to further improve and extend our understanding of this complex catalytic system[105].

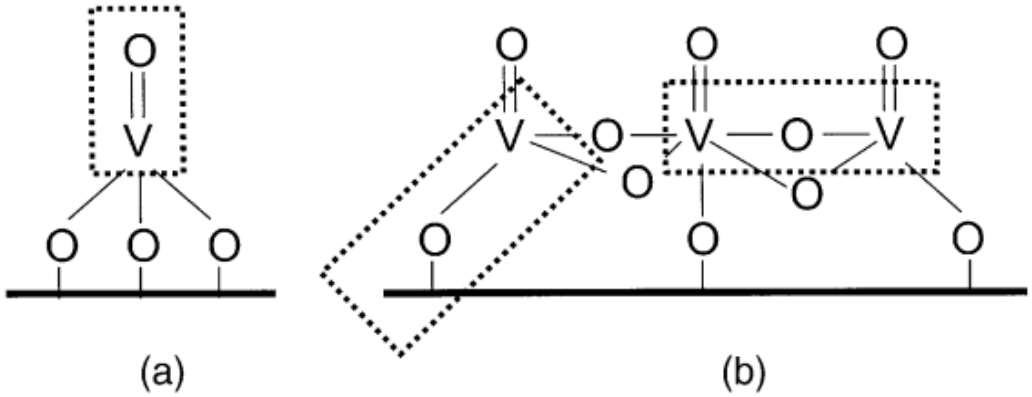

Figure 5.1. *Various types of V-O bonds that might be involved in a catalytic reaction. (a) monomeric VO_4 species, (b) polymeric VO_4 species characterized by V=O, V-O-V and V-O support bonds.*[4]

5.2 Experimental Methods

The experimental methods are described in detail in chapter four as these measurements were carried out on the same sample. Just as a reminder, some of the main experimental steps are mentioned in this chapter as well. Atomic layer deposition (ALD) was used to grow ½ ML of VO_x on a rutile α-TiO_2 (110) surface. All other surface preparation details are provided in chapter 4. Ex-situ AFM and LEED images are shown in Fig. 4.4. Back-reflection XSW-XPS [99, 106] was used at I09 to measure the distributions of oxygen atoms relative to the substrate TiO_2 lattice with both sub-Å spatial resolution and chemical state specificity. One specular *(110)* and three off-specular *(101, 111, 200)* XSW data sets were collected to triangulate the atomic positions in of the oxygens in 3D. Each set of *hkl* measurements were repeated after each redox treatment to study the dynamic changes in the surface structure under in-situ reaction conditions.

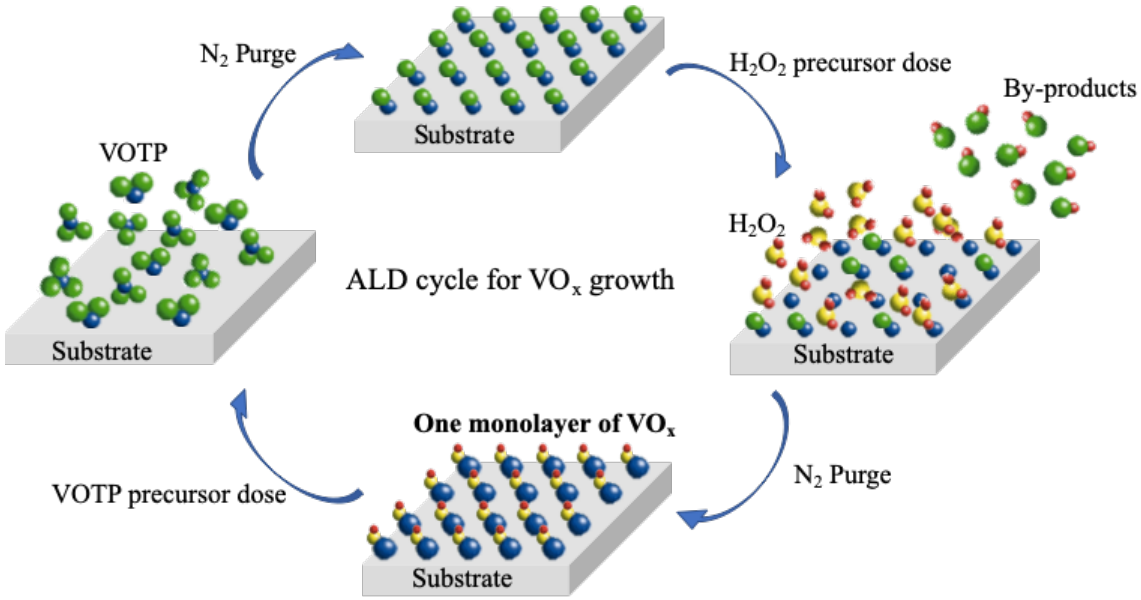

Figure 5.2. *Schematic showing one cycle of atomic layer deposition for growing vanadium oxide film on α-TiO_2 (110) substrate.*

X-ray standing wave excited X-ray photoelectron spectroscopy

Back-reflection XSW excited XPS measurements were carried out at the I09 beamline at Diamond Light Source (DLS) in Didcot, UK. In chapter 3, we have discussed the XSW-XPS method in details and in chapter 4 some details about of DLS are discussed. The calculated f_{calc} and P_{calc} values from Eq. 3.13 for bulk-like O atoms are listed in Tables 5.1 and 5.2 with comparison to their XSW-XPS measured values. A vibrational amplitude of σ = 0.1 Å was used for estimating the Debye-Waller factor in these calculations. XSW-XPS measurements used a Scienta EW4000 hemispherical XPS analyzer with its lens axis aligned horizontally along the polarization direction of the incident X-ray beam. For the off-specular reflections, since the full cone is collected, the integration of Q' over the full 2π radians in ϕ_p leads to Q' = 0 and thus $S_R = |S_I| = 1$ and $\psi = 0$. For the specular (110) reflection the surface cuts out half of this cone, in which case we calculate Q' by setting $\theta_p = 18°$ and $\phi_p = 0°$. For the specular (110) reflection, the incident Bragg energy = 1911 eV. Bulk O 1s binding energy is 530.5 eV, thus kinetic energy = 1380.5 eV. At this kinetic energy for O1s:

$\Delta = \delta_d - \delta_p = 0.757 - 1.114 = -0.357$ radians (values obtained from Ref.[73])

$\beta = 1.98$, $\delta = 0$, and $\gamma = 0.76$ (values obtained from Ref.[107])

Hence, we can calculate, Q' = 0.078

Thus, $S_R = 1.17$

Now calculating $\psi = \tan^{-1}\left(\frac{S_R-1}{S_R+1} tan\Delta\right) = 0.02$. This value is extremely small compared to 2π and hence can be ignored.

Hence, $|S_I| = ½ (S_R+1) = 1.085$

Using these S_R, S_I and ψ values in Eq. 5.1, we get the O coherent fraction and position fit determined values for the (110) reflection listed as f_{meas} and P_{meas} in Tables 5.1 and 5.2.

5.3 Results and discussion

Angle Resolved XPS

To prove that the 1.5 eV chemically shifted O 1s peak is originating from the surface we compared a surface-sensitive grazing-emission spectrum to a non-grazing-emission spectrum as depicted in Fig. 5.3.

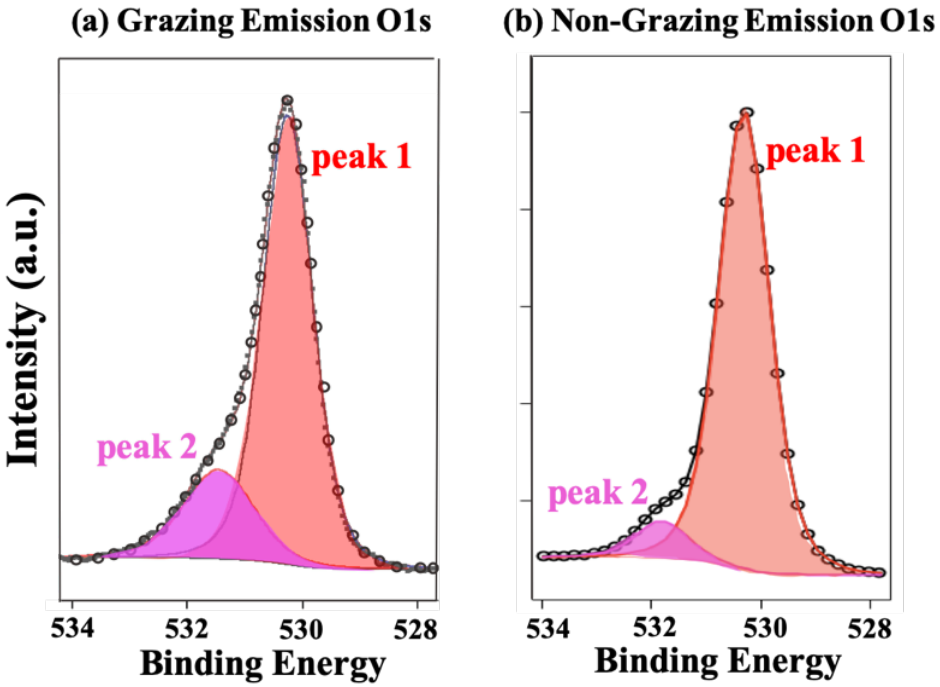

Figure 5.3. *O 1s XP spectra at 1.9 keV incident energy for the vacuum annealed surface at (a) Grazing emission (b) Non-grazing emission. The widths and positions of peak 1 in (a) and (b) are unchanged. Likewise, for peak 2. Peaks 1 and 2 both have a FWHM of 1.5 eV and a separation of 1.5 eV.*

The EAL for the XPS measurements is roughly defined as the inelastic mean free path (IMFP) * sin (take-off angle χ).[77, 108] The average take-off angle was $\chi = 18°$ and 60°, respectively, for the

grazing emission and non-grazing emission measurements. At Eγ = 1.9 keV, the IMFP for O 1s is 24 Å. Thus, the information depth = 7.5 Å and 20.8 Å, respectively, for the grazing emission and non-grazing emission measurements. Referring to Fig. 5.3, the peak1 to peak 2 area ratio is 5.3 and 12.3, respectively, for the grazing emission and non-grazing emission measurements. From this we can observe that as the information depth increased the intensity of peak 2 reduced at almost the same proportion (20.8 : 7.5 = 2.7 and 12.3 : 5.3 = 2.3). This confirms that O 1s electrons contributing to the chemically shifted peak 2 originate roughly from the top 1.5 Å of the sample; thus corresponding to surface oxygens (SO), while peak 1 is from bulk oxygens (BO).

Referring to the 2019 paper by Bagus et al. in PCCP[109-110], the binding energy for the 1s surface oxygens for ionic oxides, without any hydroxylation, is expected to be around 0.8 eV higher than the bulk oxygens. From references[88, 100, 102, 105-106], and also from our DFT calculations, we observe that the hydroxylated surface oxygens have a binding energy 1.5 eV higher than the bulk oxygens. Due to the bulk peak 1.5 eV FWHM caused by the energy width of the incident X-rays, resolution of our X-ray photoelectron spectrometer and 0.2 eV lifetime broadening of O 1s, it is not possible to determine if there is a small 0.8 eV shifted component of the O 1s peak. From our experimental results we can only draw conclusions about the 1.5 eV chemically shifted surface oxygens. Adding a 3rd peak at a separation of 0.8 eV from the bulk O 1s peak increases χ^2 by 26% and has a peak area of less than 3%. Hence three peaks is not a well matched model for our data. Thus, we experimentally cannot resolve the SO peak into hydroxylated and non-hydroxylated peaks. This is where DFT helps us in coming up with the probable models, which structurally matches our XSW-XPS results.

Soft and Hard X-ray Photoelectron Spectroscopy

Soft X-ray (Eγ = 900 eV) beam was used for obtaining high-resolution XPS survey spectra.

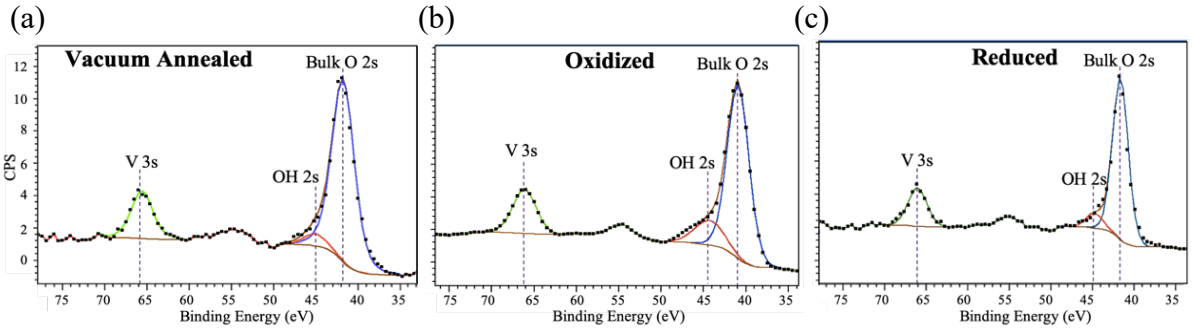

Figure 5.4. *Eγ = 900 eV soft-XP spectra showing V 3s and O 2s peaks of the (a) Vacuum annealed surface (b) Oxidized surface and (c) Reduced surface.*

From Fig. 5.4, the area ratio of the OH 2s and V 3s peaks after normalizing with photoelectron cross-section for the vacuum annealed (VA) surface is 0.98, for the oxidized surface (Ox) is 1.77, and for the reduced surface (Re) is 0.87. Knowing that the V coverage is 0.50 ML from a calibrated XRF measurement, the VA surface has 0.50 ML, Ox surface has 0.88 ML and the Re surface has 0.44 ML of chemically shifted surface oxygens (SO). (1 ML corresponds to 1 SO per Ti surface site). As a cross check, we also obtain the same coverage values from O1s peak analysis (Fig. 5.5).

The XP spectra in Fig. 5.5 show that the O 1s photoelectrons experience roughly 1.5 eV higher binding energy when emitted from surface oxygens (SO) than from bulk oxygens (BO). This is in agreement with previous results for similar surfaces[88, 102, 105-106]. Density functional theory (DFT) calculations indicate that these SO atoms are partially hydroxylated. While DFT calculations were primarily used to optimize structures, the DFT calculations are also in general agreement with the XP spectra, predicting a chemical shift of 1.3 eV for hydroxylated SO on V and 1.0 eV on Ti. Details of DFT calculations will be provided in subsequent sections of this chapter.

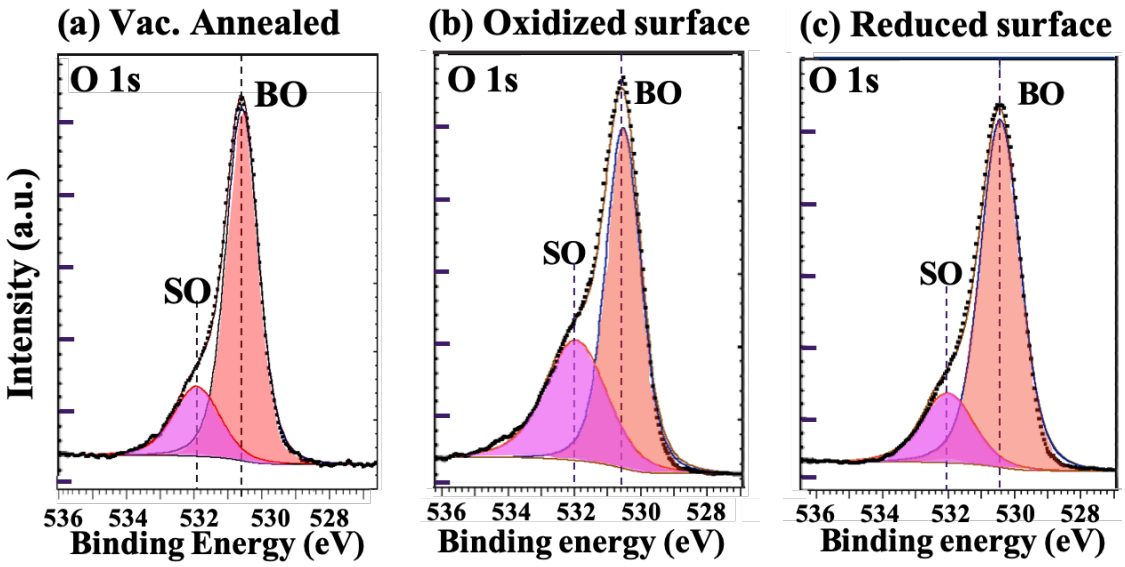

Figure 5.5. *O 1s XP spectra at 1.9 keV incident energy for the (a) vacuum annealed surface (b) oxidized surface (c) reduced surface.*

X-ray standing wave excited XPS

The in-situ XSW measurements induced distinctive modulations for the two O 1s XPS peaks from scans across four reflections. The XSW data and analysis are shown in Figs. 5.6-5.9 with the resulting four sets of f_H and P_H measured values for each chemical state of oxygen listed in Tables 5.4-5.6 as f_{meas} and P_{meas}. A Fourier summation of these four sets of Fourier components and their symmetry equivalents is then used to generate model-independent 3D atomic density $\rho(\mathbf{r})$ maps.

Since there is a signal from each type of atom at this interface, we combine these maps into a 3D composite atomic map. Using the Ti 2p, V 2p, bulk O 1s and surface O 1s XSW-XPS results, we show such composite maps for the oxidized and reduced surfaces in Figs. 5.10 (a) and 5.10 (b), respectively. The initial vacuum annealed surface has a 3D composite atomic map (Fig. 5.11)

similar to that of the reduced surface. For all three surfaces, the bulk Ti and O show up in their expected positions in the composite maps and show no redox induced changes.

For the oxidized surface, the V cations, which are 64% V^{5+} and 36% V^{4+}, laterally occupy 32% of the atop (AT) sites and 24% of the bridging (BR) sites with heights above the TiO (110) bulk-like plane listed in Fig. 5.10 (a). The chemically shifted surface oxygens show up at the A, B and C sites with heights as indicated in Fig. 5.10 (a). The oxidized surface DFT model (Fig. 5.10 (c)) shows good agreement with these experimentally determined V and SO heights.

For the reduced surface, chemically shifted surface oxygens are detected at the B and C sites, but not at the A site (Fig. 5.10 (b)). The DFT (Fig. 3d) is in good agreement showing no A-site oxygen and closely agreeing with the XSW experimental heights for B and C sites. V ions are 78% V4+ and 22% V5+ for the reduced surface and occupy 44% of the AT and 42% of the BR. Since the initial vacuum annealed surface had a similar composite 3D map as the reduced surface, we would conclude that the redox process was reversible for this surface.

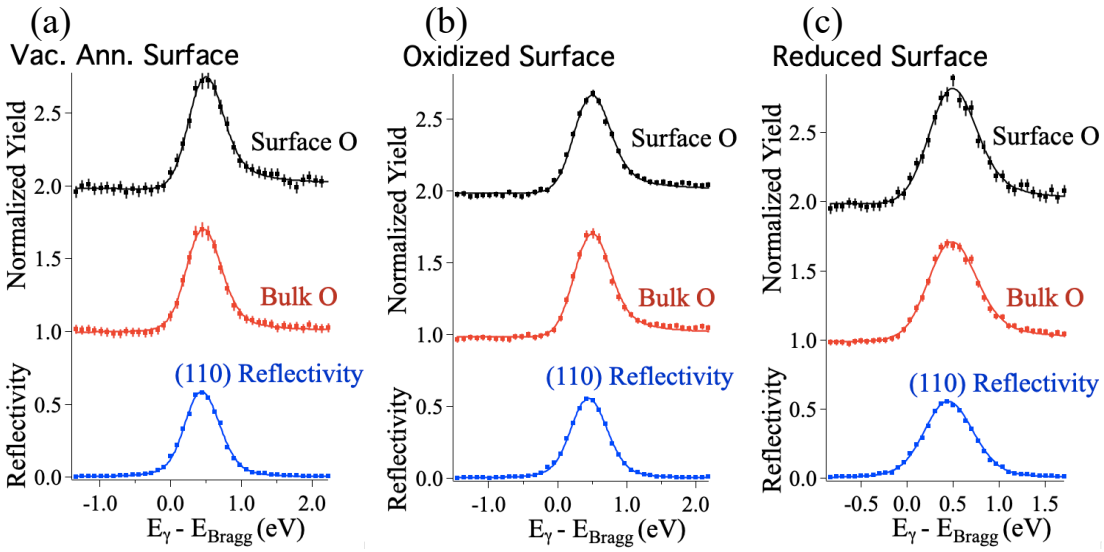

Figure 5.6. (a-c) *Modulations in bulk O and chemically shifted surface O XPS yields through the (110) reflection energy scan of the VA, Ox, Re surfaces, respectively.*

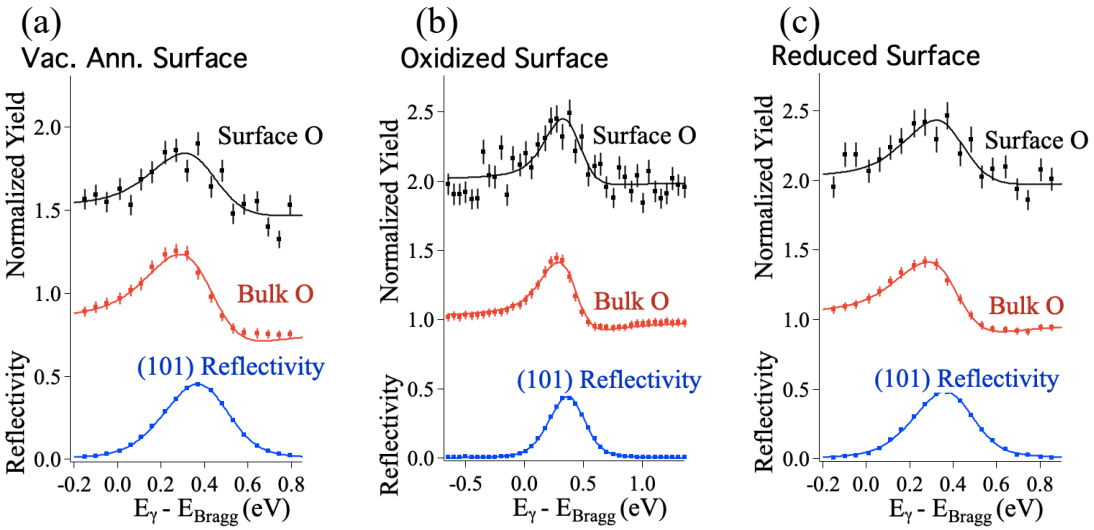

Figure 5.7. (a-c) *Modulations in bulk O and chemically shifted surface O XPS yields through the (101) reflection energy scan of the VA, Ox, Re surfaces, respectively.*

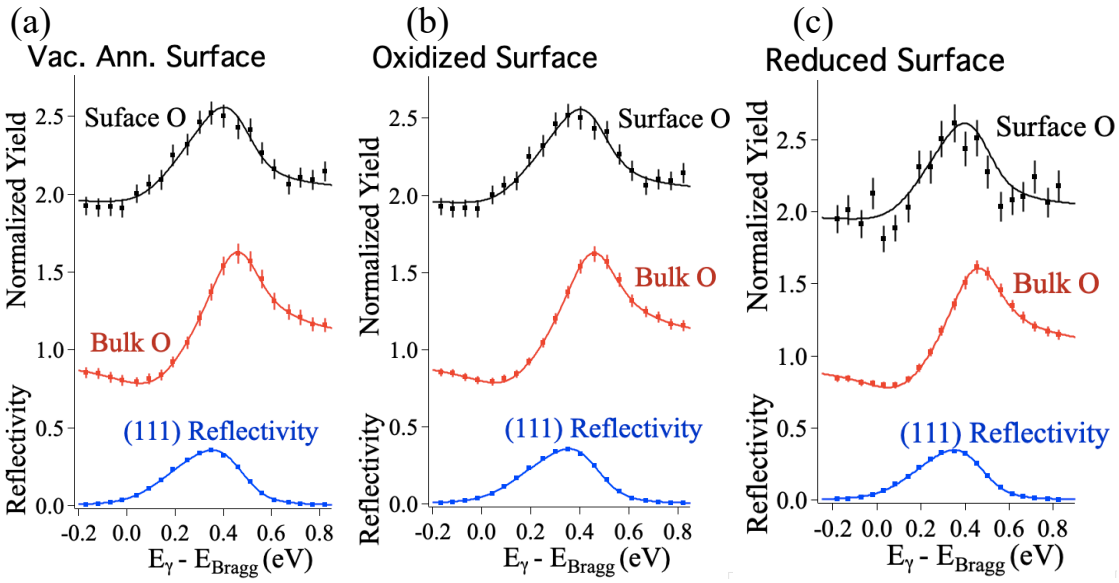

Figure 5.8. (a-c) *Modulations in bulk O and chemically shifted surface O XPS yields through the (111) reflection energy scan of the VA, Ox, Re surfaces, respectively.*

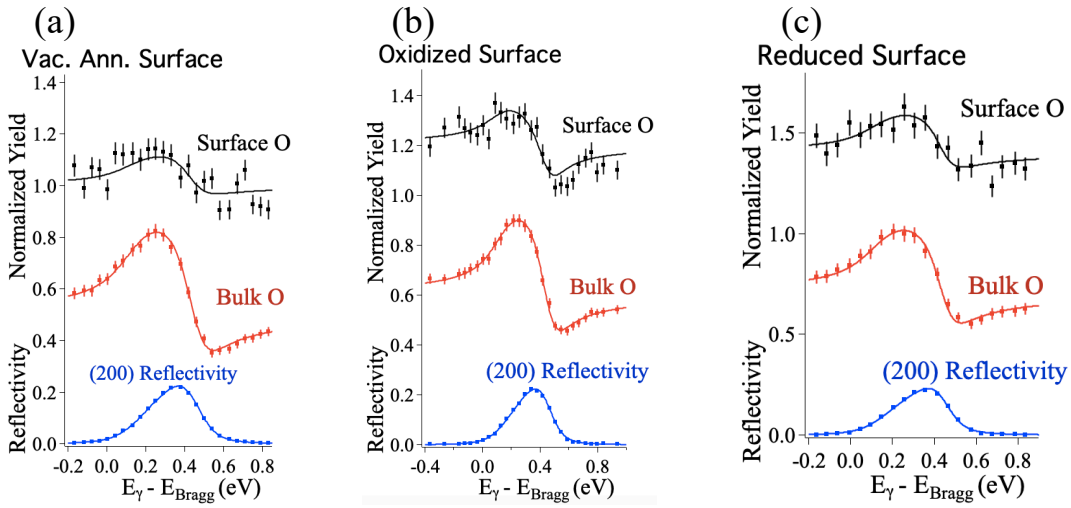

Figure 5.9. (a-c) *Modulations in bulk O and chemically shifted surface O XPS yields through the (200) reflection energy scan of the VA, Ox, Re surfaces, respectively.*

Density functional theory

DFT calculations were carried out by Dr. Haesun Park from the group of Dr. Peter Zapol at Argonne National Laboratory. Density functional theory calculations were performed as implemented in Vienna Ab initio Simulation Package (VASP). The interactions between core and valence electrons are treated by the projector-augmented wave (PAW) potentials and the plane-wave cutoff energy of 520 eV was used. The generalized gradient approximation (GGA) form of the electron exchange-correlation functional formulated by Perdew – Burke – Ernzerhof (PBE) was used. The delocalization of d-electrons of V species was remedied by adding the Hubbard U correction (U = 3.25eV). The atom positions are fully relaxed to the atomic force tolerance of 0.03 eV/Å using conjugated gradient method. The unit cell geometry was fully relaxed for bulk TiO_2 and in-plane cell parameters were kept at bulk values in surface calculations using periodic slab of 11 TiO_2 tri-layers and adsorbed vanadia. The shift in O 1s energy level is calculated with the final-state approximation where the core electron is removed, and the removed electron is added to the lowest unoccupied valence state for the complete screening of the localized core-hole pair. The

final-state approximated as implemented in VASP was used and the 0.5 electron count is excited. The shifts in O 1s energy level of the O atoms on or near the surface are referenced to that of the O atom in the deep bulk of the slab model.

Each one of the distinct oxygen atoms of supported vanadia has its own spectroscopic fingerprint. First principles calculations based on DFT were previously used to calculate chemical shifts in several studies of the different types of oxygen sites on reduced and oxidized vanadium oxide surfaces, as well as vanadium oxidation states[101]. We have performed DFT calculations of chemical shifts for oxygen atoms on the reduced V surface. The shifts in 1s orbital energy levels of each O atom near the surface with respect to that of O in the bulk region are plotted in Fig. 5.13. The hydroxylated oxygen shows a sizable shift in 1s orbital energy level (~1.3 eV) comparable to the experimental measurement (~1.5 eV). Assuming an island model in which VO_x partially covers the TiO_2 surface, a portion of the surface still has TiO_2 termination on which the hydroxylated oxygen can bond. The presence of hydroxylated oxygen on the TiO_2 surface possibly could also contribute to the observed O 1s energy level shift. To confirm it, we calculated the 1s energy level shift of O atoms on the TiO_2 surface with and without the hydroxyl group. Without the hydroxylated O on the surface (Fig. 5.14), the O 1s energy shift of surface O is relatively marginal with the largest shift in Fig. 5.14 of ca. 0.6 eV, whereas the hydroxylated O atoms on the TiO_2 surface exhibit a sizable shift in O 1s level (~1 eV) for both bridging and atop sites (Fig. 5.15). The degree of shift in O 1s level by hydroxyl group on the TiO_2 surface is comparable to the experimental observation. This indicates that hydroxylated oxygens of the TiO_2 surface can also contribute to the O 1s shift observed from XSW-XPS. However, from XSW-XPS measurements of Ti 2p, we don't see any chemical shift or change in heights of the Ti atoms which indicates that the hydroxylation primarily occurred only with the SO bonded to V. Also, the fact that the coverage of correlated oxygens is less than coverage of vanadium, supports this conclusion.

XSW-XPS model-independent 3D maps and DFT calculated structure

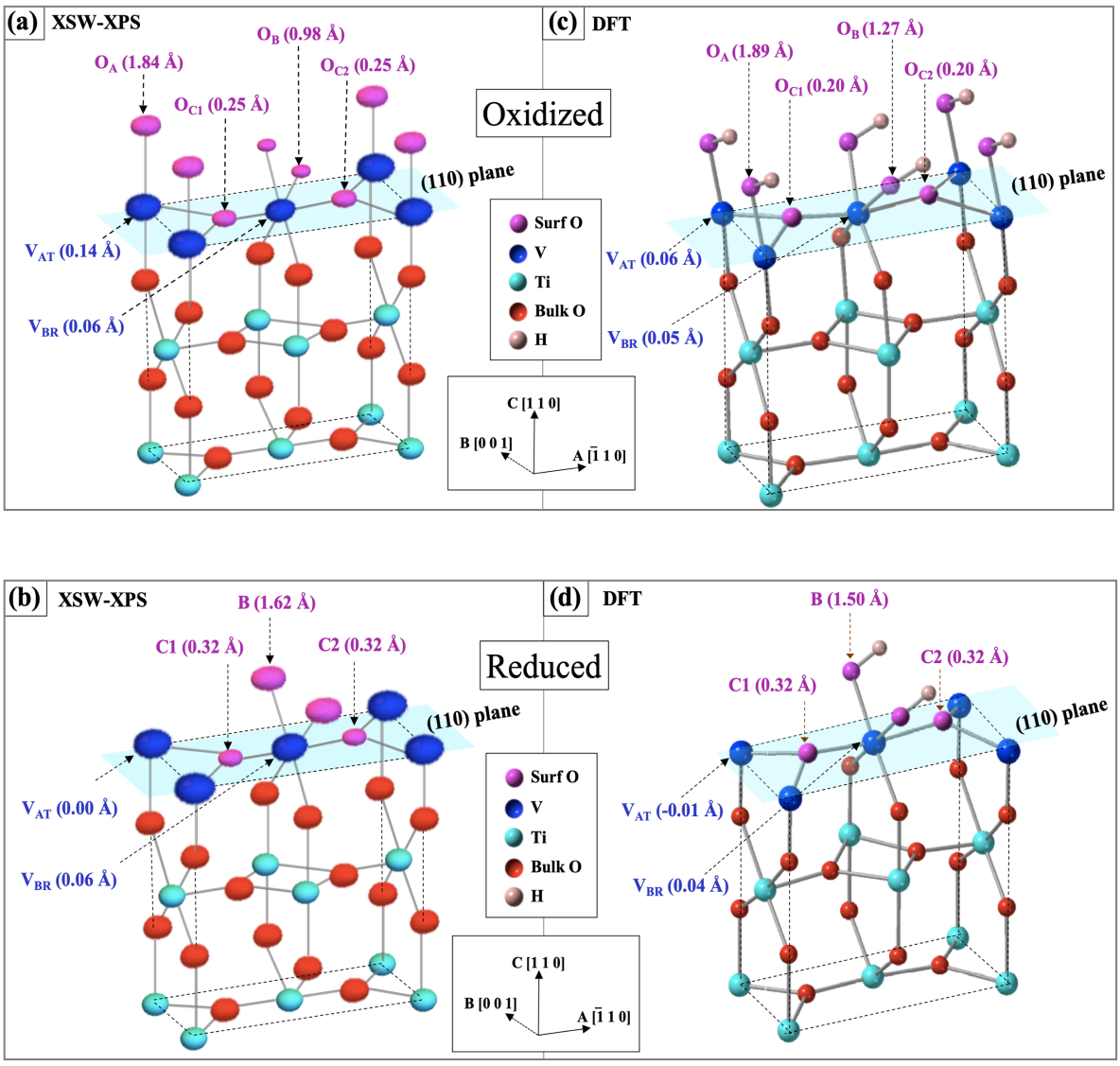

Figure 5.10. (a) *and* ***(b)****: XSW-XPS determined model-independent composite atomic maps of SO, BO, V and bulk Ti for* ***(a)*** *oxidized* ***(b)*** *reduced surface. The size of each V and SO oval is proportional to its fractional occupancy.* ***(c)*** *and* ***(d)****: DFT calculated model for* ***(c)*** *oxidized* ***(d)*** *reduced surface.*

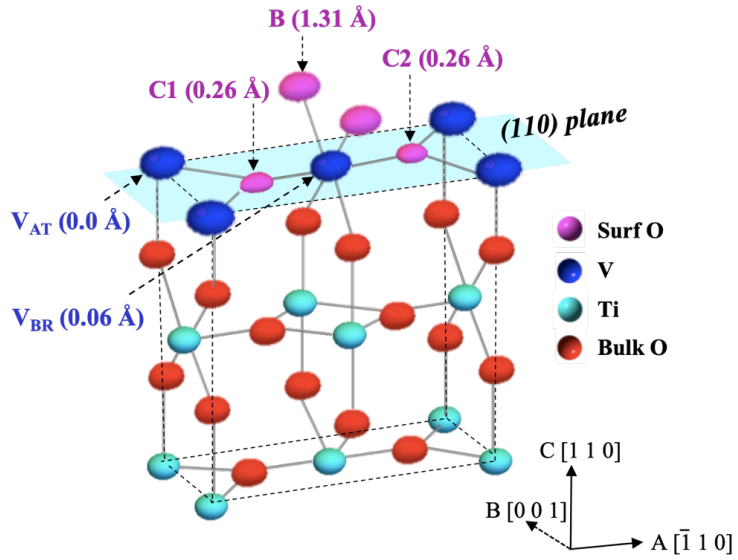

Figure 5.11. *Vacuum Annealed surface: XSW-XPS model-independent composite atomic map of surface O, bulk O, V and bulk Ti obtained from Eq. 5.1. The vertical heights of the oxygens are labelled in Å with respect to light blue (110) TiO bulk-like plane.*

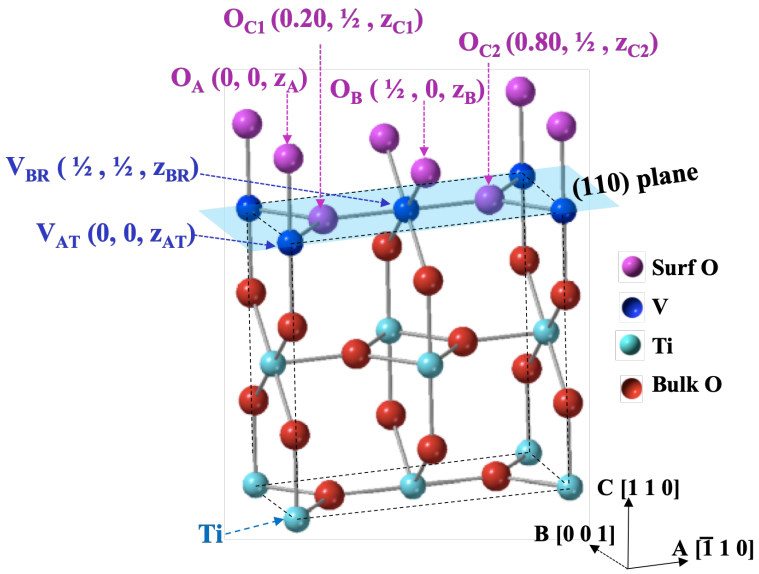

Figure 5.12. *A depiction of the (110) termination of a rutile α-TiO_2 crystal showing three symmetry inequivalent surface oxygens (A, B, C). Also shown are the surface Ti atop (AT) and bridging (BR) sites, which are partially occupied by V atoms. The dotted lines outline a conveniently chosen nonprimitive tetragonal unit cell with its C axis perpendicular to the TiO_2 (110) surface.*

Additional DFT Figures

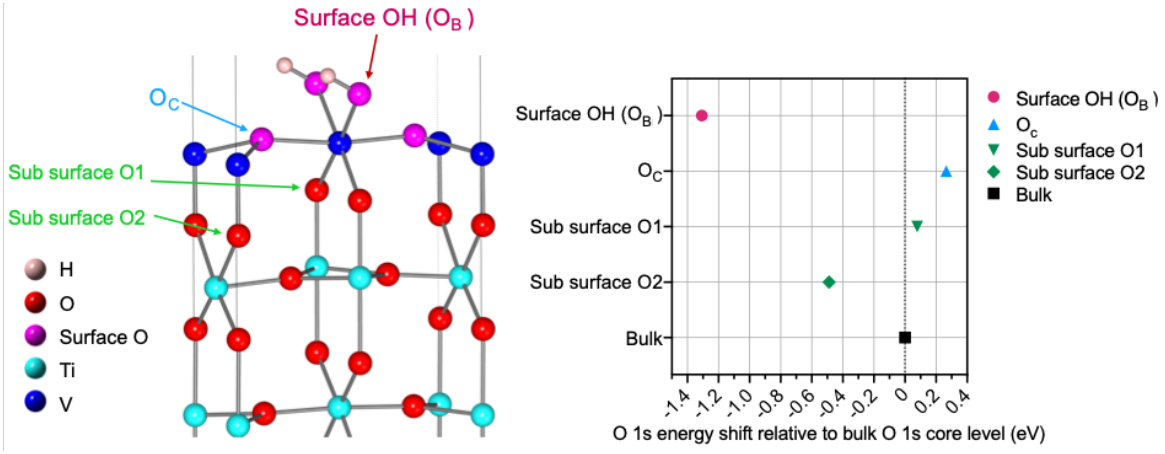

Figure 5.13. *Ball and stick image of the reduced surface model of ½ monolayer vanadia on TiO_2(110) optimized with DFT (left). The calculated shifts in O 1s energy level with respect to the bulk O (right).*

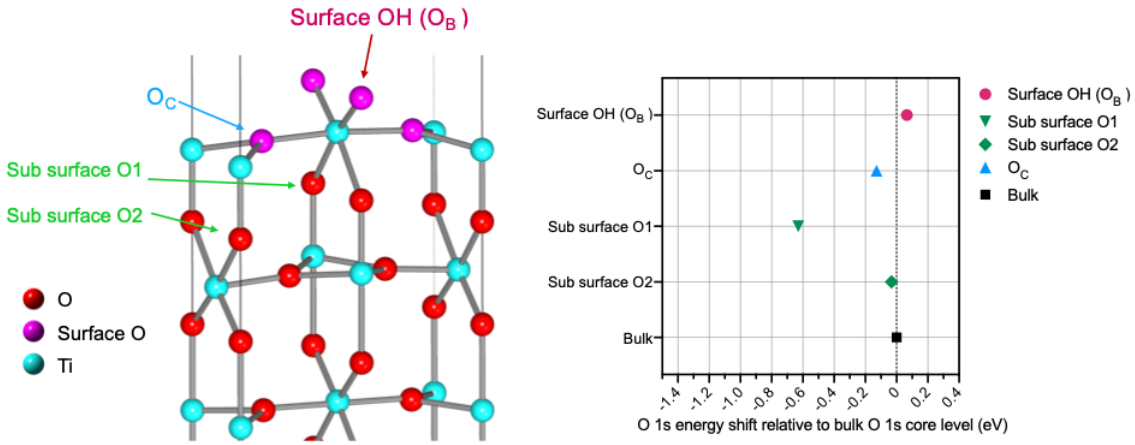

Figure 5.14. *Ball and stick image of the stoichiometric TiO_2(110) optimized with DFT (left). The calculated shifts in O 1s energy level with respect to the bulk O (right).*

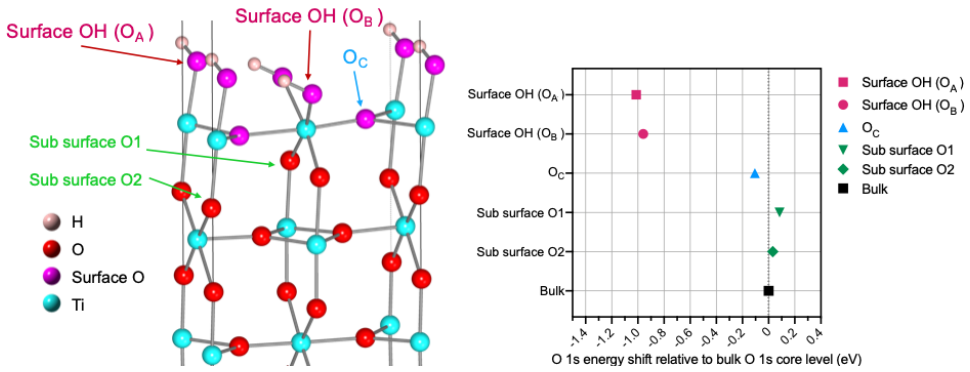

Figure 5.15. *Ball and stick image of the TiO2(110) with dissociated water molecule on the surface calculated with DFT (left). The calculated shifts in O 1s energy level with respect to the bulk O (right).*

Model-dependent analysis

To improve our understanding of this complex system, we created a 3-site model illustrated in Fig. 5.12 to quantitatively analyze the experimental data. The model, which is based on the model-independent 3D atomic maps, partitions the surface O to laterally sit at A, B, C sites or to be uncorrelated with the substrate lattice. (There are 2 symmetry equivalent C-sites, C1 and C2.) To quantify the structural parameters associated with these three adsorption sites, we performed a least-squares global fit of this model to the experimentally measured f_H and P_H values for each redox condition. Here, the Hth Fourier component for the SO atomic distribution is defined as:

$$\mathrm{F_H} = f_{\mathbf{H}}\, \mathrm{e}^{i2\pi \mathrm{P_H}} = \alpha_A \mathrm{e}^{i2\pi \mathbf{H}.\mathbf{r_A}} + \alpha_B \mathrm{e}^{i2\pi \mathbf{H}.\mathbf{r_B}} + \alpha_{C1} \mathrm{e}^{i2\pi \mathbf{H}.\mathbf{r_{C1}}} + \alpha_{C2} \mathrm{e}^{i2\pi \mathbf{H}.\mathbf{r_{C2}}} \qquad (5.4)$$

where α_x denotes the fraction of surface O occupying site X = A, B, C1, C2 with positions r_A = (0 0 z_A), r_B = (½ 0 z_B), r_{C1} = (0.2 ½ z_{C1}), r_{C2} = (0.8 ½ z_{C2}). z_x is the height of O above the TiO (110) bulk-like plane. The global fits of Eq. 5.4 to the sets of measured f_H and P_H values, give α and z at each SO site. Table 5.1 for the Ox and Table 2 for the Re surface list the heights above the (110) plane of TiO_2 in Å using Z = z C, where C = $2d_{110}$ = 6.496 Å. The tables also list the heights obtained from the DFT calculations for comparison. Also listed are the values of α for SO.

XSW-XPS and DFT data tables

Table 5.1. *Oxidized surface: XSW determined best fit vertical heights of surface oxygens (SO) above the bulk TiO (110) plane and heights obtained from DFT. Z(Å) is the displacement in the C-axis direction relative to the bulk like TiO plane of the centroid of the local O distribution. Also listed is the fraction of SO at each site. 42% of the SO atoms are uncorrelated.*

Site	Exp Z (Å)	DFT Z (Å)	α
A	1.84 (3)	1.89	0.23
B	0.98 (3)	1.27	0.03
C1	0.25 (3)	0.20	0.16
C2	0.25 (3)	0.20	0.16

Table 5.2. *Reduced surface: XSW determined best fit vertical heights of SO and heights obtained from DFT. Also listed is the fraction of SO at each site. 50% of the SO atoms are uncorrelated.*

Site	Exp Z (Å)	DFT Z (Å)	α
A	--	--	0.00
B	1.62 (3)	1.50	0.32
C1	0.32 (3)	0.32	0.09
C2	0.32 (3)	0.32	0.09

Table 5.3. *Vacuum Annealed surface: XSW determined best fit vertical heights of surface oxygen (in Å) above the bulk TiO (110) plane. Also listed is the fraction of SO at each site. 48% of the SO atoms are uncorrelated.*

Site	Exp Z (Å)	α
A	--	0.00
B	1.31(3)	0.28
C1	0.26(3)	0.12
C2	0.26(3)	0.12

The number in () represents the error. Example: 1.31(3) implies the value is within the range 1.31 ± 0.03

Coherent fractions and positions

The following tables list and are used to show consistency between XSW model-independent (meas), XSW model-dependent (calc) and density functional theory (DFT) determined values for coherent fractions (f) and positions (P).

Table 5.4. XSW-XPS results of O for Vacuum Annealed surface of ½ ML VO_x / α-TiO_2 (110)

	Bulk Oxygen				Surface Oxygen			
h k l	f_{meas}	f_{calc}	P_{meas}	P_{calc}	f_{meas}	f_{calc}	P_{meas}	P_{calc}
1 1 0	0.06(1)	0.11	0.06(1)	0	0.15(2)	0.27	0.07(2)	0.23
1 0 1	0.36(2)	0.34	0.55(2)	0.5	0.22(2)	0.23	0.61(2)	0.52
1 1 1	0.89(1)	0.88	0.51(1)	0.5	0.42(3)	0.42	0.61(3)	0.50
2 0 0	0.67(2)	0.77	0.50(2)	0.5	0.31(2)	0.31	0.67(2)	0.56

Table 5.5. XSW-XPS results of O for the Oxidized surface of the ½ ML VO_x / α-TiO_2 (110)

	Bulk Oxygen				Surface Oxygen					
h k l	f_{meas}	f_{calc}	P_{meas}	P_{calc}	f_{meas}	f_{calc}	f_{DFT}	P_{meas}	P_{calc}	P_{DFT}
1 1 0	0.14(1)	0.11	0.07(1)	0.00	0.12(2)	0.10	0.08	0.04(3)	0.01	0.05
1 0 1	0.34(2)	0.33	0.57(1)	0.50	0.19(3)	0.20	0.25	0.53(3)	0.62	0.39
1 1 1	0.89(1)	0.87	0.50(1)	0.50	0.44(2)	0.54	0.53	0.61(3)	0.65	0.57
2 0 0	0.68(2)	0.75	0.51(2)	0.50	0.56(3)	0.48	0.44	0.62(2)	0.57	0.57

Table 5.6. XSW-XPS results of O for the Reduced surface of the ½ ML VO_x / α-TiO_2 (110)

	Bulk Oxygen				Surface Oxygen					
h k l	f_{meas}	f_{calc}	P_{meas}	P_{calc}	f_{meas}	f_{calc}	f_{DFT}	P_{meas}	P_{calc}	P_{DFT}
1 1 0	0.11(1)	0.11	0.06(1)	0.00	0.19(2)	0.21	0.24	0.15(2)	0.25	0.24
1 0 1	0.38(1)	0.33	0.56(2)	0.50	0.19(6)	0.19	0.21	0.55(5)	0.51	0.51
1 1 1	0.90(2)	0.87	0.50(1)	0.50	0.51(5)	0.49	0.48	0.63(4)	0.55	0.54
2 0 0	0.70(2)	0.75	0.51(1)	0.50	0.37(4)	0.40	0.38	0.59(6)	0.61	0.61

Discussion

We see from Tables 5.1 and 5.2 that SO atoms in B and C positions are shifted upward on the reduced surface compared to the oxidized. Both experiment and DFT calculations show the same trend. This suggests that the reduced charge on V ions leads to weakening of ionic interactions between V and SO, resulting in elongation of V-O bonds. To gain further insights into the SO behavior, several different oxidized and reduced surface models were evaluated using DFT calculations to optimize the structures. The best agreement with the SO vertical positions for the reduced surface is obtained for the model structure shown in Fig. 5.10 (d), where the V ions are in isomorphic positions with the rutile substrate and surface oxygens in the VO layer are partially hydrogenated. The presence of H atoms determines the vertical height of V at the BR-site where the V atom shifts upward from the bulk-like Ti position, however, the absence of such a terminal O atom at A site keeps the vertical position of AT-site V unchanged as seen from both XSW measurements and DFT calculations. On the basis of these results, a possible interpretation of the reduced surface structure is the formation of 2D islands of hydrogenated VO_2 coherent with TiO_2.

Upon oxidation, surface oxygens show up at all 4 possible sites in the surface periodic cell as seen in Figs. 5.10 (a) and 5.10 (c). Comparing experiment and DFT results we see similar shifts in the heights at each site. The presence of H at both A and B sites results in V at both AT and BR sites to be shifted upward. Also, as seen from DFT the amount of chemically shifted oxygens on the oxidized surface is twice that on the reduced surface which agrees with the coverage calculated from experiment shown in Fig.5.5. Thus, the XSW experiment and DFT calculations agree for the various chemically distinct surface oxygen atoms and V atoms in both reduced and oxidized surfaces. It is very interesting to observe that both DFT and XSW show that reduction removes only the A-site oxygen. This can be interpreted as the A-site being the catalytically active site.

5.4 Conclusion

In this chapter, we discussed about the unique and exciting possibility of using X-ray standing wave excited X-ray photoelectron spectroscopy to observe chemically distinct surface oxygens. We presented the results and discussions on the system that we studied, supported vanadium oxide, demonstrating chemical-state specific atomic-scale analysis for the redox-driven cation dynamics, under reversible oxidation and reduction processes. XSW-XPS analysis allowed us to generate 3D composite atomic density maps that show surface O atoms distinct from the bulk oxygens along with surface V and bulk Ti atoms. These observations are in good agreement with the DFT calculations. Thus, we can use this approach to study various different functionalized crystalline surface and locate catalytically active surface atomic sites.

Chapter 6

MoO_x / α-TiO_2 (110) Interface

6.1 Introduction

Currently the reduction of greenhouse gas emissions has become highly important and to do so, new ways are being developed to convert CO_2, which is one of the main greenhouse gases, into useful hydrocarbons and oxygenates through catalytic hydrogenation. An example of this is the production of methanol from syngas which prefers highly active and selective catalysts.

Low-coverage molybdenum are one of the most widely used catalysts in petroleum refining and catalytic conversion of syngas to alcohol. MoO_x supported on TiO_2 is well known for photocatalysis and hydrodesulfurization[111]. The TiO_2 support also plays an important role in the catalytic activity of the molybdenum. The interface between the support and the catalyst (Mo-O-Ti bonds) plays a major role in controlling the structure and in turn the activity of the catalyst. During a redox reaction, these sites undergo structural and chemical changes as they participate in the overall catalytic process. Hence, it is important to understand the atomic-scale structures with chemical state specificity of the MoO_x/TiO_2 catalyst under reaction conditions since a better knowledge of the structure-function relationships would enable further improvement of the catalysts.

In this chapter, we present X-ray standing wave excited XPS studies of α-TiO_2(110) supported monolayer MoO_x grown by atomic layer deposition. XSW-XPS measurements were carried out at our UHV surface analysis station at sector 5ID-C of DND-CAT at the Advanced Photon Source. (Details of the end-station are provided in the Appendix of this thesis.) This novel XSW-XPS method allowed us to create model-independent composite 3D atomic maps of the catalytic interface. This enables us to identify catalytically active atomic surface sites and observe in-situ redox induced changes to the catalyst-support interface. These observations of structural transformations accompanying changes of the oxidation state Mo^{6+} to Mo^{4+} under redox cycling provides information on the structure of active sites and helps in understanding complex catalytic reactions. In addition, we have used density functional theory (DFT) calculations to further improve our understanding of this complex catalytic system.

6.2 Experimental Methods

Surface preparation

Sample growth

Rutile α-TiO_2 (110) single crystals, float zone grown by MTI Corp., were used as substrates. The single crystals were 10 x 10 x 1 mm^3 with one-side polished and with a surface miscut < 0.1°. α-TiO_2 substrates were annealed in a tube furnace with flowing O_2 (~500 sccm) at 400°C for 0.5 h, followed by 900 °C for 1 h. Atomic force microscopy (AFM) showed the formation of flat atomically clean step-separated terraces, 0.1 to 0.5 μm in width.

Prior to atomic-layer deposition (ALD), the substrates were first immersed in DI water (resistivity > 10^7 Ω cm) for 1 h at 90°C to hydroxylate the surface. This was followed by a dip in a 10% HCl

solution, a thorough DI water rinse, and then drying under ultra-high pure nitrogen (99.999%). The treated substrates were then loaded into a custom built cross-flow ALD reactor, heated to 200°C and maintained under ultra-high-purity nitrogen flow of 360 sccm at a pressure of 1 Torr for 1 h. Surface cleaning of the substrates was then carried out in-situ by flowing 400 sccm of ozone over the surface. A molybdenum oxide (MoO_x) layer was grown at 200°C on the treated α-TiO_2 (110) substrate by sequential exposure of MoF_6 and Si_2H_6. The first precursor MoF_6 was dosed for 2s followed by a 10s purge of N_2 to remove any by-products and then the second precursor Si_2H_6 was dosed for 1s followed by another 10s purge of N_2. This four-step dose-purge-dose-purge ALD cycle was repeated three times to get a 1 ML film of Molybdenum oxide on α-TiO_2 (110). The film was grown by Dr. Devika Choudhury from the group of Dr. Jeff Elam at Argonne National Laboratory.

ALD reaction: $MoF_6 + Si_2H_6 \rightarrow Mo + 2\ SiHF_3 + 2\ H_2$, ΔH = -221 kcal and ΔG = -235 kcal

Redox treatment

The sample was annealed at 350°C for 1 h inside the UHV surface analysis chamber at sector 5ID-C of DND-CAT at the Advanced Photon Source. This vacuum annealing helped remove any surface impurities or adventitious carbon that might be have been present on the surface. An Oxford Applied Research TC50 thermal gas cracker cell which is installed on this chamber was used for oxidation and reduction of the surface. Molecular oxygen was slowly leaked through the fine bore inert cracker tubes, into the chamber until the chamber pressure stabilized at 1 x 10^{-6} Torr. The cracker cell power was set to 60 W, which gave a 50% cracking efficiency indicating that 50% of the molecular O_2 was converted to atomic oxygen. The cracker cell was directed almost perpendicular to the sample surface and was at a distance of 10 cm from the surface. The sample was heated to 300°C and the cracker cell was directed towards the sample for 1 h which

oxidized the 1 ML MoO_x film. The reduced surface was produced in a similar manner by using molecular H_2 at a pressure of 1 x 10^{-6} Torr. The cracker cell power was set to 60 W which converted 50% of the molecular H_2 to atomic hydrogen. For reduction the sample was kept at room temperature and the cracker cell was directed towards the sample for 1 h which completely reduced the 1 ML MoO_x film.

Surface characterization

A Bruker Dimension FastScan Atomic Force Microscope (AFM) was used at the NUANCE SPID facility at Northwestern University for ex-situ examination of the surface morphology before and after the MoO_x film growth and after the redox reactions. AFM was operated in tapping mode using Si cantilever tips.

XSW-XPS measurements were carried out at sector 5ID-C of DND-CAT at the Advanced Photon Source. The UHV chamber at sector 5ID-C is also equipped with a dual anode X-ray source. We used the Al source for soft X-ray photoelectron spectroscopy to get high resolution XPS lines in order to observe the shifts in Mo 3d binding energy upon redox reactions. A Specs Phoibos 150 HV XPS analyzer is used. XSW-XPS was used to measure the distributions of interfacial atoms relative to the substrate TiO_2 lattice with both sub-Å spatial resolution and chemical state specificity. Analysis of the XSW induced modulation to a photoemission signal determines the amplitude (f_H) and phase (P_H) of the H^{th} Fourier component of the spatial distribution for molybdenum. One specular *(110)* and two off-specular *(101, 111)* XSW data sets were collected to triangulate the atomic positions in 3D. Each set of *hkl* measurements were repeated after each redox treatment to study the dynamic changes in the surface structure under in-situ reaction conditions. Details of XSW-XPS technique have been described in chapter three.

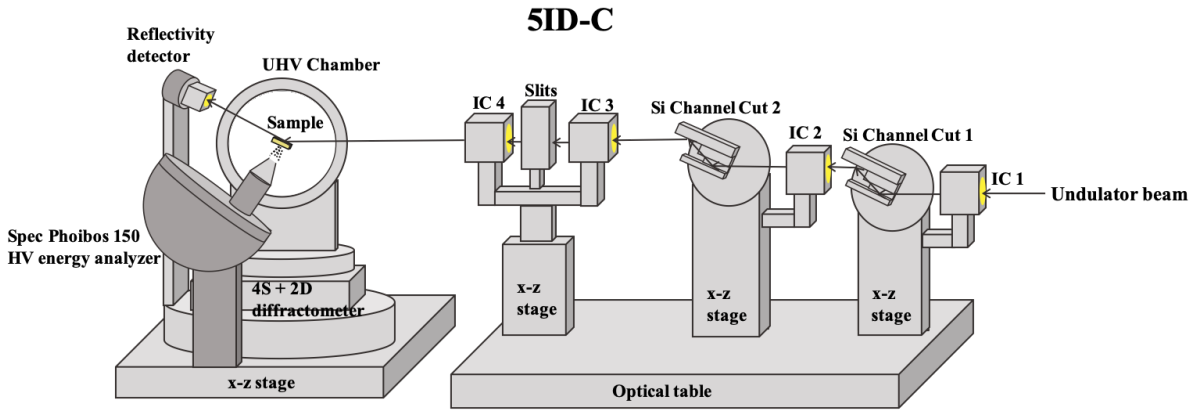

Figure 6.1. *The 5ID beamline layout in the 5ID-C station for the XSW-XPS experiment. Components at the upstream end of the 5ID-C hutch include: an optical table that accommodates post-monochromator Si channel cuts (CC1 and CC2), ion chambers (IC), and beam-defining slits. At the downstream end of 5ID-C sits the 4S+ 2D diffractometer and the UHV chamber with photoelectron spectrometer.*

Computational Methods

Density functional theory (DFT) calculations to support the experimental observations were carried out by Dr. Leighton Jones from the Northwestern University Chemistry group of Prof. George Schatz. The DFT calculations used the Perdew−Burke−Ernzerhof (PBE) functional and a basis as follows: Ti (SZP), O (SZP), Mo (DZP), H (DZP), in the Spanish Initiative for Electronic Simulations with Thousands of Atoms (SIESTA[37], version 4.1-b4) program; using a k-grid size of 3×3×1, a density matrix tolerance of 1.0×10^{-4} and a force tolerance of 0.05 eV $Å^{-1}$.

6.3 Results and discussion

AFM

The AFM image shows a rough surface for the as-received TiO_2 (110) surface (Fig. 6.2 (a)). After O_2 annealing (Fig. 6.2(b)) the surface atoms rearrange to form atomically-clean flat ~360 nm wide terraces separated by 0.3 nm steps with an rms surface roughness of 0.1 nm. After 1 ML MoO_x growth and after redox reactions, steps are still seen, indicating a uniform MoO_x growth (Fig. 6.2(c)) and no clustering as a result of the redox reactions (Fig. 6.2(d)).

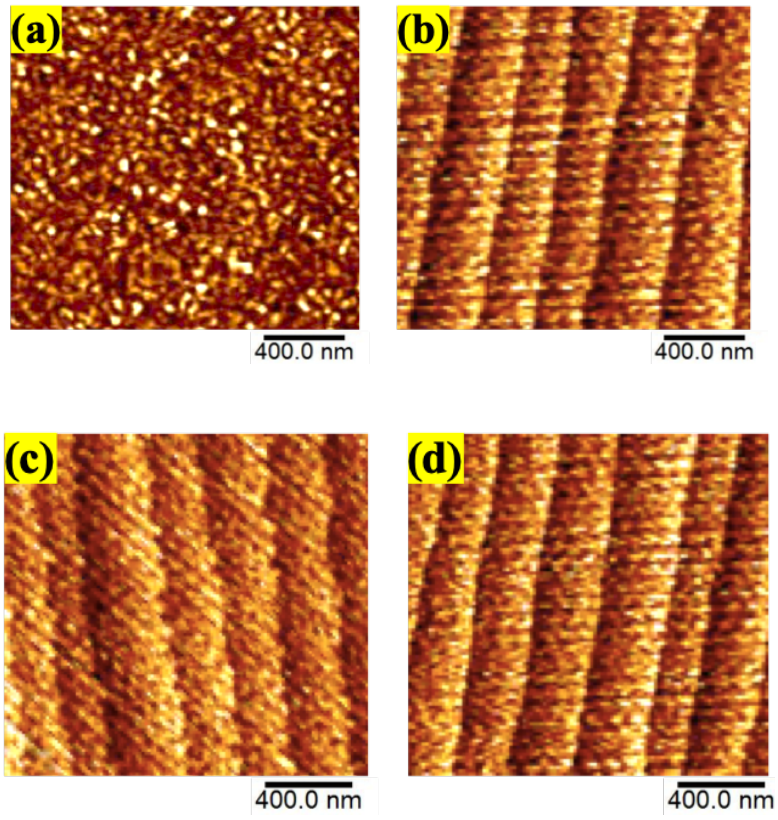

Figure 6.2. *Tapping-mode AFM images of α-TiO_2 (110) surface:* ***(a)*** *As-received;* ***(b)*** *After annealing in O_2;* ***(c)*** *After 1 ML MoO_x growth;* ***(d)*** *After redox reactions.*

Soft X-ray photoelectron spectroscopy

Soft X-rays using an Al source (Eγ = 1486 eV) were used for obtaining high-resolution XPS survey spectra. After each redox treatment, Mo 3d spectrum was measured using the Al source to know the Mo oxidation state. The spectra were calibrated using C 1s peak. Fig. 6.3 shows soft XPS survey scan. From the survey scan we see the main XPS peaks of O 1s, Ti 2p, Mo 3p and Mo 3d. We also have negligible amount of adventitious carbon signal and no residual Si from the ALD process. Thus, the soft XPS survey scan shows a clean surface for the 1 ML MoO_x / α-TiO_2 (110) sample.

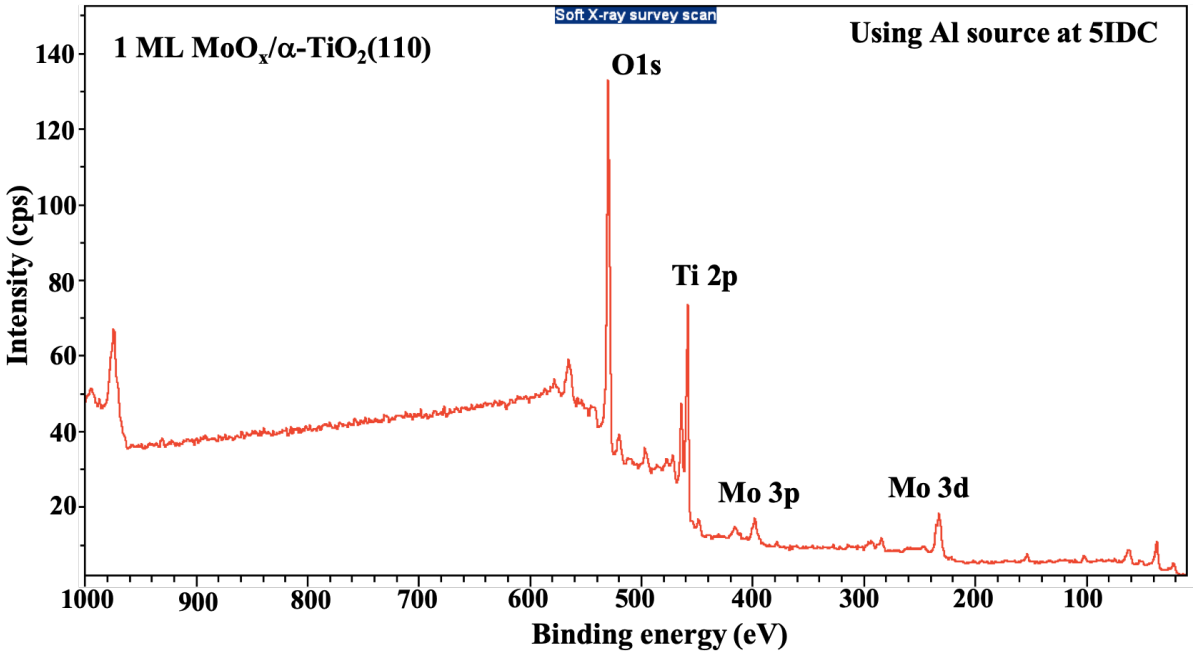

Figure 6.3. *Soft XPS survey scan using Al source (E_γ = 1486 keV) at 5ID-C showing the important XPS peaks. XPS measurement parameters are explained in Appendix A. For this survey scan, dwell time was 1 sec at each point with a step size of 0.1 eV. The sample angle eta was 0 degree and chi was 60 degree for all soft XPS scans.*

Fig. 6.4 shows the Mo 3d XPS peak at higher resolution for the oxidized and reduced surface. As can be seen the oxidized peak has shifted towards higher binding energy due to reduction in screening effect resulting in increased binding energy for the core shell electrons. Fig. 6.5 (a) and (b) shows the Mo 3d peaks fitted with the doublet of $3d_{5/2}$ and $3d_{3/2}$. Noting the binding energy value for the $3d_{5/2}$ peak, for the reduced surface it is at 229.77 eV and for the oxidized surface it is at 232 eV. These correspond to Mo^{4+} and Mo^{6+} $3d_{5/2}$ peaks respectively based on several references[112-115].

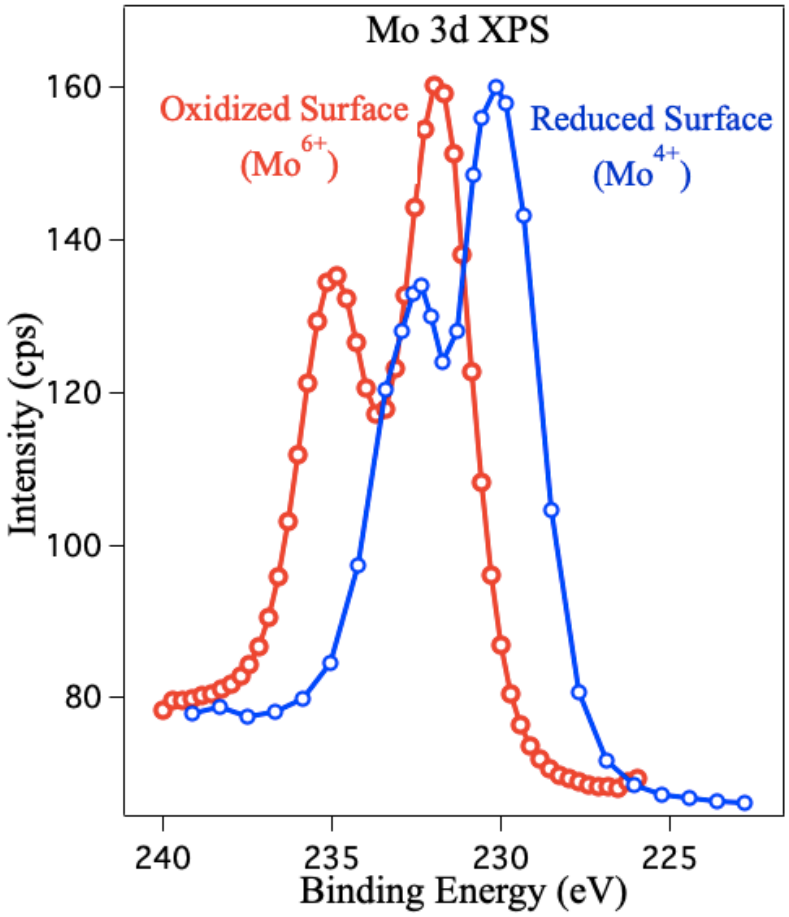

Figure 6.4. *Soft XPS scan of Mo $3d_{3/2}$ and $3d_{5/2}$ XPS peaks for the oxidized and reduced surface of the 1 ML MoO_x / α-TiO_2 (110) sample. Measurement parameters were same as Fig. 6.3.*

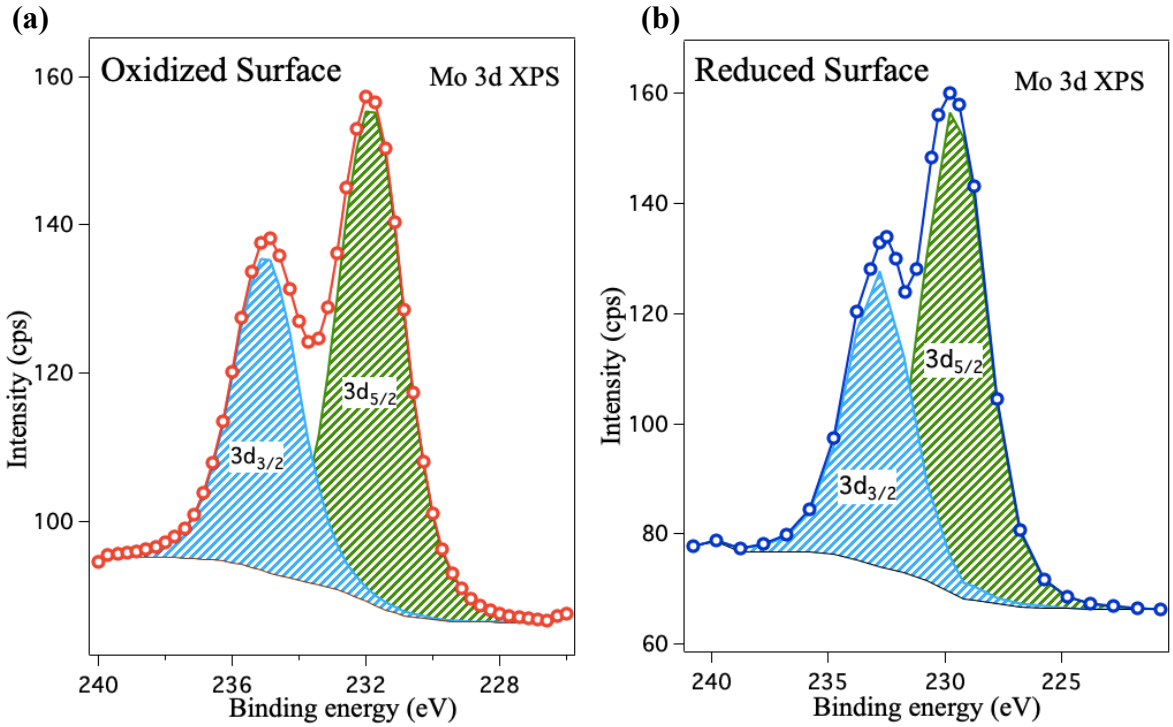

Figure 6.5. *Mo 3d XPS peak fitted with Mo $3d_{5/2}$ and $3d_{3/2}$ peaks for the* ***(a)*** *oxidized surface and* ***(b)*** *reduced surface of the 1 ML MoO_x / α-TiO_2 (110) sample*

X-ray standing wave excited hard X-ray photoelectron spectroscopy

For the XSW-XPS measurements, the synchrotron X-ray was tuned at an energy of 6.95 keV. At this incident energy, we measured the XSW induced modulations in Mo $2p_{3/2}$ XPS signal to determine the coherent fraction and position of the H^{th} Fourier component of the spatial distribution of Mo. One specular *(110)* and two off-specular *(101, 111)* XSW data sets were collected to triangulate the atomic positions in 3D. Each set of *hkl* measurements were repeated after each redox treatment to study the dynamic changes in the surface structure under in-situ reaction

conditions. We also measured modulations in O 1s XPS signal for each reflection to map redox induced changes in the surface oxygens.

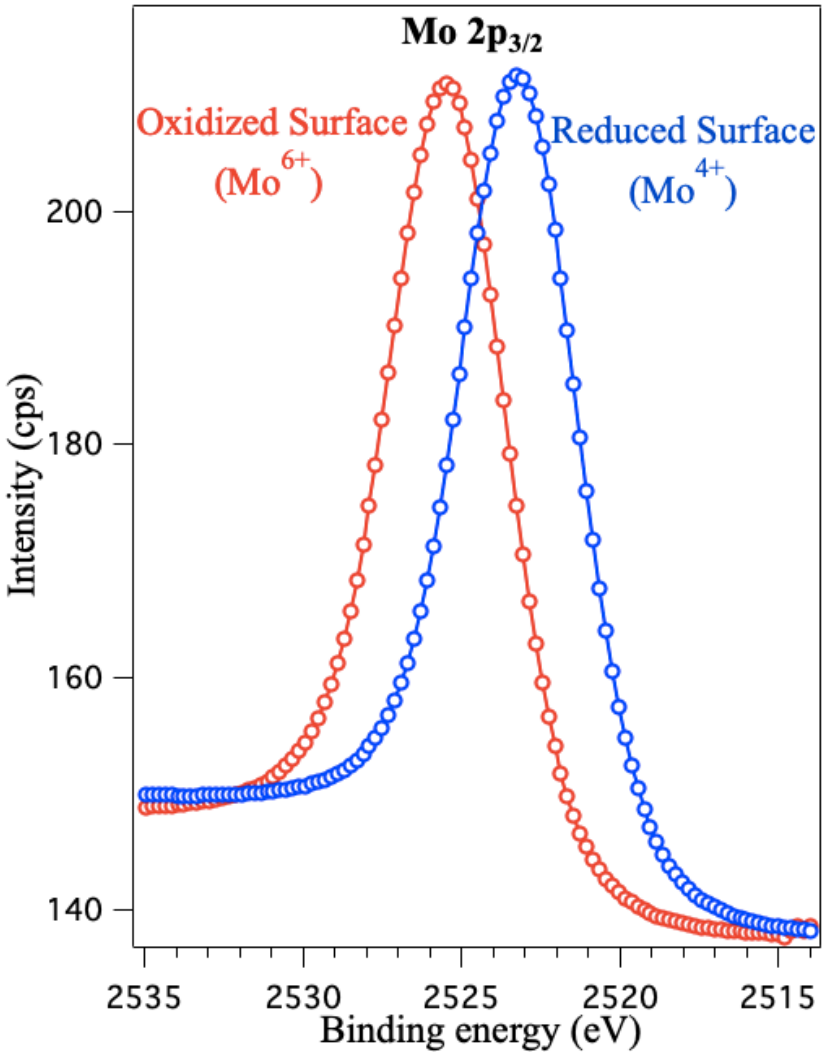

Figure 6.6. *Mo $2p_{3/2}$ XPS peak for the oxidized surface and reduced surface at 6950 eV incident energy. Incident beam size was 1 mm x 0.5 mm. One Si 220 channel cut was used to monochromatize the incident beam. The incident photon flux at the sample is roughly 10^{11} photons/s.*

The oxidized Mo 2p XPS peak is shifted by 2 eV towards higher binding energy as compared to the reduced surface Mo 2p peak which is at a lower binding energy. From soft XPS we already know that the reduced peak is from Mo^{4+} and the oxidized peak is from Mo^{6+}. Also deconvoluting each Mo 2p peak showed that the surface has been completely oxidized and completely reduced and each peak can be completely fitted with a single Gaussian curve.

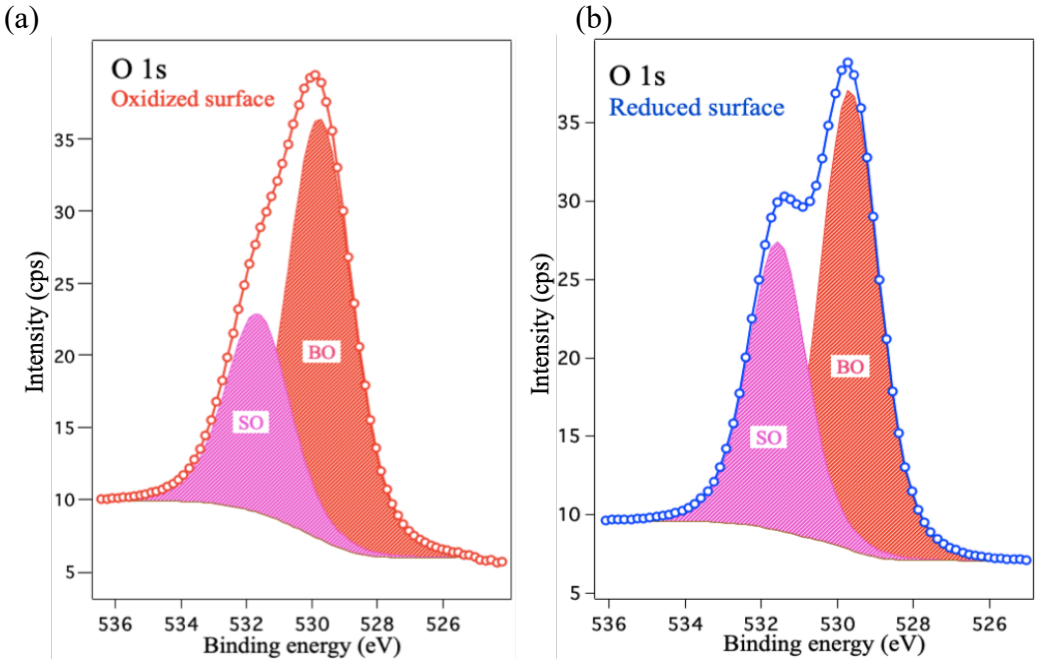

Figure 6.7. *O 1s XP spectra at 6.95 keV incident energy for the (a) oxidized surface (b) reduced surface.*

Each O 1s peak consists of two chemically shifted peaks. The bulk oxygen (BO) peak is at lower binding energy and remains unchanged upon oxidation and reduction. The peak at higher binding energy, which is shifted from the BO peak by 2 eV, corresponds to surface oxygen peak and has been referred to as SO. This peak consists of partially hydroxylated surface oxygens. The amount of surface oxygen can be quantified from the area under the peak. For the oxidized surface the amount of SO is roughly 0.8 ML and for the reduced surface it is almost 1.00 ML.

X-ray standing wave results: Titanium

As a system check, XSW-XPS analysis is used on the Ti 1s signal to show that the Ti atoms show up at bulk like positions. f_{meas} and P_{meas} are the values obtained from experiment and f_{calc} and P_{calc} are values calculated considering ideal Ti positions. As we can see from Table 4.3, the values match very well indicating the validity of our measurements and analysis.

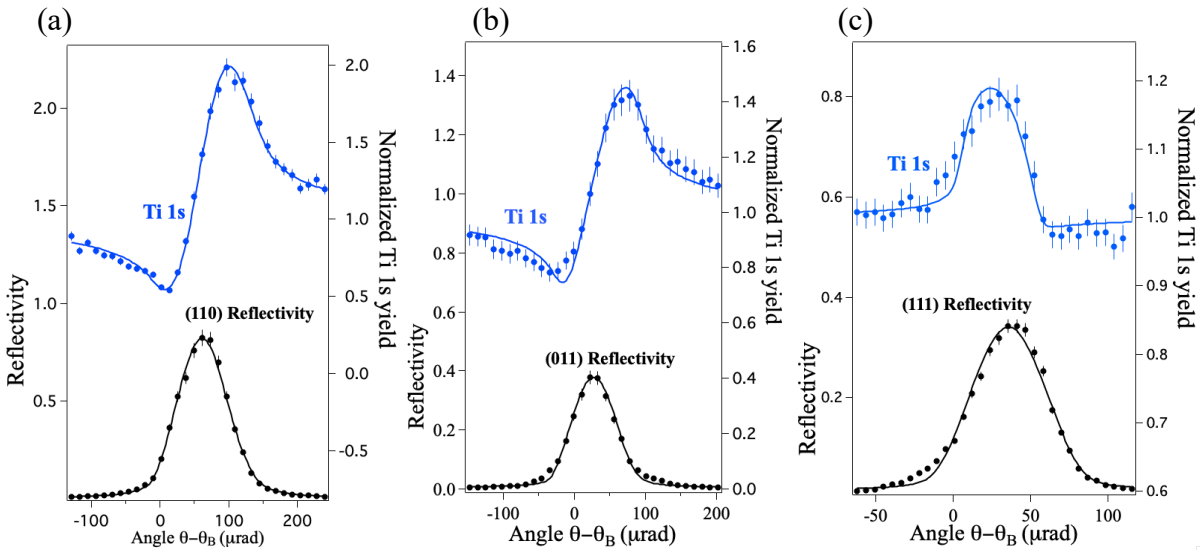

Figure 6.8. *Modulations in Ti 1s XPS yields for oxidized surface from the angle scans through the* ***(a)*** *(110)* ***(b)*** *(011)* ***(c)*** *(111) reflections.*

Table 6.1. *XSW-XPS measured and calculated values of f_H and P_H for bulk Ti atoms for oxidized surface*

	Titanium			
h k l	**f_{meas}**	**f_{calc}**	**P_{meas}**	**P_{calc}**
1 1 0	0.95 (1)	0.98	0.00 (1)	0
1 0 1	0.82 (2)	0.97	-0.01 (1)	0
1 1 1	0.10 (1)	0	---	--

Table 6.2. *XSW-XPS measured and calculated values of f_H and P_H for bulk Ti atoms for reduced surface.*

	Titanium			
h k l	**f_{meas}**	**f_{calc}**	**P_{meas}**	**P_{calc}**
1 1 0	0.96 (1)	0.98	0.01 (1)	0
1 0 1	0.81 (2)	0.97	-0.02 (1)	0
1 1 1	0.11 (1)	0	---	--

From Tables 6.1 and 6.2 we see that the coherent fractions and positions of the bulk Ti are close to calculated values. The slightly lower coherent fraction could be caused due to a small percentage of disordered Ti on the surface. The coherent positions are ~0 as expected. The coherent fractions and positions remain unchanged upon oxidation and reduction thus proving that the bulk Ti atoms in the TiO_2 crystal are located in bulk like positions and are stable under redox conditions. Also note that there was no redox induced chemical shift of the Ti 1s XPS peak.

X-ray standing wave results: Molybdenum

This section shows the results for XSW induced modulation in Mo $2p_{3/2}$ XPS signal as the sample was scanned across 3 symmetry inequivalent *hkl* reflections. This gave us 3 sets of f_H and P_H for both oxidized and reduced surfaces.

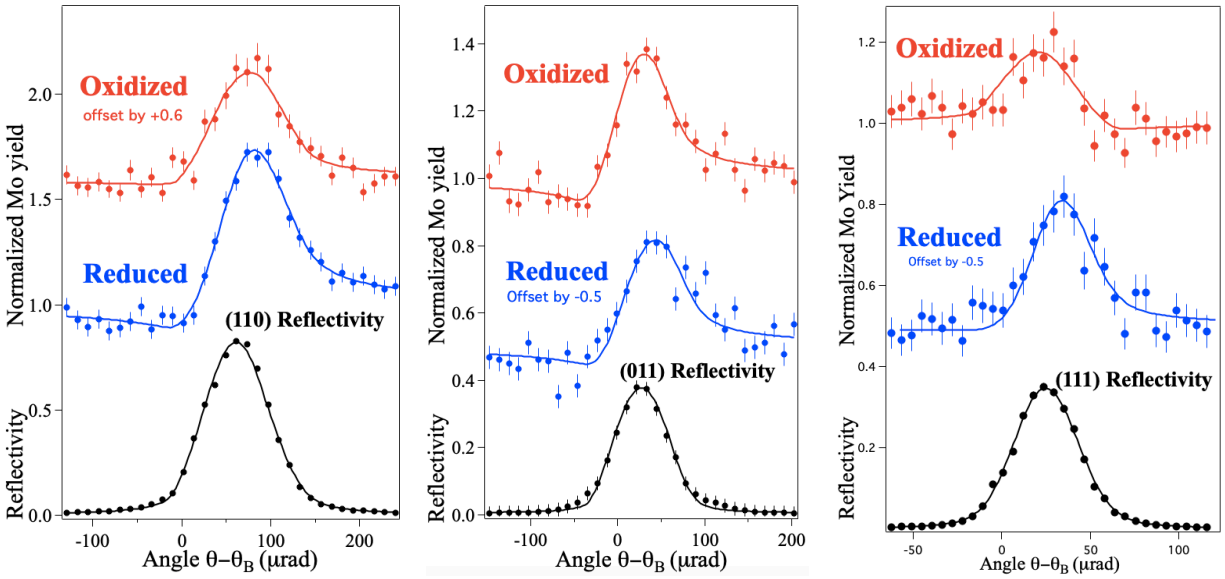

Figure 6.9. *Modulations in Mo XPS yields for the oxidized surface and reduced surface from the angle scans through the (110), (011) and (111) reflections.*

X-ray standing wave results: Oxygen

This section shows the results for XSW induced modulation in O 1s XPS signal as the sample was scanned across 3 symmetry inequivalent *hkl* reflections. This gave us 3 sets of f_H and P_H for bulk oxygens and surface oxygens for both oxidized and reduced surfaces.

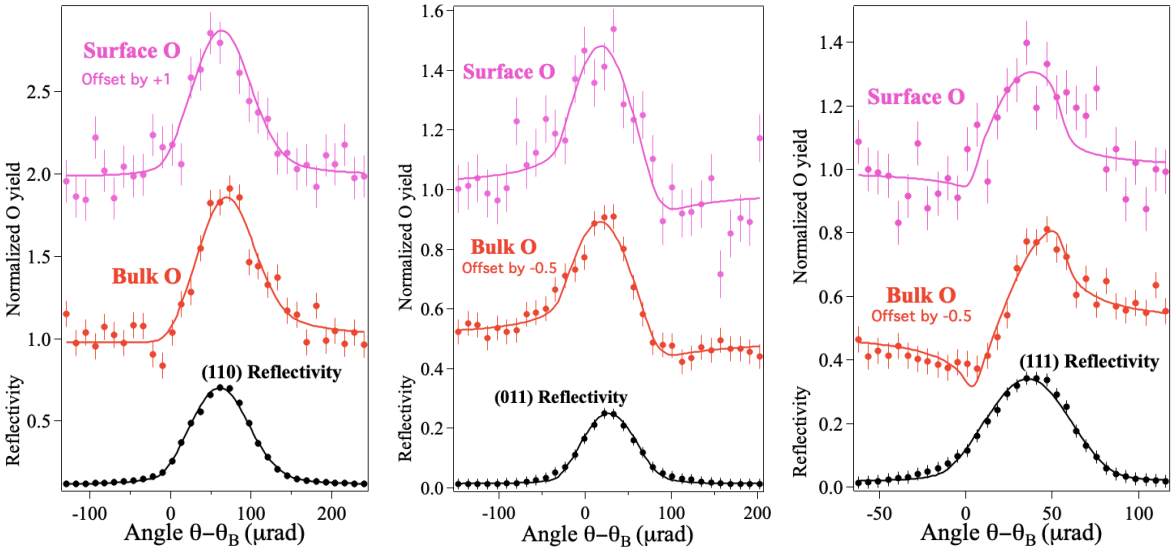

Figure 6.10. *Modulations in O1s XPS yields from BO and SO for the oxidized surface from the energy scans through the (110), (011) and (111) reflections.*

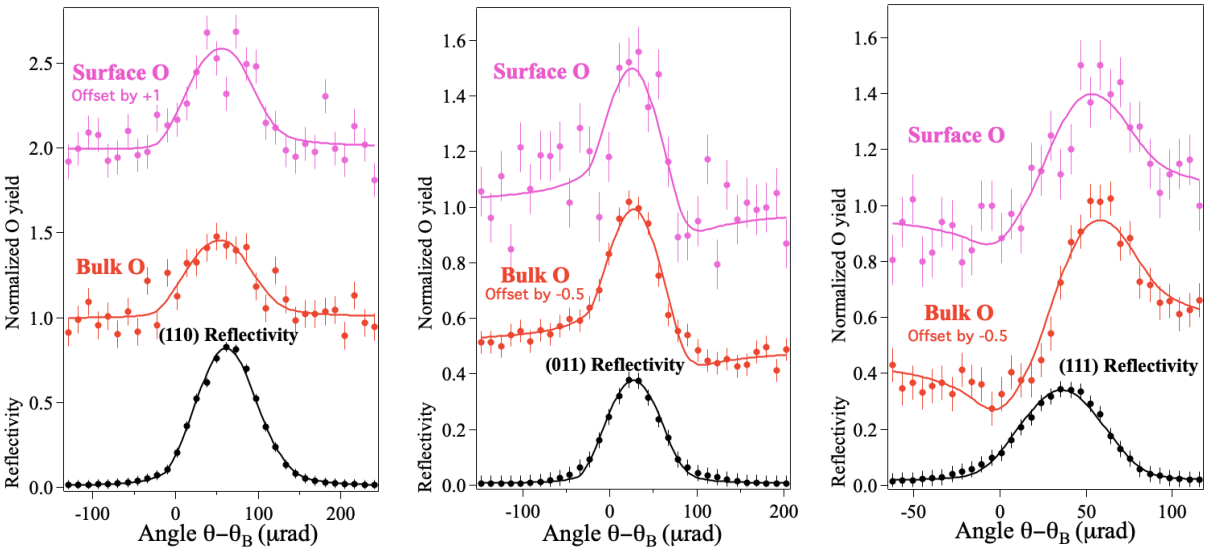

Figure 6.11. *Modulations in O1s XPS yields from BO and SO for the reduced surface from the energy scans through the (110), (011) and (111) reflections.*

XSW-XPS model-independent 3D maps and DFT calculated structure

A Fourier summation of the three sets of Fourier components and their symmetry equivalents is used to generate model-independent 3D atomic density $\rho(\mathbf{r})$ maps

$$\rho(\boldsymbol{r}) = 1 + 2 \sum_{\substack{H \neq -H \\ H \neq 0}} f_H \cos[2\pi(P_H - \boldsymbol{H}.\boldsymbol{r})] \qquad (6.3)$$

We combine the maps of Mo and SO using the Mo 2p and surface O 1s XSW-XPS results and show such maps for the oxidized and reduced surfaces in Figs. 6.12(a) and 6.12(b), respectively. The initial vacuum annealed surface has a 3D composite atomic map (Fig. 5.11) similar to that of the reduced surface. For all three surfaces, the bulk Ti and O show up in their expected positions in the composite maps and show no redox induced changes.

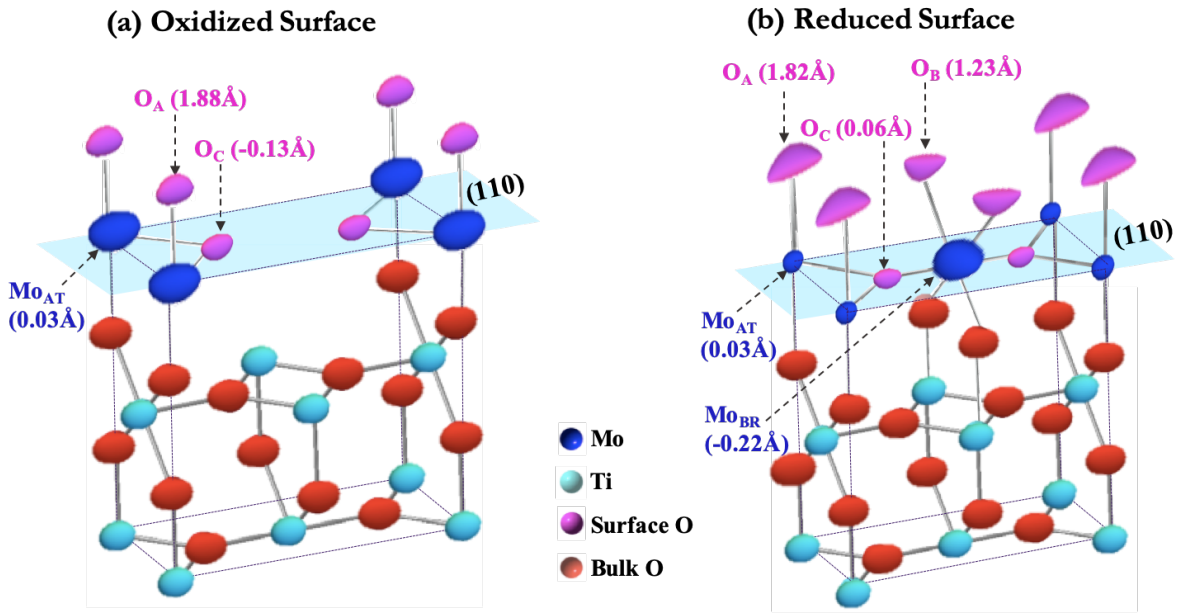

Figure 6.12. *XSW-XPS determined model-independent composite atomic maps of SO and Mo for* ***(a)*** *oxidized* ***(b)*** *reduced surface. The size of each Mo and SO oval is proportional to its fractional occupancy.*

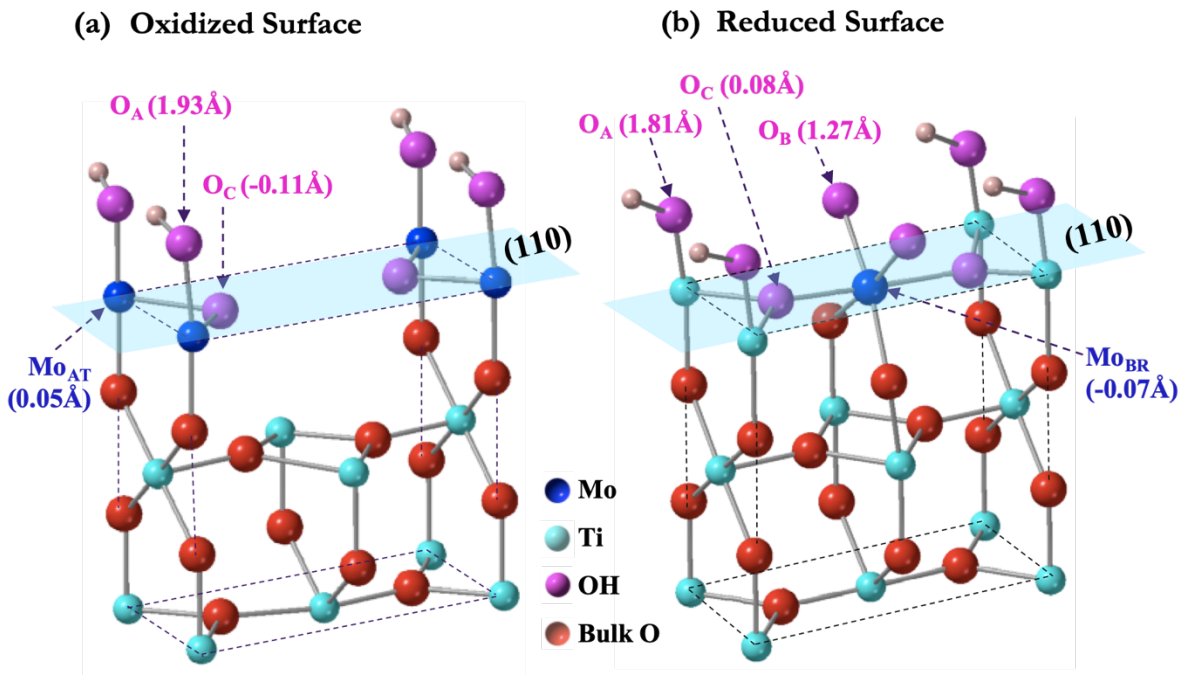

Figure 6.13. *DFT calculated model for* ***(a)*** *oxidized* ***(b)*** *reduced surface.*

The DFT models shown in Figure 6.13 (a) and 6.13 (b) are the closest match with the XSW-XPS determined model-independent results and the vertical heights of both Mo and SO match closely as can be seen from tables 6.7 – 6.10.

For comparison several different DFT models were evaluated. As we see from the XSW results, in the oxidized surface, the coherent Mo atoms occupy only the AT sites and hence the BR site can either be vacant or can be occupied by a Ti atom. Both these models were evaluated through DFT calculations and the model with a vacancy at the BR site better matches with the experimental results. Fig. 6.14 (a) shows that DFT model for the oxidized surface where TiO atoms were added at the BR site. The C-site surface oxygens are displaced upwards from the (110) TiO plane in this model, however, in the experimental results these C-site oxygens are displaced downwards which agrees with the DFT model in Fig. 6.13 (a).

For the reduced surface most of Mo is at the BR site and trace amount of Mo are at the AT sites. Three different DFT models were evaluated for the reduced surface. Model 1 with Mo atoms in both the AT and the BR sites, model 2 with Mo at the BR site and half of the AT sites and Ti in the other half of the AT sites and model 3 with Mo only at the BR site and Ti at the AT sites. Among these models, model 3 shown in Fig. 6.13 (b) had the best agreement with the experimental results. Model 1 and 2 are shown in Fig. 6.14 (b) and (c) respectively.

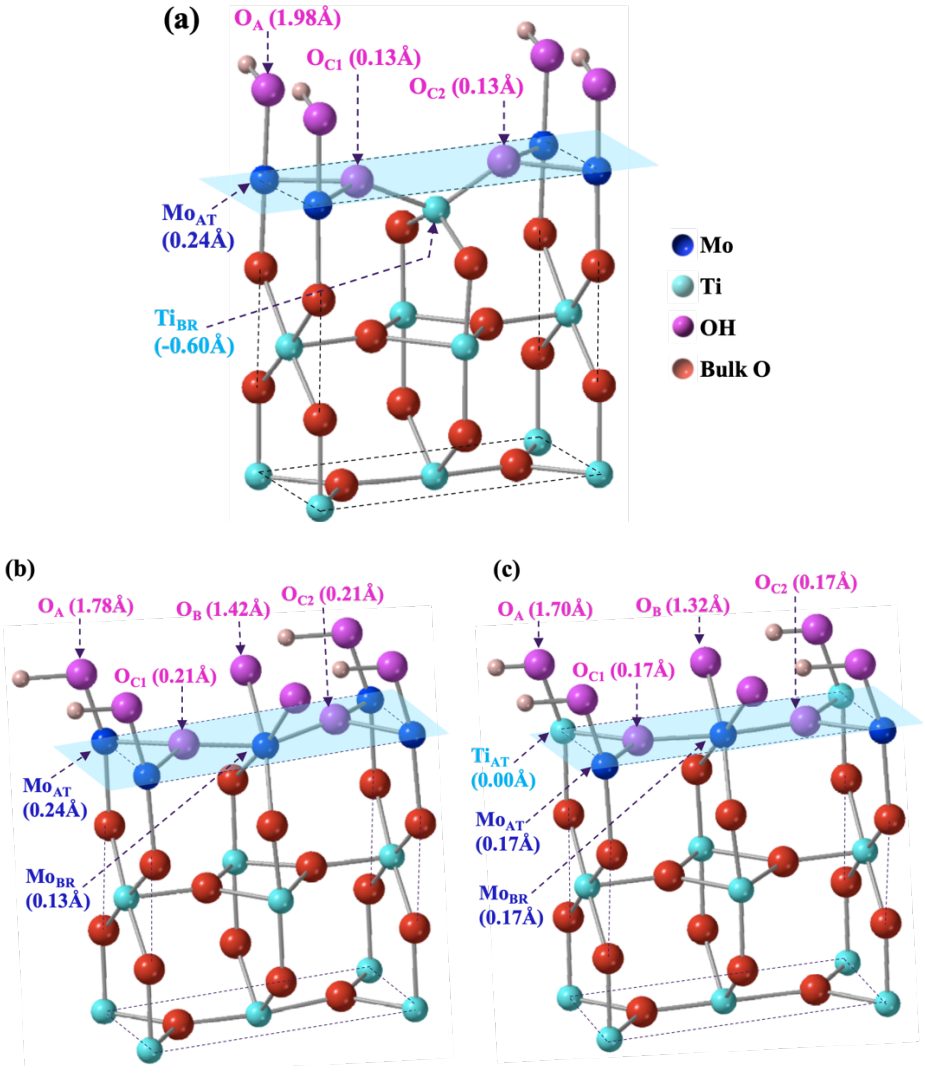

Figure 6.14. *Alternate DFT model for the* ***(a)*** *oxidized surface* ***(b)*** *reduced surface model 1* ***(c)*** *reduced surface model 2*

Model-dependent analysis for Molybdenum

To further improve our understanding of this complex catalytic system, based on the model independent results, we created a 2-site model to quantitatively analyze the experimental data. Then a global fitting procedure helped refine the parameters to get information such as the ordered fraction of adsorbed atoms at certain sites and heights of those atoms. The model partitions the Mo to sit at either atop (AT) or bridging (BR) sites or to be random. To quantify the structural parameters associated with these two adsorption sites, we performed a least-squares global fit of each condition to the experimentally measured f_H and P_H values. Here, the H^{th} Fourier component for the V atomic distribution is defined as

$$\mathrm{F}_{\mathbf{H}} = f_{\mathbf{H}}\, \mathrm{e}^{i2\pi \mathrm{P}_{\mathbf{H}}} = \alpha_{AT}\, \mathrm{e}^{i2\pi \mathbf{H}.\mathbf{r}_{\mathbf{AT}}} + \alpha_{BR}\, \mathrm{e}^{i2\pi \mathbf{H}.\mathbf{r}_{\mathbf{BR}}} \quad (6.1)$$

where α_X denotes the fraction of Mo occupying site X = AT or BR with positions $\mathbf{r}_{AT}$ = (0 , 0 , $\mathbf{z}_{AT}$) and $\mathbf{r}_{BR}$ = ($\frac{1}{2}$, $\frac{1}{2}$, $\mathbf{z}_{BR}$). z_x is the height of Mo at site X = AT or BR above the TiO (110) bulk-like plane. The global fits of Eq. 6.1 to the sets of measured f_H and P_H values in Tables 6.3 - 6.4, gives the occupation fractions of Mo^{4+} for the reduced surface and of Mo^{6+} for the oxidized surface along with the z heights of each site for each species. Tables 6.7 - 6.8 lists the amount (in ML) that each chemical state of Mo occupies at the AT and BR sites for the Ox and Re surfaces respectively. Table 6.7 - 6.8 also lists the heights of Mo^{6+} and Mo^{4+} above the (110) plane of TiO_2 at each site for the Ox and Re surfaces respectively obtained from model-independent XSW-XPS experiments and from DFT calculations.

Model-dependent analysis for Surface Oxygen

To improve our understanding of this complex system, we created a 3-site model to quantitatively analyze the experimental data. The model, which is based on the model-independent 3D atomic maps, partitions the surface O to laterally sit at A, B, C sites or to be uncorrelated with the substrate lattice. (There are 2 symmetry equivalent C-sites, C1 and C2.) To quantify the structural parameters associated with these three adsorption sites, we performed a least-squares global fit of this model to the experimentally measured f_H and P_H values for each redox condition. Here, the H^{th} Fourier component for the SO atomic distribution is defined as:

$$\mathrm{F_H} = f_{\mathbf{H}}\, \mathrm{e}^{i2\pi \mathrm{P_H}} = \alpha_A \mathrm{e}^{i2\pi \mathbf{H}.\mathbf{r_A}} + \alpha_B \mathrm{e}^{i2\pi \mathbf{H}.\mathbf{r_B}} + \alpha_{C1} \mathrm{e}^{i2\pi \mathbf{H}.\mathbf{r_{C1}}} + \alpha_{C2} \mathrm{e}^{i2\pi \mathbf{H}.\mathbf{r_{C2}}} \qquad (6.2)$$

where α_x denotes the fraction of surface O occupying site X = A, B, C1, C2 with positions r_A = (0 0 z_A), r_B = (½ 0 z_B), r_{C1} = (0.2 ½ z_{C1}), r_{C2} = (0.8 ½ z_{C2}). z_x is the height of O above the TiO (110) bulk-like plane. The global fits of Eq. 6.2 to the sets of measured f_H and P_H values in Tables 6.5 - 6.6, give α and z at each SO site. Table 6.9 for the Ox and Table 6.10 for the Re surface list the heights above the (110) plane of TiO_2 in Å using Z = z C, where C = $2d_{110}$ = 6.496 Å. The tables also list the heights obtained from the DFT calculations for comparison. Also listed are the values of α for SO.

Coherent fractions and positions

The following tables list and are used to show consistency between XSW model-independent (meas), XSW model-dependent (calc) and density functional theory (DFT) determined values for coherent fractions (f) and positions (P).

Table 6.3. *XSW-XPS results of Mo^{6+} for the Oxidized surface of 1 ML MoO_x / α-TiO_2 (110)*

hkl	f_{meas}	f_{calc}	f_{DFT}	P_{meas}	P_{calc}	P_{DFT}
1 1 0	0.37(2)	0.32	0.31	0.01(1)	0.01	0.02
1 0 1	0.31(4)	0.31	0.31	-0.04(2)	-0.02	-0.02
1 1 1	0.17(7)	0.23	0.22	-0.07(7)	-0.05	-0.05

Table 6.4. *XSW-XPS results of Mo^{4+} for the Reduced surface of 1 ML MoO_x / α-TiO_2 (110)*

hkl	f_{meas}	f_{calc}	f_{DFT}	P_{meas}	P_{calc}	P_{DFT}
1 1 0	0.24(2)	0.25	0.19	-0.03(1)	-0.08	-0.08
1 0 1	0.33(4)	0.28	0.19	-0.01(1)	-0.03	-0.04
1 1 1	0.12(5)	0.13	0.18	0.43(7)	0.39	0.42

Table 6.5. *XSW-XPS results of O for the Oxidized surface of 1 ML MoO_x / α-TiO_2 (110)*

	Bulk Oxygen				Surface Oxygen					
h k l	f_{meas}	f_{calc}	P_{meas}	P_{calc}	f_{meas}	f_{calc}	f_{DFT}	P_{meas}	P_{calc}	P_{DFT}
1 1 0	0.15(1)	0.11	0.10(1)	0.00	0.04(2)	0.10	0.15	--	--	--
1 0 1	0.30(2)	0.33	0.54(1)	0.50	0.35(3)	0.20	0.20	0.48(3)	0.52	0.52
1 1 1	0.86(1)	0.87	0.49(1)	0.50	0.50(2)	0.42	0.42	0.62(3)	0.62	0.62

Table 6.6. *XSW-XPS results of O for the Reduced surface of 1 ML MoO_x / α-TiO_2 (110)*

	Bulk Oxygen				Surface Oxygen					
h k l	f_{meas}	f_{calc}	P_{meas}	P_{calc}	f_{meas}	f_{calc}	f_{DFT}	P_{meas}	P_{calc}	P_{DFT}
1 1 0	0.07(1)	0.11	0.10(1)	0.00	0.09(2)	0.20	0.20	--	--	--
1 0 1	0.33(2)	0.33	0.50(1)	0.50	0.38(3)	0.37	0.35	0.51(3)	0.51	0.51
1 1 1	0.84(1)	0.87	0.49(1)	0.50	0.59(2)	0.61	0.70	0.51(3)	0.51	0.49

XSW-XPS and DFT obtained heights and occupation fractions

Table 6.7. *Oxidized surface: XSW determined best fit vertical heights of Mo^{6+} above the bulk TiO (110) plane and heights obtained from DFT. Z(Å) is the displacement in the C-axis direction relative to the bulk like TiO plane of the centroid of the local Mo distribution. Also listed is the fraction of Mo at each site and the amount of uncorrelated Mo^{6+}.*

Sites (Mo^{6+})	Exp Z (Å)	DFT Z (Å)	α
AT	0.03Å	0.05 Å	0.29
BR	--	--	0
Uncorrelated	--	--	0.71

Table 6.8. *Reduced surface: XSW determined best fit vertical heights of Mo^{4+} above the bulk TiO (110) plane and heights obtained from DFT. Also listed is the fraction of Mo at each site and the amount of uncorrelated Mo^{4+}.*

Sites (Mo^{4+})	Exp Z (Å)	DFT Z (Å)	α
AT	0.03 Å	--	0.08
BR	-0.22 Å	-0.07 Å	0.21
Uncorrelated	--	--	0.71

Table 6.9. *Oxidized surface: XSW determined best fit vertical heights of surface oxygens (SO) above the bulk TiO (110) plane and heights obtained from DFT. Also listed is the fraction of SO at each site. 49% of the SO atoms are uncorrelated.*

Site (SO)	Exp Z (Å)	DFT Z (Å)	α
A	1.88 (3)	1.93	0.21
B	--	--	--
C1	-0.13 (3)	-0.11	0.15
C2	-0.13 (3)	-0.11	0.15

Table 6.10. *Reduced surface: XSW determined best fit vertical heights of surface oxygens (SO) above the bulk TiO (110) plane and heights obtained from DFT. Also listed is the fraction of SO at each site. 5% of the SO atoms are uncorrelated.*

Site (SO)	Exp Z (Å)	DFT Z (Å)	α
A	1.82 (2)	1.81	0.45
B	1.23 (2)	1.27	0.30
C1	0.06 (2)	0.08	0.10
C2	0.06 (2)	0.08	0.10

Discussion

The XSW-XPS experimental results, supported by DFT calculations, allowed us to follow the dynamics that occur during the redox reaction resulting in transition between two different oxidation states of Mo (4+ and 6+). The α-TiO_2 (110) surface has a (1x1) surface reconstruction and is terminated with both AT and BR sites occupied by Ti. The as-grown MoO_x is incoherent with the substrate due to the low growth temperature. After vacuum annealing certain percentage of the Mo becomes coherent with the substrate and can occupy either the AT or the BR site. The incoherent Mo can be in the form of MoO_3 or MoO_2 molecules on the surface in the oxidized or reduced surface respectively. These Mo are laterally not correlated however from XPS we can see that in the oxidized surface the Mo is completely in Mo^{6+} state and in the reduced surface it transitions to complete Mo^{4+}. Oxidation caused the Mo^{6+} cations to completely migrate to the AT sites. O-bonded Mo cations are locked in AT sites, and the Mo do not exchange with either the Ti or the vacancies at the BR sites. In the reduced surface, Mo is in 4+ state and the structure is rutile which is isomorphic with the substrate rutile TiO_2 and hence the Mo occupies both the Ti like sites AT and BR, however the Mo^{4+} cation prefers the BR site and hence reduction causes most of the

Mo from the AT site to migrate to the BR sites. The uniqueness of the XSW-XPS method also adds the ability to map surface oxygens (SO) distinct from the bulk oxygens (BO). Hence this shows that on the oxidized surface, SO atoms are present only at the A and C sites. Since there is a vacancy at the BR site, hence there is no oxygen at the B site. Upon reduction, when the Mo from the AT site migrates to the BR site, SO atoms show up at all three A, B and C sites.

6.4 Conclusion

XSW excited XPS technique was used to study ALD grown 1 ML MoO_x / α-TiO_2 (110). Furthermore, DFT calculations were carried out to better understand this complex catalytic interface. We demonstrated redox-driven cation dynamics for the MoO_x catalyst on the TiO_2 support. We were able to create composite 3D atomic maps of the oxidized and reduced surfaces which showed the cationic migration of Mo atoms and subsequent exchange of surface oxygens. This method can be extended to study catalytic reaction mechanisms on several other complex systems. In previous related work, element specific atomic maps from XSW excited X-ray fluorescence (XRF) measurements were used to study the 0.38 ML WO_x/α-TiO_2 (110) interface[93]. The W results can be compared with the presented case of one monolayer (ML) molybdenum on α-TiO_2(110), where the XSW-XPS method was used to directly observe *in situ* structural and chemical state modifications. Comparing this with the previous results of WO_x/α-TiO_2 surface, it was observed that tungsten showed no change in its chemical state or structural distribution and positions upon reduction. This observation further proves that compared to Mo, W oxides are much more difficult to reduce and are reluctant to generate any catalytic active sites[116] whereas Mo oxides are more easily reducible. For the 0.38 ML W sample α_A = 0.36(7), α_B = 0.38(8), Z_A = 3.28(8)Å and Z_B = 3.60(8)Å for both oxidized and reduced surface.

Chapter 7

X-ray absorption spectroscopy studies of MoO_x / C

7.1 MoO_2 / Reduced Graphene Oxide

7.1.1 Introduction

High-valent oxo-molybdenum complexes serve as excellent catalysts in numerous laboratory-scale oxidation and reduction reactions. Single-site heterogeneous catalysts derived from molecular precursors with well-dispersed metal centers on solid supports offer a means to bridge the homogeneous-heterogeneous catalysis gap. Carbon materials can have high surface areas, good thermal stability and varying degrees of structural regularity, providing versatile supports in conventional heterogeneous catalysis. To explore the scope of Carbon/MoO_2 catalysis and to develop a well-defined structure-activity-selectivity description of the C/MoO_2 surface sites, graphene-based materials, such as graphene oxide (GO) and reduced graphene oxide (rGO) have recently been tested as supports for conventional heterogeneous catalysis and they exhibit tunable surface functionality. Therefore, supporting Mo dioxo complexes on graphitic materials may afford single-site catalysts with informative spectroscopic/structural and catalytic performance properties. In this section we describe a novel reduced graphene oxide (rGO) supported single-site molybdenum dioxo catalyst characterized by Mo EXAFS and backed by DFT computation. It was seen from EXAFS and DFT that the structure had a four-coordinate Mo center with two single -CO-Mo bonds and two Mo=O multiple bonds. This structural study strongly enhances the fundamental understanding of carbon-supported MoO_2 catalysts and their chemistry.

7.1.2 Experimental Methods

Sample preparation

In brief, to prepare rGO/MoO_2, direct grafting of the precursor onto rGO was employed. rGO was weighed into a Schlenk flask, dried under vacuum overnight was then attached to a N_2 line. Dry dichloromethane was added to the flask to disperse the rGO. In a glove box, (dme)MoO_2Cl_2 was added into a second Schlenk flask. The flask was removed from the glove box and attached to a Schlenk line under N_2. Dichloromethane was added to dissolve the (dme)MoO_2Cl_2 and the solution was then filtered into the Schlenk flask containing rGO. After the mixture was stirred at room temperature overnight, the supernatant solution was removed, and the solid product was washed with dichloromethane and finally vacuum dried overnight. The sample was prepared by Yiqi Liu from the Northwestern University Chemistry group of Prof. Tobin Marks.

XANES and EXAFS

X-ray absorption near edge structure (XANES) and extended X-ray absorption fine structure (EXAFS) measurements at Mo K-edge (20,000 eV) were performed at the 5 BM-D beamline of the DND-CAT at the Advanced Photon Source. A double Si (111) monochromator was used for energy selection with energy resolution of $\Delta E/E = 1.4\times10^{-4}$. The X-ray energy was calibrated using a metallic Mo foil (EXAFS Materials). The incident X-ray intensity was measured by a spectroscopy-grade ionization chamber (FMB-Oxford) filled with 600 He/100 N_2 (Torr) and was detuned to 60 % of its maximum for harmonic rejection. The powder catalyst rGO/MoO_2 with a loading of 1.3 wt% was pressed into a sample holder for the EXAFS measurements. The EXAFS spectra were collected in fluorescence mode using a passivated implanted planar silicon (PIPS) detector (Canberra). The sample and the detector were positioned 45° and 90°, respectively, to the X-ray beam direction. For data analyses, two standard reference materials were used: powder

(dme)MoO_2Cl_2 and [(2,4,6-tri-tBu)$C_6H_2O]_2MoO_2$ (denoted as Ref1), which were measured in transmission mode. The transmitted intensity was measured using an identical ionization chamber filled with 1150 He/250 N_2 (Torr) placed behind the sample. Energy scans were executed from 260 eV below to 750 eV above the Mo K edge which produces the EXAFS spectra up to the wavenumber of 14 $Å^{-1}$. The Mo foil spectrum was collected simultaneously for each energy scan using a third ionization chamber filled with 760 Torr Ar. The XAS measurements were done under inert Argon environment. The XANES spectra of (dme)MoO_2Cl_2, Ref1, and the rGO/MoO_2 catalyst are shown in Fig 7.1. The structure of Ref1 is the closest to that of the catalyst, and thus was used as the reference for the experimental Mo-O phase shift and back-scattering amplitude. XANES data extraction, normalization, and background subtraction were performed using the software Athena. EXAFS data analysis was done using the software Artemis. The EXAFS analysis fitted results are shown in Table 7.1. The bond lengths (R) and coordination number (N) were obtained by a least-square fit in the R-space of the nearest neighbors using k_2-weighted Fourier transform fitting parameter. The standard deviations in the EXAFS-determined bond lengths came from the standard python error analysis procedure and are given in parentheses accompanying each bond length where (1) signifies +/- 0.01 Å.

In the EXAFS fitting analysis various parameters, (which can either be guess or set) are used. These parameters are used to set up a fitting model consisting of an amplitude term, a ΔE_0 shift, a ΔR for each path, and a correlated Debye-Waller factor $\Delta\sigma^2$ for each path. The energy shift parameter, ΔE_0, is used to align the theoretical calculated spectrum to the energy grid of the measured spectrum. The edge energy E_0 is determined in ATHENA during the data reduction steps. These steps that ATHENA carries out are as follows[79]:

- Converts the measured intensities to $\mu(E)$

- Subtracts a smooth pre-edge function from μ(E)
- Identifies the threshold energy E_0, which is roughly energy of maximum derivative of μ(E)
- Normalizes μ(E) to go from 0 to 1
- Removes a smooth post-edge background function to approximate $\mu_0(E)$
- Isolates the EXAFS χ(k), where $k = (2m(E - E_0)/\hbar^2)^{1/2}$ and Fourier transforms into R-space.

During the fitting process, for each scattering path, the Debye-Waller factor has been allowed to vary and an average value of 0.001 $Å^2$ is obtained after the fitting procedure is complete. For each path the Debye-Waller factor is within 0.001 +/- 0.0005 $Å^2$. The individual Debye-Waller factors for each path are added in Table 7.1.

We have considered many different probable models to fit the EXAFS results and the model presented in this work is the preferred model that gives the best fit and agrees with DFT and other characterization methods. The models that were compared had different coordination numbers (N) for each type of bond (Mo-O and Mo=O) and had varying ΔR for each path. Among all the models, the model shown here gave the best fitted curve and the lowest statistical error. The various models were quantitatively compared in a statistical way by calculating the R-factor. This calculation of the statistical R-factor in ARTEMIS is as follows[117]:

$$R = \frac{\sum_{i=min}^{max}[\mathrm{Re}(\chi_d(r_i) - \chi_t(r_i))^2 + \mathrm{Im}(\chi_d(r_i) - \chi_t(r_i))^2]}{\sum_{i=min}^{max}[\mathrm{Re}(\chi_d(r_i))^2 + \mathrm{Im}(\chi_d(r_i))^2]}$$

where *d* represents "data" and *t* represents theoretical "fitted values".

The model shown here has an R value of 0.004 which was the lowest that we obtained amongst all the models that were tried. Alternate models had the following R-factors:

One Mo-O and two Mo=O bonds (after optimizing the bond lengths ΔR): R-factor of 0.01

Two Mo-O and one Mo=O bonds (after optimizing the bond lengths ΔR): R-factor of 0.02

Three Mo-O and two Mo=O bonds (after optimizing the bond lengths ΔR): R-factor of 0.08

The fitting parameters that were used to set up a model were an amplitude term, an E_0 shift, a ΔR for each path, and a correlated Debye-Waller factor $\Delta\sigma^2$ for each path. The Debye-Waller factor was limited to only positive values. ΔR for each path was allowed to change freely. The amplitude for each path was also a free parameter and for each path it came out to be ~1. In our parameter set the free parameters were amplitude, ΔR, coordination number and $\Delta\sigma^2$. Once each parameter was optimized, that parameter was fixed thus limiting the number of free parameters to get the best possible fit.

7.1.3 Results and Discussion

rGO/MoO_2 EXAFS: The EXAFS fitting results revealed that rGO/MoO_2 has two Mo=O bond distances of 1.69(3) Å and two Mo-O bond distances of 1.90(3) Å (Table 7.1). This is similar to the EXAFS data reported for the previously synthesized AC/MoO_2 catalyst[118]. Therefore, rGO/MoO_2 and AC/MoO_2 have very similar active-site structures, and it is reasonable to assume that rGO/MoO_2 can serve as a representative model for this Carbon/MoO_2 catalytic system. Furthermore, the EXAFS metrical data are in excellent agreement with those of the model compound as well as the DFT results. Moreover, the EXAFS data show that the catalyst structure is unchanged upon heating overnight at 150 °C, demonstrating the thermal stability of rGO/MoO_2.

rGO/MoO_2 Model Compound Structure. To obtain a further understanding of the rGO/MoO_2 structure, $[(2,4,6\text{-tri-tBu})C_6H_2O]_2MoO_2$ was chosen as a model. The four-coordinate isostructural geometry has two Mo=O bond distances of 1.69 (8) Å and two Mo-O bond distances of 1.85 (7) Å, in accord with the experimental EXAFS and computed DFT results (Table 7.2). Comparing the bond lengths of the model compound to that of rGO/MoO_2, it can be concluded that there is a very

strong similarity, and that this well-defined four-coordinate model further supports the proposed rGO/MoO_2 catalyst structure.

(dme)MoO_2Cl_2 precursor structure: EXAFS rand DFT results indicate Mo=O distances of 1.70 Å and 1.71 Å (Table 7.1).

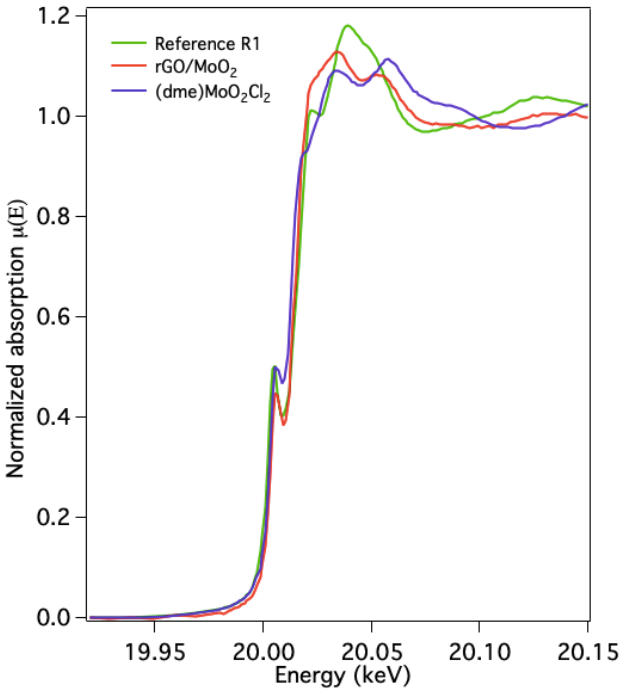

***Figure 7.1**. Mo K-edge XANES for Reference R1, (dme)MoO_2Cl_2, and rGO/MoO_2.*

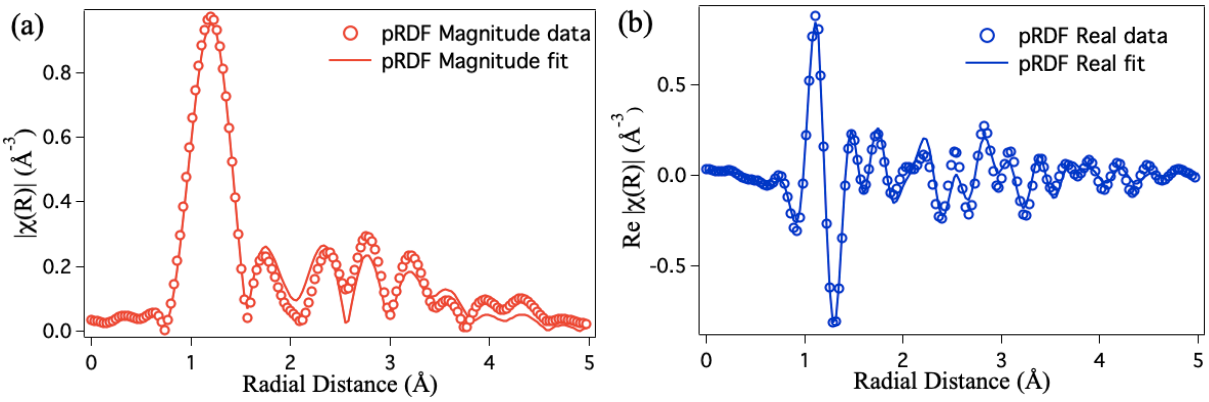

***Figure 7.2.** Mo K-edge EXAFS derived pRDFs of rGO/MoO_2 **(a)** Magnitude FT **(b)** Real FT*

Table 7.1. *EXAFS fitting results for rGO/MoO_2, the precursor, standard samples and reference samples.*

Sample	Edge Energy (keV)	Bond type	N	R (Å)	$\Delta\sigma^2$ (x 10^{-3} Å^2)	ΔE_0 (eV)
Mo foil	20.000	--	--	--	--	--
Reference R1	20.004	Mo=O	2	1.70(2)	0.9	6
		Mo-O	2	1.88(2)	1.5	6
		Mo-C	6	3.2-3.4	1.7	7
(dme)MoO_2Cl_2	20.002	Mo=O	2	1.70(2)	1.2	2
		Mo-O	2	2.25(2)	1.4	2
		Mo-Cl	2	2.35(3)	1.8	3
rGO/MoO_2 (raw)	20.004	Mo=O	2	1.69(3)	0.9	7
		Mo-O	2 0.1	1.90(3) 2.25(3)	1.3	7
		Mo-C	6	2.9-3.3	1.7	8
rGO/MoO_2 (heat treated)	20.004	Mo=O	2	1.69(3)	0.9	7
		Mo-O	2 0.1	1.90(3) 2.25(3)	1.3	7
		Mo-C	6	2.9-3.3	1.7	8
^{118}AC/MoO_2	19.995	Mo=O	2	1.68(2)	0.9	6
		Mo-O	1 1	1.98(2) 2.29(2)	1.4 1.3	6

Table 7.2. *Comparison between EXAFS results and DFT calculated bond lengths*

Sample	Bond Type	Bond Number	Bond Length (Å)	
			EXAFS	DFT
(dme)MoO_2Cl_2	Mo=O	2	1.70(2)	1.71
[(2,4,6-tri-^{t}Bu)C_6H_2O]$_2MoO_2$	Mo=O	2	1.70(2)	1.72
	Mo-O	2	1.88(2)	1.88
rGO/MoO_2	Mo=O	2	1.69(3)	1.71 ; 1.72
	Mo-O	2 0.1	1.90(3) 2.25 (3)	1.91 2.25

DFT Computation. To complement the experimental results, DFT calculations were carried on an rGO/MoO_2 model (Figure 7.3c). DFT calculations were carried out by Dr. Yosi Kratish from the Northwestern University Chemistry group of Prof. Tobin Marks. The calculations reveal that rGO/MoO_2 has two 1.71 Å/1.72 Å Mo=O bonds and two 1.91 Å Mo-O bonds and some scattered long-range Mo-O bond with H_2O with a bong length of 2.25 Å. All of this is in good agreement with the EXAFS data (Table 7.2). Furthermore, the Mo-C interaction is detected via Mo-EXAFS, and the experimental bond length is in the range of 3.1-3.3 Å, which is in good agreement with the DFT model, indicating that sufficient carbon atoms are included in the present DFT model.

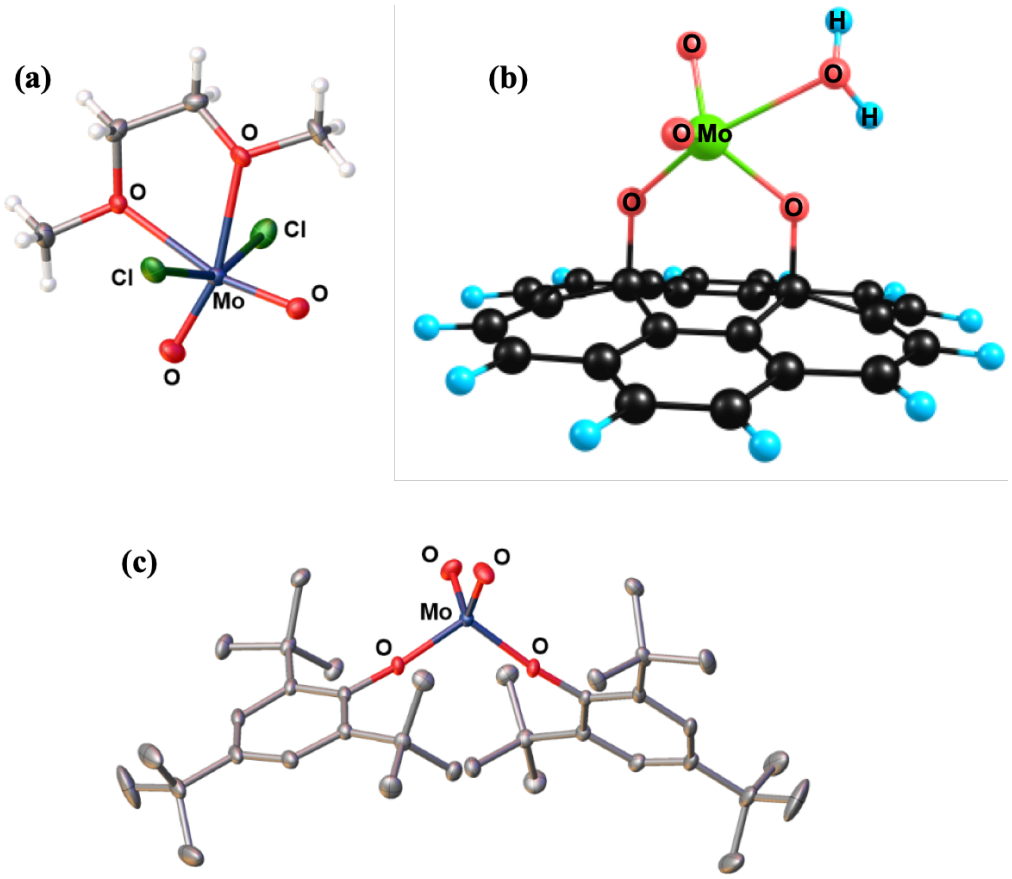

Figure 7.3. (a) *Crystal structure of (dme)MoO_2Cl_2 precursor* ***(b)*** *DFT model of rGO/MoO_2 structure* ***(c)*** *Crystal structure of [(2,4,6-tri-tBu)$C_6H_2O]_2MoO_2$ model compound*

7.1.4 Conclusion

The graphitic carbon-supported single-site catalyst, rGO/MoO_2, was synthesized and characterized in detail both experimentally and computationally. Mo=O and Mo-O bond lengths of 1.69(3) Å and 1.90(3) Å, respectively, are obtained from EXAFS. These experimental data align well with DFT computational results as well as model compound single-crystal data, affording detailed structural understanding of single-site Carbon/MoO_2 catalysts and demonstrating their potential in future catalyst design, new reaction modalities, and structure-function studies. Overall, rGO/MoO_2 shows promise as a well-defined, efficient, and scalable catalytic system.

7.2 MoO_2 / Activated Carbon

7.2.1 Introduction

Alcohol dehydration enables the conversion of alcohols to olefins with oxygen atom removal and is of particular significance in the context of bio-intermediates conversion. As an endothermic reaction, alcohol dehydration requires elevated temperatures and the presence of a catalyst, and therefore clear understanding of the reaction mechanism mediated by an efficient catalyst is of crucial importance. Many catalytic systems have been developed since the debut of this reaction in publications and subsequent industrialization, among which groups VI and VII metal oxo species, *e.g.,* Mo, W, Re, have provided excellent performance. In this section we discuss the surface structural characterization and mechanism of a single-site Mo-dioxo catalyst supported on activated carbon, which rapidly and selectively mediates the dehydration of a broad spectrum of tertiary and secondary alcohols under mild conditions. Architecture and electronic structure are deduced by XANES and EXAFS, supported by DFT computation, which probes electronic structure, the nature of Mo binding to the carbon surface, and the details by which this single-site heterogeneous oxo catalyst efficiently mediates the dehydration of diverse alcohols[119-125].

7.2.2 Experimental Methods

Sample preparation

In brief, a Schlenk flask was charged with solid (dme)MoO_2Cl_2 in a glove box, then removed from the glovebox and attached to a Schlenk line. Under N_2 atmosphere, anhydrous dichloromethane was added to the flask forming a colorless solution. Under N_2 atmosphere, anhydrous dichloromethane was added to another flask containing pre-dried activated carbon. Then the

MoO_2Cl_2(dme) solution was cannulated into the second flask with the activated carbon suspension. The resulting suspension was stirred gently for 18h at room temperature. The supernatant solution was filtered off and the filtrate was washed with anhydrous DCM and dried in vacuum overnight to obtain the AC/MoO_2 sample. The sample was prepared by Dr. Jiaqi Li from the Northwestern University Chemistry group of Prof. Tobin Marks.

XANES and EXAFS

X-ray absorption near edge structure (XANES) and extended X-ray absorption fine structure (EXAFS) measurements were conducted at the 5 BM-D beamline of the DND-CAT at the Advanced Photon Source. Measurements were performed at Mo K-edge (20.00 keV). For energy selection, a double Si (111) monochromator was used which has a resolution of $\Delta E/E = 1.4\times10\text{-}4$. The X-ray energy was referenced to a metallic Mo foil (EXAFS Materials) whose spectrum was collected simultaneously for each energy scan. The incident X-ray intensity was measured in an ionization chamber (FMB-Oxford) filled with 600 Torr He/100 Torr N_2 and was detuned to 60 % of its maximum intensity for harmonic rejection. The Mo foil was measured using an ionization chamber filled with 760 Torr Ar. The powder catalyst AC/MoO_2 with a loading of 2 wt% were pressed into a sample holder for the EXAFS measurements. The absorption spectroscopy data were collected in fluorescence mode using a passivated implanted planar silicon (PIPS) detector (Canberra). The sample was positioned at 45° and the detector at 90° to the incident X-ray beam direction. For data analyses, two standard reference materials were used: MoO_3 and [(2,4,6-tri-tBu)C_6H_2O]$_2MoO_2$ (denoted as Ref1), which were measured in transmission mode (Figure 7.4). The transmitted X-ray intensity was measured using an ionization chamber filled with 1150 Torr He/250 Torr N_2 placed behind the sample. Energy scans were excuted from 300 eV below to 750 eV above the Mo K edge. For EXAFS analyses, the Demeter:Artemis software was used and the

MoO_3 standard was used for EXAFS phase and amplitude calibration. The data fittings were carried in the R-spcae using the k_2-weighted EXAFS spectra.

7.2.3 Results and Discussion

X-ray Absorption Spectroscopy Analysis. To obtain a more detailed understanding of the surface species, i.e., catalyst-bound organic moieties, that are present along the reaction coordinate and gain "molecular-level" understanding of this heterogeneous system, thorough XANES/EXAFS analyses were conducted over a set of AC/MoO_2 samples. Initial X-ray absorption spectroscopy was carried out with the fresh AC/MoO_2 catalyst. The EXAFS fitting of freshly prepared AC/MoO_2 samples reveals two M=O bonds at a distance of 1.68 Å and two Mo-O bonds at distances of 1.84 Å and 2.53 Å. When the sample was heat treated at 250°C, the longer non-equivalent Mo-O bonds evolved into two Mo-O bonds at a distance of 1.88 Å, suggesting the formation of a more stable Mo species **A** (Table 7.3 entry 1, Figure 7.6 species **A**). This species is used for later EXAFS experiments and for DFT modelling. Next, to mimic the reaction conditions, tert-butanol was added to the AC/MoO_2 then heated to 50°C under Ar. According to the EXAFS analysis, addition of tert-BuOH to the catalyst leads to a decrease in the number of Mo=O bonds from two to one, and to an increase in the number of Mo-O single bonds from two to four (Table 7.3 entry 2, Figure 7.6 species **C**). Interestingly, when the tert-butanol treated sample (species **C**) was heated at 200℃ and placed under vacuum, isobutene was evolved and the original tetrahedral Mo-dioxo structure (species **A**) was regenerated, further supporting the durable nature of this catalyst (Figure 7.7). Lastly, to reconfirm the stability of this AC/MoO_2 catalyst, recycled catalyst was characterized and found to exhibit an identical EXAFS pattern as the fresh catalyst (Table 7.3 entry 3, Figure 7.6 species **recycled A**). Next, since water has demonstrated a substantial role in

the reaction, water was added to the AC/MoO_2 with the goal of detecting a possible interaction between water molecules and the surface Mo species. According to the EXAFS fitting, the water adduct has two Mo=O double bonds at the distances of 1.68 Å and 1.67 Å, three Mo-O bonds at the distances of 1.95 Å, 1.87 Å, and 2.26 Å, and two Mo-O long-range interactions at distances ranging from 3.60 Å to 3.85 Å (Table 7.3 entry 4, Figure 7.6 species **F**). Furthermore, the interaction between the support carbon atoms and Mo was also detected for all samples in the range 3.05-3.75 Å (Figure 7.6, 7.7). Fig. 7.4 shows the Mo K-edge of the species A, the MoO_3 standard and Ref1 standard. Note that the edge positions, defined as the inflection point or the first maximum in the first derivative of the edge, are referenced to that of metal Mo which is at 20,000 eV. On overall the edge shape and position (19990-20020 eV) of the speices A (and others shown in Fig. 7.5) compares well with those of Ref1 and MoO_3, implying that the Mo ions in the AC/MoO_2 samples are of Mo(VI). Upon close inspection the sample edge is ~0.6 eV higher than that of Ref1, but ~1.2 eV lower than that of MoO_3. In addition, the leading K edge, following the pre-edge peaks ($1s \rightarrow 4d$), of the species A overlaps with that of the Ref1 standard. We attribute these differences to the variations in the electronic screening conditions[126] around Mo(VI) and argue that the detailed electronic emvironment around Mo(VI) in the sample is closer, probably unsurprsingly, to that around Mo(VI) in the Reference sample 1.

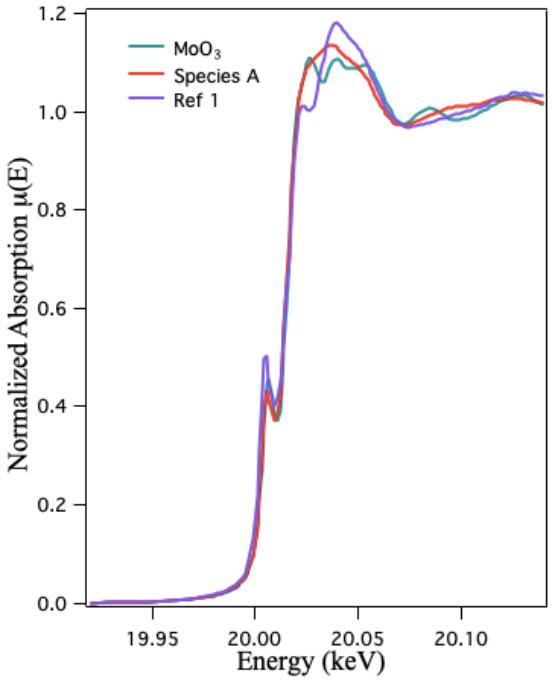

Figure 7.4. *Mo K-edge XANES for AC/MoO_2 species A and the two standards MoO_3 and [(2,4,6-tri-tBu)C_6H_2O]$_2MoO_2$ (Ref 1 standard). The edge positions are referenced to 20,000 eV of metallic Mo.*

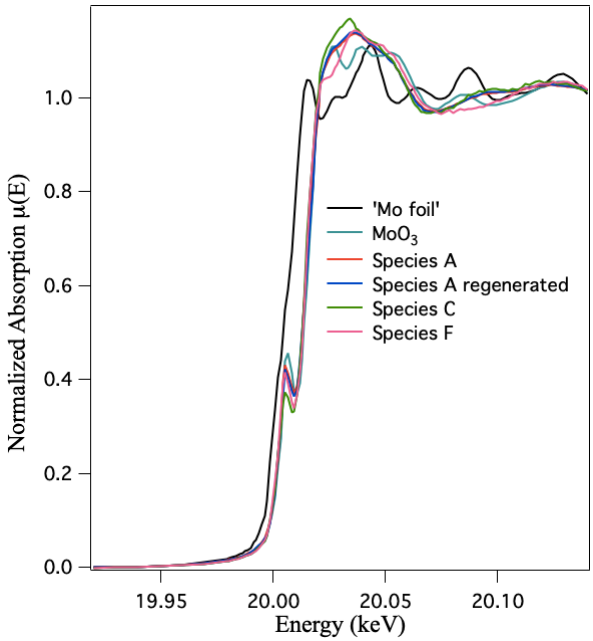

Figure 7.5. *Mo K-edge XANES of species A, C, F, and A (regenerated). Mo(VI) prevails in all the samples.*

Computational Investigation: To shed more light on the reaction mechanism and to understand the role of water molecules in the catalytic cycle, DFT calculations were conducted. On the basis of the precursor structure, the known surface chemistry and XANES/EXAFS results, a tetrahedral Mo(VI)-dioxo species bound through two surface oxygen atoms on a graphene sheet is constructed to model the surface species (Fig. 7.9 complex A). This computed model structure has two Mo=O and two Mo-O bonds at the distances of 1.67 Å and 1.87 Å, respectively (Table 7.3 entry 1), and six Mo-C interactions at distances ranging from 3.0-3.5 Å, which are in good agreement with EXAFS data. Tert-butanol is chosen as the model substrate for catalytic cycle. In the proposed water-assisted pathway, the initial step is alcohol adsorption to the Mo center. In the next step, the alcohol O-H bond is inserted into the Mo=O bond generating a Mo-oxo-hydroxyl-alkoxide. According to DFT, complex **C** has one Mo=O bond at a distance of 1.66 Å, four Mo-O bonds at distances of 1.94 Å, 1.87 Å, 1.89 Å, and 1.85 Å. This structure is supported by EXAFS spectroscopy which is in good agreement with the DFT computed geometry. Supported by the EXAFS results it can be observed that complex **C** can be fully converted to the starting catalyst **A** and isobutylene by heating under vacuum at the end of the reaction, supporting that **C** is an intermediate in the proposed reaction pathway. DFT was used to calculate reaction barriers for all the steps including steps to get complex D and E. We do not have EXAFS data for complexes D and E since it is difficult to isolate these complexes. Interestingly, complex **F** can be also prepared and isolated by adding water directly to AC/MoO_2(Figure 7.6 species **F**), supporting the viability of proposed reaction intermediate **F** in the dehydration reaction.

Furthermore, the experimentally derived structure is in very good agreement with the DFT computed geometry, demonstrating the validity of the applied DFT model. Overall, the good

agreement between the experimental and computational data, argue for the water-assisted AC/MoO_2 catalyzed alcohol dehydration mechanism, as shown in Fig. 7.9 (a).

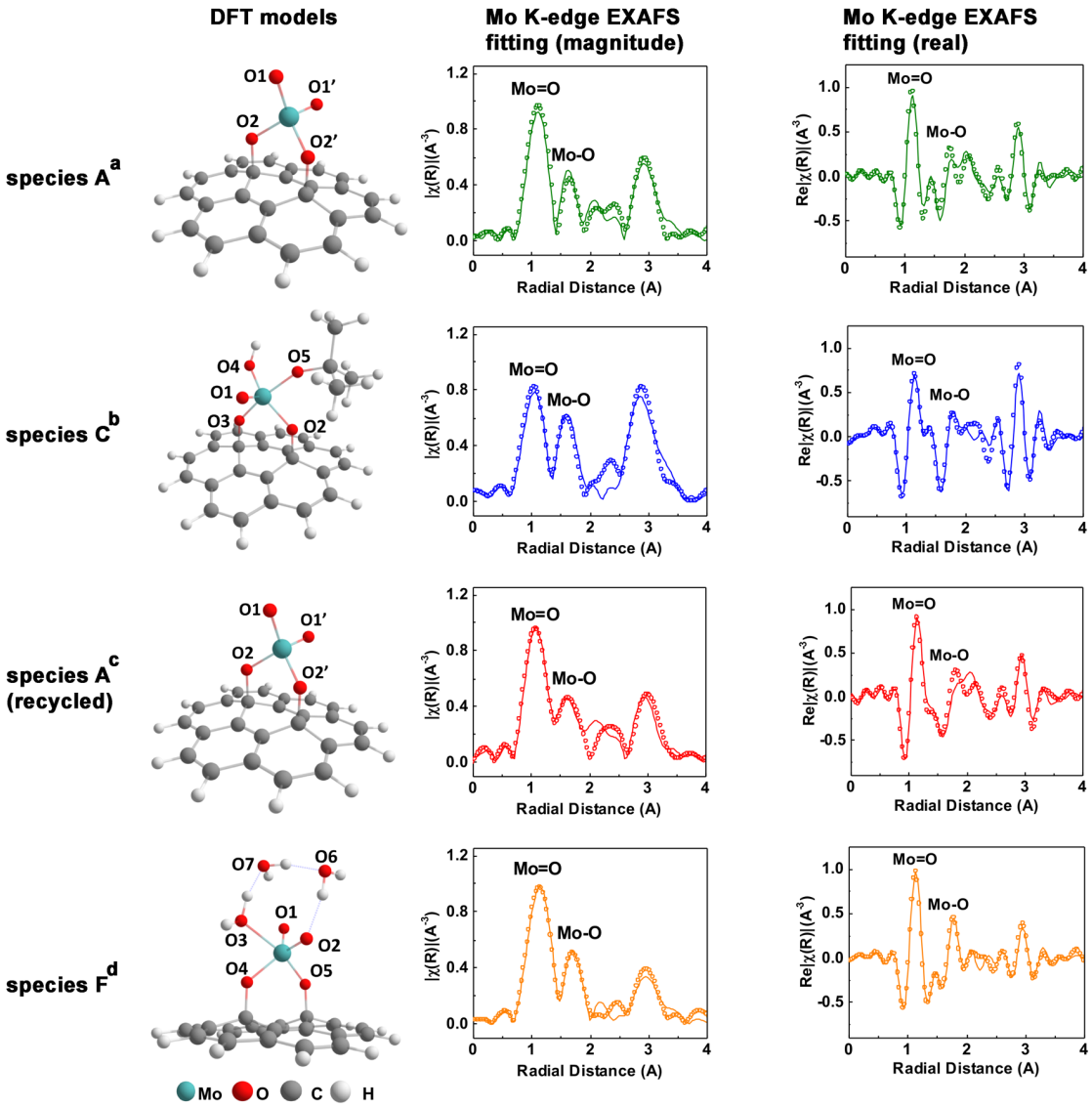

Figure 7.6. *DFT models and Mo K-edge EXAFS fitting results (pRDF magnitude and real part; experimental: dots, fitting: lines where all fittings are normalized to one standard) of the AC/MoO_2 surface species. Sample treatment conditions:* ***(a)*** *250 ℃ vacuum.* ***(b)*** *60 mg AC/MoO_2, 2.0 mL tert-butanol, 400 rpm, 50 ℃, under Ar.* ***(c)*** *recycled via filtration, wash, and dry.* ***(d)*** *60 mg AC/MoO_2, 0.5 mL deionized water.*

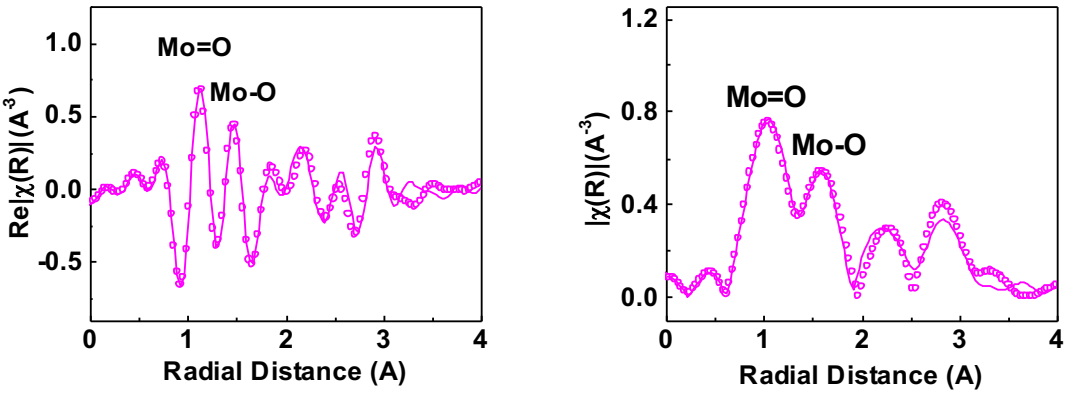

Figure 7.7*. Mo K-edge EXAFS fitting results (pRDF real part on the left and magnitude on the right) of the tert-butanol and vacuum treated AC/MoO_2 surface species. Experimental data is shown in dot and the fitting is in line.*

Table 7.3. *Mo K-edge EXAFS fitting data and DFT modelling results for AC/MoO_2 surface species.*

Entry	Species	Number of bonds	Bond length (Å)	
			EXAFS	DFT
1	A	2 (Mo=O1)	1.68(2)	1.67
		2 (Mo-O2)	1.88(2)	1.87
2	C	1 (Mo=O1)	1.67(3)	1.66
		1 (Mo-O2)	1.93(2)	1.94
		1 (Mo-O3)	1.87(3)	1.87
		1 (Mo-O4)	1.88(3)	1.89
		1 (Mo-O5)	1.85(3)	1.85
3	recycled A	2 (Mo=O1)	1.69(2)	1.67
		2 (Mo-O2)	1.88(2)	1.87
4	F	1 (Mo=O1)	1.67(3)	1.69
		1 (Mo=O2)	1.68(3)	1.70
		1 (Mo-O3)	2.26(3)	2.18
		1 (Mo-O4)	1.95(3)	1.93
		1 (Mo-O5)	1.87(3)	1.88
		2 (long range Mo-O interaction, with O6 and O7)	3.60-3.85	3.69-3.79

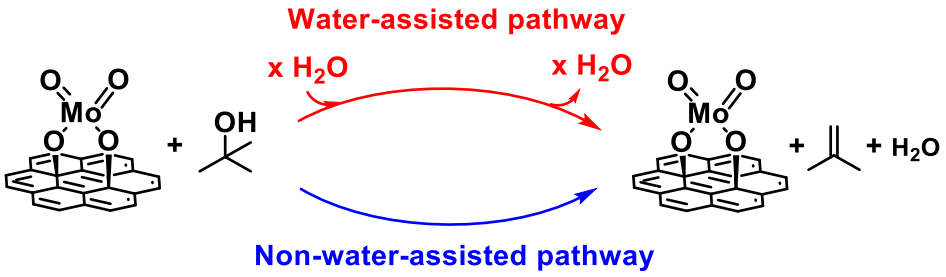

Figure 7.8. *Plausible alcohol dehydration pathways.*

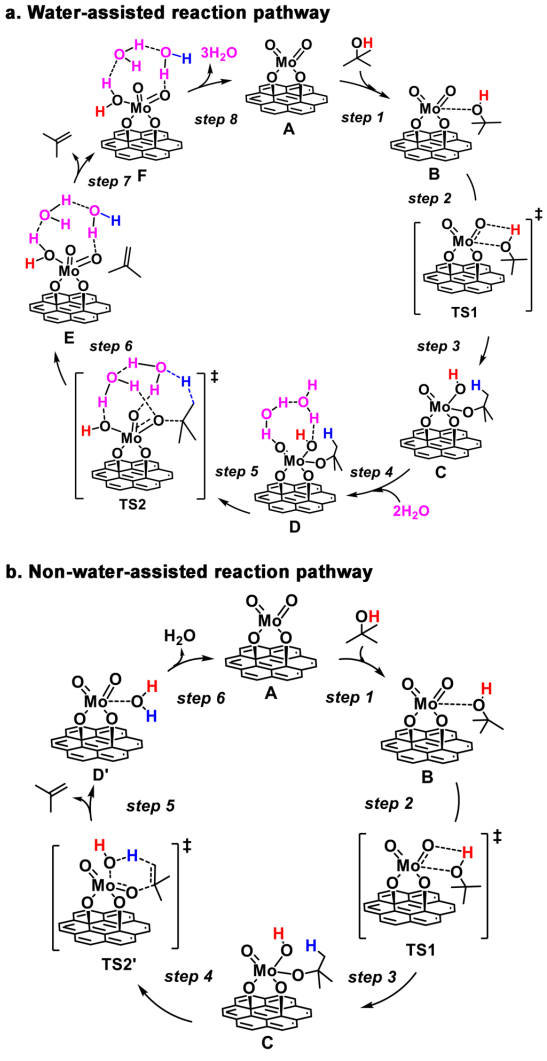

Figure 7.9. *Reaction mechanism for tert-butanol dehydration,* ***(a)*** *water-assisted and* ***(b)*** *non-water-assisted pathways catalyzed by AC/MoO_2.*

7.2.4 Conclusion

A heterogeneous single-site Mo-dioxo catalyst is reported for efficient and versatile alcohol conversions. AC/MoO_2 lies at the intersection of traditional heterogeneous and homogeneous catalysis, which allows us to gain “molecular-level” understanding of a versatile heterogeneous catalyst and to shed light on new reaction pathways. With a combined experimental and computational study, an in-depth understanding of the surface species is achieved, and a water-assisted reaction pathway is elucidated for the lowest energy barrier mechanism. Overall, this structurally and mechanistically well-defined single-site molybdenum-dioxo species serves as a catalytically efficient and economically effective catalyst, while providing crucial insights into rational catalyst design.

Chapter 8

Summary and Future Directions

8.1 Summary

Vanadium and molybdenum oxides are extremely interesting because of their wide application in many catalytic processes of industrial relevance belonging to redox or acid-base processes. There are several factors responsible for the catalytic behavior such as the mobility of surface/lattice oxygen atoms, the existence of Lewis acid-base sites as well as different reactivity of different crystal faces. The knowledge of the structural properties of these oxides is necessary to understand their physical and chemical behavior. In single valency oxides of both vanadium and molybdenum the building units are distorted MeO_6 octahedra linked by corners or/and edges. The richness of arrangements of these octahedra is a source for the existence of differently coordinated oxygen ions and has an important impact for surface properties of the oxide systems. In-spite of the importance of vanadium and molybdenum oxides as catalytic materials, many details of their atomic behavior are still unknown.

The focus of this thesis work has been to study the atomic-scale structure of supported vanadium and molybdenum oxide catalysts and to better understand the structure-function relationship through various X-ray characterization techniques. The UHV X-ray scattering and spectroscopy surface analysis endstation at DND-CAT sector 5ID-C at the Advanced Photon Source was integrated with a Specs Phoibos 150HV hard X-ray photoelectron spectrometer. This set-up was used for conducting XSW excited XPS measurements to map oxide supported atomic species in

distinctive chemical states with sub-angstrom resolution. Prior to adding the XPS detector, the instrument was limited to element-specific atomic imaging via XSW excited XRF which generated atomic density maps not sensitive to the chemical state of the absorbing atom. This integration helped us in understanding the structural and chemical changes during a catalytic reaction doing in-situ redox reaction studies, thus helping in understanding complicated reaction mechanisms. Another novel opportunity was to map the changes in surface oxygen atoms in the supported vanadium and molybdenum oxide catalysts that gave us composite 3D atomic maps of the catalyst/support interface. (Note that XSW excited XRF is not able to detect surface oxygens or other low-Z atoms due to a weak signal.) In this thesis work, we also used the unique I09 beamline at the Diamond Light Source which had the capability of both soft X-ray and hard X-ray converging into the same experimental chamber thus giving us the unique opportunity to simultaneously do high resolution soft XPS and higher energy XSW-XPS studies. These experimental results coupled with DFT calculations gave unique insights into oxide supported vanadium and molybdenum oxide catalysts. Another interesting work in this thesis focused on studying the coordination environment of powder molybdenum oxide catalysts supported on various carbon supports. For this study X-ray absorption spectroscopy was used which involved both XANES and EXAFS analysis to give coordination and bond lengths of different Mo-O bonds. This ability to study the structure of reaction intermediates helped in identifying reaction pathways that were being followed. These experimental results were further supported by DFT calculations which provided a theoretical background and helped explaining the redox induced structural changes.

These atomic-scale surface studies combined with catalytic reaction studies will lead to the designing of more selective, energy saving, durable, intrinsically clean and safer catalytic materials which will reduce waste and by-product production.

8.2 Ongoing and Future directions

X-ray standing wave excited X-ray photoelectron spectroscopy method can be used in many unique experiments. This thesis work has explored some of those capabilities. However, there are many more avenues and materials of interest that can be explored. One can use XSW-XPS to study redox induced changes of surface oxygens on a clean oxide surface, such as α-TiO_2 (110). This would help in understanding the larger picture of oxide surfaces supporting a sub-monolayer catalyst.

XSW-XPS study of supported bimetallic nanoparticles

Bimetallic nanoparticles are attracting increased attention for novel solid-state properties applicable to catalysis, sensing and magnetic storage. Specifically, Au based bimetals are of great interest due to their optical and catalytic properties. Bimetallic Au–Cu on TiO_2 is highly active and selective towards propene epoxidation by nitrous oxide and several other important catalytic reactions. XSW excited XPS has the unique capability of measuring the distribution of Au and Cu atoms relative to the TiO_2 substrate lattice with sub-Å resolution and chemical state specificity. Studying the as-grown, oxidized and reduced surface and alloy-substrate interface for these supported AuCu nanoparticles will help explain complex catalytic reactions and in turn optimize their catalytic properties. Supports which exhibit strong structural epitaxy to a particular bimetallic phase will stabilize this phase near the interface. In turn, this will precisely control surface structures by inducing metal segregation either towards or away from the particle-support interface[127].

Inspecting redox induced changes in AuCu layer grown on α-TiO_2 (110) substrate will enable more detailed structural study of this catalytic material. The effectiveness of combining ensemble-averaged X-ray information with LEED and STM will be significant in obtaining novel results important in understanding the complex catalytic reactions of the supported AuCu system. Due to the complexity of experimental studies on this heterogeneous catalytic system, the microstructure and electronic structure of the AuCu/TiO_2 interface have mostly been studied only theoretically based on the framework of density functional theory. DFT calculations showed that the modification in which an Au co-catalyst is replaced with a bimetallic AuCu co-catalyst to build a TiO_2-based composite photocatalyst not only enhances the interaction of the metal layer with the TiO_2 substrate, but also promotes electron transfer and charge separation across the interface. The calculation results of the interfacial structures provided a possible range for the interface spacing of each hetero-structure, and showed that the m/TiO_2 [m=Au, Cu and AuCu] heterostructures with an interface spacing greater than 3 Å cannot be formed. AuCu/ TiO_2 has smaller interface spacings as compared to Au/TiO_2 which may be related to the stronger interaction of the AuCu layer with the TiO_2 substrate[128-129].

Previous structural and electronic experimental studies have mostly focused on ex-situ XPS (Fig 8.1(a,b)), XRD (Fig 8.1(c)), STEM (Fig 8.2(a)) and HRTEM (Fig 8.2(b)). These studies have not been able to resolve the structure along surface normal and distinguish the distribution of each oxidation state of Au and Cu. XSW-XPS has the unique capability of measuring the distribution of Au and Cu atoms relative to the substrate TiO_2 lattice with both sub-Å spatial resolution and chemical state specificity. It will be a uniquely powerful way to determine the structure of the buried alloy-support interface. This will also help to investigate the changes in the surface structure

during in-situ oxidation and reduction reactions. Hence this structural information will help to better understand and optimize the catalytic properties of the material.

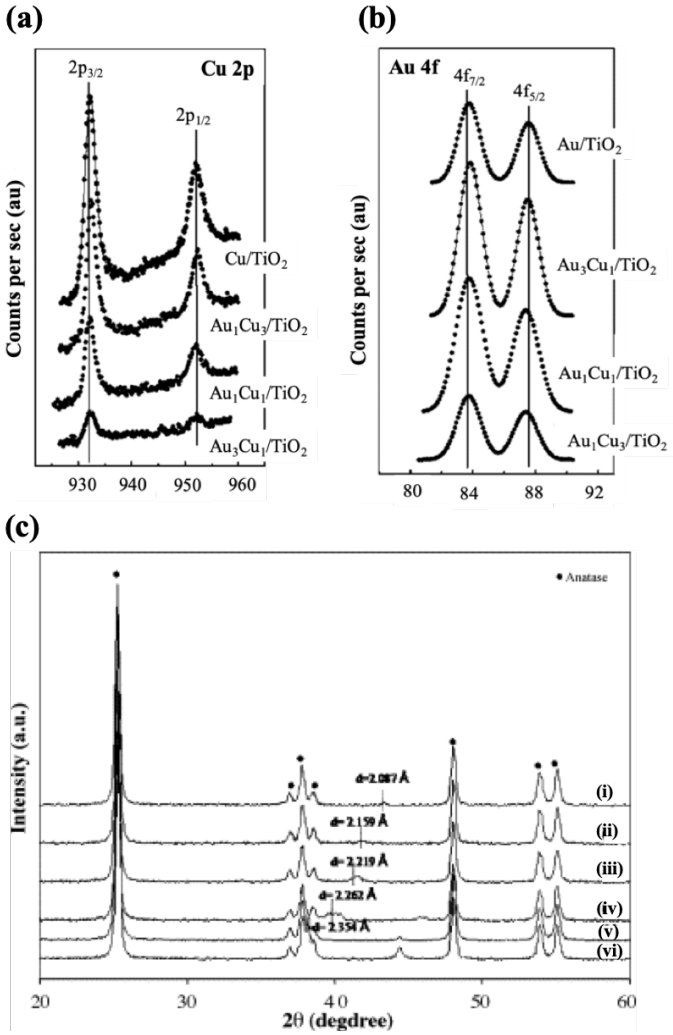

Figure 8.1. *(a) Cu 2p and (b) Au 4f XPS spectra of 4% Cu/TiO_2, 4% Au / TiO_2 and 4% Au–Cu / TiO_2 catalysts (c) XRD patterns of (i) 4% Cu / TiO_2, (ii) 4% Au_1Cu_3 / TiO_2, (iii) 4% AuCu / TiO_2, (iv) 4% Au_3Cu_1 / TiO_2, (v) 0.5% Au / TiO_2 and (vi) 4% Au / TiO_2* [130]

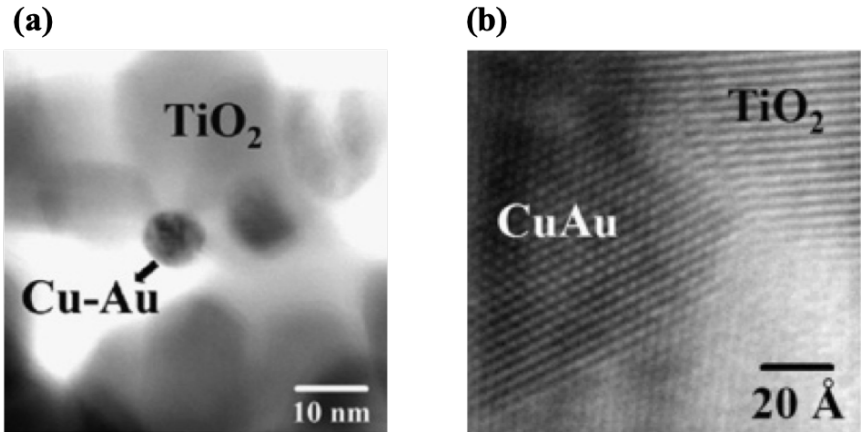

Figure 8.2. *(a) STEM image and (b) HRTEM image of catalyst 4% AuCu / TiO_2*[130]

Site-specific valence band structure via XSW excited photoemission

Another novel direction is the study of site-specific surface atom valence band structure via x-ray standing wave excited photoemission. Pt on $SrTiO_3$ is an important catalytic system for water-splitting photocatalysis. As Pt layers are reduced down to several atomic layers in nanocrystals, a larger fraction of the Pt atoms are at the interface which strongly influences catalytic properties. While much research focuses on the Pt catalyst application, there are still open questions over the atomic and electronic properties, especially at the catalyst/support interface. We have used XSW-XPS to measure site-specific valence band for ½ ML Pt grown on $SrTiO_3$ (001) substrate. Dr. Yanna Chen from our research group has been leading this project. The XSW induced modulations in the core level (CL) and VB photoemission from the surface and substrate atoms were monitored for three hkl substrate Bragg reflections. The XSW CL analysis showed the Pt to have an fcc-like cube-on-cube epitaxy with the substrate. The XSW VB information compared well to a density functional theory calculated projected density of states from the surface and substrate atoms. This site-specific valence band spectroscopy represents a novel method for determining the contribution to the density of states by valence electrons from specific atomic surface sites. In future works, the

focus would be on investigating the changes in the site-specific valence band upon in-situ oxidation and reduction of the Pt film. Presently, we have the capability and set-up to make such measurements for monolayer coverages of high-Z elements such as Pt or Au with the use of 3rd generation synchrotron x-ray sources. The predicated 10^2 gain in brightness from the 4th generation synchrotron sources coming on line would make it possible to apply this method to monolayer coverages of lower-Z elements[131].

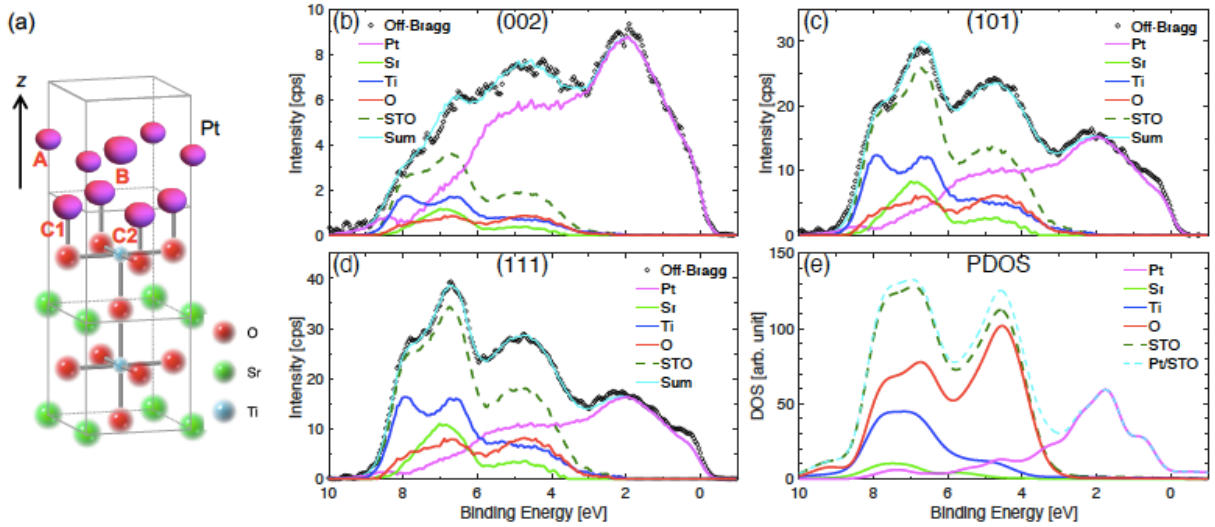

Figure 8.3. *(a) Model-independent XSW measured 3D Pt atomic distribution relative to the STO unit cell shown with a TiO_2 terminated STO (001) surface. A, B, and C1(C2) refer to the three symmetry-inequivalent Pt sites. (b-d) The collected off-Bragg VB spectra and separated components from (b) (002), (c) (101), and (d) (111) $SrTiO_3$ Bragg reflections. (e) DFT calculated projected density of states (PDOS) of the Pt/STO valence band*[131].

These future directions of the XSW-XPS method have great prospects and can lead to a high impact understanding of metal-support interfaces for various functionalized crystalline surfaces.

References

1. Hossain, S. T.; Almesned, Y.; Zhang, K.; Zell, E. T.; Bernard, D. T.; Balaz, S.; Wang, R., Support structure effect on CO oxidation: A comparative study on SiO2 nanospheres and CeO2 nanorods supported CuOx catalysts. *App. Surf. Sci.* **2018,** *428*, 598-608.

2. Henrich, V. E.; Cox, P. A., The Surface Science of Metal Oxides. *University Press, Cambridge, UK* **1994**, 464.

3. Das, A.; Park, H.; Chen, Y.; Choudhury, D.; Lee, T.-L.; Elam, J. W.; Zapol, P.; Bedzyk, M. J., Atomic-Scale Structure of Chemically Distinct Surface Oxygens in Redox Reactions. *J. Am. Chem. Soc.* **2021,** *143* (43), 17937-17941.

4. Weckhuysen, B. M.; Keller, D., Chemistry, spectroscopy and the role of supported vanadium oxides in heterogeneous catalysis. *Catalysis Today* **2003,** *78*, 25-46.

5. Dulub, O.; Hebenstreit, W.; Diebold, U., Imaging Cluster Surfaces with Atomic Resolution: The Strong Metal-Support Interaction State of Pt Supported on TiO2 (110). *Phys. Rev. Lett.* **2000,** *84*, 3646.

6. Tauster, S. J.; Fung, S. C.; Garten, R. L., Strong metal-support interactions. Group 8 noble metals supported on titanium dioxide. *J. Am. Chem. Soc.* **1978,** *100* (1), 170-175.

7. Diebold, U., The surface science of titanium dioxide. *Surf. Sci.* **2003,** *48*, 53-229.

8. Fujishima, A.; Honda, K., Electrochemical photolysis of water at a semiconductor electrode. *Nature* **1972,** *238*, 37-38.

9. Haider, A. J.; Jameel, Z. N.; Al-Hussaini, I. H. M., Review on: Titanium Dioxide Applications. *Energy Procedia* **2019,** *157*, 17-29.

10. Mele, G.; Sole, R. D.; Lü, X., Applications of TiO2 in sensor devices In *Titanium Dioxide (Tio_2) and Its Applications* Parrino, F.; Palmisano, L., Eds. Elsevier: 2021; Vol. 18.

11. Diebold, U., Structure and properties of TiO2 surfaces: a brief review. *App. Phys. A* **2003,** *76* (5), 681-687.

12. Lam, E.; Luong, J. H. T., Carbon Materials as Catalyst Supports and Catalysts in the Transformation of Biomass to Fuels and Chemicals. *ACS Catal.* **2014,** *4* (10), 3393-3410.

13. Seidel, A.; Bickford, M., *Kirk-Othmer Encyclopedia of Chemical Technology*. John Wiley and Sons: 2004.

14. Bansal, R. C.; Goyal, M., *Activated Carbon Adsorption*. Boca Raton: Taylor & Francis Group: 2005.

15. Marsh, H.; Rodríguez-Reinoso, F., *Activated Carbon*. Elsevier: 2006.

16. Heidarinejad, Z.; Dehghani, M. H.; Heidari, M.; Javedan, G.; Ali, I.; Sillanpää, M., Methods for preparation and activation of activated carbon: a review. *Environ. Chem. Lett.* **2020,** *18*, 393-415.

17. Gao, J.; Liu, D.; Xu, Y.; Chen, J.; Yang, Y.; Xia, D.; Ding, Y.; Xu, W., Effects of two types of activated carbon on the properties of vegetation concrete and Cynodon dactylon growth. *Sci Rep* **2020,** *10*, 14483.

18. Ray, S. C., Application and Uses of Graphene Oxide and Reduced Graphene Oxide. In *Applications of Graphene and Graphene-Oxide Based Nanomaterials*, William Andrew Applied Science Publishers: 2015; Vol. 2, pp 39-55.

19. Kovtyukhova, N. I.; Ollivier, P. J.; Martin, B. R.; Mallouk, T. E.; Chizhik, S. A.; Buzaneva, E. V.; Gorchinskiy, A. D., Layer-by-Layer Assembly of Ultrathin Composite Films from Micron-Sized Graphite Oxide Sheets and Polycations. *Chem. Mater.* **1999,** *11* (3), 771-778.

20. Ganguly, A.; Sharma, S.; Papakonstantinou, P.; Hamilton, J., Probing the Thermal Deoxygenation of Graphene Oxide Using High-Resolution In Situ X-ray-Based Spectroscopies. *The Journal of Physical Chemistry C* **2011,** *115* (34), 17009-17019.

21. Pavoski, G.; Maraschin, T.; Milani, M. A.; Azambuja, D. S.; Quijada, R.; Moura, C. S.; de Sousa Basso, N.; Galland, G. B., Polyethylene/reduced graphite oxide nanocomposites with improved morphology and conductivity. *Polymer* **2015,** *81*, 79-86.

22. Kim, F.; Luo, J.; Cruz-Silva, R.; Cote, L. J.; Sohn, K.; Huang, J., Self-Propagating Domino-like Reactions in Oxidized Graphite. *Adv. Funct. Mater.* **2010,** *20* (17), 2867-2873.

23. Luo, J.; Cote, L. J.; Tung, V. C.; Tan, A. T. L.; Goins, P. E.; Wu, J.; Huang, J., Graphene Oxide Nanocolloids. *Journal of the American Chemical Society* **2010,** *132* (50), 17667-17669.

24. Liu, Y.; Li, J.; Das, A.; Hacksung, K.; Jones, L. O.; Ma, Q.; Kratish, Y.; Bedzyk, M. J.; Schatz, G.; Marks, T., Synthesis and Structure–Activity Characterization of a Single-Site MoO2 Catalytic Center Anchored on Reduced Graphene Oxide. *J. Am. Chem. Soc.* **2021,** *143* (51), 21532–21540.

25. Liu, Y.; Li, J.; Das, A.; Hacksung, K.; Jones, L. O.; Ma, Q.; Kratish, Y.; Bedzyk, M. J.; Schatz, G.; Marks, T., Synthesis, Structural, and Catalytic Characterization of a Single-Site Mo(=O)2 Functionality Supported on Reduced Graphene Oxide. **Under revision**.

26. Gates, B. C., Supported Metal Clusters: Synthesis, Structure, and Catalysis. *Chem. Rev.* **1995,** *95*, 511-522.

27. Weckhuysen, B. M.; Voort, P. V. D.; Gatana, G., *Spectroscopy of Transition Metal Ions on Surfaces*. Leuven University Press: 2000.

28. Bond, G. C., Mechanism of the oxidation of o-xylene to phthalic anhydride. *J. Catal.* **1989,** *116* (2), 531-539.

29. Wachs, I. E., Catalysis science of supported vanadium oxidecatalysts. *Dalton Trans.* **2013,** *42*, 11762-11769.

30. Banas, J.; Najbar, M.; Tomasic, V., Kinetic Investigation of the NO Decomposition over V−O−W/Ti(Sn)O2 Catalyst. *Catal. Today* **2008,** *137*, 267-272.

31. Sambi, M.; Sangiovanni, G.; Granozzi, G.; Parmigiani, F., Early stages of epitaxial growth of vanadium oxide at theTiO2(110) surface studied by photoelectron diffraction. *Phys. Rev. B* **1996,** *54* (19), 13464-13467.

32. Wang, Q.; Madix, R. J., Partial oxidation of methanol to formaldehyde on a model supported monolayer vanadia catalyst: vanadia on TiO2(). *Surf. Sci.* **2002,** *496*, 51-63.

33. Wong, G.; Kragten, D.; Vohs, J., Temperature-programmed desorption study of the oxidation of methanol to formaldehyde on TiO2(110)-supported vanadia monolayers. *Surf. Sci.* **2000,** *452*, 293-297.

34. Bahlawane, N.; Lenoble, D., Vanadium Oxide Compounds: Structure, Properties, and Growth from the Gas Phase. *Chem. Vap. Dep.* **2014,** *20* (7-9), 299-311.

35. Andersson, G., Studies on Vanadium Oxides. *Acta Chem. Scand.* **1954**.

36. Schwarz, G.; Mendel, R. R.; Ribbe, M. W., Molybdenum cofactors, enzymes and pathways. *Nature* **2009,** *460* (7257), 839-847.

37. Hernández-Ruiz, R.; Sanz, R., Dichlorodioxomolybdenum(VI) Complexes: Useful and Readily Available Catalysts in Organic Synthesis. *Synthesis* **2018,** *50* (20), 4019-4036.

38. Karunadasa, H. I.; Chang, C. J.; Long, J. R., A molecular molybdenum-oxo catalyst for generating hydrogen from water. *Nature* **2010,** *464* (7293), 1329-1333.

39. Chakrabarti, A.; Wachs, I. E., Molecular Structure–Reactivity Relationships for Olefin Metathesis by Al2O3-Supported Surface MoOx Sites. *ACS Catalysis* **2018,** *8* (2), 949-959.

40. Shetty, M.; Murugappan, K.; Green, W. H.; Román-Leshkov, Y., Structural Properties and Reactivity Trends of Molybdenum Oxide Catalysts Supported on Zirconia for the Hydrodeoxygenation of Anisole. *ACS Sustainable Chemistry & Engineering* **2017,** *5* (6), 5293-5301.

41. Merle, N.; Le Quéméner, F.; Bouhoute, Y.; Szeto, K. C.; De Mallmann, A.; Barman, S.; Samantaray, M. K.; Delevoye, L.; Gauvin, R. M.; Taoufik, M.; Basset, J.-M., Well-Defined Molybdenum Oxo Alkyl Complex Supported on Silica by Surface Organometallic Chemistry: A Highly Active Olefin Metathesis Precatalyst. *Journal of the American Chemical Society* **2017,** *139* (6), 2144-2147.

42. Pucino, M.; Zhai, F.; Gordon, C. P.; Mance, D.; Hoveyda, A. H.; Schrock, R. R.; Copéret, C., Silica-Supported Molybdenum Oxo Alkylidenes: Bridging the Gap between Internal and Terminal Olefin Metathesis. *Angewandte Chemie International Edition* **2019,** *58* (34), 11816-11819.

43. Lohr, T. L.; Mouat, A. R.; Schweitzer, N. M.; Stair, P. C.; Delferro, M.; Marks, T. J., Efficient catalytic greenhouse gas-free hydrogen and aldehyde formation from aqueous alcohol solutions. *Energy & Environmental Science* **2017,** *10* (7), 1558-1562.

44. Mouat, A. R.; Lohr, T. L.; Wegener, E. C.; Miller, J. T.; Delferro, M.; Stair, P. C.; Marks, T. J., Reactivity of a Carbon-Supported Single-Site Molybdenum Dioxo Catalyst for Biodiesel Synthesis. *ACS Catal.* **2016,** *6* (10), 6762-6769.

45. Liu, S.; Li, J.; Jurca, T.; Stair, P. C.; Lohr, T. L.; Marks, T. J., Efficient carbon-supported heterogeneous molybdenum-dioxo catalyst for chemoselective reductive carbonyl coupling. *Catal. Sci. Technol.* **2017,** *7* (11), 2165-2169.

46. Inzani, K.; Nematollahi, M.; Vullum-Bruer, F.; Grande, T.; Reenaas, T. W.; Selbach, S. M., Electronic properties of reduced molybdenum oxides. *Phys. Chem. Chem. Phys* **2017,** *19*, 9232-9245.

47. *Handbook of Thin Film Deposition*. Elsevier: 2018.

48. George, S. M.; Ott, A. W.; Klaus, J. W., Surface Chemistry for Atomic Layer Growth. *J. Phys. Chem.* **1996,** *100*, 13121-13131.

49. Elam, J. W.; Libera, J. A.; Pellin, M. J.; Zinovev, A. V.; Greene, J. P.; Nolen, J. A., Atomic layer deposition of W on nanoporous carbon aerogels. *App. Phys. Lett.* **2006,** *89*, 053124.

50. Ritala, M.; Leskelä, M., Atomic layer deposition. In *Handbook of Thin Films Materials*, Nalwa, H. S., Ed. Academic Press, San Diego, Calif, USA: 2001; Vol. 1, pp 103-156.

51. Elam, J. W.; Routkevitch, D.; Mardilovich, P. P.; George, S. M., Conformal coating on ultrahigh-aspect-ratio nanopores of anodic alumina by atomic layer deposition. *Chem. Mater.* **2003,** *15* (18), 3507-3517.

52. Badot, J. C.; Ribes, S.; Yousfi, E. B.; Vivier, V.; Pereira-Ramos, J. P.; Baffier, N.; Lincotb, D., Atomic layer epitaxy of vanadium oxide thin films and electrochemical behavior in presence of lithium ions. *Electrochem. Solid-State Lett.* **2000,** *3* (10), 485-488.

53. Puurunen, R. L., A Short History of Atomic Layer Deposition: Tuomo Suntola's Atomic Layer Epitaxy. *Chem. Vap. Dep.* **2014,** *20* (10-12), 332-344.

54. Suntola, T.; Antson, J. Atomic Layer Epitaxy. 1974.

55. Johnson, R. W.; Hultqvist, A.; Bent, S. F., A brief review of atomic layer deposition: from fundamentals to applications. *Mat. Today* **2014,** *17* (5), 236-246.

56. Chang, S. L., Kinematical Theory of Diffraction. In *Multiple Diffraction of X-Rays in Crystals*, Springer, Berlin, Heidelberg: 1984; Vol. 50, pp 35-71.

57. Laanait, N.; Saenrang, W.; Zhou, H.; Eom, C.; Zhang, Z., Dynamic X-ray diffraction imaging of the ferroelectric response in bismuth ferrite. *Adv. Struc. and Chem. Imag.* **2017,** *3* (1).

58. Pateras, A.; Park, J.; Ahn, Y.; Tilka, J.; Holt, M.; Kim, H.; Mawst, L.; Evans, P., Dynamical scattering in coherent hard x-ray nanobeam Bragg diffraction. *Phys. Rev. B* **2018,** *97* (23).

59. Bedzyk, M. J.; Materlik, G., Two-beam dynamical diffraction solution of the phase problem: A determination with x-ray standing-wave fields. *Phys. Rev. B* **1985,** *32* (10), 6456-6463.

60. Batterman, B. W.; Cole, H., Dynamical Diffraction of X Rays by Perfect Crystals. *Rev. Mod. Phys.* **1964,** *36* (3), 681-717.

61. Cheng, L.; Fenter, P.; Bedzyk, M. J.; Sturchio, N. C., Fourier-expansion solution of atom distributions in a crystal using x-ray standing waves. *Phys. Rev. Lett.* **2003,** *90*, 255503.

62. Golovchenko, J. A.; Patel, J. R.; Kaplan, D. R.; Cowan, P. L.; Bedzyk, M. J., Solution to the Surface Registration Problem Using X-Ray Standing Waves. *Phys. Rev. Lett.* **1982,** *49* (8), 560-563.

63. Bedzyk, M. J.; Materlik, G., Determination of the position and vibrational amplitude of an adsorbate by means of multiple-order x-ray standing-wave measurements. *Phys. Rev. B* **1985,** *31*, 4110.

64. Bedzyk, M. J.; Materlik, G., X-ray standing wave analysis for bromine chemisorbed on germanium. *Surf. Sci.* **1985,** *152-153*, 10-16.

65. Bedzyk, M. J.; Fenter, P., XSW Imaging. In *The X-Ray Standing Wave Technique: Principles and Applications*, Zegenhagen, J.; Kazimirov, A., Eds. World Scientific: Singapore, 2013; pp 289-302.

66. Bedzyk, M. J.; Fenter, P.; Zhang, Z.; Cheng, L.; Okasinski, J. S.; Sturchio, N. C., Xray Standing Wave Imaging. *Synchrotron Radiation News* **2004,** *17*, 5-10.

67. Batterman, B. W., Detection of Foreign Atom Sites by Their X-Ray Fluorescence Scattering. *Physical Review Letters* **1969,** *22* (14), 703-&.

68. Bedzyk, M. J.; Bommarito, G. M.; Schildkraut, J. S., X-Ray Standing Waves at a Reflecting Mirror Surface. *Physical Review Letters* **1989,** *62* (12), 1376-1379.

69. Bedzyk, M. J.; Bilderback, D.; White, J.; Abruna, H. D.; Bommarito, M. G., Probing Electrochemical Interfaces with X-Ray Standing Waves. *J. Phys. Chem.* **1986,** *90* (21), 4926-4928.

70. Lee, T.-L.; Bihler, C.; Schoch, W.; Limmer, W.; Daeubler, J.; Thieß, S.; Brandt, M. S.; Zegenhagen, J., Fourier transform imaging of impurities in the unit cells of crystals: Mn in GaAs. *Phys. Rev. B* **2010,** *81*, 235207.

71. Meier, M.; Jakub, Z.; Balajka, J.; Hulva, J.; Bliem, R.; Thakur, P. K.; Lee, T.-L.; Franchini, C.; Schmid, M.; Diebold, U.; Allegretti, F.; Duncan, D. A.; Parkinson, G. S., Probing the geometry of copper and silver adatoms on magnetite: quantitative experiment versus theory. *Nanoscale* **2018,** *10*, 2226-2230.

72. Vartanyants, I. A.; Zegenhagen, J., Theoery of photoelectron emission from an X-ray interference field. In *The X-ray standing wave technique: Principles and Applications*, Zegenhagen, J.; Kazimirov, A., Eds. 2013; Vol. 7.

73. Jablonski, A.; Salvat, F.; Powell, C. J., NIST Electron Elastic Scattering Cross-Section Database-Version 3.0. National Institute of Standarts and Technology: Gaithersburg, MD, 2002.

74. Moulder, J. F., Handbook of X-Ray Photoelectron Spectroscopy: A Reference Book of Standard Spectra for Identification and Interpretation of XPS Data. *Phys. Elec. Inc.* **1995**.

75. Krause, M. O., Atomic radiative and radiationless yields for K and L shells. *J. Phys. and Chem. Ref. Data* **1979,** *8* (2), 307-327.

76. CasaXPS Manual 2.3.15 Rev 1.0.

77. Jablonski, A., Photoelectron transport in the surface region of solids: universal analytical formalism

for quantitative applications of electron spectroscopies. *J. Phys. D: Appl. Phys* **2015,** *48*, 075301-075318.

78. Salmeron, M.; Schlögl, R., Ambient pressure photoelectron spectroscopy: A new tool for surface science and nanotechnology. *Surf. Sci. Rep.* **2008,** *63* (4), 169-199.

79. Newville, M., Fundamentals of XAFS. *Consortium for Advanced Radiation Sources, University of Chicago (USA)[http://xafs.org]* **2004,** *78*.

80. Penner-Hahn, J. E., X-ray Absorption Spectroscopy. *eLS* **2005**.

81. Woodruff, D. P., Low Energy Electron Diffraction. *Ref. Mod. in Mat. Sci. and Mat. Eng.* **2016**, 1-4.

82. Giessibl, F. J., Advances in atomic force microscopy. *Rev. Mod. Phys.* **2003,** *75* (3), 949-983.

83. Kim, C. Y.; Escuadro, A. A.; Stair, P. C.; Bedzyk, M. J., Atomic-scale view of redox-induced reversible changes to a metal-oxide catalytic surface: VOx/(alpha-Fe2O3(0001). *J Phys Chem C* **2007,** *111* (5), 1874-1877.

84. Feng, Z. X.; Kim, C. Y.; Elam, J. W.; Ma, Q.; Zhang, Z.; Bedzyk, M. J., Direct Atomic-Scale Observation of Redox-Induced Cation Dynamics in an Oxide-Supported Monolayer Catalyst: WOx/alpha-Fe2O3(0001). *Journal of the American Chemical Society* **2009,** *131* (51), 18200-+.

85. Kim, C. Y.; Klug, J. A.; Stair, P. C.; Bedzyk, M. J., Hydration and Reduction of Molecular Beam Epitaxy Grown VOx/alpha-Fe2O3(0001): Ambient Pressure Study. *J Phys Chem C* **2009,** *113* (4), 1406-1410.

86. Kim, C. Y.; Elam, J. W.; Stair, P. C.; Bedzyk, M. J., Redox Driven Crystalline Coherent-Incoherent Transformation for a 2 ML VOx Film Grown on alpha-TiO2(110). *J Phys Chem C* **2010,** *114* (46), 19723-19726.

87. Feng, Z. X.; Kazimirov, A.; Bedzyk, M. J., Atomic Imaging of Oxide-Supported Metallic Nanocrystals. *ACS Nano* **2011,** *5* (12), 9755-9760.

88. Feng, Z.; Cheng, L.; Kim, C.-Y.; Elam, J. W.; Zhang, Z.; Curtiss, L. A.; Zapol, P.; Bedzyk, M. J., Atomic-Scale Study of Ambient-Pressure Redox-Induced Changes for an Oxide-Supported Submonolayer Catalyst: VOx/α-TiO2(110). *J. Phys. Chem. Lett.* **2012,** *3*, 2845-2850.

89. McBriarty, M. E.; Bedzyk, M. J.; Ellis, D. E., Structure and properties of a model oxide-supported catalyst under redox conditions: WOx/alpha-Fe2O3 (0001). *Surf Sci* **2012,** *606* (17-18), 1367-1381.

90. Feng, Z.; Lu, J.; Feng, H.; Stair, P. C.; Elam, J. W.; Bedzyk, M. J., Catalysts Transform While Molecules React: An Atomic-Scale View. *The Journal of Physical Chemistry Letters* **2013,** *4* (2), 285-291.

91. Feng, Z.; McBriarty, M. E.; Mane, A. U.; Lu, J.; Stair, P. C.; Elam, J. W.; Bedzyk, M. J., Redox-Driven Atomic-Scale Changes in Mixed Catalysts: VOX / WOX / α-TiO2(110). *RSC Adv.* **2014,** *4*, 64608–64616.

92. Feng, Z.; Ma, Q.; Lu, J.; Feng, H.; Elam, J. W.; Stair, P. C.; Bedzyk, M. J., Atomic-scale cation dynamics in a monolayer VOX/α-Fe2O3 catalyst. *RSC Advances* **2015,** *5* (126), 103834-103840.

93. Kim, C. Y.; Elam, J. W.; Pellin, M. J.; Goswami, D. K.; Christensen, S. T.; Hersam, M. C.; Stair, P. C.; Bedzyk, M. J., Imaging of atomic layer deposited (ALD) tungsten monolayers on alpha-TiO2(110) by X-ray standing wave Fourier inversion. *J Phys Chem B* **2006,** *110* (25), 12616-12620.

94. McBriarty, M. E.; Campbell, G. P.; Drake, T. L.; Elam, J. W.; Stair, P. C.; Ellis, D. E.; Bedzyk, M. J., Atomic-Scale View of VOx-WOx Coreduction on the alpha-Al2O3 (0001) Surface. *J Phys Chem C* **2015,** *119* (28), 16179-16187.

95. Kim, T.; Wachs, I. E., CH3OH oxidation over well-defined supported V2O5 / Al2O3 catalysts : Influence of vanadium oxide loading and surface vanadium – oxygen functionalities. *J. Catal.* **2008,** *255*, 197-205.

96. Kim, C.-Y.; Elam, J. W.; Stair, P. C.; Bedzyk, M. J., Redox Driven Crystalline Coherent-Incoherent Transformation for a 2 ML VOx Film Grown on α-TiO2(110). *J. Phys. Chem. C* **2010,** *114*, 19723-19726.

97. Solokha, V.; Garai, D.; Wilson, A.; Duncan, D. A.; Thakur, P. K.; Hingerl, K.; Zegenhagen, J., Water Splitting on Ti-Oxide-Terminated SrTiO3(001). *J. Phys. Chem. C* **2019,** *123* (28), 17232-17238.

98. Waters, T.; Khairallah, G. N.; Wimala, S. A. S. Y.; Ang, Y. C.; O'Hair, R. A. J.; Wedd, A. G., Mononuclear metavanadate catalyses gas phase oxidation of methanol to formaldehyde employing dioxygen as the terminal oxidant. *Chem. Comm.* **2006,** *43*.

99. Campbell, G. P.; Mannix, A. J.; Emery, J. D.; Lee, T.-L.; Guisinger, N. P.; Hersam, M. C.; Bedzyk, M. J., Resolving the Chemically Discrete Structure of Synthetic Borophene Polymorphs. *Nano Lett.* **2018,** *18*, 2816-2821.

100. Köhler, L.; Kresse, G., Density functional study of CO on Rh(111). *Phys. Rev. B* **2004,** *70*, 165405.

101. Kolczewski, C.; Hermann, K.; Guimond, S.; Kuhlenbeck, H.; Freund, H.-J., Identification of the vanadyl terminated V2O3(0 0 0 1) surface by NEXAFS spectroscopy: A combined theoretical and experimental study. *Surf. Sci.* **2007,** *601*, 5394–5402.

102. Hugenschmidt, M. B.; Gamble, L.; Campbell, C. T., The interaction of H2O with a TiO2(110) surface. *Surf Sci* **1994,** *302*, 329-340.

103. Woodruff, D. P., Surface structure determination using x-ray standing waves: a simple view. *Rep. Prog. Phys.* **2005,** *68*, 743-798.

104. Zegenhagen, J., Surface structure determination with X-ray standing waves. *Surf. Sci. Rep.* **1993,** *49*, 202-271.

105. Benkoula, S.; Sublemontier, O.; Patanen, M.; Nicolas, C.; Sirotti, F.; Naitabdi, A.; Gaie-Levrel, F.; Antonsson, E.; Aureau, D.; Ouf, F.-X.; Wada, S.-I.; Etcheberry, A.; Ueda, K.; Miron, C., Water adsorption on TiO2 surfaces probed by soft X-ray spectroscopies: bulk materials vs. isolated nanoparticles. *Sci Rep* **2015,** *5*, 15088.

106. Kroger, E. A.; Allegretti, F.; Knight, M. J.; Polcik, M.; Sayago, D. I.; Woodruff, D. P.; Dhanak, V. R., Structural characterisation of ultra-thin VOx films on TiO2(1 1 0). *Surf. Sci.* **2006,** *600*, 4813-4824.

107. Trzhaskovskaya, M. B.; Nefedov, V. I.; Yarzhemsky, V. G., Photoelectron angular distribution parameters for elements z = 1 to z = 54 in the photoelectron energy range 100–5000 eV. *Atomic Data and Nuclear Data Tables* **2001,** *77*.

108. Weiland, C.; Rumaiz, A. K.; Pianetta, P.; Woicik, J. C., Recent applications of hard x-ray photoelectron spectroscopy. *J. Vac. Sci. Technol A* **2016,** *34*, 030801.

109. Bagus, P. S.; Nelin, C. J.; Levchenko, S. V.; Zhao, X.; Davis, E. M.; Kuhlenbeck, H.; Freund, H.-J., Surface core level BE shifts for CaO(100): insights into physical origins. *Phys. Chem. Chem. Phys* **2019,** *21*, 25431.

110. Bagus, P. S.; Nelin, C. J.; Zhao, X.; Levchenko, S. V.; Davis, E.; Weng, X.; Späth, F.; Papp, C.; Kuhlenbeck, H.; Freund, H.-J., Revisiting surface core-level shifts for ionic compounds. *Phys. Rev. B* **2019,** *100*, 115419.

111. Ciambelli, P.; Sannino, D.; Palma, V.; Vaiano, V.; Eloy, P.; Dury, F.; Gaigneaux, E. M., Tuning the selectivity of MoOx supported catalysts for cyclohexane photo oxidehydrogenation. *Catal. Today* **2007,** *128* (3-4), 251-257.

112. Patterson, T. A.; Carver, J. C.; Leyden, D. E.; Hercules, D. M., A Surface Study of Cobalt–Molybdena–Alumina Catalysts Using X-Ray Photoelectron Spectroscopy. *J. Phys. Chem.* **1976,** *80*, 1700-1708.

113. Fleisch, T. H.; Mains, G. J., An XPS study of the UV reduction and photochromism of MoO3 and WO3. *J. Chem. Phys.* **1982,** *76* (780).

114. Ho, S. F.; Contarini, S.; Rabalais, J. W., Ion-beam-induced chemical changes in the oxyanions (Moyn-) and oxides (Mox) where M = chromium, molybdenum, tungsten, vanadium, niobium and tantalum. *J. Phys. Chem.* **1987,** *91* (18), 4779-4788.

115. Kim, K. S.; Baitinger, W. E.; Amy, J. W.; Winograd, N., ESCA studies of metal-oxygen surfaces using argon and oxygen ion-bombardment. *J. Electron Spectrosc. Relat. Phenom.* **1974,** *5* (1), 351-367.

116. Coperet, C., Single-Sites and Nanoparticles at Tailored Interfaces Prepared via Surface Organometallic Chemistry from Thermolytic Molecular Precursors. *Acc.Chem.Res.* **2019,** *52*, 1697-1708.

117. Ravel, B., Advanced Topics in EXAFS Analysis. 2010.

118. LiBretto, N. J.; Xu, Y.; Quigley, A.; Edwards, E.; Nargund, R.; Vega-Vila, J. C.; Caulkins, R.; Saxena, A.; Gounder, R.; Greeley, J.; Zhang, G.; Miller, J. T., Olefin oligomerization by main group Ga3+ and Zn2+ single site catalysts on SiO2. *Nature Communications* **2021,** *12* (1), 2322.

119. Dutta, S., Deoxygenation of Biomass-Derived Feedstocks: Hurdles and Opportunities. *ChemSusChem* **2012,** *5* (11), 2125-2127.

120. Morschbacker, A., Bio-Ethanol Based Ethylene. *Polymer Reviews* **2009,** *49* (2), 79-84.

121. Tshibalonza, N. N.; Monbaliu, J.-C. M., The deoxydehydration (DODH) reaction: a versatile technology for accessing olefins from bio-based polyols. *Green Chemistry* **2020,** *22* (15), 4801-4848.

122. Kilyanek, K. A. D. S. M., Deoxydehydration of vicinal diols by homogeneous catalysts: a mechanistic overview. *R. Soc. open sci* **2019,** *6* (11), 191165.

123. Korstanje, T. J.; Jastrzebski, J. T. B. H.; Klein Gebbink, R. J. M., Catalytic Dehydration of Benzylic Alcohols to Styrenes by Rhenium Complexes. *ChemSusChem* **2010,** *3* (6), 695-697.

124. Korstanje, T. J.; de Waard, E. F.; Jastrzebski, J. T. B. H.; Klein Gebbink, R. J. M., Rhenium-Catalyzed Dehydration of Nonbenzylic and Terpene Alcohols to Olefins. *ACS Catalysis* **2012,** *2* (10), 2173-2181.

125. Shiramizu, M.; Toste, F. D., Deoxygenation of Biomass-Derived Feedstocks: Oxorhenium-Catalyzed Deoxydehydration of Sugars and Sugar Alcohols. *Angewandte Chemie International Edition* **2012,** *51* (32), 8082-8086.

126. Shadle, S. E.; Penner-Hahn, J. E.; Schugar, H. J.; Hedman, B.; Hodgson, K. O.; Solomon, E. I., X-ray absorption spectroscopic studies of the blue copper site: metal and ligand K-edge studies to probe the origin of the EPR hyperfine splitting in plastocyanin. *J. Am. Chem. Soc.* **1993,** *115* (2), 767-776.

127. Mouat, A. R.; Whitford, C. L.; Chen, B.-R.; Liu, S. S.; Perras, F. A.; Pruski, M.; Bedzyk, M. J.; Delferro, M.; Stair, P. C.; Marks, T. J., Synthesis of Supported Pd0 Nanoparticles from a Single-Site Pd2+ Surface Complex by Alkene Reduction. *Chem. Mater.* **2018,** *30* (3), 1032-1044.

128. Hai, Z.; Kolli, N. E.; Uribe, D. B.; Beaunier, P.; J.-Yacaman, M.; Vigneron, J.; Etcheberry, A.; Sorgues, S.; Colbeau-Justin, C.; J. Chena, H. R., Modification of TiO2 by bimetallic Au–Cu nanoparticles for wastewater treatment. *J. Mat. Chem. A* **2013,** *1*, 10829-10835.

129. Jiang, Z.-Y.; Zhao, Z.-Y., Comparison studies of interfacial energetic and electronic properties of bimetallic AuCu/TiO2 hetero-structures from DFT calculations. *Inorganic Chemistry Frontiers* **2018,** *5*, 1062-1075.

130. Chimentão, R. J.; Medina, F.; Fierro, J. L. G.; Llorca, J.; Sueiras, J. E.; Cesteros, Y.; Salagre, P., Propene epoxidation by nitrous oxide over Au–Cu/TiO2 alloy catalysts. *J. Mol. Catal. A: Chem.* **2007,** *274*, 159-168.

131. Chen, Y.; Jones, L. O.; Lee, T.-L.; Das, A.; Mosquera, M. A.; Keane, D. T.; Schatz, G. C.; Bedzyk, M. J., Site-specific surface atom valence band structure via x-ray standing wave excited photoemission. *(Under Review)* **2021**.

Appendix A

Setup for XSW experiments at 5-ID-C Beamline at APS

Combining hard X-ray Photoelectron Spectroscopy (HAXPES) with the X-ray standing wave technique allows us to generate 3D atomic density maps with chemical state sensitivity. The DuPont-Northwestern-Dow Collaborative-Access Team (DND-CAT) at sector 5 of the Advanced Photon Source (APS) has a UHV surface analysis endstation (5ID-C) for X-ray scattering and spectroscopy studies of surfaces and interfaces. In the past, the instrument has been used for X-ray standing wave (XSW) measurements with X-ray fluorescence (XRF). This has generated element specific atomic density maps not sensitive to the chemical state of the absorbing atom. Now, a Specs Phoibos 150 HV energy analyzer has been added for collecting photoelectron spectra excited by an XSW. The XSW is generated by dynamical Bragg diffraction from a substrate single crystal. By collecting the modulation in an XPS peak while scanning in angle through a substrate hkl Bragg reflection one can obtain an hkl Fourier component for that atomic species. After collecting several such hkl components (specular and off-specular peaks), their Fourier summation generates a model-independent real-space 3D atomic map with sub-Å level resolution. This enables 3D elemental mapping of individual substrate surface sites with oxidation state specificity of each occupied atom. Fig. A1 shows a schematic of the beamline setup at 5ID. Fig. A2 (a)-(c) shows some schematics of the UHV chamber along with the XPS hemispherical analyzer and the diffractometer from various angles and Fig. A2 (d) shows a photograph of the UHV chamber. Fig. 27(b) shows a more detailed schematic of the hemispherical analyzer and Fig. 27(c) shows the actual setup of the UHV chamber at Sector 5ID-C.

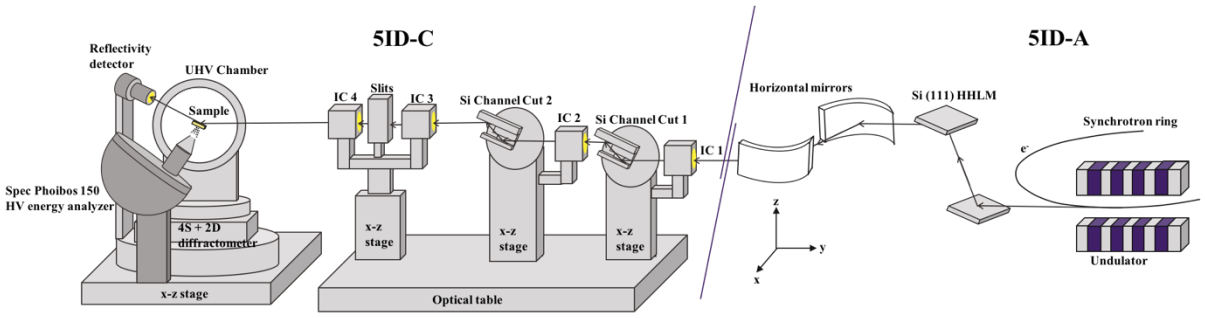

Figure A1. *The 5ID beamline layout in the 5ID-A and 5ID-C stations for the XSW-HAXPES experiment. Components at the upstream end of the 5ID-C hutch include: an optical table that accommodates post-monochromator Si channel cuts (CC1 and CC2), ion chambers (IC), and beam-defining slits. At the downstream end of 5ID-C sits the 4S+ 2D diffractometer and the UHV chamber with photoelectron spectrometer.*

For introducing the sample into the UHV analysis chamber, a load-lock chamber that can store up to four samples is connected to the main chamber to ease sample transfer without breaking the vacuum in the analysis chamber. As shown in Fig. A3, the sample is mounted on a platen, which is locked into the sample manipulator. The manipulator has a tungsten filament to heat the sample radiatively up to 1100 K and has a flexible Cu braid for cooling with liquid nitrogen down to 115 K. The UHV chamber has additional sample preparation and characterization tools, including a Oxford TC50 Thermal cracker cell with O_2 and H_2 vials connected to it, a low-energy electron diffraction (LEED) system, a residual gas analyzer (RGA), an dual anode X-ray gun (Al and Cr sources) and an electron flood gun.

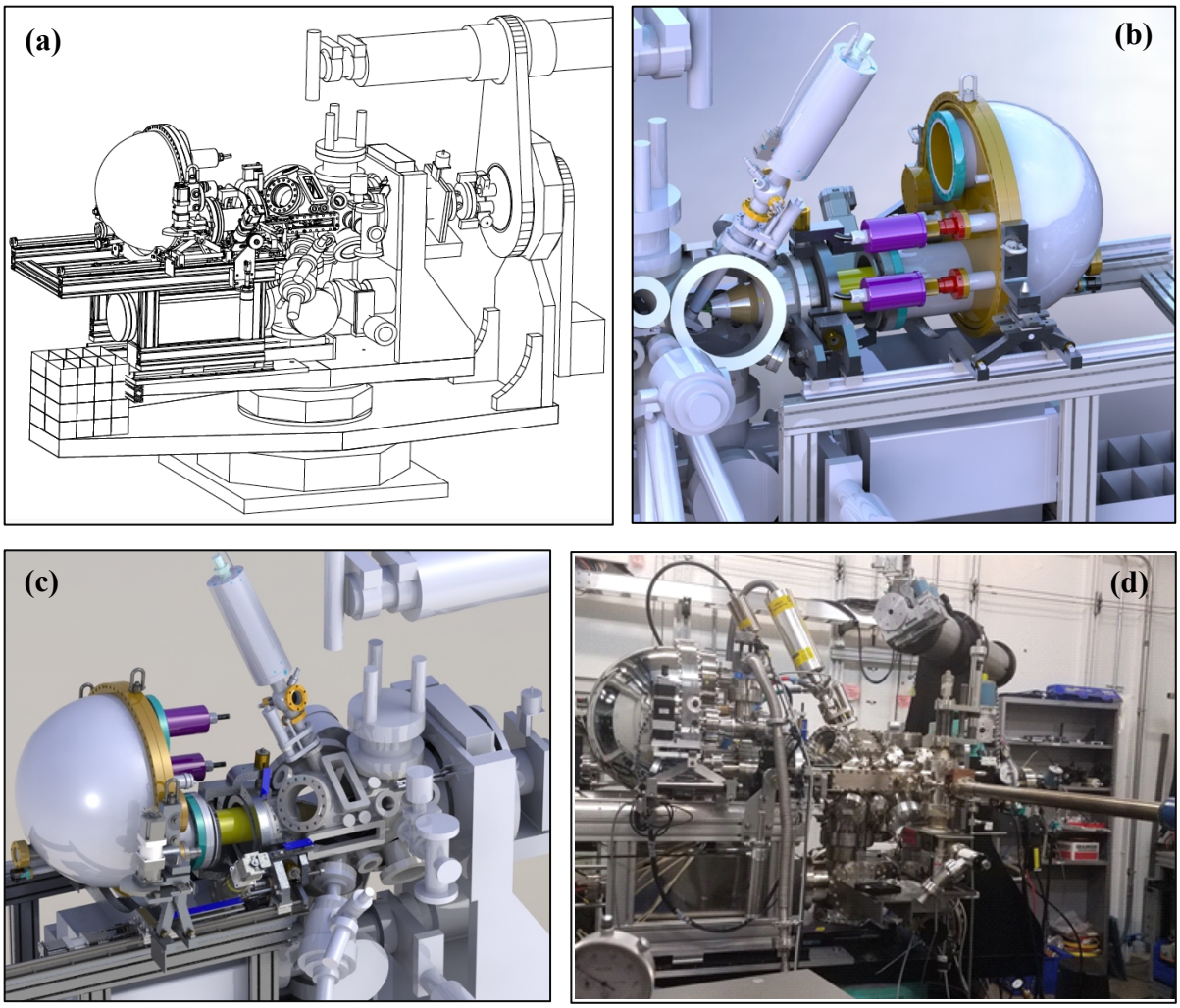

Figure A2. *(a) Line drawing of the UHV endstation at 5-ID-C (b) Schematic showing the XPS analyzer and the X-ray anode source (c) Schematic showing the complete chamber along with the XPS and Reflectivity detectors (d) Photograph of the UHV chamber.*

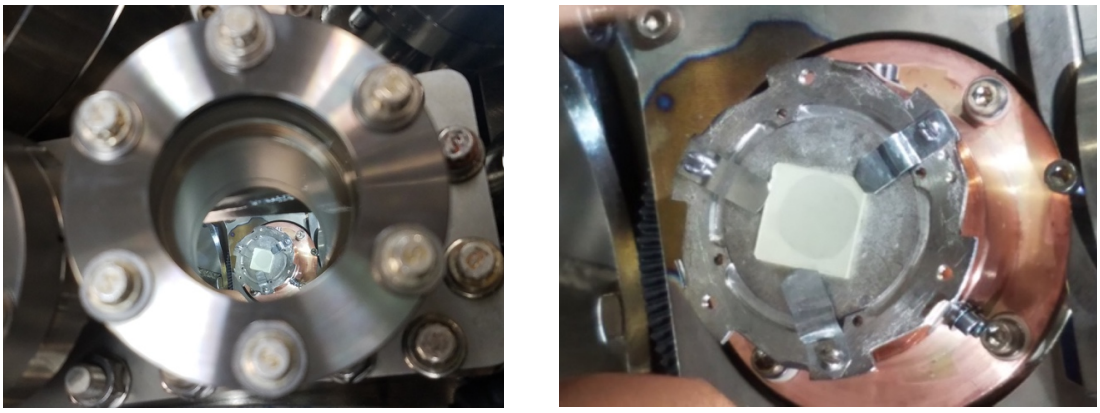

Figure A3. *A 10x10 mm^2 α–TiO_2(110) single crystal substrate inside the UHV chamber mounted on a Thermionics platen*

The sample and detector motors are operated using SPEC. SPEC is a UNIX-based software package for instrument control and data acquisition widely used for X-ray experiments at synchrotrons around the world and in universities, national and industrial laboratories. The sample stage is centered on a 5-circle goniometer and SPEC is used to move the motors to obtain each Bragg reflection. To obtain a specific reflection, the sample is first rotated to the Bragg angle wrt the incident beam (this angle is denoted as *eta* in SPEC) and then angle *chi* (in SPEC) is rotated so that the reflecting plane normal is in the same direction as the specular plane normal. An X-ray eye is mounted behind the reflectivity ion chamber to make sure that the reflection is centered on the detector arm. The UHV chamber has two Beryllium windows, one at the upstream end through which the incident beam enters and hits the sample and another Be window on the downstream end through which the reflected beam comes out and passes through the ion chamber and seen by the X-ray eye. Fig. A4 shows a schematic of the various important directions wrt the sample.

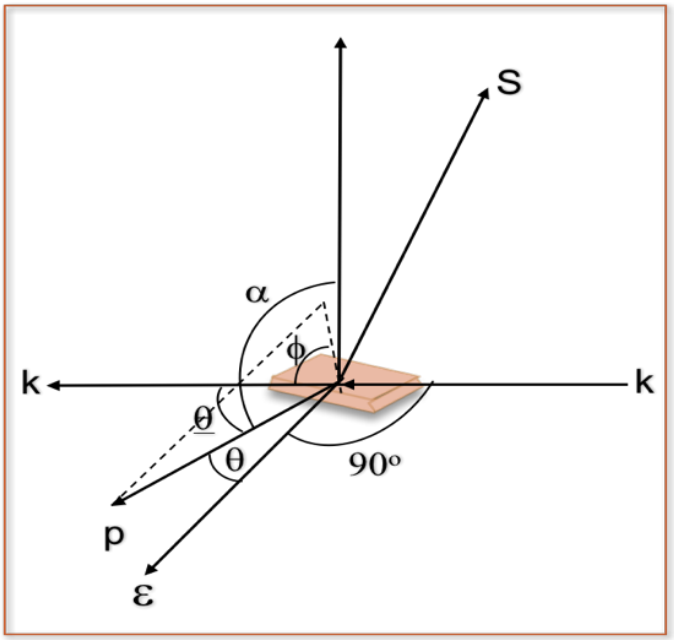

Figure A4. *A schematic of the directions of the different vectors important for understanding and analyzing the XSW data.* ***k*** *and* ***p*** *represent the photon and photoelectron directions, respectively,* ***ε*** *gives the photon polarization direction and* ***S*** *is the direction normal to the target.*

Due to the positioning of the downstream Be window, there is a limitation on which reflections can come out through the window. Only reflections with Bragg angle below 25° can exit through that window. So, in order to detect higher Bragg angle reflections, we installed photodiodes inside the UHV chamber wall. Fig. A5 (a) and (b) shows schematics of the photodiodes installed on the inner wall of the UHV chamber. When the reflected X-ray hits the photodiodes, a current signal is generated which is then outputs in the SPEC software. Thus, for each reflection SPEC is used to collect the reflectivity data in the form of an angle-scanned rocking curve.

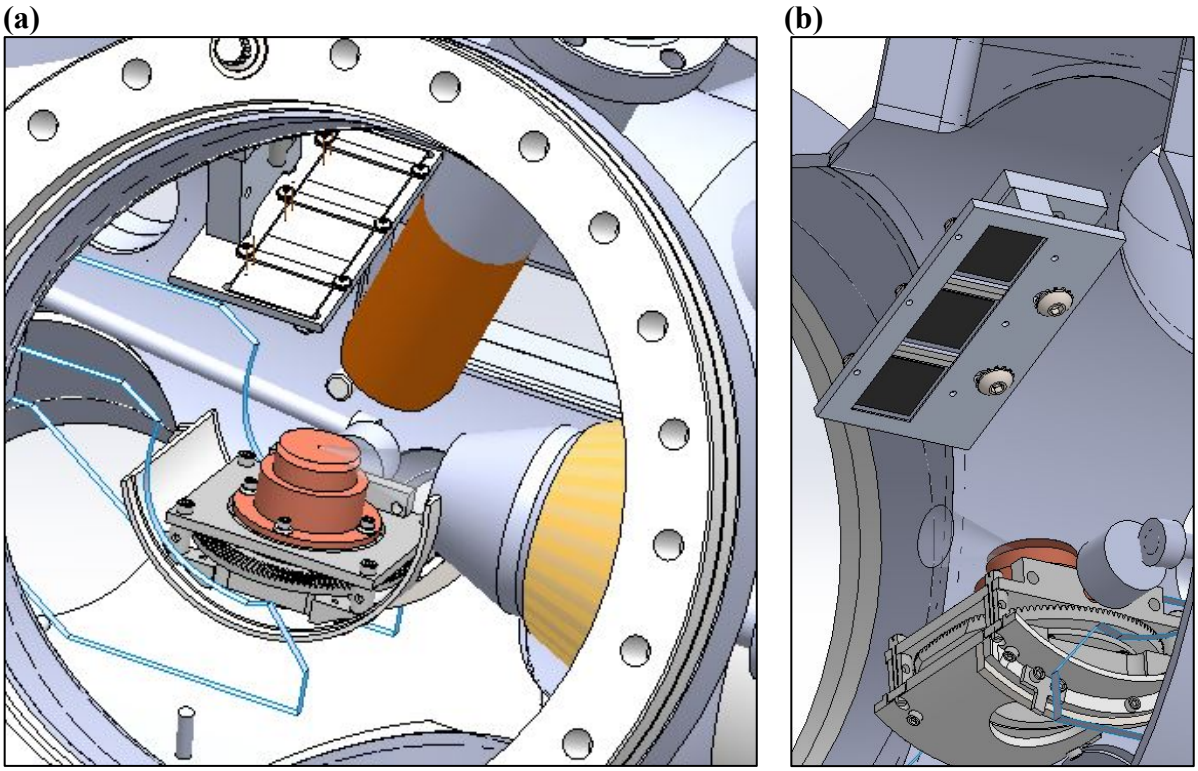

Figure A5. *(a) Schematic view through a downstream window of the inside of the UHV chamber showing the photodiodes (b) View of the photodiodes from inside the chamber.*

To perform the XSW experiments, we have to collect the X-ray photoelectron signal at each point of the rocking curve. The 150 HV Specs X-ray photoelectron analyzer is operated using the software *Specslab Prodigy*. To set-up a XPS scan the input parameters are: Scan mode (we use Fixed Analyzer Transmission mode), Scan range (either 1.5 kV or 3.5 kV), Entrance slit (7x20), Exit slit (open), Lens mode (we mainly use Large Area mode), Pass energy, Scan start binding energy, Scan end binding energy, Step size, Dwell time. Once these scan parameters are optimized to obtain the best possible signal, this scan is saved as a template (.slt file). Next step is to go to the Remote Control tab. From the drop down menu select the template that was just saved. Then in the top right corner click on Allow Remote Control.

Next, for the XSW experiment, SPEC is used to run this template XPS scan at each step of the rocking curve. In order to do so, multiple SPEC macros were written by Dr. Boris Harutyunyan and Dr. Denis Keane. The first macro is named as *xps_v0_1_npt150.mac* and is read into SPEC using the command:

dofile("/home/user5idc/5IDC/macros/phoibos/xps_v0_1_npt150.mac")

The macro is as follows:

```
> #*********************************************************
> # DTK attempt to extract only xps macros from
> # Boris Harutyunyan original xsw xps update
> # The XSW macro running the detector through EPICS, be it an AIM unit or a vortex electronic box.
> #   Modified from the previous DXP version xswdxp.mac
> # By Zhan Zhang, last modified on Nov. 30, 2007
> #*********************************************************
> # The first part is the definition of the global variables and constants.
> # Note some constants could be changed during the run.
> #*********************************************************
> global xps_integrate
> xps_integrate = 1 # value set to 0 means no intergation, so both energy and non-energy channels are saved. Value set to 1 would integrate over non-energy channels.
> global StartEnergy
> StartEnergy = 2020.2
> global EndEnergy
> EndEnergy = 2040
> global DwellTime
> DwellTime = 0.2
> global ScanRange
> ScanRange = "\"3.5kV\"" # three options only: 3.5kV, 1.5kV, 400V
> global LensMode
> LensMode = "\"LargeArea\""
> global Samples
> Samples = 1
> global StepWidth
> StepWidth = 0.2
> global PassEnergy
> PassEnergy = 40.0
> global Energy_low_channel
> Energy_low_channel = 0
> global Energy_high_channel
> Energy_high_channel = 149
> global Non_energy_channel
> Non_energy_channel = 50
> global dat_size
> dat_size = Non_energy_channel * (Energy_high_channel - Energy_low_channel + 1)
> float array data_array[dat_size]
> float array data_array_integrate[(Energy_high_channel - Energy_low_channel + 1)]
```

```
> float array data_array_integrate_x[(Energy_high_channel - Energy_low_channel + 1)]
> global data_sum
> global xps_wait_time
> xps_wait_time = 1.0
> global xps_count_time
> xps_count_time = 1.0
> global xps_debug
> xps_debug=1
> global xps_plot
> xps_plot=1
> def xps_down'
> {
>       sock_put("cardamom1:7010","?0002 Start SetSafeStateAfter:\"true\"\n")
>       s1 = sock_get("cardamom1:7010")
>       xps_st = index(s1, "OK")
>       while (xps_st == 0){
>               sleep(xps_wait_time)
>               s1 = sock_get("cardamom1:7010")
>               xps_st = index(s1, "OK")
>       }
>       sock_put("cardamom1:7010","?0002 SetSafeState\n")
>       sock_get("cardamom1:7010")
> }'
> def xps_wait'{
>       s1 = sock_get("cardamom1:7010")
>       if (xps_debug) {print s1}
>       xps_st = index(s1, "OK")
>       while (xps_st == 0){
>               sleep(xps_wait_time)
>               s1 = sock_get("cardamom1:7010")
>           if (xps_debug) {print s1}
>               xps_st = index(s1, "OK")
>       }
> }'
> def xps_check_spectrum '{
>       local arrt[]
>       local v
>       sock_put("cardamom1:7010","?0002 ClearSpectrum\n")
>       if (xps_debug) {print "?0002 ClearSpectrum\n"}
>       xps_wait
> #     v= sprintf("?0002 DefineSpectrumSFAT StartEnergy:%f EndEnergy:%f Samples:%u DwellTime:%f LensMode:%s ScanRange:%s\n" ,StartEnergy, EndEnergy, Samples, DwellTime, LensMode, ScanRange )
>       v= sprintf("?0002 DefineSpectrumFAT StartEnergy:%f EndEnergy:%f StepWidth:%f DwellTime:%f PassEnergy:%f LensMode:%s ScanRange:%s\n" ,StartEnergy, EndEnergy, StepWidth, DwellTime, PassEnergy, LensMode, ScanRange )
>       sock_put("cardamom1:7010", v)
>       if (xps_debug) {print v}
>       xps_wait
>       sock_put("cardamom1:7010","?0002 ValidateSpectrum\n")
>       if (xps_debug) {print "?0002 ValidateSpectrum\n"}
>       xps_wait
> }'
```

```
> #GET DATA FROM XPS
> def xps_acquire'{
>       local arrt[]
>       local v
>       sock_put("cardamom1:7010","?0002 ClearSpectrum\n")
>       xps_wait
> #     v= sprintf("?0002 DefineSpectrumSFAT StartEnergy:%f EndEnergy:%f Samples:%u DwellTime:%f LensMode:%s ScanRange:%s\n" ,StartEnergy, EndEnergy, Samples, DwellTime, LensMode, ScanRange )
> #     v= sprintf("?0002 DefineSpectrumFAT StartEnergy:%f EndEnergy:%f StepWidth:%f DwellTime:%f PassEnergy:%f LensMode:%s ScanRange:%s\n" ,StartEnergy, EndEnergy, StepWidth, DwellTime, PassEnergy, LensMode, ScanRange )
> #     sock_put("cardamom1:7010", v)
> #     xps_wait
>       sock_put("cardamom1:7010","?0002 ValidateSpectrum\n")
>       xps_wait
> # now modify to count as well
>       if (xps_debug) {print "start tcount at ", date()}
>       tcount(xps_count_time)
>       if (xps_debug) {print "start Phoibos at ", date()}
>       sock_put("cardamom1:7010","?0002 Start SetSafeStateAfter:\"false\"\n")
>       xps_wait
>       wait(2)
>       if (xps_debug) {print "tcount finished at ", date()}
>       if (xps_debug) {print "start waiting for Phoibos at ", date()}
>       sock_put("cardamom1:7010","?0002 GetAcquisitionStatus\n")
>       s1 = sock_get("cardamom1:7010")
>       xps_st = index(s1, "finished")
>       while (xps_st == 0){
>               sleep(xps_wait_time)
>               sock_put("cardamom1:7010","?0002 GetAcquisitionStatus\n")
>               s1 = sock_get("cardamom1:7010")
>               xps_st = index(s1, "finished")
>       }
>       if (xps_debug) {print "Phoibos done at ", date()}
>       xps_g = sprintf( "?0002 GetAcquisitionData FromIndex:%u ToIndex:%u\n" , Energy_low_channel, Energy_high_channel )
>       sock_put("cardamom1:7010", xps_g)
>       ac_data=sock_get("cardamom1:7010")
>       nt = index(ac_data, "]")
>       while (nt == 0 ) {
>               ac_data_temp = sock_get("cardamom1:7010")
>               ac_data = sprintf("%s%s", ac_data, ac_data_temp)
>               nt = index(ac_data, "]")
>       }
>       #splitting the data string
>       m = index(ac_data, "[")
>       n = index(ac_data, "]")
>       ac_data = substr(ac_data, m+1, n-m-1)
>       #converting into an array
>       split(ac_data, arrt, ",")
>       for (ii=0; ii<dat_size; ii++){
>               sscanf(arrt[ii], "%f", data_array[ii])
```

```
>       }
>       dat_int = (Energy_high_channel - Energy_low_channel + 1)
>       if (xps_integrate != 0) {
>               data_sum=0
>               for (ii=0; ii < dat_int; ii++){
>                       temp = 0
>                       for (jj=0; jj < Non_energy_channel; jj++){
>                               temp = temp + data_array[(jj * dat_int)+ii]
>                       }
>                       data_array_integrate[ii] = temp
>                       data_array_integrate_x[ii] = StartEnergy+ii*(EndEnergy-StartEnergy)/(dat_int-
1)
>                       data_sum += temp
>               }
>       }
>       if (xps_plot) {
>               plot_cntl("filter2")
>               plot_cntl("erase")
>               array_plot(data_array_integrate_x,data_array_integrate)
>               plot_cntl("filter1")
>       }
>       if (xps_debug) {print "data_sum= ", data_sum}
>       show_cnts
> }'
> #*********************************************************
> # End of the macro file
> #*********************************************************
```

The second macro is named as xps_v8_outputs_tables_npt150.mac and is read into SPEC using the command:

dofile("/home/user5idc/5IDC/macros/phoibos/xps_v8_outputs_tables_npt150.mac")

The macro is as follows:

```
> #*********************************************************
> # The XSW macro running the detector through EPICS, be it an AIM unit or a vortex electronic box.
> #   Modified from the previous DXP version xswdxp.mac
> # By Zhan Zhang, last modified on Nov. 30, 2007
> # The first part is the definition of the global variables and constants.
> # Note some constants could be changed during the run.
> #*********************************************************
> global xsw_step       # 32    steps per rocking curve scan
> global xsw_ctime      # 1     counting time
> global xsw_scan       # 800   total scan number
> global xsw_saveset    # 20    total savesets
> global xsw_slp        # 0.5   sleeping time
> global xsw_dir                        #       data file directory
> global xsw_fname              #       data file name
```

```
> global xsw_version          #       data file version
> global xsw_title            #       data file title
> global xsw_shift            #       rocking scan center shift of the first device
> global xsw_accumulate       #       flag of data accept (1) or not (0)
> global xsw_drift_cntl # 0     flag of drift control
> global xsw_max_drift        #       maxmium drift allowed between two adjacent scans
> global num_device           #       number of devices used in the scan
> global vortex_PV            # EPICS device name for the vortex detector--should already be set in
vortex.mac
> global device_string  # scan device (String)
> global center_string    # scan center (String)
> global range_string     # scan range (String)
> global chan_ll                      # These two are the higher and lower channel limit of one
element
> global chan_ul
> global de_sa_dist           # These two for output purpose. Given by user. Indicating the geometry
of detector to sample.
> global de_sa_height  # de_sa_dist and de_sa_height are the distance and height from the detector to
the sample
> global xsw_last_fwhm        # FWHM of the last scan.
> global refl1                # reflectivity counter
> global pexam_flag           # flag global to indicate whether parameter exam is carried out or not.
> global sync_dev             # synchronization flag for device number
> global sync_cent            # synchronization flag for scan center
> global sync_range           # synchronization flag for scan range
> constant TOT_P_NUM      19      # total number of parameters in setxsw
> constant CHAN_RANGE     10              # minimum number of channels to be recorded
> constant NUM_ELE        1               # number of the detector elements
> constant VORTCHAN               2048    # Maximum number of channels for vortex
> #*********************************************************
> # The end of the constants and global variables
> #*********************************************************
> # Here Goes pre-load checks and user specific macros.
> #*********************************************************
> # load the vortex macro if it is not already loaded.
> global xps_integrate
> xps_integrate = 1 # value set to 0 means no intergation, so both energy and non-energy channels are
saved. Value set to 1 would integrate over non-energy channels.
> global total_counts
> total_counts = 0
> global StartEnergy
> StartEnergy = 107.9595947108
> global EndEnergy
> EndEnergy = 122.0404052892
> global StepWidth
> StepWidth = 1
> global DwellTime
> DwellTime = 10
> global ScanRange
> ScanRange = "\"1.5kV\"" # three options only: 3.5kV, 1.5kV, 400V
> global LensMode
> LensMode = "\"LargeArea\""
> global Samples
```

```
> Samples = 1
> global Energy_low_channel
> Energy_low_channel = 0
> global Energy_high_channel
> Energy_high_channel = 149
> global Non_energy_channel
> Non_energy_channel = 50
> global dat_size
> dat_size = Non_energy_channel * (Energy_high_channel - Energy_low_channel + 1)
> float array data_array[dat_size]
> float array data_array_integrate[(Energy_high_channel - Energy_low_channel + 1)]
> global analyzer_mode
> analyzer_mode = "FAT"
> global PassEnergy
> PassEnergy = 100
> #some new variables defined in the manual which I don't know what they do. Exported in vms file
> global regions
> regions = 3
> global variables
> n_variables = 1
> global scan_mode
> scan_mode = "REGULAR"
> global Analyzer_slit
> Analyzer_slit = "4:7x20c\B:open"
> global Scan_mode
> Scan_mode = "FixedAnalyzerTransmission"
> global Kinetic_energy_base
> Kinetic_energy_base = 0
> global beam_energy
> beam_energy = 7000
> global source_polar_angle
> source_polar_angle = 54.5
> global source_azimuth
> source_azimuth = 180
> global analyzer_resolution_characteristic
> analyzer_resolution_characteristic = 30
> global magnification_of_analyzer
> magnification_of_analyzer = 1
> global analyzer_work_function
> analyzer_work_function = 4.279
> global target_sample_bias
> target_sample_bias = 0
> global Analysis_width_x
> analysis_width_x = 0
> global Analysis_width_y
> analysis_width_y = 0
> global Analyzer_axis_polar_angle
> analyzer_axis_polar_angle = 0
> global Analyzer_azimuth
> analyzer_azimuth = 0
> global charge_of_analyzed_particle
> charge_of_analyzed_particle = -1
> def write_to_tables '{
```

```
>       #First argument is the filename as string
>       en =  Energy_high_channel - Energy_low_channel + 1                      #energy channels
>       for (ii=0; ii < Non_energy_channel; ii++){
>               fname = sprintf("%s__non_E_%02d.txt", $1, ii)
>               on(fname)
>               for (jj=0; jj < en; jj++){
>                       offt
>                       if (analyzer_mode != "FAT"){
>                               xe = StartEnergy + jj*(EndEnergy - StartEnergy)/(en-1)
>                       } else{
>                               xe = StartEnergy + jj*StepWidth
>                       }
>                    printf("%.8f\t%.8f\n", xe, data_array[ii*en + jj])
>                       ont
>               }
>            off(fname)
>               close(fname)
>       }
>       fname = sprintf("%s__integrated.txt", $1)
>       print fname
>       on(fname)
>       for (jj=0; jj < en; jj++){
>               offt
>            printf("%.8f\t%.8f\n", data_array_integrate_x[jj], data_array_integrate[jj])
>               ont
>       }
>       off(fname)
>       close(fname)
> }'
```

After that, in SPEC, open a new window and go to the directory */home/user5idc/5IDC/cycle number/bedzyk* (here cycle number will change with each APS cycle when the experiment is carried out for example the 1st run of 2022 will be named as 2022-1).

Step 1: Make a new directory within this directory (command example: *mkdir scan1*)

Step 2: Return back to the main directory //*home/user5idc/5IDC* (twice command: *cd..*)

Step 3: Copy one of the previous scan macros into the new directory (command example: *cp ./2021-3/bedzyk/scan1/scan1.mac ./2022-1/bedzyk/scan1/scan1.mac ,* this will copy the macro named scan1.mac from the directory scan1 inside the directory 2021-3 and then paste it in the new directory that was made in step1.

Step 4: Edit the macro that was copied (command example: *gedit ./2022-1/scan1/scan1.mac*)

Step 5: The macro is the following where some example parameters are added and will change based on each scan. There are comments beside the lines that will change:

```
on("log_scan1.log") (comment: change the scan number with each scan)
StartEnergy=6950.0-1968 (comment: Incident X-ray energy – start Kinetic energy of the XPS scan)
EndEnergy=6950.0-1988 (comment: Incident X-ray energy – end Kinetic energy of the XPS scan)
StepWidth=-0.1342281879 (comment: XPS scan step width from the template)
for (set_ii=1; set_ii < 2 ; set_ii++) (comment: number of rocking curve scans you want to perform)
{
        xps_delta = 0.00068 (comment: width in mdeg between two points on the rocking curve)
        plotselect refl
        dscan eta -0.02 0.02 80 1
        plot_res
        mv eta CEN-32.0*0.5*xps_delta
        waitmove
        getangles
        xps_start_pos = A[eta]
        float array xps_refl[2][32]
        float array xps_cyber[2][32]
        waitmove
        local dtk_ii
        for (dtk_ii=0 ; dtk_ii < 32 ; dtk_ii++) {
                mv eta xps_start_pos+dtk_ii*xps_delta
                waitmove
                getangles
                xps_refl[0][dtk_ii] = A[eta]
                xps_cyber[0][dtk_ii] = A[eta]
                xps_acquire
            out_filename = sprintf("set%02d_point_%02d",set_ii,dtk_ii)
            write_to_tables out_filename
                xps_refl[1][dtk_ii] = S[refl]
                xps_cyber[1][dtk_ii] = S[cyb]
        }
        plot_cntl("filter1")
        plot_cntl("erase")
        array_plot(xps_refl)
        print "refl FWHM ",array_op("fwhm",xps_refl[0][],xps_refl[1][])
        print "refl CFWHM ",array_op("cfwhm",xps_refl[0][],xps_refl[1][])
        mv eta array_op("cfwhm",xps_refl[0][],xps_refl[1][])
        waitmove
    out_filename = sprintf("set%02d_refl_data",set_ii)
        on(out_filename)
        for (dtk_ii=0; dtk_ii < 32; dtk_ii++){
                print xps_refl[0][dtk_ii],xps_refl[1][dtk_ii]
        }
        close(out_filename)
    out_filename = sprintf("set%02d_cyber_data",set_ii)
        on(out_filename)
        for (dtk_ii=0; dtk_ii < 32; dtk_ii++){
```

```
                print xps_cyber[0][dtk_ii],xps_cyber[1][dtk_ii]
        }
        close(out_filename)
}
sock_put("cardamom1:7010","?0002 SetSafeState\n")
xps_wait
plotselect refl
dscan eta -0.02 0.02 80 1
plot_res
mv eta CEN
close("log_scan1.log") (comment: change the scan number with each scan)
```

Step 6: In the original window type *p sock_put("cardamom1:7010","?0001 Connect\n")*

This will connect the SPEC computer with the SpecsLab Prodigy computer

Step 7: Type *xps_wait*

The output should say

!0001 OK: ServerName:"SpecsLab Prodigy 4.64.3-r88789 " ProtocolVersion:1.14

Step 8: Type *p sock_put("cardamom1:7010","?0002 ValidateSpectrum\n")*

Step 9: Type *xps_wait*

This should show you the parameters of the template that you have selected in SpecsLab Prodigy. This is an example of an output:

!0002 OK: StartEnergy:4405 EndEnergy:4435 StepWidth:0.2013422819 Samples:150 DwellTime:1 PassEnergy:100 LensMode:"LargeArea" ScanRange:"3.5kV"

Step 10: Make sure that in your macro the start energy, end energy and step width match with the ones you see after step 9. The step width will be the negative of what's in the macro.

Step 11: Make sure you are in the directory of the scan for example

/home/user5idc/5IDC/2022-1/bedzyk/scan1

Step 12: Type *dofile("scan1.mac")*

The above 12 steps will collect all the necessary XSW-XPS data. Appendix B describes the process of analyzing the XSW-XPS data using the Matlab code SWAM developed in the Bedzyk group.

Appendix B

XSW data analysis using Matlab program SWAM

B.1 Origin of SWAM

Originally a Fortran program DARE (Data Analysis Routine) was written by Michael Bedzyk and Jörg Zegenhagen in ~1986 to perform basic analysis of XSW data. In 1998 the Fortran program, SWAN (Standing Wave Analysis), was written by Likwan Cheng and Bedzyk with the main goal of extending XSW analysis to any arbitrary crystalline structure via the introduction of .ctl files. SWAN was written in Fortran and translated to C using MACF2C (Mac OS 9 or in the classic environment). Subsequently, CodeWarrior, a now-discontinued MacClassic-based integrated development environment, was then employed to handle the translated source code. SWAN was routinely updated by group members as late as 2005 (SWANv2.1.3), when Anthony Escuadro added some functionality to streamline SWAN analysis and improve rocking-curve fitting (See Escuadro Thesis A.1.2). However, by 2009 the utilization of SWAN as the main XSW analysis tool for the group had become impractical because it is limited only to Macs which could run Classic (Classic compatibility with Mac OS was dropped in 2005), requires tedious command-line operation, and is therefore largely inaccessible for operation or modifications.

In 2009 Phillip Lin transcribed SWAN's Fortran code into a set of Matlab subroutines and enabled a dialog-box-based interface to prompt the user for input. This became SWAM (Standing Wave Analysis for Matlab). In 2011 Zhenxing Feng began to expand SWAM in order to allow for Gaussian broadening of rocking curves to account for sample mosaic (as opposed to approximating

mosaic by artificially increasing the crystal asymmetry factor b) as well as adding an option for analyzing data acquired using energy scans (E-scans) as opposed to angular scans (θ scans). The initialization function (SWAM.m) allowed the user to choose from 3 options: cr.m, r0.m, and f1.m, the names of which are holdouts from DARE. cr.m prompts the user for experimental parameters and crystal structure information (stored in .ctl files), and then calculates and outputs the single-crystal diffraction parameters. r0.m is the rocking curve fitting procedure which takes user input and calculates the intensity for the Bragg reflectivity (R_B) of the monochromator and sample crystal, convolutes the two, and subsequently fits the result to the measured rocking curve data by tuning the experimental scan range, angular offset, and/or intensity. With the information acquired from the fit, r0.m outputs the so-called rcf file, which contains relevant parameters for XSW yield fitting. The rcf file is loaded in f1.m and used to calculate the phase (ν) of the standing wave for a given reflection, which is subsequently broadened to account for sample mosaicity and beamline optics. This sub-routine then loads in X-ray fluorescence/photoemission (XRF or XPS) yield data for the measured Fourier component, and fits the yield data to the theoretical XSW yield. The fit reveals the amplitude and phase of the measured Fourier component, also known as the coherent fraction (f_H) and coherent position (P_H) or the atomic/chemical species of interest. These final values are then interpreted to formulate structural models of the system of interest.

Since 2011, SWAM has been an extremely useful tool for analyzing XSW data acquired by monitoring XRF yields during angular scans (θ scans) across the single-crystal Bragg reflections at Bragg angles (θ_B) less than 87°. The most current version of SWAM is v5.1.

B.2 Contents and primary initialization

B.2.1 Contents

The SWAM directory contains version information (VersionInfo.txt), the 5 main SWAM routines (SWAM.m, cr.m, r0.m, f1.m, and chi2.m), a automatically-produced path file (pathdef.m), and 3 sub-directories. SWAMv5.1 was written using Matlab version R2019b.

1.) .\DefaultFiles\ contains .mat files populated with saved default parameters. All the default values are saved in these file crdef.m, and the file is re-written after each run so that parameters do not have to be constantly modified for a particular experiment.

2.) \.Reference\ contains .ctl files, atomic form factor libraries, and other elemental information needed to calculate structure factors.

3.) \SubFunctions\ contains secondary functions. Archive functions are those sub-functions included in previous versions of SWAM but were phased out for one reason or another, usually because of the transition to cromer- calculation of dispersion corrections.

B.2.2 Initialization

Navigate to the SWAM directory. Double-click on SWAM, which will cause it to open in the Matlab editor. Press F5 to run. Make sure you change the path to the SWAM folder and add all folders and subfolders to the path.

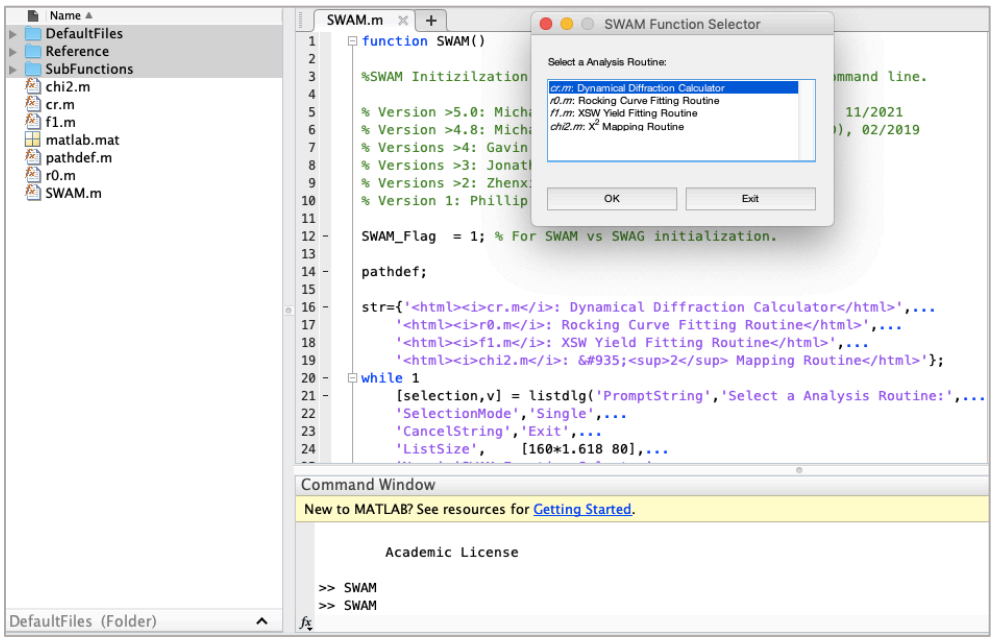

B.3 *cr.m: Dynamical Diffraction Calculator*

cr.m is the base subroutine used to calculate pertinent parameters for single-crystal diffraction. The routine is organized into three parts: initialization, calculation, and display/output. A synopsis of the analysis tree is shown in the **structural flow chart**, below.

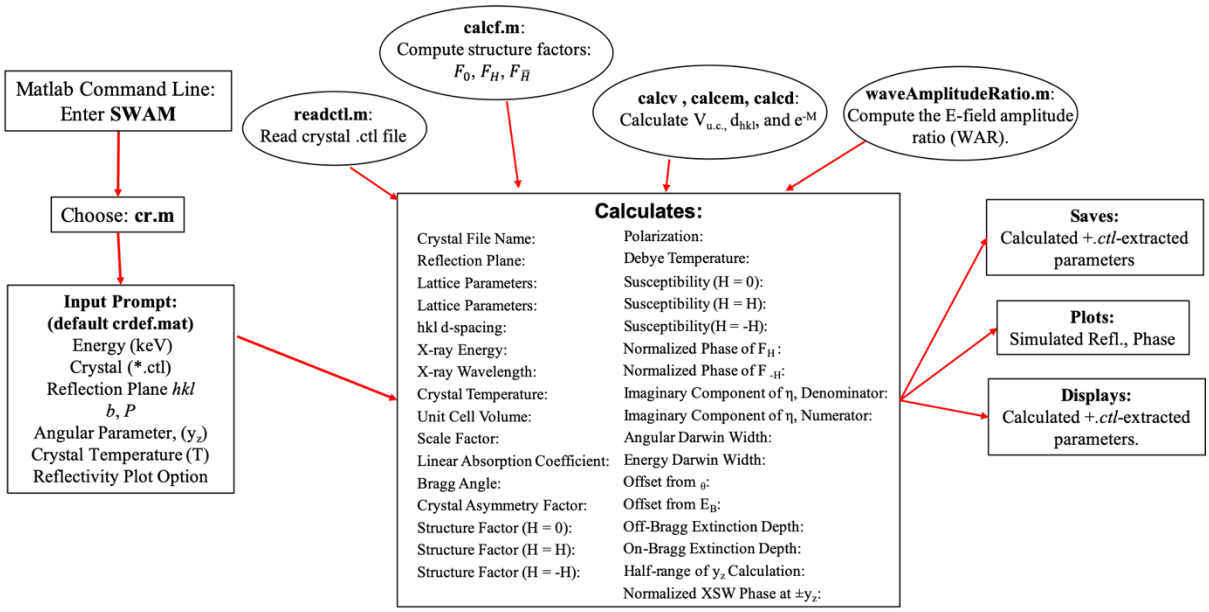

B.3.1 Parameter selection

There is a single input prompt for the Dynamical Diffraction Calculator, shown below:

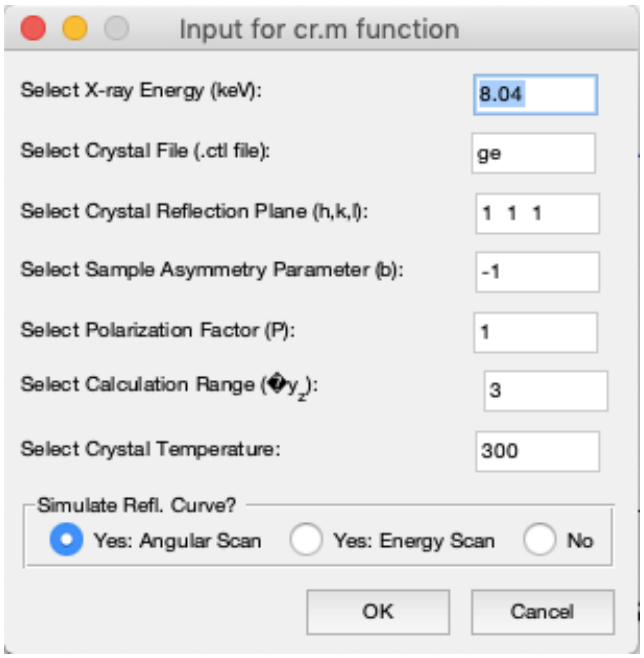

1.) The **Energy** is the incident photon beam energy, in keV.

2.) **Crystal i**dentifies the crystal for which the calculations will be made. The choice will access .ctl file from the library, so it must precisely match the ctl file name in the .\ctl\ file directory.

3.) **Crystal Reflection Plane** is the H = h,k,l set of planes for which the calculations will be performed.

4.) **Crystal Asymmetry Factor**: b defines the degree of reflection asymmetry and is defined as the ratio of the direction cosines. $b=\frac{\hat{s}_0\cdot\hat{n}}{\hat{s}_H\cdot\hat{n}}$ where $\hat{s}_0$, $\hat{s}_H$, are unit vectors in the incident and diffracted beam directions and n̂ is a unit vector in the outward surface normal direction.

For Bragg reflection geometry b is negative. (For Laue transmission geometry b is positive.)

SWAM assumes a Bragg reflection geometry.

For a miscut crystal, $\hat{s}_0$, $\hat{s}_H$, $\boldsymbol{H}$ and $\hat{n}$ all lie in the same plane,

$|b| = \frac{\sin(\theta_B - \Phi)}{\sin(\theta_B + \Phi)}$, where Φ is the miscut angle or the angle between $\boldsymbol{H}$ and $\hat{n}$

Where Φ is the miscut angle or the angle between $\boldsymbol{H}$ and $\boldsymbol{n}$ and $\boldsymbol{\theta_B}$ is the Bragg angle

For a symmetric Bragg reflection |b| = 1. For a glancing exit asymmetric condition |b| > 1. For a glancing incidence asymmetric condition |b| < 1.

Refraction optically affects the Bragg reflectivity in the following way:

a) $(\omega_{out} / \omega_{in}) = |b|$, where ω_{out} is the angular emission width and ω_{in} is the angular acceptance width of the reflection.

b) Due to refraction the center of the Bragg peak is found at a higher angle than predicted by Braggs' Law. This offset increases as the incident angle becomes more glancing.

Note that when performing an **H** = hkl off-specular XSW measurement, it is desirable to simplify the analysis by adjusting the sample goniometer to make |b|=1.

This is done by tilting the goniometer χ angle to the angle separating **H** and $\hat{\mathbf{n}}$ and then rotating the goniometer azimuthal ϕ angle until the reflection appears in the same scattering plane as used for the specular XSW measurement. This alignment is most easily done by using an X-ray camera on the 2θ arm for imaging the specular reflected beam and then later finding the off-specular reflected beam.

5.) **Polarization Factor**: P, is defined by the E-field X-ray polarization directions of the incident and diffracted plane waves as: $P = \hat{\epsilon}_0 . \hat{\epsilon}_H$

i.) For π polarization geometry, where $\hat{\epsilon}_0 \; and \; \hat{\epsilon}_H$ lie in the scattering plane defined by the incident and scattered wave vectors, $P = \cos(2\theta_B)$. (typical case at Diamond I09)

ii.) For σ polarization geometry, where $\hat{\epsilon}_0 \; and \; \hat{\epsilon}_H$ lie ⊥ to scattering plane, P = 1 (typical case at APS-5IDC)

iii.) For unpolarized (lab source), the 2 cases need to be added together at the level of intensity with a weighting factor determined by the upstream optics.

6.) **+/- y_z Range**: Range over which Mono emission function is calculated. This is input range for the calculations of normalized angle (or energy) parameter y_z. Note that we define y_z as a positive going angle (or energy) scale. Whereas, η is a backward normalized scale parameter used in Batterman and Cole and in Bedzyk MSE461 Notes. The monochromator reflectivity emission function is calculated in even steps over this y_z range and then convoluted with the acceptance reflectivity and yield of the sample. The SWAM y_z is the negative of Pinsker's y_z, which was used in DARE and SWAN and earlier versions of SWAM.

$$y_Z(\Delta\theta) = \frac{|b|\Delta\theta \mathrm{Sin}\,(2\theta_B) - \frac{(1+|b|)}{2}\chi_0{}'}{|P|\sqrt{|b|}\mathrm{Re}\,(\sqrt{\chi_H\chi_{\bar{H}}})}$$

or, in terms of ΔE,

$$y_Z(\Delta\mathrm{E}) = \frac{2|b|\frac{\Delta\mathrm{E}}{E}\mathrm{Sin}^2(\theta_B) - \frac{(1+|b|)}{2}\chi_0{}'}{|P|\sqrt{|b|}\mathrm{Re}\,(\sqrt{\chi_H\chi_{\bar{H}}})}$$

y_z , which is real, is a normalized angle (or energy) scale parameter.

$y_z = 0$ → center of Bragg band gap, mid point between dispersion surfaces in k-space

$y_z = -1$ → low-angle (or low-energy) edge of Bragg band gap, α-branch diameter point of dispersion surface

$y_z = 1$ → high-angle (or high-energy) edge of Bragg band gap, β-branch diameter point of dispersion surface.

Note here that straightforward transitions between ΔE and Δθ can be made by using the double-angle formula, $\mathrm{Sin}(2\theta_B) = 2\,\mathrm{Sin}(\theta_B)\,\mathrm{Cos}(\theta_B)$ and the substitution $\Delta\theta = -\frac{\Delta\mathrm{E}}{E}\mathrm{Cot}\,(\theta_B)$, derived

from differentiating Braggs' law. The value is typically set at y_z Range = 3 in order to calculate R_B across the entire Darwin range as well as include significant off-Bragg regions.

7.) The **Crystal Temperature**: (300 K) is used in the calculation of the Debye-Waller factor.

8.) **Reflectivity Plot Option**: (1) allows the user to plot the Darwin curve on the θ-scale or E-scale. Select 0/1/2 for no plot / θ–plot / E-plot.

B.3.2 Calculations

Once all the crystal information is loaded, the relevant parameters are calculated. Each parameter is defined and referenced within the code, but symbolic definitions are supplied below for reference. These definitions are consistent throughout the routines. Note that values are often appended with a M or S to distinguish monochromator crystal values from sample crystal values, especially in r0.m and f1.m functions. Definitions persist through the other main functions.

Crystal and Diffraction Parameters

Most critical parameters are listed below.

1.) Energy is the incident beam energy, in keV.

2.) Crystal is the crystal- needs to match the .ctl file..

3.) hkl are the (h,k,l) indicies of the reflection plane.

4.) b is the crystal asymmetry factor.

5.) P is the polarization factor for the scattering geometry.

6.) yzRange defines half-range in yz over which the rocking-curve calculations will take place, as defined in Pinsker.

7.) T is the crystal temperature in Kelvin.

8.) lambda (λ), the X-ray wavelength (Å).

9.) re is r_e the classical electron radius (Å).

10.) Vuc is $V_{u.c.}$, the unit cell volume ($Å^3$). Note that although the .ctl includes linear expansion coefficient, SWAM does not use the values and therefore temperature is not taken into account during calculation of $V_{u.c.}$

11.) d-spacing is the d_{hkl} of the chosen set of planes (Å). Note that although the .ctl includes linear expansion coefficient, SWAM does not use the values and therefore temperature is not taken into account during calculation of d_{hkl}.

12.) thB is the Bragg angle, θ_B (rad) based on Braggs' Law.

13.) gam is the dimensionless scale factor $\Gamma = \frac{r_e \lambda^2}{\pi V_{u.c.}}$

14.) hkl0 defines the forward-scattering condition: (h,k,l) = (0,0,0).

T_D: Debye Temperature (K) from ctl file, T_D → Thermal vibrational amplitude → Debye Waller Factor $eM=e^{-M}$ where $M \propto T/T_D^2/d_{hkl}^2$

15.) F0, FH, and Fhb are the H = 0,H, and -H complex structure factors (= $= F_0, F_H,$ and$F_{\bar{H}}$.). The H≠0 structure factor should be multiplied by eM.

16.) ChiF0, ChiFh, and ChiFhb are the susceptibilities, χ_0, χ_H and $\chi_{\bar{H}} = -\Gamma F_0, -\Gamma F_H$ and $-\Gamma F_{\bar{H}}$. Note the negative sign.

17.) g is the imaginary part of the numerator in the equation (from Pinsker) used to define the dimensionless angular parameter, y, used in the calculation of the E-field amplitude ratio (see below).

18.) rkappa is the imaginary part of the denominator of the equation (from Pinsker) used to define the dimensionless angular parameter, y, used in the calculation of the E-field amplitude ratio (see below).

19.) omegaTh is the acceptance angular Darwin width $\omega_\theta = \frac{2/P/\Gamma\sqrt{F_H' F_{\bar{H}}' + F_0''^2 - F_H'' F_{\bar{H}}''}}{\sqrt{|b|}\sin(2\theta_B)}$, in μrad.

20.) omegaE is the energy Darwin width $\omega_E = E\,\omega_\theta \cot(\theta_B)$, in eV. (Based on the derivative of Braggs' Law.)

21.) AngOffSet is the offset of Bragg peak from θ_B due to refraction, $\Delta\theta_{yz=0} = \frac{|\chi_0'|}{\mathrm{Sin}\,(2\theta_B)}\frac{1+|b|}{2|b|}$ in μrad.

22.) EnergyOffSet is the offset of Bragg peak from geometrical Bragg condition $\Delta E_{yz=0} = \frac{E|\chi_0'|}{2\mathrm{Sin}\,(\theta_B)^2}\frac{1+|b|}{2|b|}$, in eV.

23.) Refl is the calculated $|\frac{E_H}{E_0}|^2$ across the Darwin curve, R_B.

24.) chir = $\chi_r = \sqrt{\chi_H'\chi_{\bar{H}}' - \chi_H''\chi_{\bar{H}}'' + (\chi_0'')^2}$, is a component used during the calculation of the Darwin width, \[Omega]. See Bedzyk and Cheng, RMG, 2002.

25.) The phase (v) of $\frac{E_H}{E_0}$, v = ArcTan (Im $(\frac{E_H}{E_0})$/Re $(\frac{E_H}{E_0})$). v decreases by π as $\Delta\theta$ or ΔE is advanced across the Bragg band gap (strong reflection condition). On the high angle or energy side of the Bragg band gap, v → the phase of F_H.

Parameters for calculation of wave amplitude ratio WAR = $\frac{E_H}{E_0}$

The next two parameters are defined by L. Cheng as g and r_κ, and are inputs for the calculation of the E-field amplitude ratio, = $= \frac{E_H}{E_0} = \frac{|P|}{P}\sqrt{|b|}(\frac{F_H}{F_{\bar{H}}})^{1/2}\left(y \pm (y^2-1)^{1/2}\right)$. We follow Pinsker's definition (Eq. 8.78), which gives complex y = $\frac{y_z+ig}{1+ir_\kappa}$, where:

1.) $g = \frac{1}{2}\frac{\chi_0''}{\mathrm{Re}\,(\sqrt{\chi_H\chi_{\bar{H}}})}\frac{(1+|b|)|P|}{\sqrt{|b|}}$

2.) $r_\kappa = \frac{\mathrm{Im}(\sqrt{\chi_H\chi_{\bar{H}}})}{\mathrm{Re}(\sqrt{\chi_H\chi_{\bar{H}}})}$

Absorption and Extinction Parameters:

1.) delta, beta, and alphac, are the components of the index of refraction, $n = 1 - \delta - i\beta$, and the critical angle alphac = $\alpha_c = \sqrt{2\delta}$.

2.) rmuin is the linear absorption coefficient, $\mu_0 = \frac{2\pi}{\lambda}\Gamma F_0'' = -\frac{2\pi}{\lambda}\chi_0''$, (1/Å).

3.) SinPhi appears to be (I think) the sine of back-calculated offcut Φ.

4.) phi is the angle, Φ, between the diffraction planes and the surface normal.

5.) zpref is the penetration depth prefactor for calculations of ZeffOffB and Zeff. zpref = $\frac{\lambda}{2\pi}\mathrm{Sin}\,(\theta_B - \Phi)$

6.) ZeffOffB is the effective off-Bragg penetration depth, $Z_{\mathrm{eff}}(\eta >> 1)$ = - $\frac{\mathrm{Sin}\,(\theta_B - \phi)}{\chi_0''}$, reported in μm.

7.) ZeffOnB = is the effective on-Bragg penetration depth $Z_{\mathrm{eff}}(\eta = 0) = \frac{\lambda}{2\pi}\frac{\mathrm{Sin}\,(\theta_B - \phi)}{\frac{\sqrt{|b|}}{|P|}\sqrt{|\frac{\chi_H}{\chi_{\bar{H}}}| - \chi_0''}}$, reported in μm.

B.3.3 Output

Calculated values are then output in figure box below, and the user is given the option to write results into a text file. A theoretical rocking curve is also calculated and displayed:

Dynamical Diffraction Calculations

Parameters	Symbol	Values	Units
Crystal File Name:	-	ge.ctl	-
Reflection Plane:	hkl	(1,1,1)	-
Lattice Parameters:	(a, b, c)	(5.6575,5.6575,5.6575)	(A)
Lattice Parameters:	(α, β, γ)	(90,90,90)	(deg)
hkl d-spacing:	d_{hkl}	3.2664	(A)
X-ray Energy:	E	8.04	(keV)
X-ray Wavelength:	λ	1.5421	(A)
Crystal Temperature:	T_{xtal}	300	(K)
Unit Cell Volume:	V_{uc}	181.0852	(A^3)
Scale Factor:	Γ	1.1779e-07	-
Linear Absorption Coefficient:	μ_{in}	340.5869	cm^{-1}
Bragg Angle:	θ_B	13.6538	(deg)
Crystal Asymmetry Factor:	b	-1	-
Polarization:	P	1	-
Debye Temperature:	T_D	400	K
Structure Factor (H = 0):	F_0	246.5975+7.0964 i	-
Structure Factor (H = H):	F_H	107.588-100.5431 i	-
Structure Factor (H = -H):	F_{-H}	100.5431+107.588 i	-
Susceptibility (H = 0):	χ_0	-2.9047e-05-8.3591e-07 i	-
Susceptibility (H = H):	χ_H	-1.2673e-05+1.1843e-05 i	-
Susceptibility(H = -H):	χ_{-H}	-1.1843e-05-1.2673e-05 i	-
Normalized Phase of F_H:	φ(H)/2π	0.88039	rad/2π
Normalized Phase of F_{-H}:	φ(H)/2π	0.13039	rad/2π
Imaginary Component of η, Denominator:	r_κ	0.033848	-
Imaginary Component of η, Numerator:	g	-0.048219	-
Angular Darwin Width:	ω_θ	75.6196	μrad
Energy Darwin Width:	ω_E	2.5028	eV
Offset from θ_B:	Δθ	-63.3162	μrad
Offset from E_B:	ΔE	-2.0956	eV
Off-Bragg Extinction Depth:	Λ	6.9308	μm
On-Bragg Extinction Depth:	$\Lambda_{\eta'=0}$	0.31865	μm
Half-range of y_z Calculation:	y_z	3	0.5ω
Normalized XSW Phase at $\pm y_z$:	$\phi(\pm y_z)/2\pi$	0.378,-0.11658	rad/2π
Index of Refraction:	n = 1-δ-i β	1-1.4524e-05-4.1795e-07 i	-
Critical Angle:	α_c	5.3896	mrad

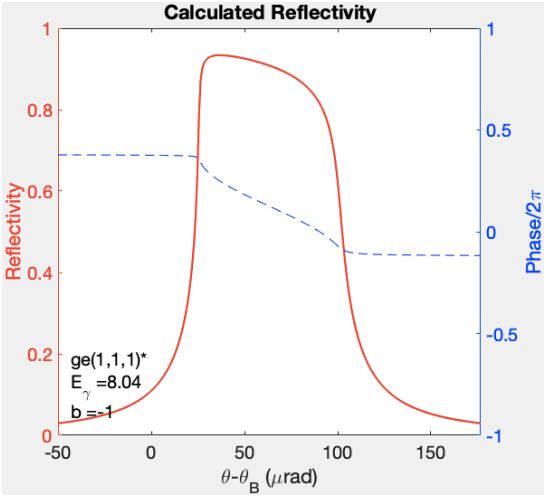

B.4 *r0.m: Rocking Curve Fitting Procedure*

r0.m is the function used to fit the measured Darwin curve to theory. It convolutes the theoretical monochromator emittance function with the sample crystal's theoretical rocking curve and uses a least-squares fitting routine (leasqrpf.m) to fit the calculated Darwin curve to the measured one.

B.4.1 Structural Flow Chart

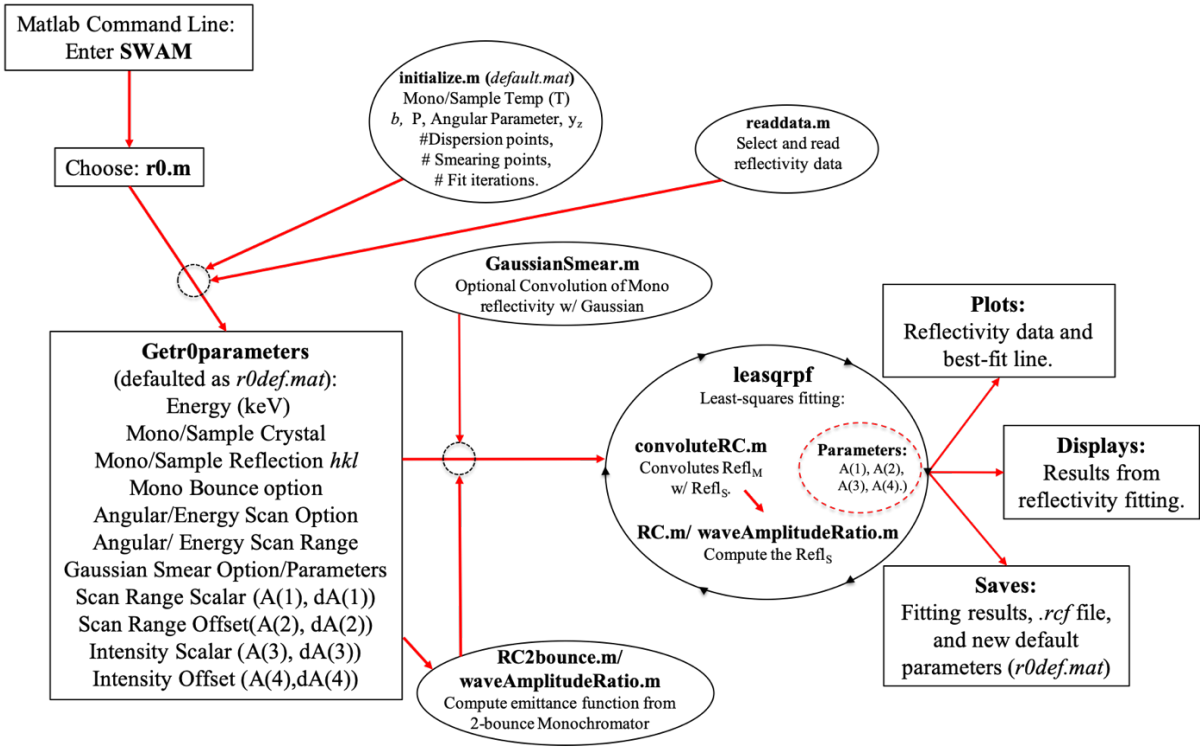

B.4.2 Initialization

The r0.m initialization routine prompts for user input that will affect the calculation and convolution of the rocking curves:

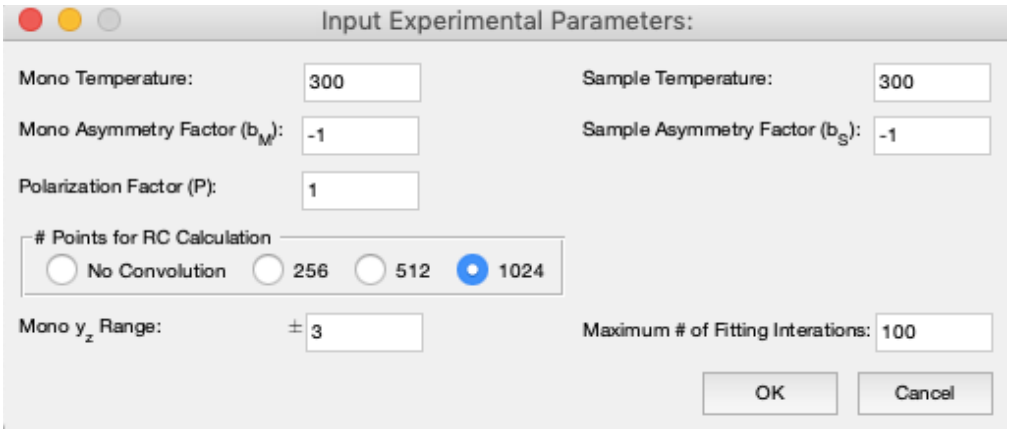

1.) Two crystal temperatures, one for the mono (TempM) and one for the sample (TempS), are used in the calculation of the Debye-Waller factor.

2.) The polarization factor, P, as defined in the cr.0 section.

3.) The b-factor of the sample, as defined in the cr.0 section.

4.) The number of calculated points for the Mono RC (ConvPoints) defines the number of simulated points for the R_B calculation for the mono.

5.) The Half-angular range of the reflectivity calculation, as defined by parameter y_z

After the experimental parameters are inputted, SWAM prompts for the reflectivity datafile, which is in a tab-delimited format with {Step, Reflectivity, Error} stored in each of the columns. Files should contain the string 'refl' somewhere within the filename so they can be easily found within the directory by the file filter. To use this interface (from uipickfiles.m) the user should select the desired file on the right-side panel, press "add", and then press "done".

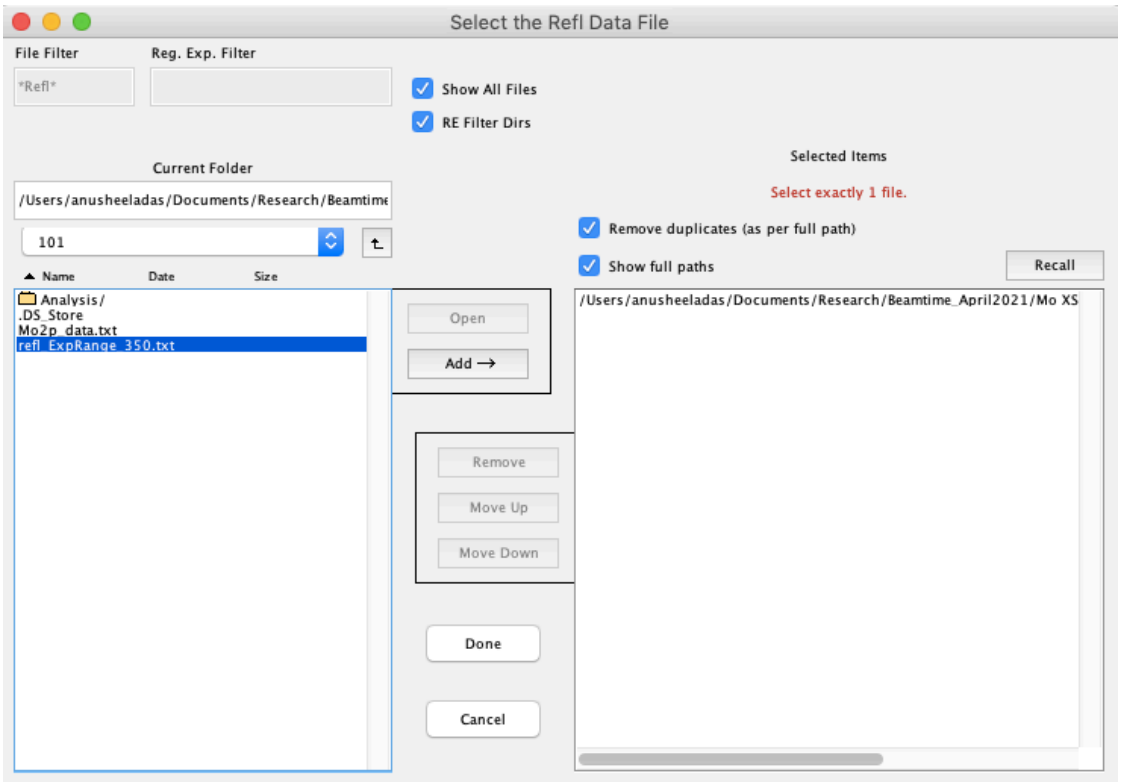

Next, the crystal information and the parameters for the rocking curve fitting are requested:

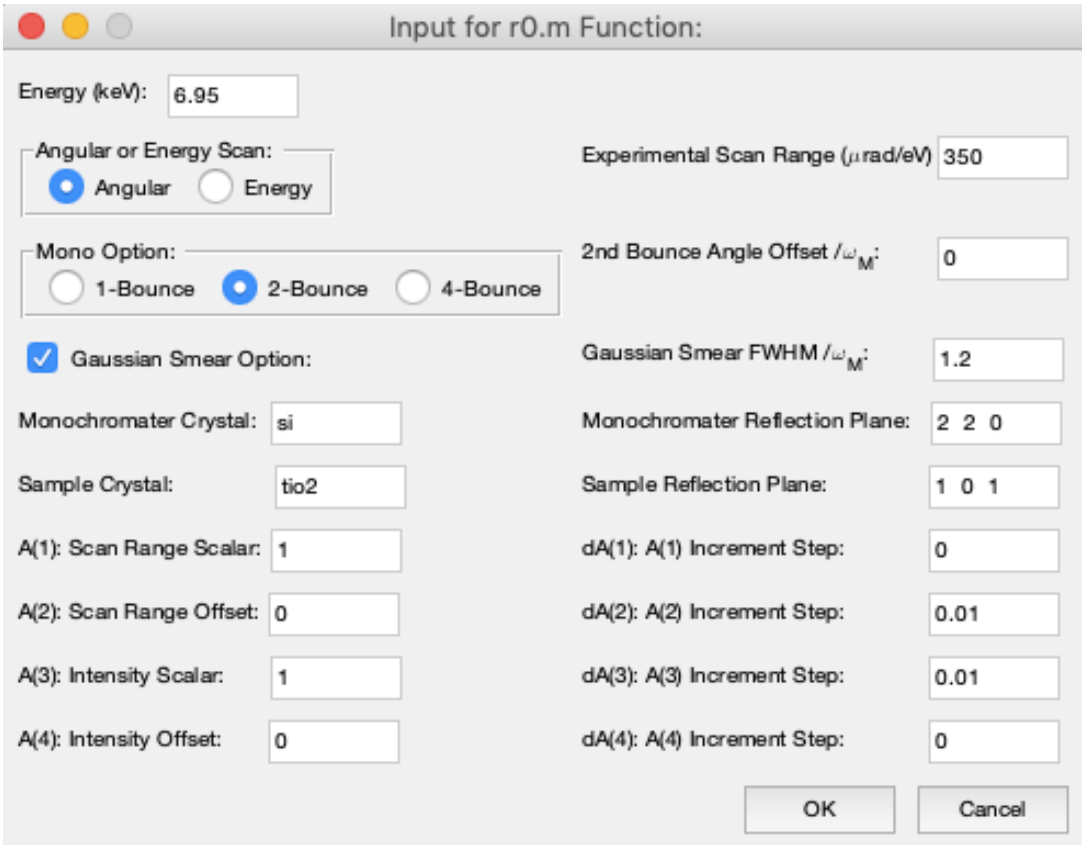

The first 8 inputs are straightforward crystal parameters and the detune option (in percent of Darwin width, discussed below). A(1-4) are the fit parameters. dA(1-4) are the allowed fractional incremental changes for numerical partials during fitting. To keep values close to the original guesses, pick dA to be small. To inhibit a parameter from fitting, set that value of dA to 0.

1.) A(1) is the scaling parameter for the scan range. Typically this should be set to 1, with no fit (i.e., A(1) = 0) because the scan ranges are generally well-known.

2.) A(2) is the angular/energy offset from the calculated Bragg center point $(\theta - \theta_B)$ in experimental steps. This is not typically well-known (slight changes in energy or misalignment) can cause this to be different from the calculated value. It is commonly fit.

3.) A(3) is the intensity scale. The absolute reflectivity may be known but is commonly unknown. This factor allows for scaling of the reflected intensity during fitting.

4.) A(4) is currently an open parameter for future allocation. It is my recommendation that we utilize this parameter for Gaussian smearing function. Currently the Gaussian smear factor is guessed, not fit, which requires tedious guess-and-check smear input. Note that if we do include a Gaussian smear fit parameter it may correlate with either A(1) or A(3), so we will need to be careful.

5.) Gaussian Smear (y/n)? This allows for the smearing of the monochromator reflectivity curve with a Gaussian in order to account for sample mosaic or strain.

6.) Gaussian Smear Factor width (omegaM): If Gaussian Smear is activated, one chooses a "Gaussian Smear Factor" (called sfactor in routine), which is related to the Gaussian width. The Gaussian FWHM is the smear factor times monochomator reflectivity width $\mathrm{sfactor} * \omega_M$, so it is not crystal-independent.

7) If there are 2 channel cuts then the 2nd channel cut will have a detune wrt to first and is marked as 2nd Bounce Angle Offset

B.4.2 Outputs

Calculated values are then output in figure box below, and the user is given the option to save the output as a text file. After that the user has to save the .rcf file which will be read into the next segment (f1.m). The user is also given the option to save the output figure which shows the data and the fit.

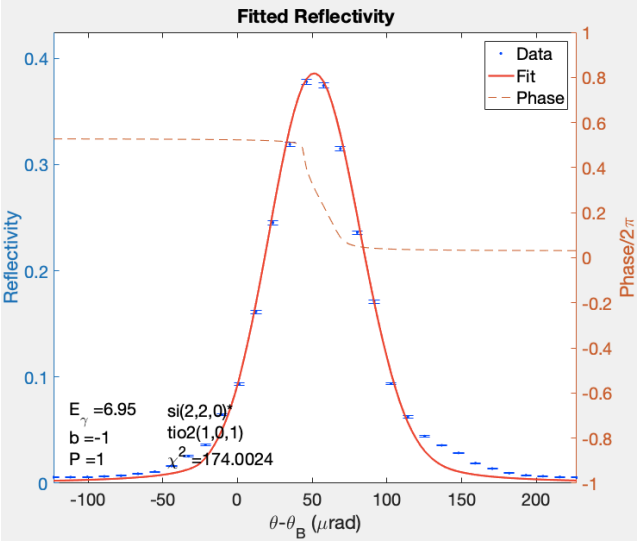

Reflectivity Fit Results

Parameters	Value/Result	Fit?
X-ray Energy, (keV):	6.95	-
Monochomater File Name:	si.ctl	-
Sample File Name:	tio2.ctl	-
Monochometer Reflection Plane, hkl_M	(2,2,0)	-
Sample Reflection Plane, hkl_S	(1,0,1)	-
Monochometer Asymmetry Factor, b_M:	-1	No
Monochometer Asymmetry Factor, b_M:	-1	No
Experimental Angular Scan Range (μrad):	350	-
Starting Input: A(1) Range Scale:	1	No
Starting Input: A(2) Angular Offset (steps):	0	Yes
Starting Input: A(3) Intensity Scale Factor:	1	Yes
Starting Input: A(4) Intensity Offset:	0	Yes
Fitting Results: Scaled Angular Range (μrad):	350	No
Fitting Results: Geometrical Bragg Angle (Step number):	10.0157	Yes
Fitting Results: Reflectivity Scaling Factor:	1.0013	Yes
Fitting Results: Maximum Reflectivity:	0.3859	Yes
Fitting result: A(1) Range Scale Factor:	1±0	No*
Fitting result: A(2) Range Offset:	-0.30398±0.064453	Yes*
Fitting result: A(3) Intensity Scale Factor:	1.0013±0.031126	Yes*
Fitting result: A(4) Intensity Offset:	0±0	No*
Final χ^2 Value:	174.0024	-

B.5 *f1.m: XSW yield Fitting Procedure*

f1.m is the function used to fit the measured XSW yield in order to extract coherent fractions (f_H) and coherent positions (P_H) of the species of interest. It loads in the results of the rocking curve fitting (the .rcf file) and the yield data, accounts for both Gaussian smearing and smearing from the mono via numerical convolutions, and then fits the data to the XSW yield equation, $Y = 1 + R_B + 2P\sqrt{R_B}f_H \mathrm{Cos}\,(\upsilon - 2\pi P_H)$. The routine can also account for the affects of absorption and contributions external contributions to the yield (Yield Offset), if desired.

B.5.1 Structural Flow Chart

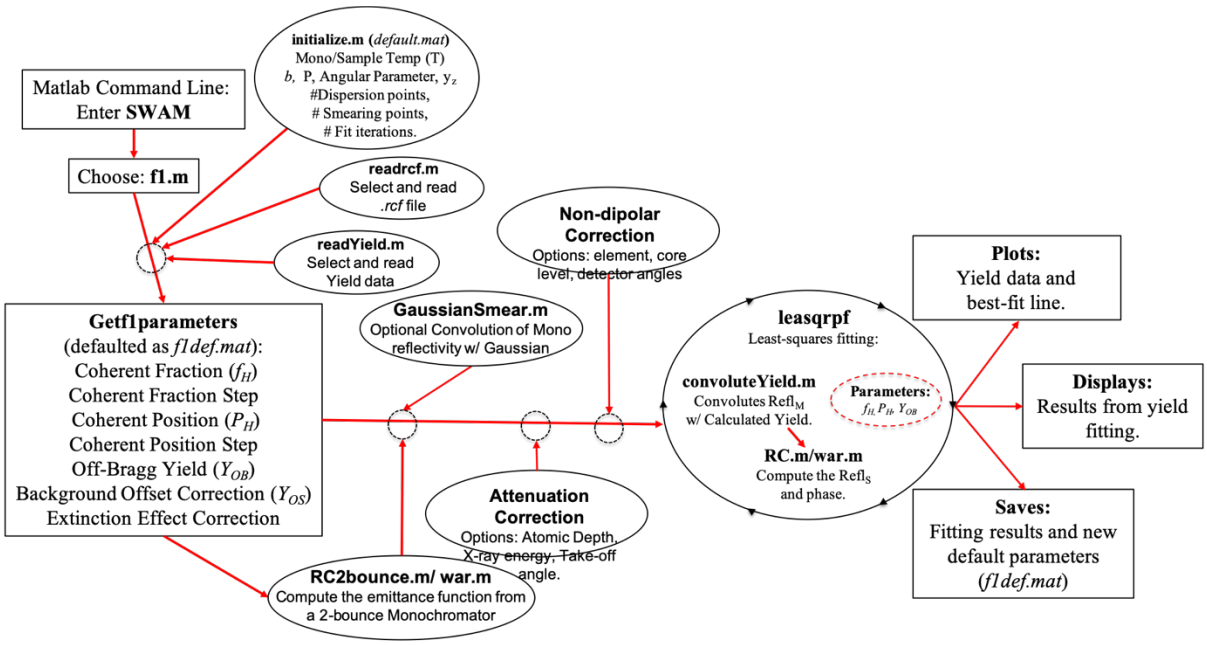

B.5.1 Initialization

The f1.m initialization routine prompts for user input that will affect the yield calculations and convolutions, as well as the fitting of the yield data. This is the same prompt found in r0.m. These values, at least the values for crystal temperatures, polarization factors, and b-factor should be

consistent with those used the r0.m. It is odd to me that those are prompted for again and not written/read in from the rcf file seeing as they should be the same as those used in r0.m.

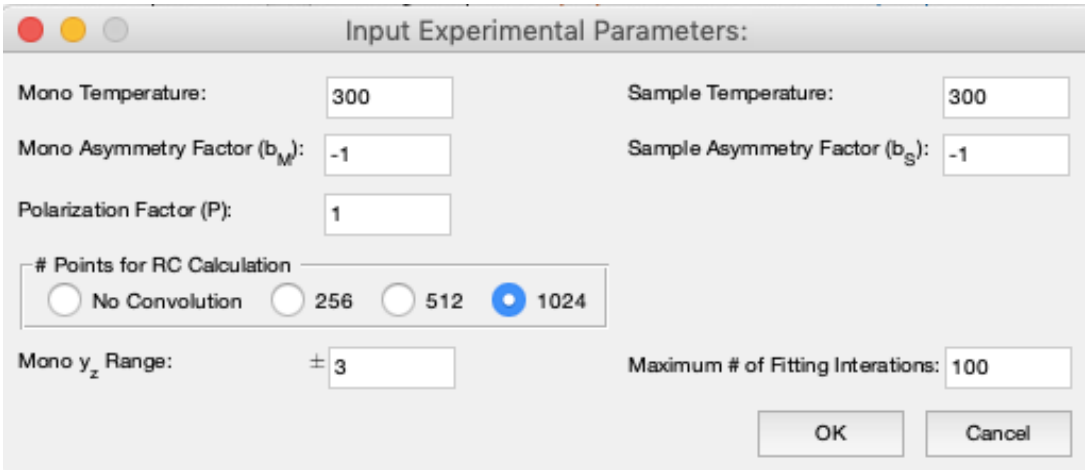

1.) Two crystal temperatures, one for the mono (TempM) and one for the sample (TempS), are used in the calculation of the Debye-Waller factor.

2.) The polarization factor, P, as defined in cr.0 section.

3.) The b-factor of the sample, as defined in cr.0 section.

4.) The number of calculated points for the Mono RC (ConvPoints) defines the number of simulated points for the mono calculation.

5.) The Half-angular range of the reflectivity calculation, as defined by parameter y_Z (see cr.0 for definition).

6.) The number of dispersion points (NDSP) defines how many points are used in the application of the dispersion spread. This is fairly ambiguous- see below.

7.) The number of smearing points per angular interval (ConvSmear) dictates the smearing extent of the numerical convolution. This value is typically ~5

After the experimental parameters are inputted, SWAM prompts for the rcf file, which contains pertinent crystal information found during the rocking curve fitting. rcf files should contain the string 'rcf' somewhere within the filename in order to be found easily by the file filter. f1.m then

prompts for the yield data file, which is a tab-delimited file with {step, yield, error} in the columns. To facilitate file retrieval, the user should include the string 'XSW_Input' somewhere within the filename. To use this interface (from uipickfiles.m) the user should select the desired file on the right-side panel, press add, and then press done. Currently, only one file can be loaded at a time.

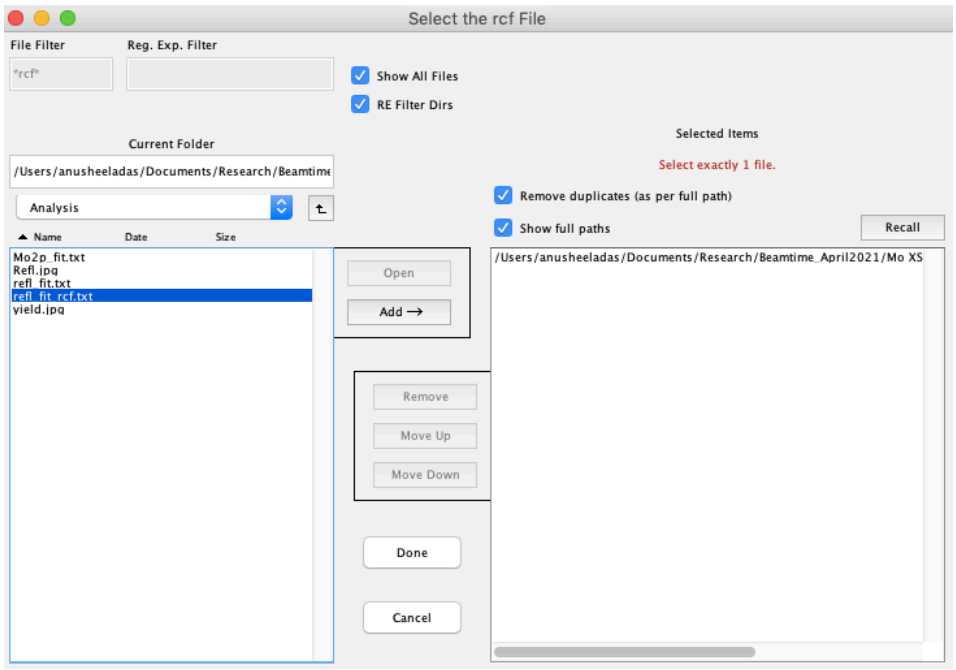

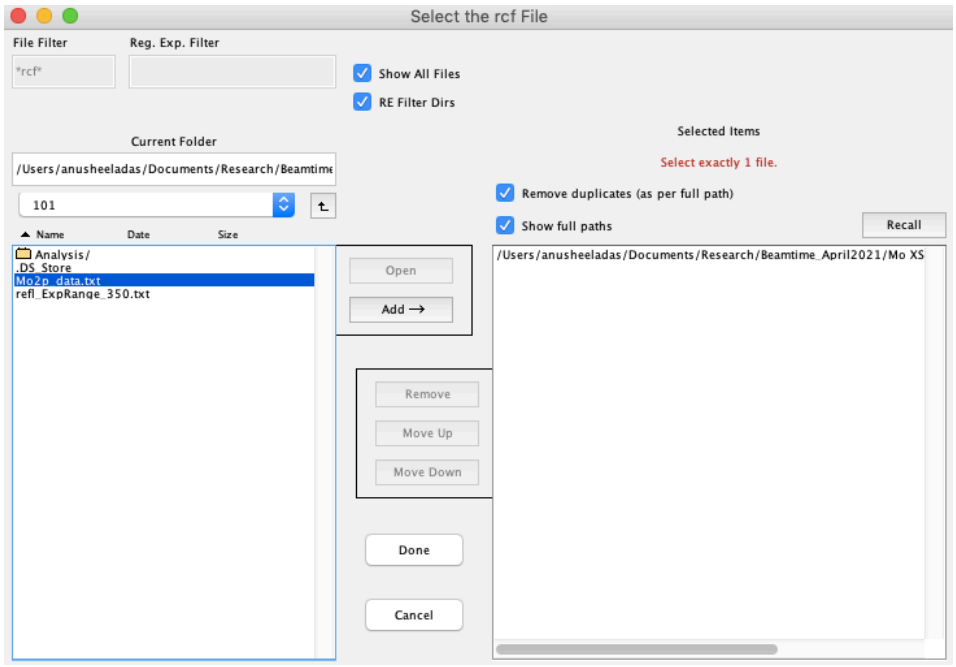

Next, the starting parameters for the yield fitting are requested:

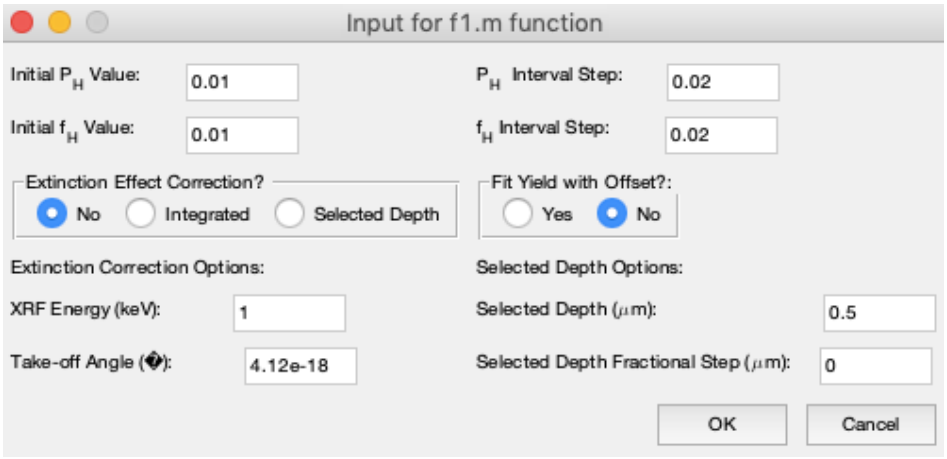

1.) The Coherent Fraction, f_H is requested in the first line. Values between 0-1 should be entered, but coherent fractions above 1.0 can be tolerated.

2.) The f_H Interval Step is requested on the second line. An input of 0 will set the coherent fraction. Small non-zero values will keep the f_H close to its default value.

3.) The Coherent Position, P_H is requested in the third line. Values between 0-1 should be entered. Coherent positions above or below these values are tolerated but are simply n x 2π phase-shifted.

4.) The P_H Interval Step is requested on the fourth line. An input of 0 will set the coherent fraction. Small non-zero values will keep the f_H close to its defaul value.

5.) Fit with Offset (y/n)? This allows for a yield offset to be included in the analysis. These may arise from background signals that are contributing to photoelectron or fluorescence background. This is typically utilized when analyzing XRF yield from transition metal elements such as Fe or Cu because these elements are common in experimental environments (sample stages, electrical leads Be domes, diffractometers) and are difficult to eliminate. Users should avoid this option unless absolutely necessary because it can greatly affect the incoherent contribution to the XSW yield.

6.) Extinction Effect Correction: This option allows the user to correct for attenuation effects when atoms are located deep within the crystal (on the order of the extinction depth). For surface species, this correction is typically 0 (sample depth << extinction depth), but the user can also choose a selected path (atoms located at a specific depth) or an integrated correction (atoms located throughout the bulk).

If extinction effect correction is used, the user has to input the characteristic X-ray energy and take-off angle (angle between crystal surface and detector axis). If the selected path option is selected, the user has to input the depth of the atomic species, and the step size over which the selected depth calculation will be performed.

Non-dipolar corrections

To analyze X-ray photoelectron yield data, non-dipolar corrections are added in the sub-function convoluteYield.m. The user is prompted to input the following parameters:

1.) The element whose XPS yield is being analyzed

2.) The XPS core level whose data was collected

3.) The detector Angles θ and ϕ are the spherical coordinates for the direction of the emitted photoelectron, where the z-axis is the polarization direction of the incident X-ray. For our experimental geometry the central axis of the acceptance cone for the photoelectron detector is aligned with the polarization direction (z-axis).

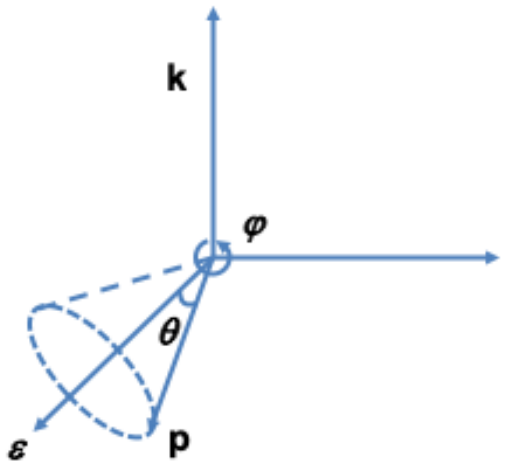

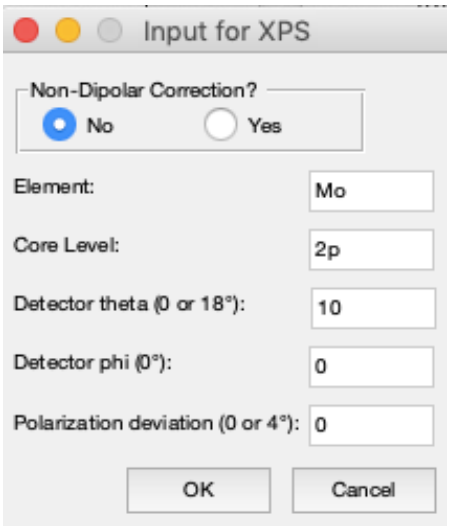

B.5.2 Outputs

Two figures are output after fitting. One is a plot of the measured yield data and the fit, shown below, left. The output has been upgraded show rounded f_H and P_H and uncertainties. The printing of these parameters, however, isn't entirely clean and should probably be upgraded using the textbp.m text placement tool, but initial efforts to use this tool weren't successful. The second panel shows results from the yield fitting.

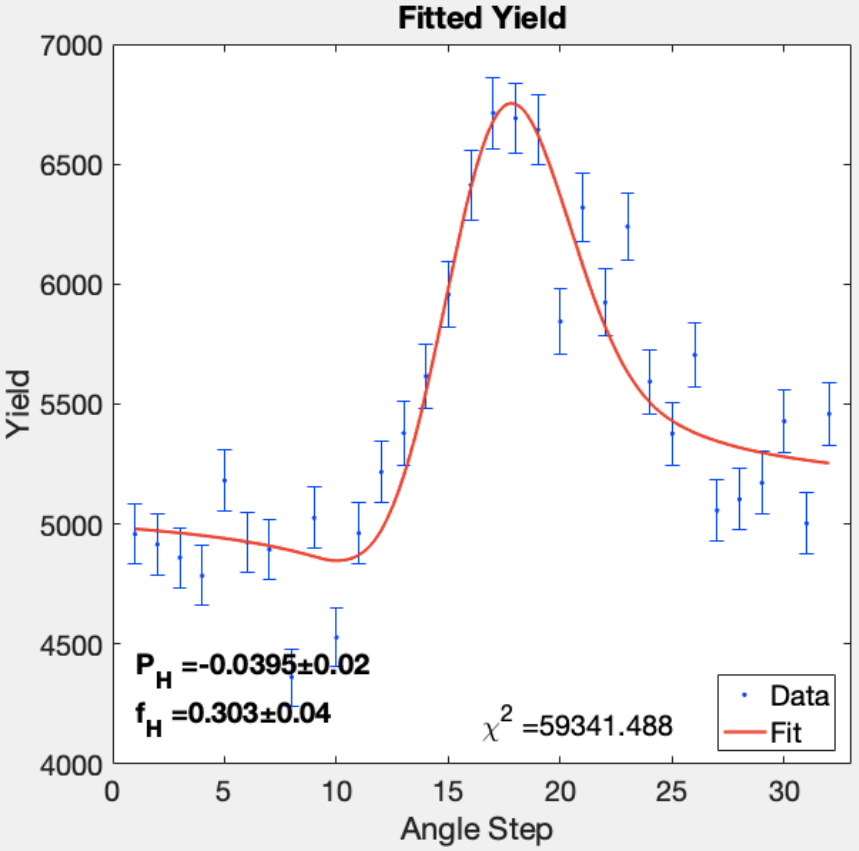

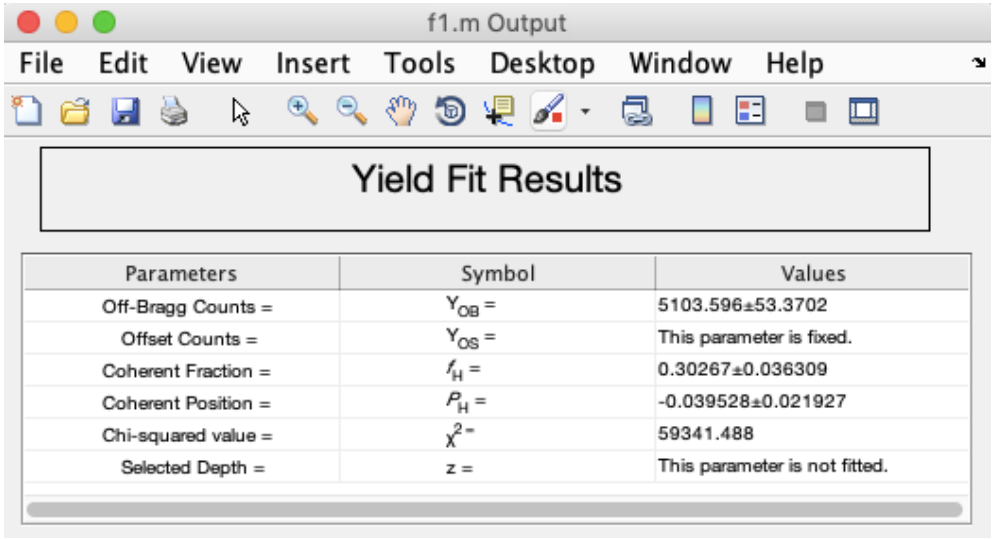

Parameters	Symbol	Values
Off-Bragg Counts =	Y_{OB} =	5103.596±53.3702
Offset Counts =	Y_{OS} =	This parameter is fixed.
Coherent Fraction =	f_H =	0.30267±0.036309
Coherent Position =	P_H =	-0.039528±0.021927
Chi-squared value =	χ^2 =	59341.488
Selected Depth =	z =	This parameter is not fitted.

B.6 *chi2.m for error analysis*

chi2.m is an error analysis routine that explores the goodness-of-fit value χ^2 about the best-fit minimum for both f_H and P_H found in the f1.m analysis routine. The magnitude of this standard deviation will, in general, provide an indication of the uncertainty value associated with the fit.

B.7 Function Directory

The initialization function is called by navigating to the most current SWAM version directory in the Matlab command window and typing SWAM (case sensitive) into the command line. SWAM provides the user with three choices: cr.m: Dynamical Diffraction Calculator, r0.m: Rocking Curve Fitting Routine, and f1.m: XSW Yield Fitting Routine.

Main functions

1.) cr.m: Dynamical Diffraction Calculator: This routine prompts the user for experimental parameter input and a crystal .ctl file, and then uses the input to perform and output relative single-crystal diffraction calculations.

2.) r0.m: Rocking Curve Fitting Routine: This routine fits theoretical rocking curves to measured data. The three main components of this routine are the rocking-curve calculators, RC.m and RC2bounce.m, the numerical convolution routine (convoluteRC.m), and the critical Levenberg-Marquardt nonlinear regression least-squares fitting routine, leasqrpf.m written by Ray Muzic and Arthur Jutan. This file outputs the so-called .rcf file, which is used in fitting of the XSW yield.

3.) f1.m: XSW Yield Fitting Routine.

Sub-functions

FileName	Function
calcd.m	Calculates $d-$ spacing.
calcem.m	Calculates Debye– WallerFactor.
calcf.m	Calculates StructureFactor.
calcphix.m	Calculates phix for Debye $-$ Waller.
calcref.m	Calculates E_H/E_0 ratio
calcv.m	Calculates unit cell volume.
convoluteRC.m	Convolutes sample RC with mono
convoluteYield.m	Convolute yield with mono
$cromermat$	Calculates $f'$and$f$".
$dfdppf$	Supplies Jacobian to leasqr.m
filesave.m	Saves data into a designated file.
GaussianSmear.m	Broadens mono reflectivity
GetAtomDepth.m	Selected depth input.
GetExitInfo.m	Broadens mono reflectivity
Getf1Parameters.m	Gets user input for f1.m
getfcoef.m	Retrieves atomic form factor info
initialize.m	Prompts for experimental details
inputsdlg.m	Creates input dialog box
leasqrpf.m	Does least $-$ squares fitting
lookup.m	Gets atomic mass for an element
MFquestdlg.m	Modified question box
RC.m	Calculates E_H/E_0 for1 $-$ bounce
RC2bounce.m	Calculates E_H/E_0 for2 $-$ bounce
$rcfFileSave$	Saves rcf file
readctl.m	Reads .ctl file
readdata.m	reads data files
readrcf.m	Reads rcf file
readReflData.m	Reads reflectivty data
readYieldData.m	Reads yield data
textbp.m	Best– placement of text boxes
uipickfiles.m	File Selector

Example of a .ctl file for TiO_2

```
TiO2
  4.5933    4.5933    2.9592     90.00    90.00    90.00
  370.
  5.2       5.2       5.2
  2   1   1
Atoms in basis # 1        ! C.R. Wie, Materials Science and Eng R13
 ti+4  22  1.00
  2
  0.000   0.000   0.000
  0.500   0.500   0.500
Atoms in basis # 2
 o -2   8  1.00
  4
  0.3053  0.3053  0.000
 -0.3053 -0.3053  0.000
  0.8053  0.1947  0.500
 -0.8053 -0.1947 -0.500
```

Example of a refl input data file

```
1       0.005642857   0.000283923
2       0.005771429   0.000287139
3       0.005928571   0.000291022
4       0.006428571   0.000303046
5       0.007114286   0.000318799
6       0.008885714   0.000356285
7       0.010928571   0.000395123
8       0.016218977   0.000481072
9       0.025385714   0.000602207
10      0.036178787   0.000718132
11      0.064457143   0.000959592
12      0.093057143   0.001152991
13      0.161328571   0.001518122
14      0.245342857   0.001872137
15      0.319142857   0.002135225
16      0.377985714   0.002323746
17      0.374442857   0.002312831
18      0.314942857   0.002121128
19      0.235971429   0.001836034
20      0.170828571   0.001562181
21      0.093878999   0.001157584
22      0.062628571   0.000945883
```

23	0.044357143	0.000796036
24	0.035714286	0.000714286
25	0.028528571	0.000638397
26	0.018943355	0.000519615
27	0.013842857	0.000444697
28	0.009514286	0.000368671
29	0.007528571	0.000327953
30	0.006642857	0.000308055
31	0.005871429	0.000289616
32	0.005414286	0.000278113

Example of an XPS yield input data file

1	4958.68	126.7522118
2	4916.13	126.2072153
3	4859.99	125.4845313
4	4784.42	124.5051035
5	5181.09	129.5636199
6	4924.71	126.3173005
7	4893.78	125.9200032
8	4361.55	118.8756577
9	5025.72	127.6061629
10	4527.48	121.1157925
11	4962.07	126.7955315
12	5217.15	130.0137147
13	5378.98	132.0147537
14	5615.92	134.8909961
15	5956.78	138.9243218
16	6412.64	144.1421299
17	6713.32	147.4827339
18	6691.11	147.2384596
19	6643.07	146.7090549
20	5844.16	137.6047906
21	6319.46	143.0910563
22	5923.04	138.5303201
23	6239.64	142.1845055
24	5593.56	134.6221913
25	5376.85	131.9886131
26	5704.98	135.9563724
27	5056.82	128.0003781
28	5103.24	128.5865374
29	5171.75	129.4467844
30	5428.54	132.6215277
31	5002.39	127.3096367
32	5458.82	132.9908899